Transformation, deformation, and formation of minerals in the Vredefort and Ries impact structure and implications for magnetic properties of impactites

FABIAN DELLEFANT

Dissertation zur Erlangung des Doktorgrades an der
Fakultät für Geowissenschaften der Ludwig-Maximilians-Universität
München

München, 21.08.2023

Erstgutachterin: Prof. Dr. Claudia A. Trepmann
Zweitgutachter: Prof. Dr. Stuart A. Gilder
Tag der mündlichen Prüfung: 08.01.2024

to Milena and Tara, who remind me what's important

and give me hold in turbulent times

Abstract

Shock effects of rock-forming minerals with a focus on Fe-Ti-oxides from the Ries- and the Vredefort impact structures were studied in relation to the magnetic properties. Therefore, samples were investigated from locations characterized by enigmatic magnetic anomalies attributed to the respective impact events. The main aim is to gain insights into the host rocks' stress, temperature and oxygen fugacity evolution. Based on different shock effects in impact breccias, the emplacement conditions of the rocks are discussed.

Archean basement gneisses within the pronounced magnetic anomaly northwest of the Vredefort impact structure center have quartz (SiO_2) grains with shock-generated planar fractures, as documented by two drill cores with ≈10 m depth. Ilmenite ($FeTiO_3$) revealed that shock loading and unloading at relatively low shock pressures (<16 GPa) can result in the formation of mechanical (0001) and $\{10\bar{1}1\}$ twins. At re-equilibration temperatures of 600-700°C, exsolution of magnetite (Fe_3O_4) within ilmenite occurred, forming a few µm-sized magnetite lamellae parallel to the $\{10\bar{1}1\}$ twin boundaries and spheroid magnetite along twin and grain boundaries. Furthermore, shearing fractured and locally melted Fe-bearing oxides, which resulted in their intrusion into adjacent shear fractures within neighboring quartz and feldspar. Dauphiné twins associated with shock-induced planar fractures within quartz suggest that the temperatures before the impact event (paleo-depth of 11-23 km resulting in 650-725°C) were higher than the Curie temperature of magnetite (580°C), which is the carrier of the paleomagnetic orientation. Therefore, uplift of the Archean gneiss upon shock-unloading and subsequent cooling in the magnetic field direction present during the Vredefort impact best explains the observed magnetic remanence. The study, furthermore, found no microstructural difference (i.e., phase assemblage, planar fracture abundance and frequency) between samples from the surface and depth of the two drill cores. Lightning strikes heavily influenced the magnetic record of the surficial rocks, however, microstructural products formed from lightning strikes are likely nm-sized and reside below the resolution of the scanning electron microscope.

Ilmenite in the Ries impact breccias recorded that at moderate shock pressures (>16 GPa), transformation twin lamellae were generated that share a common $\{11\bar{2}0\}$ plane with the host and a 109° angle between the *c*-axes of host and twin. Moreover, new grains with foam structure formed, which are characterized as orientation domains that also share a common $\{11\bar{2}0\}$ plane and whose *c*-axes span 109° or 99° angles. This crystallographic orientation relationship of new grains and the inferred twins indicates the back-transformation from $FeTiO_3$ high-pressure polymorphs (liuite and wangdaodeite). A variety of different high-temperature reactions generated rutile (TiO_2; T=850-1050°C) and minerals of the ferropseudobrookite-armalcolite solid-solution [$(Fe,Mg)Ti_2O_5$; T>1140°C] from ilmenite. Furthermore, redox reactions recorded variations in oxygen fugacity. At high temperatures, an enrichment of iron, in terms of elevated Fe/Ti ratios at the rims of ilmenite aggregates, indicates the presence of a reducing agent during the impactite formation, which generated elemental iron. Cooling and subsequent oxidation of iron formed magnetite. Below 700°C at high oxygen fugacity conditions in combination with a leaching agent, pseudorutile ($Fe_2Ti_3O_9$) was locally created around single ilmenite grains or completely replaced them.

A new occurrence of polymict crystalline breccia in the Ries impact structure at the Aumühle quarry exhibits the direct lithological relationship to the underlying Bunte Breccia and overlying suevite. The polymict crystalline breccia consists of ≈50% shocked crystalline clasts from the Variscan basement and ≈50% components from the sedimentary cover sequence, which display no apparent shock effects. Its emplacement likely occurred during the excavation stage of impact cratering. The

mathematical Maxwell Z-model describes flow fields during excavation, indicating that shocked material from the crystalline basement was ballistically ejected. A mixture with ballistically ejected sedimentary clasts was subsequently placed on top of Bunte Breccia and then covered by suevite. Reworking of Bunte Breccia and suevite to form polymict crystalline breccia can be excluded based on the absence of glass fragments, larger clast sizes, and random paleomagnetic directions of polymict crystalline breccia compared to suevite. The proposed emplacement is consistent with observations of polymict crystalline breccias from other impact structures.

Ballen SiO_2 with characteristically curved fractures within impact melt rocks from the Ries impact structure was investigated to elucidate its formation mechanisms and conditions. It likely originated from fluid-inclusion-rich quartz grains in the gneisses of the crystalline basement. Quartz transformed into diaplectic glass upon shock loading, which partly retained structural information about the precursor phase. As a result, the fluid inclusions dissolved into the amorphous phase. Upon shock unloading and subsequent cooling, dehydration caused fracturing of the glass resulting in curved interfaces as similarly observed from volcanic glasses, i.e., perlitic structures. Structural remnants within the diaplectic glass enabled topotactic crystallization, resulting in preferred crystallographic orientations within quartz. In cases without structural information within the amorphous phase, quartz as well as cristobalite (at elevated temperatures) formed with random crystallographic orientations. Dendritic cristobalite only occurs at the rim of the aggregates in correlation with adjacent vesicles and is interpreted to have formed from a fluid-rich melt.

Contents

Abstract I

Chapter 1

Introduction 1

1.1 Shock effects in minerals 2

1.2 Impactites within the Ries impact structure 3

1.3 Generation of magnetic anomalies 5

1.4 Motivations of the studies 6

1.5 Author publications and contributions 7

Chapter 2

Ilmenite and magnetite microfabrics in shocked gneisses from the Vredefort impact structure, South Africa 9

Abstract 9

Introduction 9

Geological overview 10

Sampling and methods 11

Sampling 11

Optical microscopy and universal stage measurements 13

Scanning electron microscopy 13

Raman spectroscopy 13

Results 13

Sample description 16

Ilmenite and magnetite microfabrics 17

Discussion 19

Deformation conditions 19

Shear heating and mobilization of ilmenite and magnetite 21

Ilmenite twinning 23

Exsolution of magnetite within ilmenite 23

Ilmenite alteration 27

Implications for magnetic properties 27

Conclusions and summary 27
Acknowledgements 29
References 29

Chapter 3

Ilmenite phase transformations in suevite from the Ries impact structure (Germany) record evolution in pressure, temperature, and oxygen fugacity conditions 33
Abstract 33
Introduction 34
Geological overview 35
Methods 36
Results 36
Sample description 36
Phase determination of Fe-Ti-oxides 38
Microfabrics of ilmenite and associated Fe-Ti-phases in suevite from Zipplingen 39
Microfabrics of ilmenite and associated Fe-Ti-phases in suevite from Aumühle 47
Distribution of aggregates within the samples 48
Discussion 49
Ilmenite transformation twins and associated orientation relationship between new grains 50
Ferropseudobrookite and armalcolite formation conditions 53
Formation of rutile within aggregates and magnetite outside aggregates 54
Pseudorutile formation 56
Conclusions and summary 57
Outlook and implications 59
Acknowledgements 59
References 59
Supplementary data 65

Chapter 4

Polymict crystalline breccia in the Ries impact structure - Emplacement of moderately shocked basement clasts during crater excavation and subsequent mixing with weakly shocked sedimentary clasts 66
Abstract 66
Introduction 67

The Ries impact structure and its impact breccias 68
Samples and methods 70
Results 71
Field occurrence of polymict crystalline breccia 71
Shock effects in the basement clasts 73
Maskelynite and mechanical ($\overline{1}01$) twins in amphibole from amphibolite clast 73
Diaplectic SiO_2 glass in gneiss clast 76
Metagranite cataclasite clast 77
Sedimentary clast 79
Discussion 80
Shock and deformation conditions of clasts within polymict crystalline breccia 80
Comparison of polymict crystalline breccia from the Aumühle quarry with similar outcrops in the Nördlinger Ries 81
Polymict crystalline breccia at Aumühle quarry and relation to suevites 82
Relation to dikes of polymict crystalline breccias within the Ries and other impact structures 82
Emplacement of polymict crystalline breccia 83
Conclusions 85
Acknowledgements 85
References 86

Chapter 5

Quartz and cristobalite ballen in impact melt rocks from the Ries impact structure, Germany, formed by dehydration of shock-generated amorphous phases 90
Abstract 90
Introduction 90
Methods 90
Samples 92
Results 92
Discussion 96
Transition of Quartz to Shock-Induced Amorphous Phase 96
Role of Multiple Phase Transformations 101
Formation of Ballen Shape – Dehydration of Amorphous Phase 102
Conclusions 103
Acknowledgements 103
References 103

Chapter 6

Summary, conclusions, and outlook 105

6.1 Ilmenite and magnetite, as well as associated Fe/Ti-phases within impactites 105

6.1.1 Low shock conditions (P<16 GPa) 105

6.1.2 Moderate shock conditions (P>16 GPa) 106

6.2 Implications for properties of Archean basement rocks from the magnetic anomaly northwest of the Vredefort impact structure center 109

6.3 Polymict crystalline breccia emplacement 110

6.4 Formation of ballen SiO_2 111

6.5 Conclusions 114

6.6 Outlook 115

References 116

Appendix 128

Abbreviation glossary 128

Chemical formulae of minerals 128

Acknowledgements 129

Note that this is a cumulative PhD Thesis, representing a compilation of two published (Chapters 2 and 5), one accepted (Chapter 3), and one submitted manuscript (Chapter 4), which do not contain numbered headings of their contents. Therefore, only the framework of this thesis (Chapter 1 and 6) contains numbered headings.

1 Introduction

More than 200 impact structures are confirmed on Earth, whose surface is strongly modified and recycled by plate tectonics and the biosphere, both unique features in our solar system (Osinski et al. 2022). In contrast, over 100,000 meteorite craters occur on the lunar surface (Yang et al. 2020). Since the 21st century, impact cratering has been widely recognized as one of the most fundamental geological processes in the solar system. The Moon was likely formed by the impact of the planetoid Theia into the proto-Earth (Giant Impact Hypothesis: e.g., Canup 2012; Herwartz et al. 2014). Moreover, the early crust formation (e.g., Grieve et al. 2006; Latypov et al. 2019) and the initiation of plate tectonics on Earth (e.g., Johnson et al. 2022) are discussed as a consequence of major impact events. Necessary chemical ingredients for life on Earth might have been generated or delivered by impacts, where furthermore habitats could have formed within crater lakes, impact-generated rocks, and hydrothermal systems (e.g., Reimold et al. 2005; Grieve 2013; Osinski et al. 2020 and references therein).

During impact-cratering, target rocks are subjected to extremely high pressures, stresses, strain-rates, and temperatures, as well as fast changes in redox conditions within milliseconds during shock loading, unloading, and subsequent modifications processes (e.g., Melosh 1989; Migault 1998; Nesterenko 2001; Sharp and DeCarli 2006). As a result, minerals within the target rocks can be modified by, e.g., fracturing, straining the crystal structure, creating dislocations, twinning, and re-arrangement of atomic positions, which can lead to phase changes. As for rock-forming silicate minerals (e.g., Deer et al. 2013), the analysis of Fe-Ti-oxides can reveal information about their formation and the deformation of the host rock (e.g., Rahmdor 1969; Haggerty 1991). The magnetic characteristics of iron-bearing and ferrimagnetic minerals within impact structures can be significantly influenced by shock effects, which can result in large-scale magnetic field anomalies (e.g., Pilkington and Grieve 1992; Scott et al. 1997; Plado et al. 1999; Pilkington and Hildebrand 2000; Ugalde et al. 2005; Pohl et al. 2010). However, modifications on iron-bearing and magnetic minerals within target rocks as a result of shock-pressure, shock-generated heat with subsequent changes in redox conditions, and post-shock modifications are not-well understood. Furthermore, the influence of those shock effects on the host rock's magnetic properties and how the iron-bearing minerals record the intensity and direction of the ambient field is poorly known (e.g., Reznik et al. 2016, 2017; Gilder et al. 2018). Variations in magnetic properties were attributed to changes, such as phase transitions and exsolutions of ferrimagnetic grains, crystal-plastic deformation, and grain size reduction through fracturing, however, correlations of magnetic investigations to microstructural analyzes to confirm how the magnetic recording is affected by meteorite impacts remain scarce (e.g., Mang and Kontny 2013; Mang et al. 2013; Kontny and Grothaus 2016).

This thesis aims to characterize and identify microfabrics of Fe-Ti-oxides, such as ilmenite ($FeTiO_3$) and magnetite (Fe_3O_4), which are generated and/or modified by meteorite impacts and correlate them with magnetic anomalies of the host rocks. Shock effects within silicates, such as quartz (SiO_2) and impact-generated other SiO_2 polymorphs, are investigated and used as pressure indicators. For this purpose, the Vredefort impact structure (South Africa) and the Ries impact structure (Germany) were selected for their different occurrences of shocked rock types. The Vredefort impact structure is about 2.02 Ga old (Spray 1995; Kamo et al. 1996; Gibson et al. 1997) and deeply eroded with a diameter of 80-90 km displaying mainly the crystalline basement (McCarthy et al. 1990; Gibson et al. 1998; Henkel and Reimold 1998). In contrast, the Nördlinger Ries is 14.8 Ma old (Rocholl et al. 2017, 2018; Schmieder et al. 2018a, 2018b; Schwarz et al. 2020), has a diameter of about 26 km, and is one of the best-preserved impact structures in the world, where impact rocks, such as Bunte Breccia, suevite,

and impact melt rocks, are studied extensively since the 1960s. Lithologies with enigmatic magnetic anomalies, which experienced low (<1 GPa) to high (>60 GPa) shock pressures and respective shock temperatures of up to 1300°C, were selected to investigate their emplacement conditions and/or modification mechanisms based on the correlation of field observations and microfabric analysis.

1.1 Shock effects in minerals

To correlate the shock effects observed in iron-bearing minerals, known shock effects of abundant rock-forming minerals can be used as shock pressure gauges. This chapter summarizes some significant phase transformations, deformations, and formations as well as related microfabrics.

Planar deformation features (PDFs) within quartz are diagnostic for meteorite impacts and are commonly used as shock-pressure indicators (Goltrant et al. 1991, 1992a, 1992b; Langenhorst 1994; Langenhorst and Deutsch 1994; Leroux et al. 1994; Stöffler and Langenhorst 1994; Leroux and Doukhan 1996; Trepmann et al. 2005; Trepmann and Spray 2006). During shock compression >10 GPa, PDF orientations parallel to crystallographic planes are generated, where a high-density amorphous phase (diaplectic glass) forms from quartz as a result of structural instabilities (Goltrant et al. 1992a, 1992b; Langenhorst 1994; Trepmann and Spray 2006; Trepmann 2008). Experiments on feldspar revealed a PDF generation as a function of shock pressure and chemical composition at 34 GPa within albite ($NaAlSi_3O_8$) and in the range of 18/22 – 24 GPa within anorthite ($CaAl_2Si_2O_8$) (Schaal and Hörz 1977; Ostertag 1983).

Diaplectic silica glass (SiO_2) forms at shock pressures ranging from 34 to 50 GPa as a solid-state transition from quartz (Stöffler 1971a, 1972; Stöffler and Hornemann 1972; Kowitz et al. 2013). Its density and optical refractive index are higher than glass quenched from a melt (Stöffler and Langenhorst 1994). Hörz and Quaide (1973) demonstrated a gradual lattice breakdown as a function of increasing shock pressures and a possible resulting crystallographic structural memory of diaplectic glass. Plagioclase (solid solution of albite and anorthite) transforms into diaplectic glass (maskelynite) in the range of 24/34 to 40 GPa (Stöffler and Hornemann 1972; Kieffer et al. 1976; Schaal and Hörz 1977; Ostertag 1983; Stöffler et al. 1986; Schmitt 2000). Arndt et al. (1982) proposed that diaplectic glass forms as a result of the short duration of the shock-induced transient high-temperature excursion, where the melt transition does not come to completion, i.e., an intermediate state between a supercooled liquid and a solid.

Planar fractures (PFs) within quartz occur along cleavage planes, such as (0001) and $\{10\overline{1}1\}$ (e.g., Tröger 1982), and are thus non-diagnostic (e.g., Brückner et al. *submitted*), albeit common, shock effects occurring from 5 to 34 GPa (Stöffler and Langenhorst 1994; French and Koeberl 2010; Stöffler et al. 2018). Cleavage occurs as material relaxation during tensile load as a brittle fracture process along crystallographic planes (e.g., Schultz et al. 1994). The initiation of cleavage cracks is controlled by, e.g., fracture toughness of the crystallographic plane as a function of bond density, elastic modulus, and surface free energy (e.g., Kranz 1983; Thompson and Knott 1993; Schultz et al. 1994; Armstrong 2015). In contrast, feather features (FFs) are shear fractures, which contain sets of secondary short fractures at the tensional domain during shear fracture propagation characterized by transient tensile stresses (Poelchau and Kenkmann 2011; Ebert et al. 2020). These secondary cracks are similar to those at the tensile domain related to the propagation of shear fractures during seismic rupturing (Di Toro et al. 2005). The secondary fractures of FFs are oriented parallel (0001), $\{10\overline{1}1\}$, and $\{11\overline{2}2\}$ (Poelchau and Kenkmann 2011; Ebert et al. 2020). The formation of FFs is reported for samples

below 18 GPa based on investigations of impactites (Poelchau and Kenkmann 2011) and shock experiments (Tada et al. 2022).

High-pressure polymorphs (structural change with the same stoichiometry) of minerals can form from a solid-state reaction upon shock loading. Graphite-bearing gneisses in the Ries impact structure are reported to contain shock-induced diamonds, which have formed at 30-40 GPa from graphite (El Goresy et al. 2001). At ambient temperature conditions, quartz transforms to coesite at >3 GPa and stishovite at >7 GPa (Hemley et al. 1994 and references therein). An ilmenite high-pressure polymorph named liuite (Ma and Tschauner 2018) forms >16 GPa (e.g., Liu 1975; Leinenweber et al. 1991). Upon decompression, wangdaodeite (Xie et al. 2020) is generated as a metastable polymorph (e.g., Mehta et al. 1994) and was recently identified in the Ries impact structure (Tschauner et al. 2020).

Crystal twins can be generated as a result of meteorite impacts and are generally defined as an intergrowth of at least two crystallographic domains of the same crystal species. A twin law can express their orientation relationship and represents an additional symmetry operation to those defining their space group (e.g., Hahn and Klapper 2006). Mechanical twinning of crystals results from tectonic and shock-induced shear stresses (e.g., Seybold et al. 2023). Ilmenite mechanical $\{10\bar{1}2\}$ twins due to tectonic deformation are common (e.g., Minkin and Chao 1971; Frick 1973; Reynolds 1984). Ilmenite twins with boundaries parallel $\{10\bar{1}1\}$ have been experimentally formed at a differential stress of 0.75 GPa, a confining pressure of 1.3 GPa, and a strain rate of 10^{-4}/s at 25°C (Minkin and Chao 1971). Shock-induced twinning of ilmenites has been reported from lunar rocks, as well as shock experiments, where twins with boundaries parallel (0001) and $\{10\bar{1}1\}$ are documented (Minkin and Chao 1971; Sclar et al. 1973; Syono et al. 1981). At shock compression <8 GPa, Brazil twin lamellae parallel (0001) form in quartz, which are likely the result of high differential stresses (Goltrant et al. 1992a, 1992b; Leroux et al. 1994; Leroux and Doukhan 1996; Trepmann and Spray 2005, 2006; Trepmann 2008, 2009). Transformation twinning can occur due to retrograde phase transitions either as a result of high-pressure and/or high-temperature excursions. Hexagonal β-quartz transforms to trigonal α-quartz at <573°C at ambient pressure resulting in the generation of Dauphiné twins, which are rotated 180° around their *a*-axes (e.g., Tullis 1970; Markgraaff 1986; Heaney and Veblen 1991).

Upon shock loading, the target is compressed, which leads to an increase in internal energy. This irreversible pressure-volume work results in heating (Osinski et al. 2013) in addition to frictional heat generation, which can strongly affect the mineralogy. Quartz transforms at ambient pressure conditions to tridymite (SiO_2) at >870°C, to cristobalite (SiO_2) at >1470°C, and eventually into a silica melt at >1705°C (e.g., Heaney 1994 and references therein). Ilmenite is reported to decompose into rutile (TiO_2), elemental iron (Fe), and oxygen (O_2) at 850°-1050°C and low oxygen fugacity (e.g., Taylor et al. 1972). Ferropseudobrookite ($FeTi_2O_5$) forms from ilmenite at >1140°C at a low oxygen fugacity (Lindsley 1965; Keil et al. 1970; Tuthill and Sato 1970), whereas pseudobrookite (Fe_2TiO_5) is generated at >800°C and high oxygen fugacity (Fu et al. 2010). Biotite ($K(Mg,Fe,Mn)_3[(OH,F)_2|(Al,Fe,Ti)Si_3O_{10}]$) is often used as a temperature gauge and decomposes at >600°C forming magnetite (Fe_3O_4) and hematite (Fe_2O_3) (Wones and Eugster 1965).

1.2 Impactites within the Ries impact structure

On Earth, impact-generated rocks are formed from single impact events, whereas on other planetary bodies, such as the moon, impactites likely record multiple impact events (Stöffler et al. 2018). Well-preserved impact structures, like the Nördlinger Ries, can exhibit different impactites generated during impact cratering with various degrees of experienced shock pressures. Although the heavily

eroded Vredefort impact structure is the subject of this thesis, the only impactite remnants are, e.g., pseudotachylytes (e.g., Reimold and Collision 1994) and impact melt dikes (granophyres; e.g., Huber et al. 2022) in the crater floor, which were not studied here and are, therefore, not described in this chapter.

The “Bunte Trümmermassen” (German for “varicolored debris masses”) represent a proximal allochthonous impact blanket with the largest clast sizes of impactites and encompasses the “Bunte Breccia” (German for “varicolored breccia”) and megablocks (von Engelhardt 1990; Stöffler et al. 2018). Megablocks have single clast sizes of >25 m (e.g., Sturm et al. 2015), which were fragmented and displaced as a result of the crater formation (Pohl et al. 1977; Stöffler et al. 2013, 2018). The Bunte Breccia is a lithic breccia with mm- to m-sized clasts and is commonly constituted of >90% sedimentary components without glass fragments and relatively low shock conditions (P<10 GPa; T<100°C) (e.g., Hörz et al. 1983; von Engelhardt 1990; Stöffler and Grieve 2007; Stöffler et al. 2018). The emplacement of the Bunte Trümmermassen is suggested to have occurred as a rolling-gliding base surge (Chao et al. 1987) and/or a ground level debris flow (Oberbeck 1975; Hörz et al. 1983). The latter model was used to analogize lunar ejecta formations without an atmosphere under dry conditions (Oberbeck 1975). Sturm et al. (2013) compiled data on the Ries Bunte Breccia thickness and reported a thicker accumulation at ≈1.45-2.12 Rc (crater radii) compared to reduced thickness at ≈1.00-1.45 sRc, which resembles as moat and rampart morphology. The model of a rolling-gliding base surge (Chao et al. 1987) is based on field observations, such as plastic flow and tight folding of clay-bearing units of distant stratigraphies and plastic deformation of clay ironstone and carbonatic rock at isostatic pressures of ≈3 GPa (Chao et al. 1987), as well as striations on rock surfaces (e.g., Chao 1976; Chao et al. 1987), and large ejecta deposits in pre-Ries lowlands and vallies (Bader and Schmidt-Kaler 1977). Smearing, twisting, and folding of Tertiary clays, which occur wrapped around clasts is interpreted as ductile deformation during emplacement of the Bunte Breccia (Pietrek and Kenkmann 2016).

Suevite contains cogenetic (devitrified) glass fragments (Flädle) as well as lithic clasts and minerals of the target rock within a fine-grained matrix of the same material (e.g., Pohl et al. 1977; Stöffler and Grieve 2007; Stöffler et al. 2013, 2018). Shock effects within minerals indicate shock pressures up to 45 GPa as well as temperatures likely reaching up to 900°C (e.g., von Engelhardt et al. 1995; Stöffler and Grieve 2007; Stöffler et al. 2013, 2018 and references therein). Suevite is commonly observed overlaying the Bunte Trümmermassen (Stöffler et al. 2013 and references therein); however, different emplacement models are discussed: deposition by a granular fluid-based density current similar to ignimbrite formation of volcanic systems (Siegert et al. 2017), collapse of a phreatomagmatic plume system (Artemieva et al. 2013; Stöffler et al. 2013), deposition of an impact melt flow (Bringemeier 1994; Osinski et al. 2004; Meyer et al. 2011) or density flow (Newsom et al. 1990), as well as a collapse of an ejecta plume (von Engelhardt 1997).

Impact melt rocks can be crystalline, semi-hyaline, or hyaline and solidified from an impact melt. Shock effects within clastic debris can indicate variable degrees of shock, whereas whole rock melting itself is the highest degree of shock modification representing shock pressures >60 GPa and temperatures likely up to 1500°C (e.g., Dence 1971; Grieve 1987; Stöffler and Grieve 2007; Stöffler et al. 2018 and references therein). In the Ries impact structure, impact melt occurs commonly within the megablock zone, reaching approximately 4-12 km radial distance from the impact center (e.g., von Engelhardt 1997; Buchner et al. 2010; Stöffler et al. 2013).

Polymict crystalline breccia in the Nördlinger Ries consists of allochthonous or parautochthounous clasts from various crystalline rocks of the Variscan basement, such as metagranites, amphibolites, and gneisses, which experienced shock pressures of up to a few tens of GPa. Furthermore, minor

amounts of sedimentary clasts from the sedimentary cover sequence occur within a fine-grained matrix likely derived from the clasts (Abadian 1972; von Engelhardt and Graup 1984; von Engelhardt 1990; Hüttner and Schmidt-Kaler 1999; Stöffler et al. 2013). Polymict crystalline breccias typically occur as irregular bodies on top of the Bunte Breccia (Abadian 1972; Arp et al. 2019). Their formation conditions and the exact stratigraphic relationships in the Nördlinger Ries remain unclear (Pohl et al. 1977; von Engelhardt 1990; Stöffler et al. 2013).

1.3 Generation of magnetic anomalies

Earth's magnetic field is generated by electric currents within the planet's core due to the convection of molten iron and nickel, the so-called geodynamo (e.g., Wicht and Sanchez 2019 and references therein). As a result, it forms a magnetic dipole, which is currently oriented that the magnetic north pole is almost aligned with the geographic south pole, which is defined as normal polarity (e.g., Basavaiah 2011). However, the magnetic poles slowly but continuously move over geological time scales (e.g., Schettino and Scotese 2005) and irregularly switch their polarization, which can result in a reversed polarity, i.e., the magnetic north pole is almost aligned with the geographic north pole (e.g., Clement 2004), present for example at the Vredefort and Ries impact event (Hargraves 1970; Pohl et al. 2010).

When magnetic minerals, such as (titano-)magnetite and (titano-)hematite, crystallize from a melt or precipitate from a fluid within a magnetic field, they can record the surrounding magnetic field direction and intensity (e.g., Butler 1992). An external magnetic field can also control the orientation of magnetic carriers within sediments (e.g., Katari and Bloxham 2001). Therefore, rocks can acquire a natural remanent magnetization (NRM), which records the Earth's magnetic field direction at the time the mineral was formed or deposited (e.g., Butler 1992). Remagnetization of magnetic minerals can occur due to several processes. If the new magnetic orientations differ from the initial NRM orientations, for example, the magnetic mineral formed in a reversed polarity and was remagnetized in a normal polarity of Earth, local magnetic orientation anomalies can be created. Magnetic carriers can be remagnetized by heating them above their respective Curie (ferro-/ferrimagnetism, e.g., magnetite) or Neél (antiferromagnetism, e.g., hematite) temperature, which results in a phase transition towards a paramagnetic mineral. Subsequent cooling leads to a back transformation, which records the present external magnetic field as a thermal remanent magnetization (TRM) (e.g., Dekkers 2012). However, the remanent magnetization can be modified at constant temperatures below the respective Curie or Neél temperatures to form an isothermal remanent magnetization (IRM) (e.g., Jackson 2007). For example, changes in the chemical environment, such as redox conditions, can lead to the modification and generation of new magnetic carriers, which can overprint the present magnetic record and produce a chemical remanent magnetization (CRM) (e.g., Tonti-Filippini et al. *in preparation*). Lightning strikes are characterized as strong electric currents resulting in strong magnetic field strengths (e.g., Rakov and Uman 2003), which can remagnetize the magnetic minerals and thus produce a lightning-induced remanent magnetization (LIRM) (e.g., Carporzen et al. 2012). Besides the magnetic anomalies resulting from different magnetic directions, changes in the magnetization intensities can also produce anomalies. For example, oxidation of magnetite nanoparticles to hematite nanoparticles would lower the total saturation magnetization from 39.5-70 $JT^{-1}kg^{-1}$ (Mufti et al. 2020) to 0.3 $JT^{-1}kg^{-1}$ (Teja and Koh 2009). In contrast, reducing magnetite to elemental iron would increase the total saturation magnetization to 217.6 $JT^{-1}kg^{-1}$ (Crangle and Goodman 1971).

The Vredefort impact structure displays a long-wavelength negative magnetic anomaly (<-3000 nT) northwest of the impact center, which is attributed to thermal overprinting during impact when the Earth's magnetic field was in a reversed polarity state (e.g., Hargraves 1970; Carporzen et al. 2012). Lithologies closer to the center of the structure do not show a negative field anomaly, which is explained due to lower concentrations of magnetite (e.g., Hart et al. 1995; Carporzen et al. 2005). Carporzen et al. (2012) demonstrated that the top one m surface layer within the magnetic anomaly is remagnetized by lightning strikes, which produced short-wavelength, high-amplitude anomalies, whereas deeper samples display the magnetization also documented from impact melt rocks (e.g., Hargraves 1970; Carporzen et al. 2005; Salminen et al. 2009). Within the Ries impact structure, the negative magnetic anomalies correlate with the occurrence of suevites, which are likely deposited above the Curie temperature of magnetite (580°C) and, therefore, recorded the reversed polarity magnetic field during the Ries impact event (Pohl et al. 2010).

1.4 Motivations of the studies

Generally, investigations of shock effects on iron-oxides and their correlation to magnetic anomalies of their host lithologies remain poorly understood. Therefore, ilmenite and magnetite were investigated from low- to highly shocked lithologies from impact structures with enigmatic magnetic anomalies, i.e., the Ries impact structure and the Vredefort impact structure.

Although ilmenite is a common opaque Fe-Ti-oxide in igneous and metamorphic rocks, studies on its response to shock from meteorite impacts remains scarce. $FeTiO_3$ high-pressure polymorphs were first described in meteorites, i.e., liuite in Shergotty martian meteorite (Ma and Tschauner 2018) and wangdaodite in Suizhou L6 chondrite (Xie et al. 2020). However, the structural relation of ilmenite and its high-pressure polymorphs is unclear. Due to its abundance and role as a resource for, e.g., TiO_2 (Sibum et al. 2012), ilmenite phase transformations as a function of temperature (e.g., Lindsley 1965; Taylor et al. 1972; Fu et al. 2010), and changes in redox conditions (e.g., Teufer and Temple 1966; Gupta et al. 1990; Zhao and Shadman 1990) are well-characterized. To study the response of ilmenite to low and high shock pressures with respective shock-induced temperatures, case studies were conducted with Archean basement samples from the Vredefort impact structure shocked at relatively low pressures <20 GPa (e.g., Grieve et al. 1990; Reimold and Gibson 2005) and suevite samples from the Ries impact structure that experienced high shock pressures up to 60 Gpa (e.g., Stöffler et al. 2013). The results are addressed in Chapter 2 and Chapter 3, respectively.

At the magnetic anomaly northwest of the Vredefort impact center, the magnetic directions below the top one m surface layer are aligned as those derived from impact melt rocks (e.g., Hargraves 1970; Carporzen et al. 2005). This indicates that the investigated basement rocks cooled through the Curie temperature of magnetite (580°C) after impact (e.g., Henkel and Reimold 1998, 2002; Muundjua et al. 2007; Salminen et al. 2009). However, the heat source remains unknown and will be discussed in this thesis. Furthermore, Carporzen et al. (2012) suggest that magnetite observed along shock-induced planar features, as documented in several studies in the Archean Vredefort gneisses (Grieve et al. 1990; Hart et al. 1991, 2000; Cloete et al. 1999; Carporzen et al. 2006), are a result of lightning-induced melting. Their exact emplacement mechanism, however, is not understood and will be addressed in this thesis in Chapter 2.

In the Nördlinger Ries, only a few studies have concerned polymict crystalline breccia (Abadian 1972; Abadian et al. 1973; Graup 1978). Therefore, there is no uniform definition, and the stratigraphic relation as well as the emplacement mechanism are unclear (Stöffler 1971b; Abadian 1972; Abadian

et al. 1973; Graup 1978; von Engelhardt 1990). A new outcrop of polymict crystalline breccia and characterizations of shock effects as well as insights into its emplacement with a correlation to magnetic properties and comparison to other impact structures, will be addressed in this thesis in Chapter 4.

Due to its abundance on the Earth's crust and the generation of characteristic shock effects, such as PDFs, quartz microfabrics are well-investigated and commonly used as diagnostic criteria for meteorite impacts and as shock pressure gauges (e.g., Langenhorst and Deutsch 1994; Stöffler and Langenhorst 1994; Trepmann and Spray 2005). However, the formation mechanism of aggregates comprised of globular quartz generated by meteorite impacts remains poorly understood. Those so-called "ballen" aggregates, consisting of spherical quartz with sizes ranging from 10 to few hundred µm in diameter, have been documented from several impact structures, predominantly from impactites affected by high post-shock temperatures (Short 1970; von Engelhardt 1972; Carstens 1975; Bischoff and Stöffler 1984; Rehfeldt-Oskierski et al. 1986; French 1998; Osinski 2004; Ferrière et al. 2008, 2009, 2010; Buchner et al. 2010; Chen et al. 2010; Schmieder et al. 2014; Chanou et al. 2015). Their formation is interpreted to result from a back-transformation from shock-induced states and is, therefore, argued as an impact-characteristic criterion (Carstens 1975; Bischoff and Stöffler 1984; Ferrière et al. 2009). However, their formation mechanism and the potential influence of multiple phase transformations from quartz to amorphous phases back to quartz remain unclear, as are the conditions under which ballen form (Ferrière et al. 2010). Based on melt rock samples from the Ries impact structure, a study about ballen characterization with electron backscatter diffraction (EBSD) analysis and interpretations on ballen formation mechanisms has been carried out within the framework of this thesis and is addressed in Chapter 5.

1.5 Author publications and contributions

Four research projects were designed to address the aims of this thesis, which Chapter 2 encompasses to Chapter 5. Fabian Dellefant (FD) and his supervisors Claudia Trepmann (CT) and Stuart Gilder (SG) collaborated with Iuliia Sleptsove (IS), Lina Seybold (LS), Melanie Kaliwoda (MK), Wolfgang Schmahl (WS), Kai-Uwe Hess (KUH), Ben Weiss (BW), Stefan Hölzl (SH), and Dirk Müller (DM). The respective author contributions and publication/manuscript status are addressed in the following.

- Chapter 2 (*Chap. 2*) by Dellefant et al. (2022): *"Dellefant, F., Trepmann, C.A., Gilder, S.A., Sleptsova, I.V., Kaliwoda, M., and Weiss, B.P. (2022) Ilmenite and magnetite microfabrics in shocked gneisses from the Vredefort impact structure, South Africa. Contributions to Mineralogy and Petrology, 5."*

  FD, CT, and SG designed the study. SG and BW carried out fieldwork and sampling. FD conducted thin section analyses with transmitted and reflected light microscopy, scanning electron microscope (SEM), and EBSD measurements under the supervision of CT. Phase determinations by Raman spectroscopy were carried out by FD. FD merged the data and drafted the manuscript. All authors contributed to the interpretation and discussions. The results were published online on the 5th of September, 2022.

- Chapter 3 (*Chap. 3*) by Dellefant et al. (2023): "*Dellefant, F., Trepmann, C.A., Schmahl, W.W., Gilder, S.A., Sleptsova, I.V., and Kaliwoda, M. (2023) Ilmenite phase transformations in suevite from the Ries impact structure (Germany) record evolution in pressure, temperature, and oxygen fugacity conditions. American Mineralogist, in press.*"

  FD and CT designed the study. CT carried out sampling. Under the supervision of CT, FD conducted microstructural analyses by optical microscopy with transmitted and reflected light microscopy as well as SEM and EBSD measurements. FD carried out phase determinations by Raman spectroscopy. DM and FD carried out electron microprobe (EMP) data acquisition. FD merged the data and drafted the manuscript. FD, CT, WS, SG, IS, and MK contributed to the interpretations and discussions. The results were accepted for publication on the 24th of July, 2023.

- Chapter 4 (*Chap. 4*) by Dellefant et al. (*submitted*): *"Dellefant, F., Seybold, L., Trepmann, C.A., Gilder, S.A., Sleptsova, I.V., Hölzl, S., and Kaliwoda, M. - Polymict crystalline breccia in the Ries impact structure - Emplacement of moderately shocked basement clasts during crater excavation and subsequent mixing with weakly shocked sedimentary clasts. International Journal of Earth Sciences."*

  CT, SG, and FD designed the study. Sampling was carried out by SG, IS, FD, and CT. FD and CT conducted microstructural analyses by transmitted light microscopy, SEM, and EBSD. Phase determinations by Raman spectroscopy were carried out by FD. FD merged the data and drafted the manuscript. All authors contributed to the interpretation and discussions. The results were submitted on the 15th of August, 2023.

- Chapter 5 (*Chap. 5*) by Trepmann et al. (2020): *"Trepmann, C.A., Dellefant, F., Kaliwoda, M., Hess, K.U., Schmahl, W.W., and Hölzl, S. (2020) Quartz and cristobalite ballen in impact melt rocks from the Ries impact structure, Germany, formed by dehydration of shock-generated amorphous phases. Meteoritics and Planetary Science, 55, 2360–2374."*

  CT designed the study. Under the supervision of CT, FD conducted microstructural analyses by transmitted light microscopy and phase determination by Raman spectroscopy. CT performed the SEM and EBSD measurements, merged the data, and drafted the manuscript. All authors contributed to the interpretations and the manuscript. The results were published online on the 24th of November, 2020.

Contributions to Mineralogy and Petrology (2022) 177: 88
https://doi.org/10.1007/s00410-022-01950-5

ORIGINAL PAPER

Ilmenite and magnetite microfabrics in shocked gneisses from the Vredefort impact structure, South Africa

Fabian Dellefant[1] · Claudia A. Trepmann[1] · Stuart A. Gilder[1] · Iuliia V. Sleptsova[1] · Melanie Kaliwoda[1,2] · Benjamin P. Weiss[3]

Received: 18 February 2022 / Accepted: 27 July 2022 / Published online: 5 September 2022

Abstract

We investigated microfabrics of shocked Archean gneisses from two, 10 m-deep drill cores located near the center of the Vredefort impact structure in an area that is characterized by a prominent, long-wavelength negative magnetic anomaly (< -3000 nT) together with short-wavelength, high-amplitude anomalies attributed to lightning strikes. Planar fractures and feather features in quartz, which can be partially recrystallized, indicate shock conditions less than 20 GPa. Micrometer-sized magnetite and ilmenite along shock-related shear fractures in quartz and feldspar emanate from adjacent deformed coarse (> 100 µm) ilmenite and magnetite host grains. These fine-scaled veins suggest mobilization of magnetite and ilmenite during shear deformation of host Fe-phases and adjacent silicates, probably associated with frictional heating. Coarse ilmenite has fine-lamellar mechanical twins parallel to $\{10\bar{1}1\}$ and single (0001) twins, indicative of dislocation-glide-controlled deformation under non-isostatic stresses related to shock. A few µm-wide magnetite lamellae parallel to $\{10\bar{1}1\}$ and spheroidal magnetite (diameter ≈10 µm) within coarse ilmenite document exsolution after shock. Dauphiné twins associated with planar features in quartz imply cooling from 650 to 725 °C after shock, which accords with estimates of pre-impact basement temperatures from petrographic studies. The Curie temperature of magnetite is 580 °C; therefore, the central negative magnetic anomaly was produced as a thermoremanent magnetization acquired during cooling of the initially hot crust. The long-wavelength anomaly was likely amplified by the newly created magnetite that also acquired a thermal remanence. Although the magnetic properties of surface samples are often influenced by lightning strikes, we found no microstructural evidence for lightning-related processes.

Keywords Shock effects · Ilmenite twins · Magnetite exsolution · Magnetite and ilmenite veins · Frictional heating · Planar fractures

Introduction

Large meteorite impacts impart rapid stress changes onto the target rocks during shock loading and subsequent unloading; elevated temperature conditions as well as changes in redox conditions prevail over longer time scales (Melosh 1989; Migault 1998; Nesterenko 2001; Sharp and DeCarli 2006). Upon these changes, the microstructures of the target rocks are permanently modified. Minerals undergo phase transformation (e.g., melting, amorphization, exsolution) and deformation (e.g., fracturing, twinning) on different time scales throughout the cratering process. We refer to "shock" for all processes that affect the target rocks during impact cratering and to "shock effects" for the resulting microstructures. The microstructural changes influence the magnetic properties of ferrimagnetic minerals within impact structures, leading to distinct km-scale magnetic field anomalies (Fig. 1) (Pilkington and Grieve 1992; Scott et al. 1997; Plado et al. 1999; Pilkington and Hildebrand 2000; Ugalde et al. 2005; Pohl et al. 2010). However, the effect of shock pressure, shock-generated heat, and post-shock modifications on magnetic

Communicated by Timothy L. Grove.

✉ Fabian Dellefant
fabian.dellefant@lmu.de

[1] Department of Earth and Environmental Sciences, Ludwig-Maximilians-University, Munich, Germany

[2] Mineralogical State Collection, SNSB, Munich, Germany

[3] Department of Earth, Atmospheric and Planetary Sciences, Massachusetts Institute of Technology, Cambridge, MA, USA

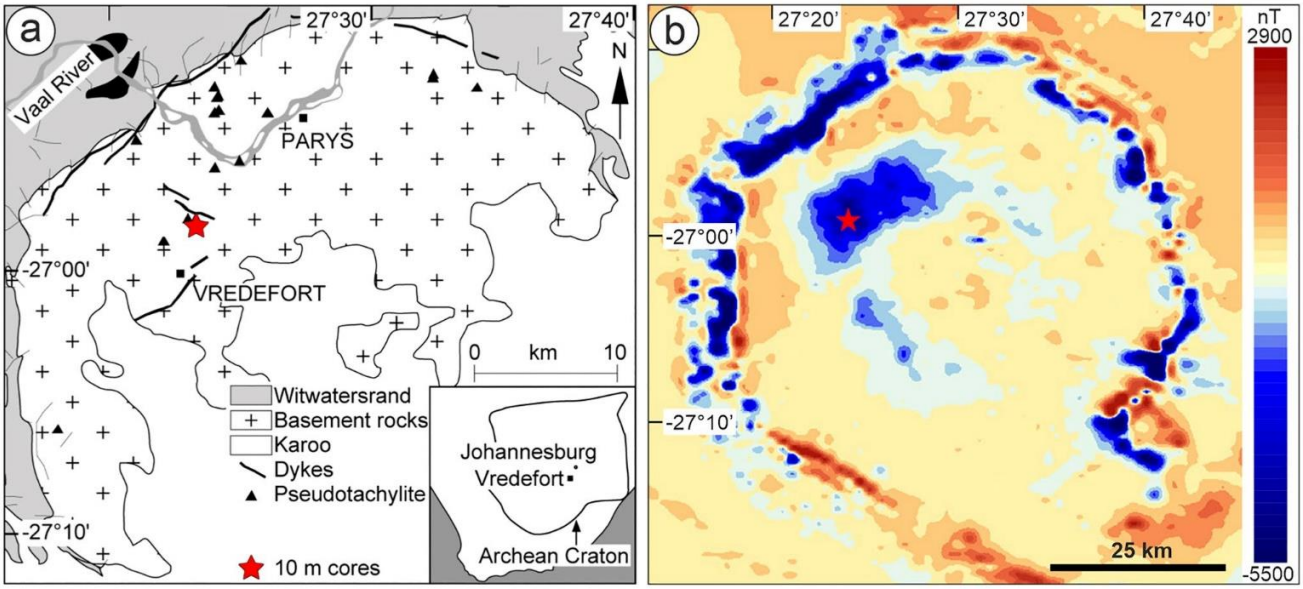

Fig. 1 **a** Simplified geological map of the Vredefort impact structure (modified after Nel 1927 and Carporzen et al. 2012). **b** Sample location (red star) in the aeromagnetic anomaly map based on data of Antoine et al. (1990) and Corner et al. (1990); modified after (Gilder et al. 2018). Sample location is shown by red star

minerals are poorly understood (Reznik et al. 2016, 2017; Gilder et al. 2018).

Lightning strikes can also effect magnetic minerals by rapidly changing temperature and redox conditions (Rakov and Uman 2003; Salminen et al. 2013). The magnetic fields produced by lightning are typically characterized by high Koenigsberger ratios, defined as the ratio of the natural remanent magnetization (NRM) to the magnetization induced by Earth's magnetic field (Koenigsberger 1938). Furthermore, lightning-induced magnetic fields can be characterized by ratios of the NRM divided by a saturating isothermal remanent magnetization that approach 1 (Kletetschka et al. 2004). As a result, long-lived crustal magnetic fields can be generated by lightning that extend a few m to several tens of m, displaying gradients of up to tens of nT/m (Sakai et al. 1998; Verrier and Rochette 2002; Appel et al. 2006; Shimizu et al. 2007).

The Vredefort impact structure is characterized by large, km-scale (> 1000 nT) magnetic anomalies (Hargraves 1970; Hart et al. 1995; Muundjua et al. 2007; Carporzen et al. 2012). Moreover, the surface is subjected to frequent lightning strikes (Gijben 2012), which includes the area northwest of the center, which possesses a km-scale negative magnetic anomaly (red star in Fig. 1) superimposed on the short-wavelength anomalies due to lightning. Single-domain (SD) magnetite observed within planar shock effects in quartz from this location has been related to both the impact shock event (Grieve et al. 1990; Hart et al. 1991; Cloete et al. 1999) and lightning strikes (Carporzen et al. 2012). Carporzen et al. (2012) showed that samples from two 10 m-deep drill cores up to 100 cm below the surface exhibit dual Verwey transition temperatures (120–130 and 90–110 K) and high remanent coercivities (≈ 40 mT). The population with higher Verwey transition temperatures and lower coercivities was ascribed to original, Archean multi-domain (MD) magnetite, while the fraction with lower Verwey transition temperatures and higher coercivities was ascribed to lightning strikes. At depths below the influence of lightning overprinting, the magnetization was interpreted as a thermoremanent magnetization acquired in the geomagnetic field following impact at 2.02 Ga (Carporzen et al. 2012).

The samples drilled within the high-amplitude anomaly of the shocked Archean basement rocks within the Vredefort Dome described by Carporzen et al. (2012) offer an ideal occasion to evaluate microstructural differences within rocks from the same locality (i.e., at similar shock conditions) to distinguish the local influence of lightning or meteorite impact on magnetite and ilmenite microfabrics and on the magnetic properties, which is the aim of this study.

Geological overview

The Vredefort Dome lies in the Witwatersrand Basin, central Kaapvaal Craton, South Africa (27° 00′ S, 27° 30′ E, Fig. 1), centered approximately 120 km southwest of Johannesburg. It is a deeply eroded, 80–90 km diameter structure formed by a meteorite impact at ca. 2.02 Ga (Spray 1995; Kamo et al. 1996; Gibson et al. 1997). A 40–50 km central

region of Archean amphibolite- to granulite-facies migmatitic gneiss is surrounded by a 15–20 km wide collar of late Archaean to early Proterozoic rocks (Armstrong et al. 1991). The oldest age estimated from the gneiss is 3.6 Ga based on a comparison to the Barberton basement rocks (Compston and Kröner 1988; Hart et al. 1990; de Wit et al. 1992; Zeh et al. 2011). The upper amphibolite- to granulite-facies metamorphism in the core region occurred at 3.09–3.07 Ga, with the metamorphic grade increasing towards the center of the structure, consistent with increasing levels of central uplift during impact cratering (Hart et al. 1999, 2004; Perchuk et al. 2002; Lana et al. 2003, 2004; Gibson 2019). Various migmatitic to more restitic gneisses (Hart et al. 1990; Stepto 1990) occur, which represent variable amounts of melt segregation, migration, and fractionation (Lana et al. 2003, 2004). Metamorphism of the surrounding lower Witwatersrand Supergroup sediments occurred at mid-amphibolite to greenschist facies conditions and is dated to about 2.9–2.7 Ga (Armstrong et al. 1991).

The original diameter of the impact structure is estimated to be 250–300 km based on geophysical modeling (Henkel and Reimold 1998), remote sensing (Phillips et al. 1999), as well as empirical relations of central uplift diameter to rim diameter, the spatial distribution of pseudotachylyte, and concentric large-scale structural patterns (Therriault et al. 1997). The amount of erosion is estimated to be 8–11 km as constrained by geobarometric analyses (Gibson et al. 1998) and geophysical considerations (Henkel and Reimold 1998); McCarthy et al. (1990) estimated 5–10 km of erosion occurred since impact based on regional stratigraphic studies. Fluid inclusions along shock-induced planar deformation features (PDFs) indicate trapping at depths of 7–15 km (Fricke et al. 1990). Together with an assumed structural uplift of about 3–12 km and an erosion of 8–11 km, the rocks exposed today in the central region were estimated to have been at depths of about 11–23 km before the impact (Gibson et al. 1998, 2019).

The prolonged thermal history of the exposed exhumed deep part of the Vredefort structure has considerably modified the shock effects which obscure estimates of the pressure conditions acting during impact (e.g., Schreyer and Medenbach 1981; Fricke et al. 1990; Grieve et al. 1990; Gibson and Reimold 2005). In the center of the dome, quartz is largely recrystallized, where at increasing distance from the center, the amount of recrystallized grains decreases and new grains are aligned along strings within coarse host grains, which are interpreted to represent annealed planar features (Lilly 1981; Schreyer and Medenbach 1981; Fricke et al. 1990; Grieve et al. 1990; Reimold 1990; Hart et al. 1991; Leroux et al. 1994). Microstructural evidence based on shock effects in feldspar suggests that shock conditions were locally very heterogeneous, with maximum shock pressures in the central parts of the dome exceeding 30–35 GPa, and locally more than 45 GPa, decreasing to about 10 GPa at a 20 km distance from the center (Gibson and Reimold 2005).

One of the largest known magnetic anomalies found in a terrestrial impact structure is a km-scale ring of negative anomalies (< − 5500 nT) surrounding the crystalline bedrock at Vredefort (Fig. 1). The ring has been attributed to ferruginous shales of the Witwatersrand Group (Corner et al. 1990). Strongly negative (< − 3000 nT) anomalies exist in the Archean basement rocks northwest of the impact structure's center, which were probably generated due to thermal overprinting when the field was in a reversed polarity state (Hargraves 1970; Antoine et al. 1990; Muundjua et al. 2007; Carporzen et al. 2012). The lack of negative anomalies closer to the impact structure's center can be explained by lithologies impoverished in magnetite and not from shock demagnetization (Hart et al. 1995; Carporzen et al. 2005). The rocks studied in this present contribution stem from the "central negative anomaly" about 10 km from the center of the structure (red star in Fig. 1).

Sampling and methods

Sampling

We investigated material from two ≈ 10 m deep bore holes (VRED2 and VRED3; Lat -26.970942° Long 27.388698°) drilled in 2008 in an area of high-amplitude magnetic anomalies within Archean basement rocks (Fig. 1), where a pronounced foliation dips nearly vertical (Lana et al. 2003; Carporzen et al. 2012). The VRED2 and VRED3 drill cores have diameters of 2.5 cm and lengths of 10.12 and 10.56 m, respectively. They were acquired using a Winkie drill at two sites located ≈ 5 m apart. VRED2 lies within a strongly negative geomagnetic anomaly (positive inclination, downward), whereas VRED3 lies in a locally strong positive geomagnetic anomaly (negative inclination, upward) (Carporzen et al. 2012). Three-component magnetic field measurements taken in a 10 m × 10 m grid at 0.55, 1.2, and 2.55 m height, together with paleomagnetic data from samples drilled at the same location on the surface, demonstrate that the magnetic anomalies were produced by a lightning strike whose line-currents travelled along the surface for > 20 m (Carporzen et al. 2012). From each core, 10 samples were selected at the following depths below the surface:

VRED2: V2 1.f (6 cm), V2 2.5 (13 cm), V2 4.2 (33 cm), V2 10.e (83 cm), V2 46.1 (456 cm), V2 54.1 (574 cm), V2 66.4 (770 cm), V2 69.1 (809 cm), V2 71.f (861 cm), and V2 78.2 (1003 cm).

VRED3: V3 2.1 (5 cm), V3 3.6 (15 cm), V3 3.16 (26 cm), V3 6.1 (87 cm), V3 34.12 (384 cm), V3 46.1 (549 cm), V3

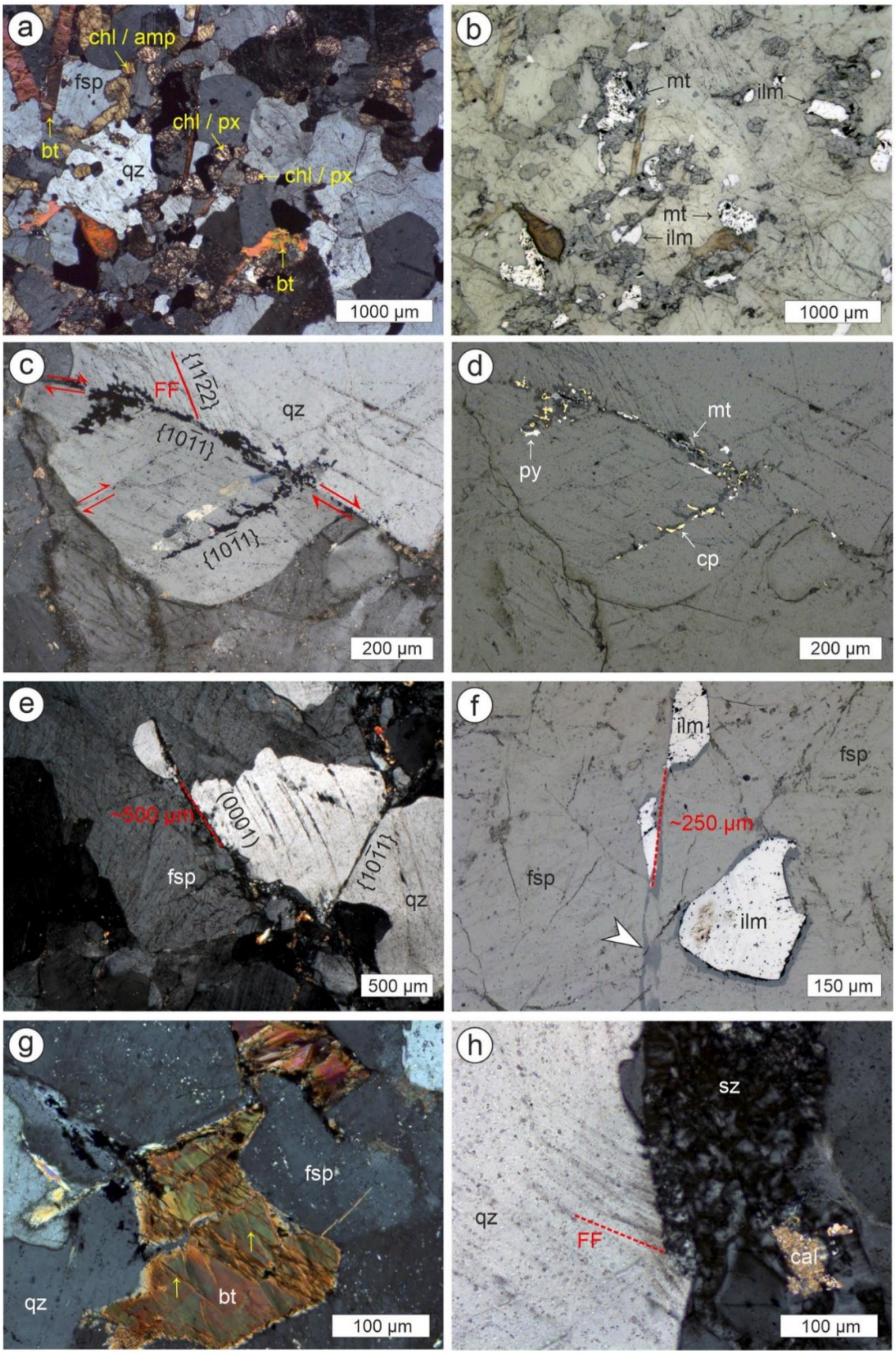
a
chl / amp
fsp
bt
chl / px
qz
chl / px
bt
1000 µm
b
mt
ilm
mt
ilm
1000 µm
c
FF
{1122}
qz
{10$\bar{1}$1}
{10$\bar{1}$1}
200 µm
d
mt
py
cp
200 µm
e
~500 µm
(0001)
{10$\bar{1}$1}
fsp
qz
500 µm
f
ilm
fsp
~250 µm
fsp
ilm
150 µm
g
fsp
qz
bt
100 µm
h
sz
qz
FF
cal
100 µm

◂**Fig. 2** Polarized light photomicrographs of the sampled Archean gneisses. **a** Main rock-forming minerals quartz (qz), feldspar (fsp), biotite (bt), chlorite (chl), amphibole (amp), and pyroxene (px); transmitted light, crossed polarizers; sample V2 54.1 (574 cm depth). **b** Magnetite (mt) and ilmenite (ilm) in reflected light; sample V2 54.1 (574 cm depth). **c, d** Feather features (FFs) with shear offset (red double arrow) in quartz (qz). Along the shear fracture magnetite (mt), pyrite (py), and chalcopyrite (cp) occurs; **c** in transmitted light, crossed polarizers and **d** in reflected light; sample V2 4.2 (33 cm depth). **e** Transgranular shear fracture (red) in feldspar (fsp) and quartz (qz). Crossed polarizers; sample V3 60.5 (659 cm depth). **f** Sheared (red) ilmenite (ilm) along fracture (white arrow) within feldspar grains. Reflected light; sample V2 4.2 (33 cm depth). **g** Kink bands (yellow arrows) in biotite (bt) between quartz (qz) and feldspar (fsp). Crossed polarizers; sample V2 1.f (6 cm depth). **h** Shear zone (sz) with calcite (cal) in contact with a quartz grain (qz). Note the feather features (FF) emanating from the phase interface. Crossed polarizers; sample V2 78.2 (1003 cm depth)

60.5 (659 cm), V3 66.13 (769 cm), V3 67.3 (805 cm), and V3 73.4 (994 cm).

Optical microscopy and universal stage measurements

Polished, uncovered thin sections (25 µm) were prepared from all samples and investigated by polarization microscopy (Leica DM2700 P) using both transmitted and reflected light. Photomicrographs were taken with a Leica MC170 HD camera and processed with the Leica Application Suite X 3.08.19082 software. A Leitz Universal-stage (U-stage) mounted on a Leitz optical microscope was used to determine the 3D orientation of the planar fractures (PFs) relative to the *c*-axis of the quartz. Uncertainty in the U-stage measurements is estimated at ± 5°; undulatory extinction in quartz crystals may increase the uncertainty. The measurements are displayed in stereographic projections of the lower hemisphere. The crystallographic orientations of the PFs were derived by measuring the angle between the pole to the fracture and the *c*-axis (Stöffler and Langenhorst 1994; Trepmann and Spray 2005; Ferrière et al. 2009). The results from the U-stage were compared with crystallographic orientations in quartz measured by electron backscattered diffraction (EBSD).

Scanning electron microscopy

Eight carbon-coated thin sections from V2 2.5 (13 cm), V2 4.2 (33 cm), V2 71.f (861 cm), V2 54.1 (574 cm), V3 2.1 (5 cm), V3 3.16 (26 cm), V3 34.12 (384 cm), and V3 60.5 (659 cm) were studied with a Hitachi SU5000 scanning electron microscope (SEM) equipped with a field emission gun, NordlysNano high-sensitivity EBSD detector (Oxford Instruments), energy-dispersive X-ray spectroscopy (EDS) detector (Oxford Instruments), and backscattered electron (BSE) detector. Full crystallographic orientation data were obtained from automatically indexed EBSD patterns acquired with AZtec analysis software 4.2 (Oxford Instruments). For EBSD, thin sections were chemo-mechanically polished with a colloidal alumina suspension (Syton) to reduce the surface damage produced from preparation. SEM observations used accelerating voltages of 20 kV and working distances of 10–25 mm. Depending on the EBSD-pattern quality and resolution, step sizes for automatic mapping have been chosen between 0.5 and 2 µm. We used a sample holder tilted at 70°. EBSD data were processed by the Channel software 5.12.74.0 (Oxford Instruments). All stereonets are equal-angle projections of the lower hemisphere.

Raman spectroscopy

In situ Raman spectroscopy was carried out to identify the iron-bearing phases and feldspar in fine-grained aggregates with an HORIBA JOBIN YVON XploRa ONE micro Raman system at the Munich Mineralogical State Collection Munich (SNSB). The Raman spectrometer was equipped with edge filters and a Peltier-cooled CCD detector. A 1800 g/mm grate was used together with a green 2ω-Nd:YAG laser (532 nm) on iron-bearing phases in an attenuated mode (10% laser power) corresponding to max. 0.9 mW on the sample surface to avoid oxidation (Bauer et al. 2011; Kaliwoda et al. 2021), which could, for example, transform magnetite-to-hematite, thereby leading to a false interpretation. Hole and slit diameters were 300 and 100 µm. An integration time of 2 × 16 s was applied. For feldspar, the green laser was used in attenuation mode with 100% laser power corresponding to maximum 9.1 mW at the surface. Hole and slit were set to 300 and 200 µm with counting times of 3 × 60 s. A 100 × long working distance objective resulted in a 0.9 µm laser spot size on the sample surface. Wavelength calibration was performed with a pure Si wafer chip on the predominant 520 ± 1 cm^{-1} peak. The wave number reproducibility was checked several times a day and deviations were found to be less than 0.2 cm^{-1}; the precision in Raman peak position is estimated at ± 1.5 cm^{-1}.

Results

We first give a general description of the shocked Archean gneisses (Fig. 2) with shocked quartz crystals (Fig. 3) and associated occurrences of fine-grained quartz and feldspar aggregates (Figs. 2h, 4). We then describe ilmenite and magnetite deformation fabrics (Figs. 5, 6, 7, 8, 9), which is followed by a description of ilmenite and magnetite alteration microfabrics (Fig. 10). All observed microfabrics occur in

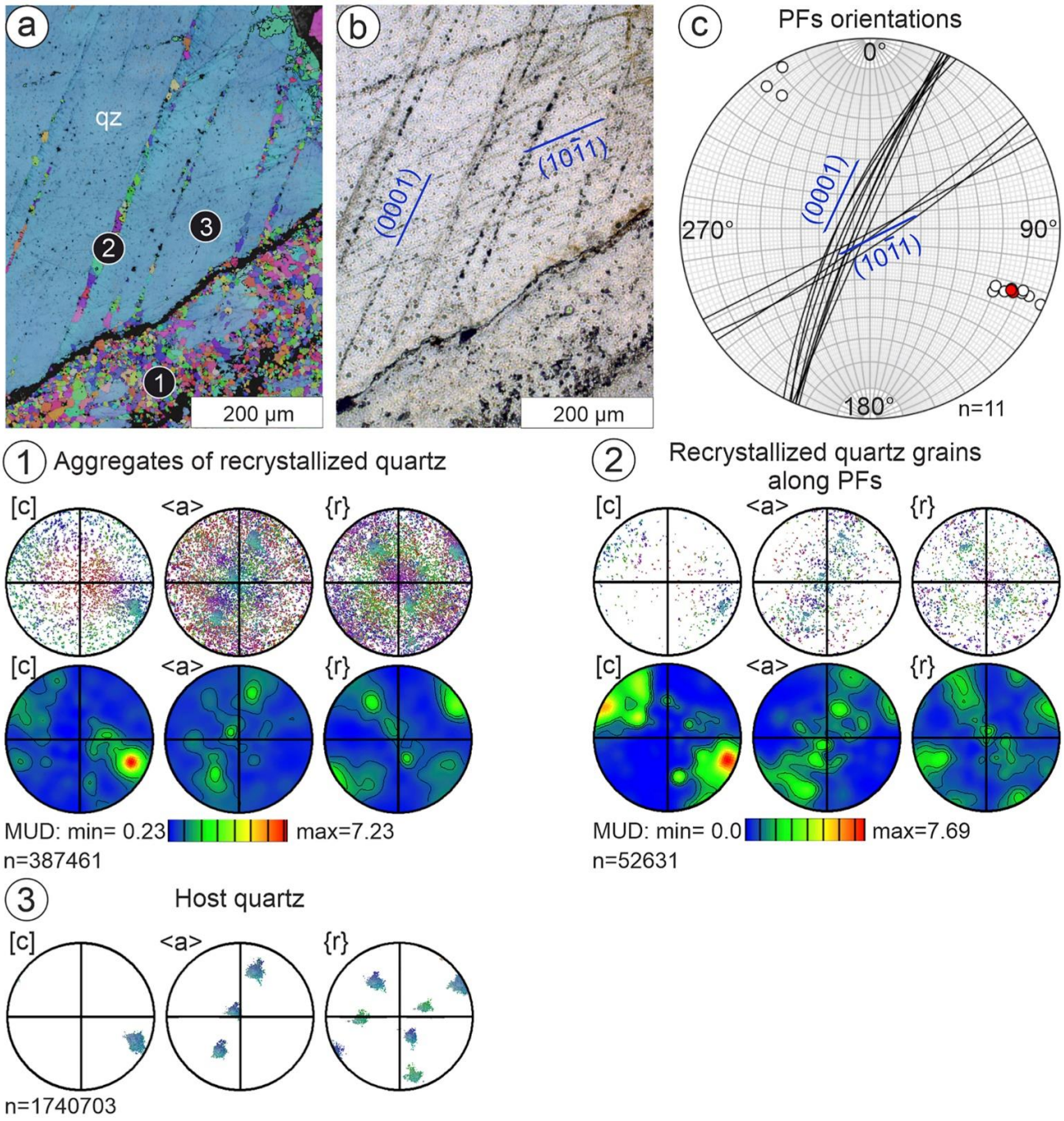

Fig. 3 EBSD and U-stage data of shocked quartz, sample V2 2.5 (13 cm depth). **a** EBSD orientation map (inverse pole figure of *z*-direction), displaying aggregates of new grains (**1**) and new grains along PFs (**2**) within a host quartz (**3**). **b** Polarized light photomicrograph with the indicated orientation of the two sets of PFs parallel to (0001) and (10$\bar{1}$1). **c** Stereographic projections (lower hemisphere) of the PFs orientations (white) displayed in **b**, measured by U-stage. The *c*-axis measurements are colored red. **1**, **2** Pole figures and density plots of the *c*- and *a*-axes and poles to r-planes of the aggregates of new quartz and new quartz grains along PFs, respectively, stereographic projections (lower hemisphere), corresponding to the orientation map in **a**. **3** Pole figures of *c*- and *a*-axes and poles to *r*-planes of the host quartz in stereographic projections (lower hemisphere), corresponding to the orientation map in **a**

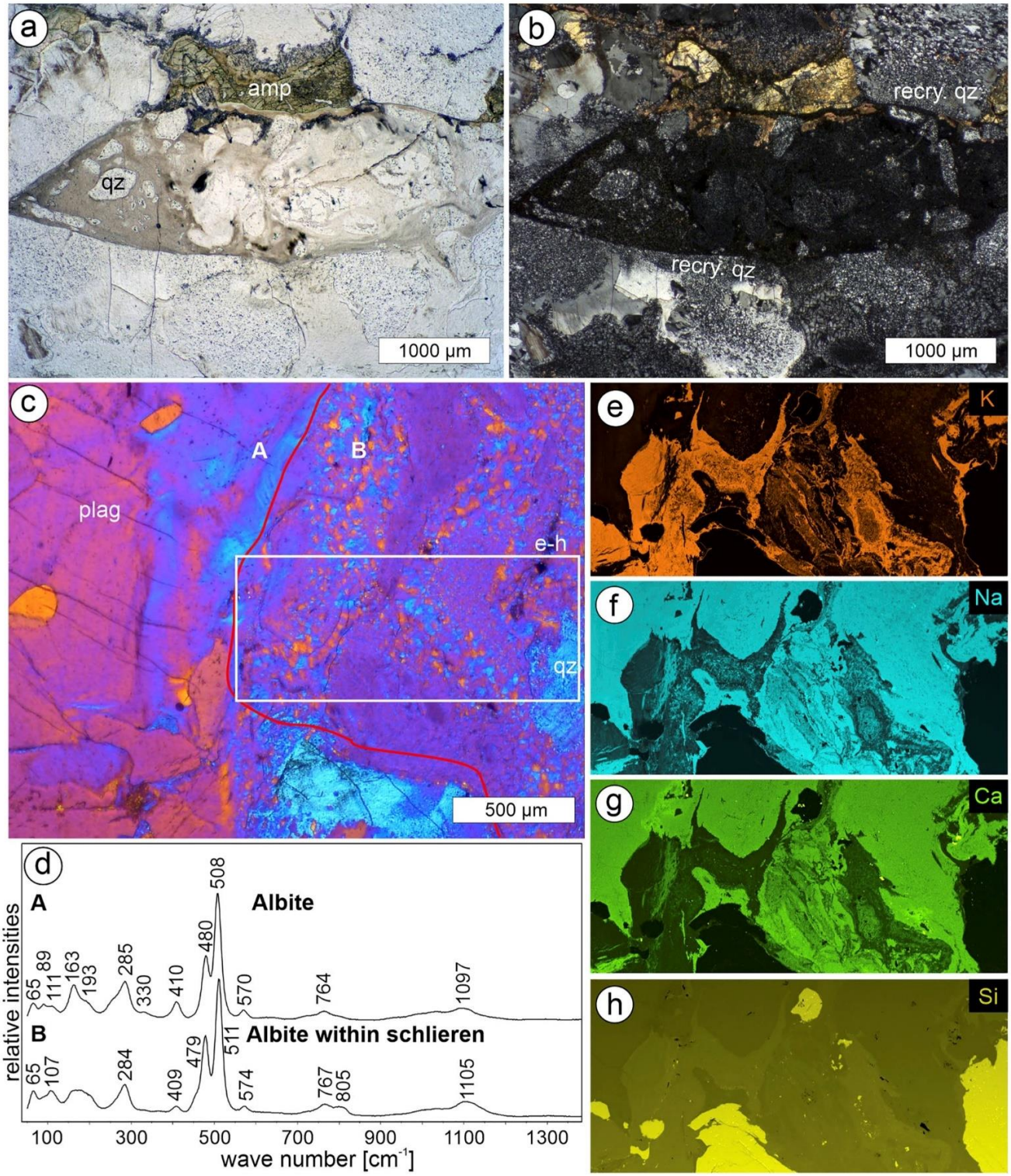

Fig. 4 Polarized light photomicrographs, EDS data, and Raman spectra of fine-grained quartz and feldspar aggregates, sample V2 71.f (861 cm depth). **a**, **b** Schlieren microstructure in contact with an altered amphibole (amp) and recrystallized quartz (recry. qz). Image **b** taken with crossed polarizers. **c** Boundary (red) between shear zone and quartz (qz) and plagioclase grains (plag). A and B indicate the Raman spots for the spectra displayed in **d**, whereas the white rectangle indicates the area scanned by EDS analysis shown in **e**–**h**. Crossed polarizers and lambda plate. **d** Raman spectra of an albite-rich plagioclase grain (A) and the albite-rich component of the vein matrix (B). **e**–**h** Distribution maps for K (**e**), Na (**f**), Ca (**g**), and Si (**h**)

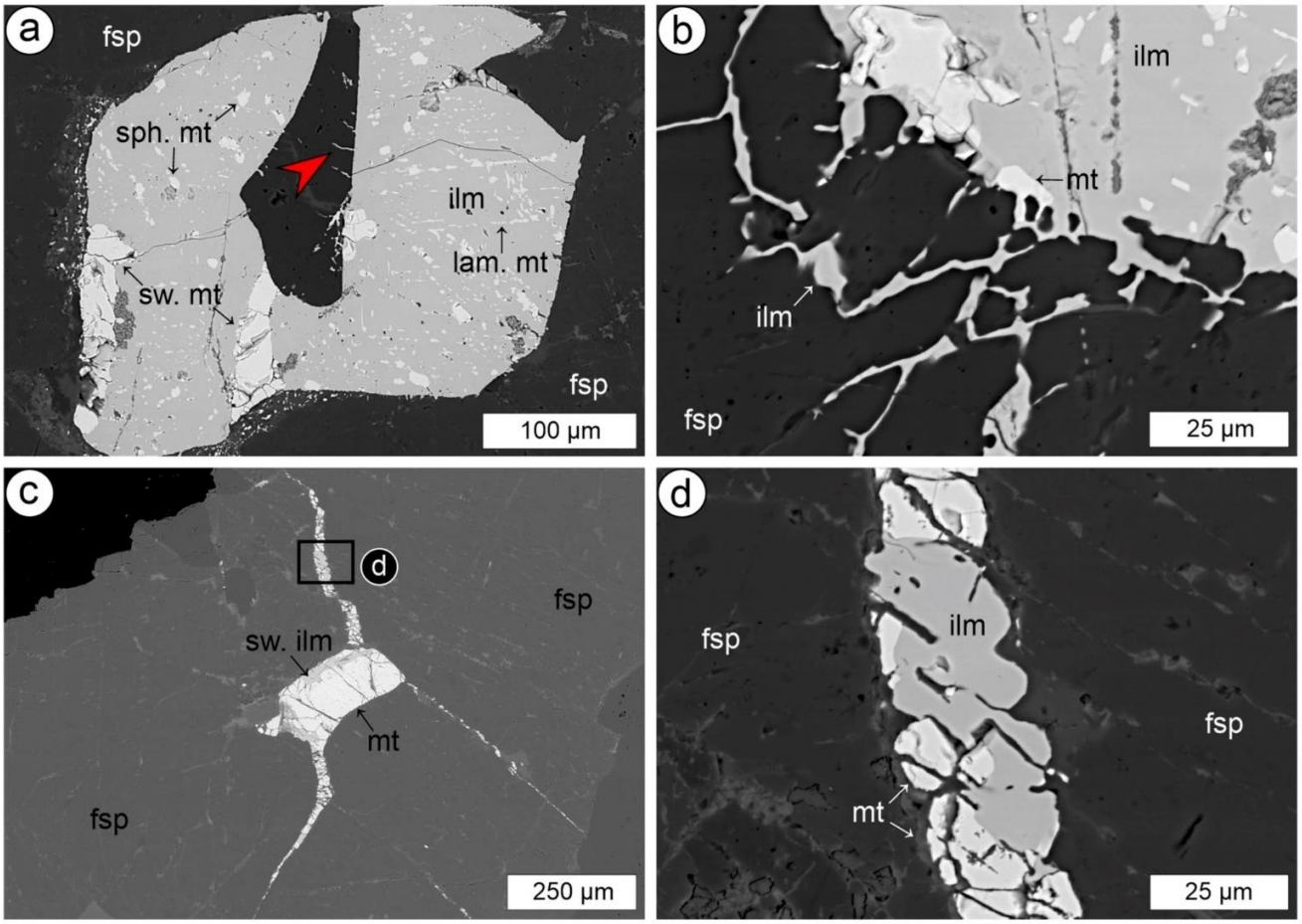

Fig. 5 BSE images of ilmenite and magnetite microstructures. **a** Ilmenite (ilm)—magnetite (sw. mt) sandwich microstructure. Note lamellar (lam. mt) and spheroid (sph. mt) magnetite exsolutions. The red arrow indicates ilmenite along fractures in feldspar (fsp). **b** Ilmenite host grain (ilm) displaying intrusions composed of ilmenite and rarely magnetite (mt), which are located within fractured feldspar (fsp). Image **a** and **b** taken from sample V2 4.2 (33 cm depth). **c** Coarse magnetite (mt) associated with ilmenite (sw. ilm) sandwich microstructure within feldspar (fsp). Magnetite and ilmenite occur along fractures in feldspar (sample V3 60.5, 659 cm depth). The area marked by the black rectangle is enlarged in **d**. **d** Ilmenite (ilm) and magnetite (mt) along a fracture in feldspar (fsp). Note the straight phase boundaries of magnetite and the rather curved ilmenite phase boundaries

both drill cores with a frequency that does not systematically vary with depth (Fig. 11).

Sample description

Based on polarized light and electron microscopy, the investigated rocks are medium- to coarse-grained gneisses composed of 60–75% feldspar and 20–40% quartz (Fig. 2). Phyllosilicates occur up to 5% and consist of chlorite and biotite, which are commonly altered to chlorite and/or anatase. Pyroxene and amphibole are often chloritized (Fig. 2a). Opaque phases comprise 1–5% of the rock (Fig. 2b–d): iron/titanium oxides consist of ≈70% ilmenite and ≈30% magnetite, with minor pyrite and chalcopyrite (Fig. 2c, d). No hematite was identified in any sample. Anatase, calcite, zircon, and apatite often occur in direct contact with magnetite and/or ilmenite.

All minerals are fractured, especially quartz (Fig. 2c–e), feldspar, and ilmenite (Fig. 2f); shear fractures show offsets of several tens of µm (Fig. 2e, f). Biotite commonly displays kink bands (Fig. 2a, g). Quartz shows sets of crystallographically controlled, parallel fractures with a spacing of up to a few tens of µm (Figs. 2c–e, h, 3). These so-called PFs are well-known but non-diagnostic shock effects (Stöffler and Langenhorst 1994; French and Koeberl 2010; Stöffler et al. 2018). On one side of such fractures, second-order, fine-lamellar, sub-parallel fractures can emanate at high angles (Fig. 2c, d, h). These so-called feather features (FFs) are also common shock effects in quartz (Poelchau and Kenkmann 2011; Ebert et al. 2020). The central fractures of the FFs typically show a marked shear offset of tens of µm (Fig. 2c). When coarse magnetite and ilmenite are in contact with PFs and FFs of quartz or with fractures of feldspar, fine-grained

magnetite and ilmenite (and more rarely pyrite and chalcopyrite) occur within the shock features (Fig. 2c, d).

We measured the 3D orientation of PFs and FFs using a U-stage microscope in 18 grains from 10 samples [V2 1.f (6 cm), V2 2.5 (13 cm), V2 4.2 (33 cm), V2 46.1 (456 cm), V2 66.4 (770 cm), V3 2.1 (5 cm), V3 3.16 (26 cm), V3 34.12 (384 cm), V3 60.5 (659 cm), and V3 73.4 (994 cm)]. Figure 3 compares the U-stage and EBSD measurements to determine crystallographic orientations. We identified 26 sets, of which 15 were characterized as (0001) with 45 individual U-stage measurements, 9 as $\{10\bar{1}1\}$ with 18 individual measurements, and one of each $\{22\bar{4}1\}$ and $\{11\bar{2}2\}$ with 2 individual measurements related to FFs. The PFs can be bent due to internal misorientation of the host quartz crystal (Fig. 2c, e).

About 30% of the quartz crystals are locally replaced by new grains (< 2%) aligned along crystallographic planes parallel to (0001) and $\{10\bar{1}1\}$ (Fig. 3), which are known quartz cleavage planes (Tröger 1982). About 20% of the PFs are decorated by secondary quartz grains. Partly recrystallized quartz in rocks from similar distances from the impact structure's center has been previously observed and interpreted to represent modified planar shock effects (e.g., Schreyer 1983; Fricke et al. 1990; Grieve et al. 1990; Reimold 1990; Leroux et al. 1994; Gibson and Reimold 2005). EBSD data show a large scatter in the crystallographic orientation of the new grains with a weak maximum close to the crystallographic orientation of the host quartz crystal, especially for the grains along PFs (Fig. 3a).

Fine-grained pure feldspar aggregates occur together with quartz replaced by new grains by about 50% (Figs. 2h, 4). These recrystallized quartz grains and fine-grained feldspar aggregates form few µm to 500 µm-wide transgranular zones. In polarized light and SEM, the fine-grained feldspar aggregates show a schlieren microstructure composed of K-feldspar ($Or_{79}Ab_{21}$) and plagioclase ($Ab_{74}An_{26}$), as indicated by EDS (Fig. 4a–c, e–h) and Raman spectroscopy (Fig. 4c, d). Characteristic Raman peaks identified albite Si/Al–O bonds at 284 cm^{-1}, 479 cm^{-1}, 511 cm^{-1}, and 574 cm^{-1}, as well as peaks associated with Na–O and Ca–O vibrations (Mernagh 1991). The main peaks of Ab-rich plagioclase in direct contact with the schlieren microstructure display similar spectra with the main peaks at 285 cm^{-1}, 480 cm^{-1}, 508 cm^{-1}, and 570 cm^{-1} (Fig. 4d). The fine-grained feldspar and quartz aggregates show curved yet sharp boundaries to the neighboring grains. Planar shock effects can be present within adjacent quartz at the immediate contact with fine-grained feldspar aggregates (Fig. 2h). Adjacent amphibole shows cataclasis and alteration (Fig. 4a, b). These microstructures occur in both drill cores at all depths [V2 4.2 (33 cm), V2 66.4 (770 cm), V2 69.1 (809 cm), V2 71.f (861 cm), V2 78.2 (1003 cm), V3 2.1 (5 cm), V3 60.5 (659 cm), V3 66.12 (769 cm), V3 67.3 (805 cm), and V3 73.4 (994 cm)]. No polymineralic pseudotachylitic breccias, as described elsewhere from the Vredefort Dome (e.g., Killick and Reimold 1990; Dressler and Reimold 2004; Reimold and Gibson 2005, 2006; Mohr-Westheide and Reimold 2010; Reimold et al. 2016), were observed in our samples.

Ilmenite and magnetite microfabrics

Coarse ilmenite grains can include a few tens of µm wide single magnetite layers, representing sandwich structures (Haggerty 1991), as well as fine-lamellar or spheroidal-shaped magnetite exsolutions of a few µm (Fig. 5a, b). Ilmenite and magnetite-filled veins emanating from the phase boundary of the host Fe-oxide phase into adjacent feldspar or quartz are µm- to tens of µm wide and become narrower with distance from the boundary (Fig. 5a–d). In the wider veins, magnetite typically shows straighter boundaries compared to ilmenite, which exhibits rather smoothly curved phase boundaries (Fig. 5d).

Coarser ilmenite is commonly twinned. A few µm to 50 µm-wide irregular lamellar twins are characterized by boundaries parallel to $\{\bar{1}012\}$, a rotation axis parallel to $<02\bar{2}1>$, and a rotation angle of 86° (black lines in Figs. 6a, 8a). Two different sets of $\{\bar{1}012\}$ twins are observed. Very straight and fine-lamellar twins with boundaries parallel to $\{10\bar{1}1\}$ crosscut the $\{\bar{1}012\}$ twins. They are characterized by a rotation of approximately 69° about the $<1\bar{1}01>$ axis, show a small spacing of ≈ 20 µm, and a width of only few µm (red lines in Fig. 6a). The $\{10\bar{1}1\}$ twins crosscut the $\{\bar{1}012\}$ twins with marked shear offset (Fig. 6a).

Fine-lamellar magnetite exsolutions within ilmenite can occur parallel to other symmetrically equivalent $\{10\bar{1}1\}$ planes. They have a spacing of several µm, a width of ≈ 1 µm, and a length of ≈ 5 µm (Figs. 5a, 6a, 7a, b). EBSD measurements show an epitactic relationship, where {110} of magnetite is parallel to $\{10\bar{1}0\}$ of the host ilmenite and (0001) of ilmenite coincides with {111} of magnetite (Fig. 7b, d, e). Crystallographically-controlled magnetite exsolution lamellae show minor relative misorientation (misorientation angles < 5°) (Fig. 7b). In contrast, the crystallographic orientation of exsolved spheroidal magnetite (≈ 10 µm diameter) is not controlled by the crystallographic orientation of the host ilmenite (Fig. 7a, c, e). These spheroid magnetite exsolutions occur preferentially along the $\{10\bar{1}1\}$ twin boundaries and along grain boundaries (Fig. 7a).

An ilmenite grain with an internal misorientation of up to 30° was observed to host another type of twin with a width of ≈ 15 µm (Fig. 8a, c). This (0001) twin is characterized by a rotation axis parallel to the *c*-axis and a misorientation angle of 178° (white line [*e*] in Fig. 8a). Within the adjacent quartz grain, a shear fracture, which is decorated

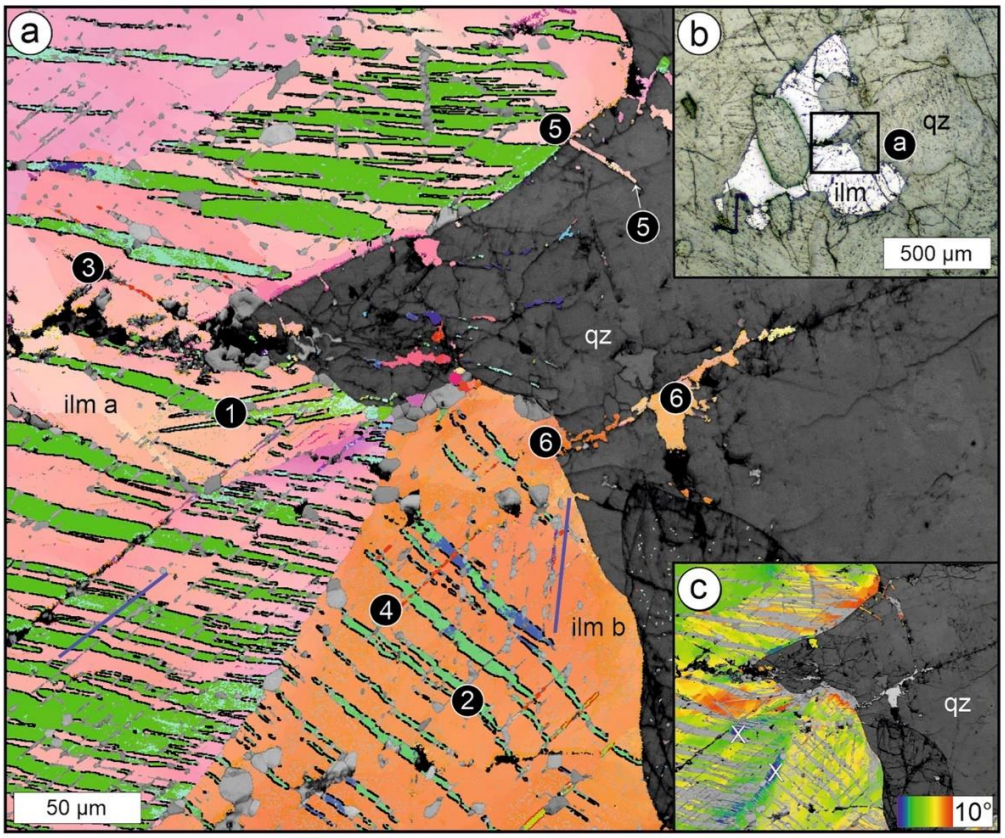
a
b
c
qz
ilm
500 µm
ilm a
ilm b
50 µm
10°
left grain (ilm a)
right grain (ilm b)
host
twin
intrusion
(Δm = 86°)
(Δm = 69°)

◂**Fig. 6** EBSD data of deformed ilmenite (sample V2 4.2, 33 cm depth). **a** Orientation map (inverse pole figure of *z*-direction) of two grains (ilm a and ilm b), where two different twins (red $\{\bar{1}012\}$ twin boundaries and black $\{10\bar{1}1\}$ twin boundaries) are identified. The numbers correspond to the respective pole figures. Note that ilmenite along PFs of quartz (qz) has a similar orientation compared to the host. Lamellar magnetite exsolutions are oriented along $\{10\bar{1}1\}$ planes of the ilmenite host (blue lines) plotted in **3** and **4**. **b** Reflected light photomicrograph of the ilmenite (ilm) and quartz (qz) grain partially displayed in **a**. **c** Relative misorientation angle (10°) maps for the two grains with their misorientation reference points marked by white Xs. **1**, **2** Stereographic projections (lower hemisphere) of the $\{\bar{1}012\}$ twins with rotation axes and misorientation angle (Δm). The great circles depict the orientation of the twin planes marked black in **a**. **3**, **4** Stereographic projections (lower hemisphere) of the $\{10\bar{1}1\}$ twins with rotation axes and misorientation angle (Δm). The great circle depicts the orientation of the twin planes marked red and blue in **a**. **5**, **6** Stereographic projections (lower hemisphere) of the (0001) and the $\{11\bar{2}0\}$ planes of the ilmenite host and intrusion of ilm a (**5**) and ilm b (**6**) into quartz fractures depicted in **a**

by fine-grained ilmenite, is emanating in contact with the (0001) twin in the host ilmenite (compare Fig. 8a, h).

Crystallographic orientations of ilmenite filling single fractures in quartz are remarkably similar to those of the coarse adjacent ilmenite grains with misorientation angles ≤ 10° (Figs. 5, 6a). Magnetite along single fractures exhibits relatively homogenous crystallographic orientations (Figs. 8f, h, 9b, d). However, a systematic relationship between the crystallographic orientations of magnetite in different fractures within the same quartz grain is not apparent (Fig. 9). No crystallographic relationship with the host quartz grain was observed. The fractures in quartz are commonly parallel to Dauphiné twin boundaries, characterized by a misorientation with a rotation of 60° around the c-axis (Fig. 8g, i).

Coarse-grained ilmenite in samples V2 1.f (6 cm), V2 66.4 (770 cm), V3 2.1 (5 cm), V3 3.6 (15 cm), V3 3.16 (26 cm), and V3 46.1 (549 cm) is altered when in direct contact to partly chloritized biotite (Fig. 10a, d). Alteration products are anatase inclusions of a few tens of µm in diameter (Fig. 10b, d), as identified by Raman spectroscopy. Chlorite commonly occurs along the magnetite exsolution lamellae within the host ilmenite grains, indicating that chlorite preferentially replaces magnetite (Fig. 10c, e). Calcite occurs within the alteration products together with anatase, chlorite, and residual ilmenite (Fig. 10d, f). Within the alteration products, magnetite grains with diameters of up to 15 µm can be identified, which have smoothly curved grain boundaries compared to the irregular grain boundaries of ilmenite and anatase (Fig. 10f).

Discussion

Figure 11 summarizes the distribution of the observed microfabrics in the samples from the two drill cores as a function of depth. Here, we first discuss the shock conditions implied by the microstructures, then the deformation, and transformation processes of ilmenite and magnetite during impact cratering and finally the implications for rock magnetism. A summary of the observed shock effects is given in Table 1.

Deformation conditions

The PFs in quartz are dominantly parallel to (0001) and $\{10\bar{1}1\}$ (Figs. 2c, e, h, 3a–c, 8g, i, 9a), which are known quartz cleavage planes (e.g., Tröger 1982) and common, albeit non-diagnostic, shock effects that represent tensile cracking (Stöffler and Langenhorst 1994; French and Koeberl 2010; Stöffler et al. 2018). Shearing is indicated by abundant shear fractures with shear offset, especially along the central fracture of FFs (Fig. 2c). Based on the spacing and the intrusion of Fe-phases, we interpret most of the planar features observed here as PFs. At lithologically equivalent locations at Vredefort, basal PDFs, i.e., Brazil twins parallel to (0001), were observed by transmission electron microscopy (TEM, Leroux et al. 1994). Some fine-lamellar (0001) planar features observed in our study (Figs. 2e, h, 3a, b) might represent basal PDFs. However, we did not perform TEM measurements, which would be required to resolve their nature as Brazil twins.

Only about 20% of the PFs are decorated by secondary quartz grains aligned along (0001) and $\{10\bar{1}1\}$ cleavage planes, yet not along other rhombohedral planes, such as $\{10\bar{1}3\}$ and $\{10\bar{1}2\}$, typical of PDFs that indicate higher shock pressures (Langenhorst and Deutsch 1994). Generally, we observed no microstructural evidence for rhombohedral PDFs, consistent with the findings that PFs and FFs develop at lower shock conditions. However, in association with fine-grained feldspar zones, adjacent quartz can be replaced by up to 50% with secondary quartz (Fig. 4), which might reflect local higher strain, i.e., higher shock conditions consistent with heterogeneous shock conditions on the grain scale (e.g., Gibson and Reimold 2005). Huffman et al. (1993) and Huffman and Reimold (1996) suggested that generally fewer PDFs might have been generated at Vredefort given the deep crustal levels with higher ambient temperature and pressure conditions.

Monomineralic fine-grained quartz aggregates that replace original grains, as observed in our samples, were previously described from similar locations (e.g., Schreyer and Medenbach 1981; Fricke et al. 1990; Grieve et al. 1990; Gibson and Reimold, 2005). However, no larger

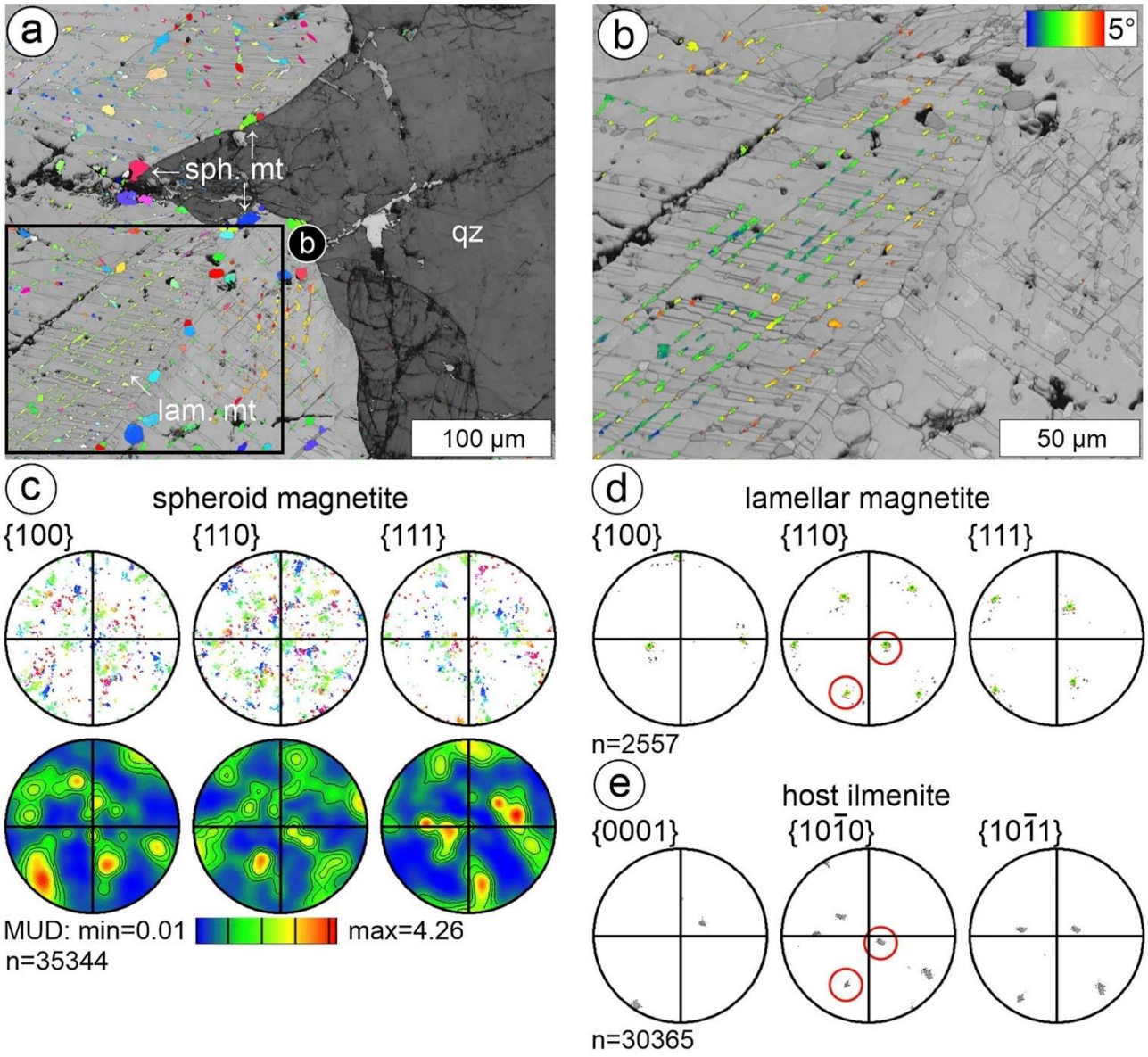

Fig. 7 EBSD data of sample V2 4.2 (33 cm depth). **a** Two different types of magnetite grains within the ilmenite host adjacent to quartz (qz). Magnetite grains display a spheroid (sph. mt) and a lamellar (lam. mt) shape. The black rectangle marks the area magnified in **b**. **b** Misorientation map of lamellar magnetite grains (color). **c** Pole figures and density plots of the {100}, {110}, and {111} planes/axes of the spheroid magnetite grains in stereographic projections of the lower hemisphere, corresponding to the orientation map in **a**. **d** Pole figures of the {100}, {110}, and {111} planes/axes of the lamellar magnetite grains in stereographic projections of the lower hemisphere, corresponding to the orientation map in **b**. The red circles indicate the epitactic relationship with the ilmenite host orientation displayed in **e**. **e** Pole figures of the {0001}, {10$\bar{1}$0}, and {10$\bar{1}$1} planes of the host ilmenite in stereographic projections of the lower hemisphere, corresponding to the orientation map in **b**. The red circles indicate the epitactic control of the lamellar magnetite orientation displayed in **d**

scale pseudotachylitic breccias with polymineralic lithic components documented elsewhere in the Vredefort dome (e.g., Killick and Reimold 1990; Dressler and Reimold 2004; Reimold and Gibson 2005, 2006; Mohr-Westheide and Reimold 2010; Reimold et al. 2016) are present in our samples. Nor did we find high-pressure SiO_2 polymorphs as described in samples within the Witwatersrand quartzites surrounding the Vredefort Dome (e.g., Martini et al. 1978, 1991, 1992). The new quartz grains are aligned parallel to crystallographic planes, which are known quartz cleavage planes with crystallographic orientations similar to that of the host grain (Fig. 3a). This suggests that the newly created quartz formed by effective strain-induced grain boundary migration, i.e., recrystallization, along the damage zone of

the cracks during static annealing without the involvement of a melt or a glass being necessary. Formation of new grains with a similar microstructure was described in high strain-rate deformation experiments with subsequent annealing ("kick-and-cook" experiments of Trepmann et al. 2007), i.e., strings of quartz grains generated along the damage zone of pre-existing cracks with a crystallographic orientation controlled by the host quartz crystal. However, the involvement of glass or melt cannot be ruled out given the prolonged post-impact thermal history of the Vredefort gneisses. This is especially true for the fine-grained aggregates replacing pre-impact quartz grains in the center (Fig. 4b), which are found only spatially related to fine-grained feldspar aggregates with K-felspar-plagioclase schlieren (Figs. 2h, 4). The fine-grained feldspar aggregates suggest some mobility, indicating either localized stronger cataclasis or even "monomineralic" melting of feldspar, consistent with the lower melting temperature and fracture toughness of feldspar compared to quartz (Spray 2010, Fig. 12). Therefore, the fine-grained quartz and feldspar microstructures defining few µm to hundreds of µm-wide, mm-long zones (Figs. 2h, 4), indicate that they represent localized higher strain compared to the host rock. This strain localization may be due to deformation after the passage of the shock wave during the modification stage of impact cratering (then these microstructures might represent cataclasites or potentially pseudotachylytes, that involve frictional melts) or due to deformation at high shock conditions related to the shock wave through the mechanical contrast between feldspar and quartz (hence, these microstructures might be called "shock veins" that potentially involve shock melting). However, it is impossible from our observed microstructures alone, and lies outside the scope of our study, to distinguish the two. For a recent review on the ongoing discussion of shock melting versus frictional melting, the reader is referred to Spray and Biren (2021) and references therein. We, therefore, use the term "shear zones" in the sense that the microstructures observed here represent localized zones of increased strain given the higher number of fine-grained aggregates when compared to the host rock.

The observed shock effects of biotite kink bands (see Fig. 2a, g), PFs and FFs, possible basal PDFs in quartz that are partly decorated by recrystallized grains, and the absence of evidence for rhombohedral PDFs in quartz, together suggest our samples experienced F-S2 to F-S3 shock stages (Stöffler et al. 2018) and between 0 and Ia shock stages according to the IUGS system (Stöffler and Grieve 2007). FFs have been reported to occur at shock pressures up to 18 GPa (Tada et al. 2022). Given the lack of annealed rhombohedral PDFs in our samples on one hand, and considering the general difficulty of constraining shock pressure, not to mention its heterogeneous character, in addition to the strong modification due to the prolonged thermal history after the impact, we conclude that shock conditions were < 20 GPa. This shock level is consistent with the observations from samples at similar positions in the Vredefort impact structure (e.g., Grieve et al. 1990; Reimold and Gibson 2005). At these relatively low shock conditions, shock-related shear deformation might be expected (Trepmann 2008; Ebert et al. 2020), which is consistent with the potential presence of (0001) Brazil twins and the abundance of shear fractures.

The fact that the Dauphiné twin boundaries lie parallel to the PFs (Fig. 8h) implies they were generated after impact, when the fracture surfaces served as preferred sites of twin nucleation, as observed at the Charlevoix impact structure (Trepmann and Spray 2005). Dauphiné twins can occur from the transformation of hexagonal β-quartz to trigonal α-quartz, when cooled below the transition temperature of $\approx$ 573 °C at atmospheric pressure (Tullis 1970; Markgraaff 1986; Heaney and Veblen 1991) or $\approx$ 25 °C/kbar under elevated confining pressure (Coe and Paterson 1969). Assuming a structural uplift of 3–12 km and an erosion of 8–11 km since then (Gibson et al. 1998, 2019) and a geothermal gradient of 30 °C/km (Gibson and Wallmach 1995) in combination with a rock density of 2700 kg/m^3, a temperature of about 650–725 °C would be required for stabilizing β-quartz. Thus, if the observed Dauphiné twins formed during cooling from β-quartz to trigonal α-quartz stability conditions, the rocks were at temperatures above 650–725 °C during impact cratering. These temperatures appear quite realistic, given the high post-shock temperatures estimated to about 650–750 °C based on petrological constraints inferred from reaction fabrics (orthopyroxene-plagioclase coronas and cordierite-orthopyroxene symplectites) in metapelites of the Archean basement, which were interpreted to have formed after the impact (Perchuk et al. 2002).

Shear heating and mobilization of ilmenite and magnetite

Several studies have observed opaque minerals in shock-induced planar features in the Vredefort gneisses (Hart et al. 1991, 2000; Cloete et al. 1999; Carporzen et al. 2006). Cloete et al. (1999) suggested that they formed by crystallization from a melt. Moreover, Cloete et al. (1999) found that magnetite crystallized with its <101> sub-parallel to $\{\bar{1}100\}$ of the host quartz grains as well as magnetite sub-parallel to an orientation of <101> on the sample scale. Our observations also show a remarkably homogeneous crystallographic orientation of magnetite, but only within single fractures, with no sub-parallel relationship of <101>, with no control of $\{\bar{1}100\}$ from the host quartz and independent of the magnetite in other fractures within the same host quartz grain (Figs 8f–i, 9). The crystallographic orientation of ilmenite within PFs of quartz seems to be controlled by the host ilmenite orientation from which the veins emanate,

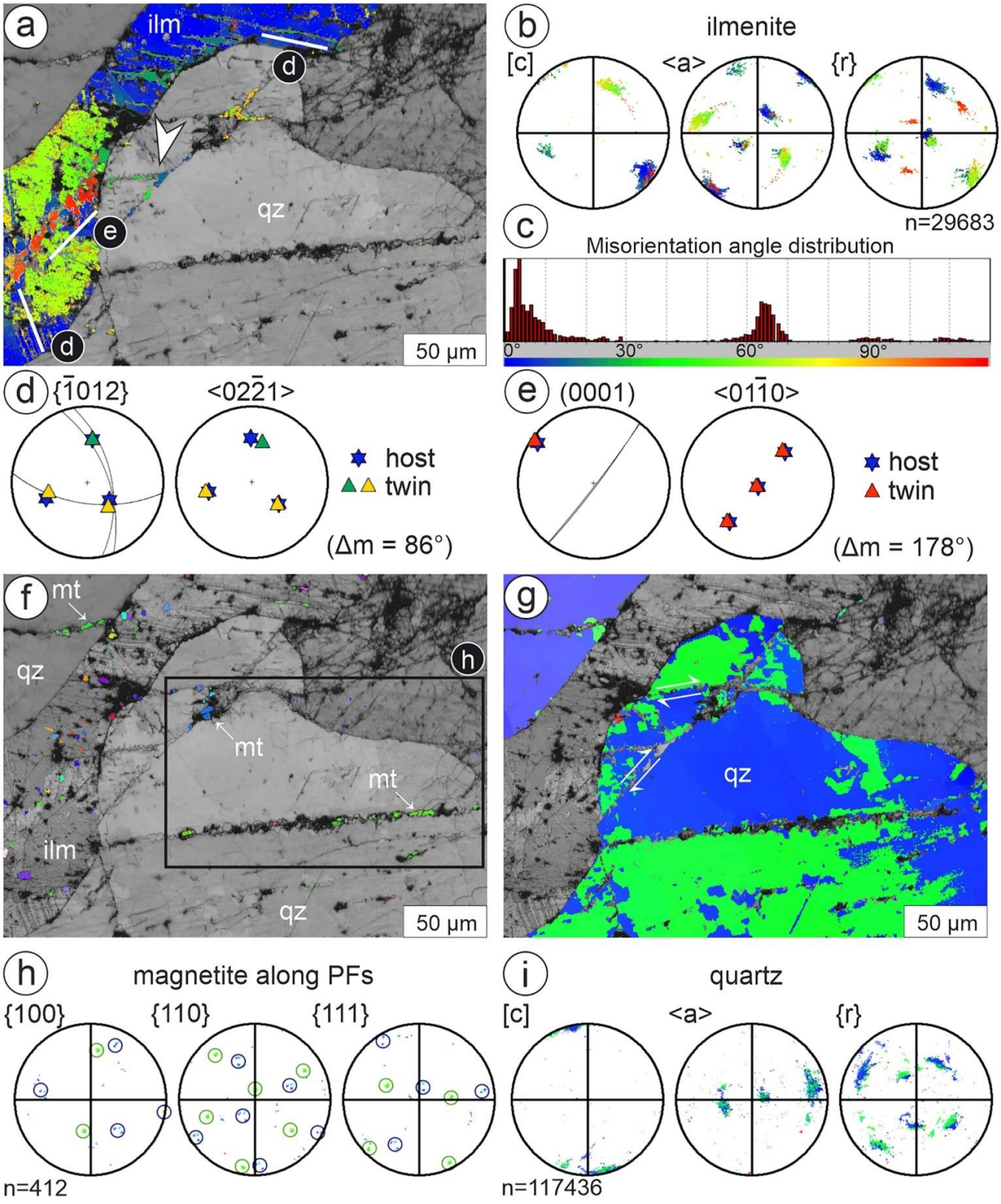

and not by the crystallographic orientation of the silicate phase (Figs. 6a, 8a). We suggest that shear heating during shock-related deformation at non-isostatic stresses of both the host Fe-phase and the adjacent silicates (Fig. 8a, g) played a major role in mobilizing ilmenite and magnetite, as well as chalcopyrite and pyrite, to intrude shear fractures within quartz and feldspar. Depending on the composition and eutectic temperature, shear heating can partially or

◂**Fig. 8** EBSD data of sample V3 2.1 (5 cm depth). **a** Misorientation map of an ilmenite grain (ilm) with two different twins (white lines) corresponding to **d** and **e** as well as associated ilmenite (white arrow) within PFs of quartz (qz). Note that the localized zone of increased misorientation in ilmenite related to the (0001) twin (red) is spatially related to shear fractures within the adjacent quartz, which are decorated by ilmenite. **b** Pole figures of the *c*-plane, as well as the *a*- and *r*-axes of ilmenite in stereographic projections of the lower hemisphere, corresponding (colored) to the misorientation map in **a**. **c** Misorientation angle distribution of the misorientation map in **a**. **d**, **e** Stereographic projections (lower hemisphere) of the $\{\bar{1}012\}$ and (0001) twins with rotation axes and misorientation angle (Δm). The great circles depict the orientation of the twin planes marked white in **a**. **f** EBSD orientation map (inverse pole figure of *z*-direction) of magnetite (mt) within an ilmenite grain (ilm) and within PFs of quartz (qz). The black rectangle indicates the data area of **h**. **g** EBSD orientation map (inverse pole figure of *z*-direction) of a quartz grain (qz) displaying a Dauphiné twin relationship (blue and green) as well as shear offsets (white double arrows) along PFs. **h** Pole figures of the {100}, {110}, and {111} planes/axes of magnetite along PFs of quartz in stereographic projections of the lower hemisphere, corresponding to the orientation map in **f**. **i** Pole figures of the *c*-plane, as well as the *a*- and *r*-axes of quartz in stereographic projections of the lower hemisphere, corresponding to the orientation map in **g**

completely melt/breakdown chalcopyrite, pyrite, ilmenite, and magnetite (Nakamura et al. 2002) and thus strongly influence their mobility. Opaque minerals have not been observed along phase or grain boundaries, but exclusively along PFs in quartz commonly associated with shear offsets (Figs. 2c, d, 8) as well as along shear fractures within feldspar. The crystallographic continuity with the source Fe-bearing phase might be explained by epitactic crystallization in the vein, where the host phase acted as a substrate that dictated the crystallographic orientation of the newly precipitated phase.

The two main controlling factors of frictional melting are the melting point/breakdown temperature (T_{MB}) of the respective phases as well as their fracture toughness (K) (Fig. 12) (Spray 1992, 2010). In relation to their melting point and fracture toughness, Spray (2010) suggested a hierarchy in the response to comminution (grain size reduction) and frictional melting of minerals. Feldspar, pyrite, magnetite, and quartz show increasing values of fracture toughness and melting/breakdown temperatures (Fig. 12), which leads to a decreasing tendency of the respective phases to fracture or melt. Those mechanical properties appear to correlate with the microstructures of pyrite (Figs. 2d, 9b) and magnetite (Figs. 2d, 5, 8f, 9b) along the fractures in quartz and feldspar. Magnetite has the highest fracture toughness and melting temperature among the iron-bearing phases and preferentially displays brittle fracturing. Ilmenite, on the other hand, displays smoothly curved phase boundaries (Fig. 5) and, in general, appears more often within fractures of adjacent silicate phases. Therefore, its mobility might be explained by the lower melting point (Eriksson and Pelton 1993) in combination with a lower fracture toughness in relation to magnetite.

Ilmenite twinning

Twins parallel to $\{10\bar{1}2\}$ are common in ilmenite (Minkin and Chao 1971; Frick 1973; Reynolds 1984). The tens of µm wide $\{10\bar{1}2\}$ twins with irregular boundaries indicate that they were modified by twin boundary migration. We, therefore, interpret them as pre-shock deformation structures. The fine-lamellar $\{10\bar{1}1\}$ twins offset and thus postdate the $\{10\bar{1}2\}$ twins (Fig. 6). They show very straight boundaries and can be wedge-shaped, indicating that they are mechanical twins. Mechanical twinning is a crystal-plastic deformation mechanism at non-isostatic stresses, involving dislocation glide, which does not require diffusion and is thus fast and not thermally controlled. The (0001) single twin, which shows irregular boundaries, is related to a site of high strain as indicated by misorientation angles and spatially related to shear fractures decorated by ilmenite in the adjacent quartz (Fig. 8). Deformation-induced $\{10\bar{1}1\}$ twins have been reported in natural samples and from experiments at confining pressures of 1.3 GPa with applied differential stress of 0.75 GPa and a strain rate of 10^{-4}/s at 25 °C (Minkin and Chao 1971). Twin planes parallel $\{10\bar{1}1\}$ and (0001) in ilmenite were reported from shock experiments as well as in ilmenite from lunar rocks (Minkin and Chao 1971; Sclar et al. 1973). Therefore, we interpret the $\{10\bar{1}1\}$ and (0001) twins to be related to the high strain rate deformation at non-isostatic stress conditions related to meteorite impacting, consistent with the quartz and feldspar microstructures.

Exsolution of magnetite within ilmenite

In contrast to twinning, exsolution requires diffusion. The magnetite exsolution lamellae, as well as the twins parallel to $\{10\bar{1}1\}$ planes of ilmenite, crosscut and offset the $\{10\bar{1}2\}$ twins (Fig. 6a) and thus postdate the $\{10\bar{1}2\}$ twins. Exsolved magnetite in ilmenite occurred during subsolidus re-equilibration from slow cooling (Buddington and Lindsley 1964;

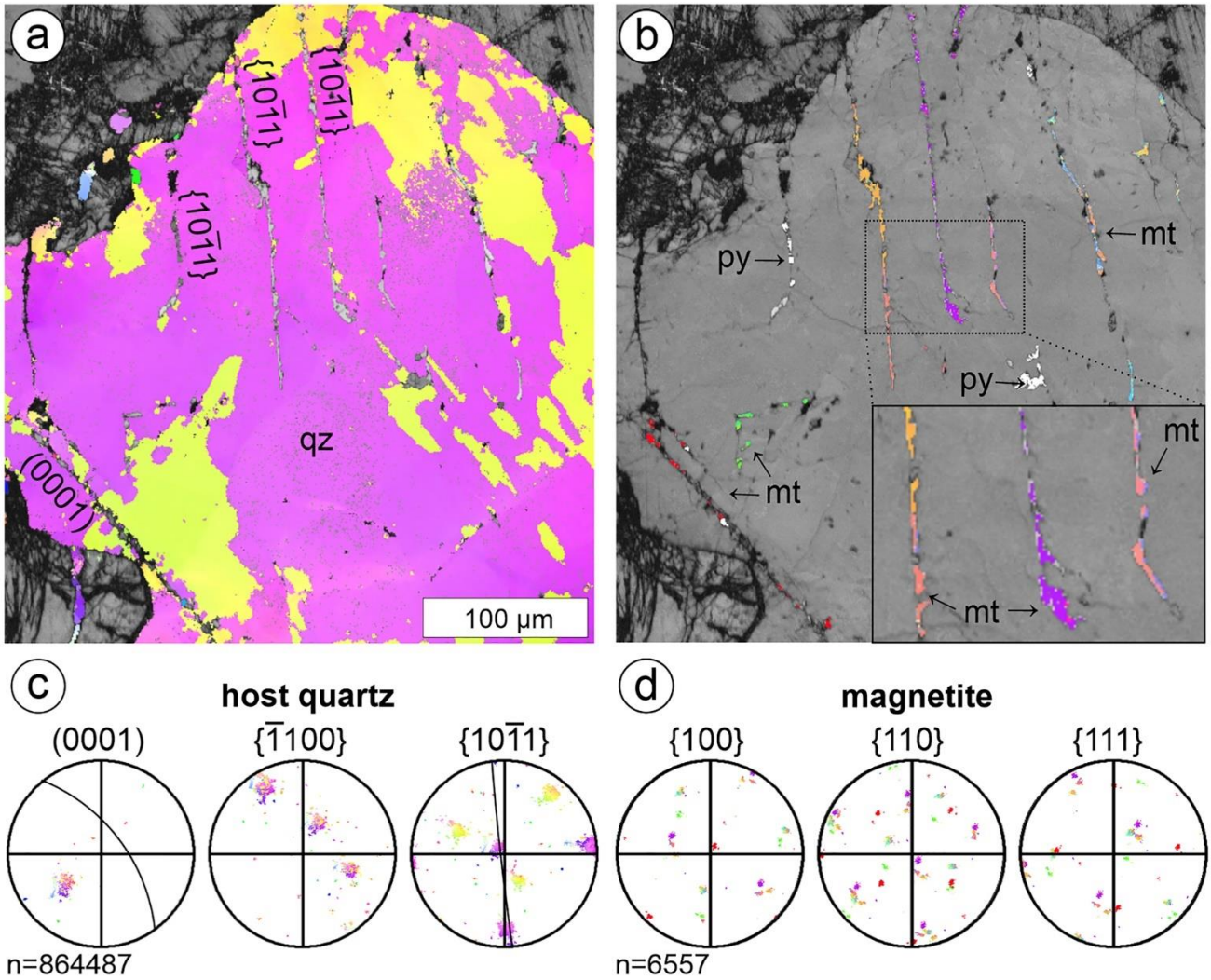

Fig. 9 EBSD and U-stage data of sample V3 34.12 (384 cm depth). **a** EBSD orientation map (inverse pole figure of *z*-direction) of a quartz grain (qz) displaying Dauphiné twins (yellow and violet) as well as PFs oriented along (0001) and {10$\bar{1}$1}. **b** EBSD orientation map (inverse pole figure of *z*-direction) of magnetite (mt) along PFs of quartz (qz). Note that magnetite shows distinct orientations in the different PFs. The occurrence of pyrite is indicated in white. **c** Pole figures of (0001), {$\bar{1}$100}, and {10$\bar{1}$1} with PF great circles of the host quartz in stereographic projections of the lower hemisphere, corresponding to the orientation map in **a**. **d** Pole figures of {100}, {110}, and {111} of magnetite along PFs of quartz in stereographic projections of the lower hemisphere, corresponding to the orientation map in **b**

Tan et al. 2016). It has also been described to form during cooling after meteorite shock events (Sclar et al. 1973). The temperatures required to exsolve magnetite from ilmenite must have been higher than the ilmenite–hematite miscibility gap at 600–700 °C; otherwise, hematite would be expected to have formed (Lindsley 1991; Harrison 2000).

Epitactic relations of magnetite exsolution in ilmenite are related to the densely packed oxygen planes of magnetite and ilmenite (Wenk et al. 2011; Tan et al. 2016). We observed an epitactic relation only for those magnetite exsolution lamellae that were controlled in shape and occurrence by the ilmenite {10$\bar{1}$1} planes (Fig. 7b, d, e). There, the magnetite {110} planes parallel the {10$\bar{1}$0} planes of the host ilmenite (Fig. 7d, e). In contrast, spheroidal magnetite exsolutions show neither shape nor crystallographic orientation that are controlled by the crystallography of the ilmenite host. However, the spheroid magnetite exsolutions occur preferentially along the {10$\bar{1}$1} twins and grain boundaries, indicating heterogeneous nucleation at sites of increased disorder that facilitated diffusion. The magnetite exsolution lamellae in ilmenite crosscut the pre-shock {10$\bar{1}$2} twins and are associated with the fine-lamellar {10$\bar{1}$1} twins that are interpreted as having been shock-induced. Therefore,

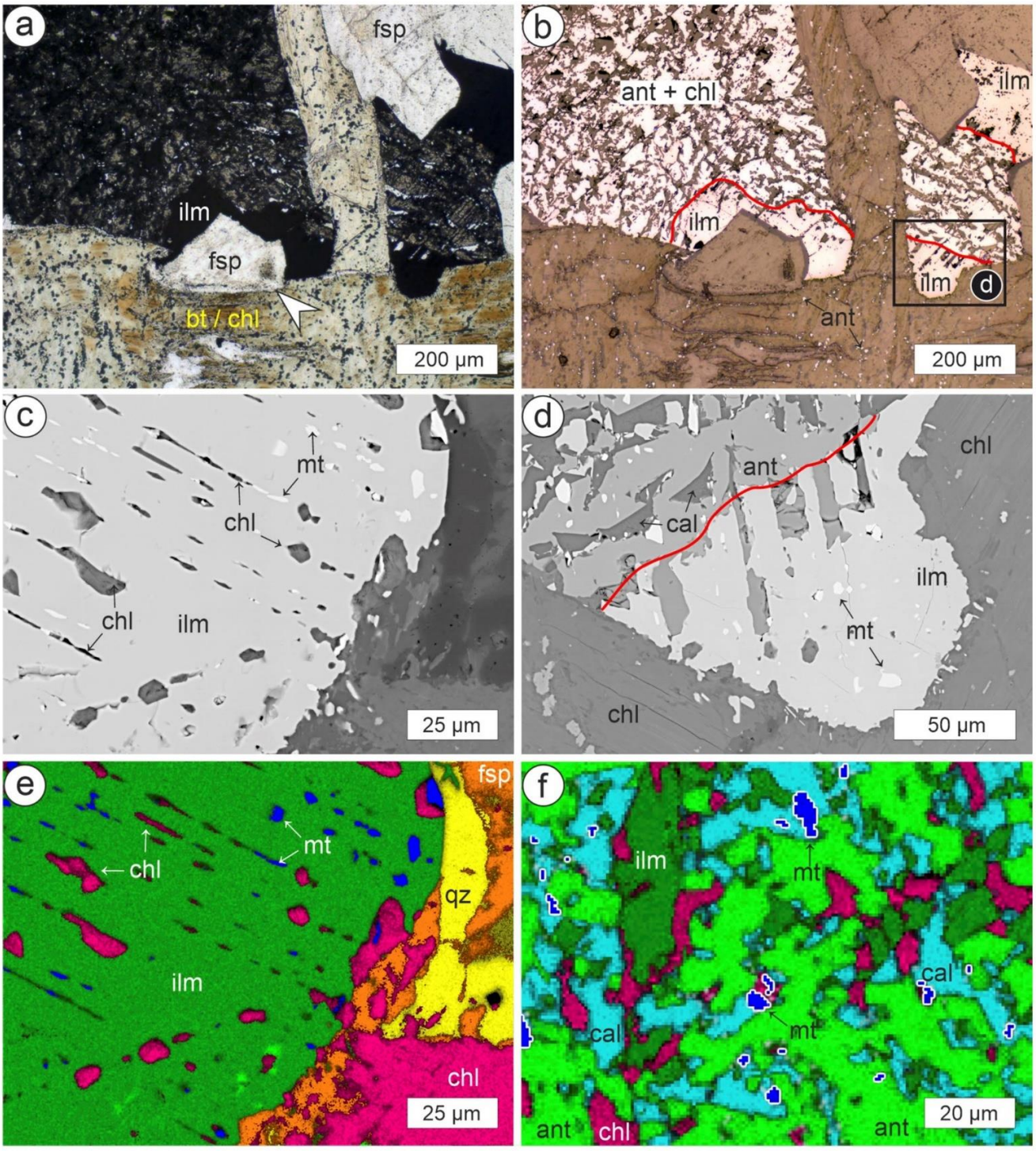

Fig. 10 Altered ilmenite. **a**, **b** Altered ilmenite in direct contact with chloritized biotite (bt/chl) and feldspar (fsp). The alteration fronts are displayed by red lines and separate the alteration products consisting of anatase and chlorite (ant + chl) from the residual ilmenite (ilm). Note the feldspar grain (white arrow) in between an ilmenite and a chloritized biotite. Few µm-sized anatase grains also occur within biotite/chlorite. The black rectangle indicates the image of **d**. Image **a** taken with transmitted light and image **b** taken with reflected light. **c** Magnetite exsolution (mt) within the host ilmenite (ilm) replaced by chlorite (chl). BSE image. **d** Altered ilmenite, where residual ilmenite (ilm) with magnetite exsolutions (mt) occurs in direct contact with chlorite (chl), which locally reacted to anatase (ant). Calcite (cal) is also observed. The red line displays the alteration front. BSE image. **e** Phase map based on EDS data displaying image section of **c** with ilmenite (ilm), magnetite (mt), chlorite (chl), biotite (bt), and quartz (qz). **f** Phase map based on EDS data showing a reaction microfabric of altered ilmenite consisting now of anatase (ant), calcite (cal), chlorite (chl), and magnetite (mt)

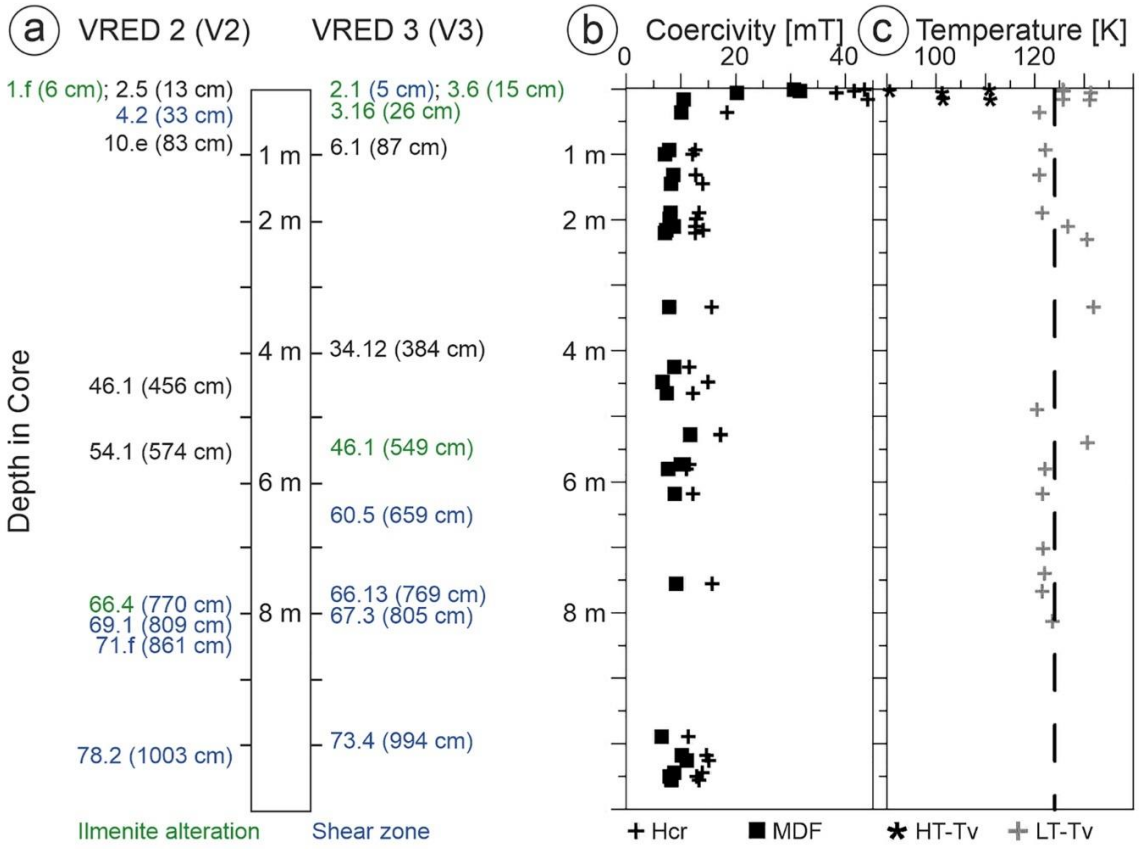

Fig. 11 Summary of microstructural observations of samples from the VRED2 (V2) and VRED3 (V3) drill cores versus magnetic properties reported for the same material by Carporzen et al. (2012). Fe-phase-bearing veins in shear fractured feldspar and quartz occur at all depths. **a** Samples of drill cores V2 and V3 displaying ilmenite alterations (green) and shear zones (blue). Note that samples V2 66.4 and V3 2.1 contain both ilmenite alterations and shear zones. **b** Remanent coercivity H_{cr} and median demagnetizing field (MDF) summarized for both drill cores. Datapoints in black adopted from Carporzen et al. (2012). **c** High- and low-temperature Verwey transitions (HT-Tv; LT-Tv) summarized for both drill cores. Vertical dashed line at 124 K displays the Verwey transition temperature for pure stoichiometric magnetite. **b**, **c** after Carporzen et al. (2012)

Table 1 Summary of the observed shock effects in different components

Mineral	Shock effect	Figure references
Ilmenite	$\{10\bar{1}1\}/(0001)$ twin	Figs. 6, 8a–c
	µm-scale veins along PFs and FFs within quartz and shear fractures in feldspar	Figs. 5, 6, 8a
	Alteration to anatase, chlorite, calcite, and magnetite	Figs. 10, 11
Magnetite	Lamellar and spheroid exsolutions within coarse ilmenite	Figs. 5a, b, 7, 10c–e
	µm-scale intrusions PFs within quartz and fractures within feldspar	Figs. 2d, 5, 8f, 9b
Quartz	PFs/FFs	Figs. 2c,e,h, 3a–c
	Dauphiné twin	Figs. 8g, 9a
	Partially recrystallized	Fig. 3
Biotite	Kink bands	Fig. 2a, g
Pyrite/Chalcopyrite	µm-scale intrusions in PFs of quartz and fractures of feldspar	Figs. 2d, 9b
Feldspar	Fine-grained schlieren structure associated with recrystallized quartz in shear zones	Figs. 2h, 4, 11

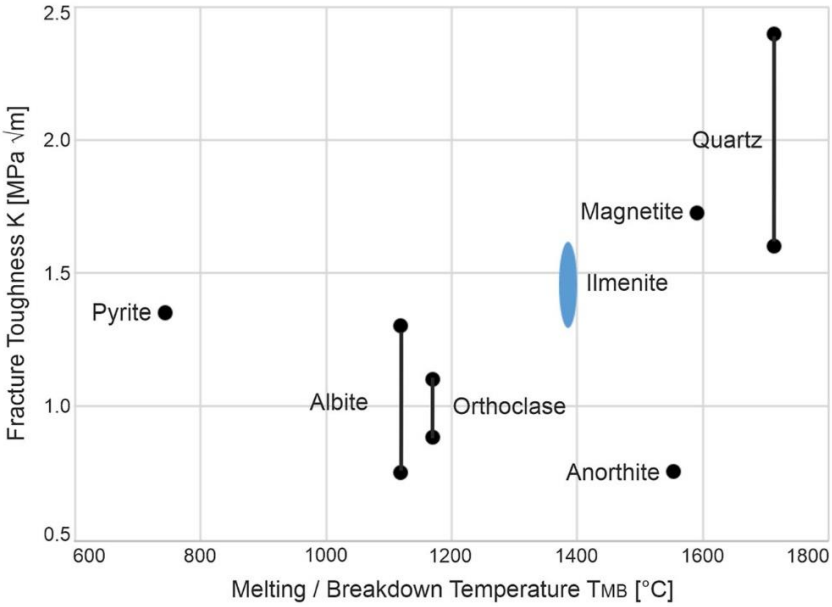

Fig. 12 Melting/breakdown temperature T_{MB} of selected mineral phases with their respective fracture toughness K (Rankin 1915; Morey and Bowen 1922; Shimada 1969; Eriksson and Pelton 1993; Galwey and Brown 1999; Tromans and Meech 2002; Broz et al. 2006; Whitney et al. 2007; Spray 2010; Deer et al. 2013). The fracture toughness of chalcopyrite and ilmenite (blue) was roughly estimated by the authors based on the observations of the investigated microfabrics of this study

the magnetite within the lamellae likely crystallized during cooling after impact.

Ilmenite alteration

Samples V2 1.f (6 cm), V2 66.4 (770 cm), V3 2.1 (5 cm), V3 3.6 (15 cm), V3 3.16 (26 cm), and V3 46.1 (549 cm) contain altered ilmenite and magnetite. Chlorite is formed at the expense of biotite and magnetite; ilmenite is partially transformed into the Ti-phase anatase. Chloritized biotite throughout the drill core often contains a few µm-sized anatase grains (Fig. 10b, d, f), which might represent alteration products. Ilmenite can be largely replaced by a mineral assemblage of anatase, chlorite, calcite, ilmenite, and small magnetite grains—the latter occur primarily in contact with calcite, chlorite, and anatase. The observation that magnetite exsolutions within an ilmenite host are only replaced by chlorite when in direct contact with altered biotite (Fig. 10a–d), but not in contact with feldspar, indicates that fluid availability, and hence alteration, depended on being in direct contact with water-bearing minerals.

Implications for magnetic properties

An important starting point of this study was to disentangle Fe-oxide microstructures that are related to shock effects from the meteorite impact event from those that might have been related to lightning. We did not find evidence for lightning-generated microstructures in the uppermost meter of either core. Carporzen et al. (2012) suggested, based on high coercivities (> 30 mT) and low Verwey transition temperatures (Fig. 11), that oxidized, SD magnetite (< 100 nm) formed from the lightning strikes at the surface. However, such small grain sizes are below the resolution of the analytical techniques we used.

Salminen et al. (2009) found that granophyre and pseudotachylitic breccia from Vredefort samples contain a few µm-sized and a second > 50 µm-sized altered generation of a magnetic phase with high Koenigsberger ratios. They suggested that the high Koenigsberger ratios could be related to high temperatures of the rocks that were uplifted due to the Vredefort impact. Nakamura et al. (2010) argued that Fe-oxides within chloritized biotite largely contribute to the magnetic remanence at Vredefort. Granophyre dikes or polymineralic pseudotachylitic breccia, however, are not present in our samples. Although altered biotite and ilmenite are common in our samples (V2 66.4, 770 cm and V3 46.1, 549 cm), the few µm-sized opaque minerals within (altered) biotite and chlorite in our samples were mostly anatase (Fig. 10b). Given the occurrence of multiple generations of magnetite at all depths in the drill core (Fig. 10), we cannot associate specific magnetite populations as principal contributors to the negative magnetic anomaly.

The temperature of the drilled samples prior to impact is an important factor to explain the magnetic remanence of the host rocks. As discussed above, the temperature of the pre-impact basement (650–725 °C) was higher than the Curie temperature of magnetite (580 °C), as already suggested by Henkel and Reimold (2002) and Salminen et al. (2009). Any additional temperature from impact (i.e., shock heating) cannot be distinguished from the thermal remanence recorded by different magnetite populations. Hence, one should not use the term shock remanent magnetization to describe the thermal remanences in the central region of the Vredefort impact structure.

Two types of magnetite exsolutions within ilmenite formed, related to preceding crystal-plastic deformation probably associated with frictional heating during impact cratering (Fig. 7b, d, e). Both the randomly oriented spheroid exsolutions as well as the crystallographically controlled lamellar exsolutions likely increase the thermal remanent magnetization of the host rock.

Fracturing of coarse magnetite leads to grain size reduction and potentially a transition from MD to SD magnetite, thereby enhancing the remanent magnetization and coercivity. As shown by Carporzen et al. (2006), locally enriched fine-grained magnetite, like that in polymineralic pseudotachylyte formed during impact cratering, can display Verwey transition temperatures ranging from 94 and 111 K. Based on our observations, both investigated drill cores contain fine-grained (albeit almost monomineralic quartz aggregates and feldspar aggregates) shear zones within the top 100 cm, and also below 6 m (Fig. 11). The occurrence of two Verwey transition temperatures within the top 100 cm might therefore arise from pre-impact coarse-grained magnetite with high Verwey transition temperatures (≈ 124 K) and potentially newly formed, fine-grained magnetite with low Verwey transition temperatures (94–111 K), which, however, are below the resolution limit of the SEM as they are skewed toward SD sizes, roughly less than a few 100 nm.

It seems possible that samples collected as a function of distance from the center should reveal systematic differences in remanent magnetization. Approaching the paleosurface (i.e., toward the sediments), the pre-impact basement temperature should have been below the Curie temperature of magnetite, so the original magnetite there should have different remanence characteristics than the thermoremanent magnetization acquired around 2.02 Ga. This could explain the lack of high-amplitude negative anomalies in the amphibolite facies aureole (Fig. 1). Carporzen (2003; 2006) tried to test this, but the lightning-induced component overprinted the 2.02 Ga (or older) remanence, because the samples were collected on the surface. To observe an influence on the remanence characteristics, one should use the Winkie-drill approach (Carporzen et al. 2012) to obtain lightning-free material along a radial transect approaching the paleo-surface.

Conclusions and summary

The studied Archean gneisses from the Vredefort impact structure reveal shock-related deformation of Fe-phases and silicates at non-isostatic stress conditions. The observed PFs and FFs in quartz, which is partially recrystallized, as well as kink bands in biotite, and the abundant shear fractures and shear zones, together with the lack of evidence for rhombohedral PDFs, indicate that shock pressures were less than 20 GPa. Our documented impact-related shock effects in Fe-bearing minerals at these shock conditions are as follows:

1. Mechanical (0001) and $\{10\bar{1}1\}$ twins in coarse pre-impact ilmenite indicate shock-related dislocation glide-controlled deformation (no diffusion required) at non-isostatic stresses.
2. Upon cooling after shock heating, crystallographically-controlled lamellar magnetite (≈ 5 × 1 µm) and spheroid magnetite (≈ 10 µm) formed by exsolution within ilmenite. The lamellar magnetite exsolutions are parallel $\{10\bar{1}1\}$ of the host ilmenite. The spheroidal magnetite exsolutions occur at sites of increased disorder, e.g., along grain boundaries and phase boundaries, aside from twin boundaries, that facilitated diffusion.
3. Shock-related shear deformation and resulting frictional heating of pre-impact magnetite and ilmenite resulted in mobilization of Fe-bearing phases such as ilmenite, magnetite, pyrite, and chalcopyrite, including injection into shear fractures of adjacent quartz and feldspar.
4. The crystallographic orientation of ilmenite within fractures of quartz and feldspar is controlled by an epitactic relationship with the host ilmenite.
5. Comparing ilmenite and magnetite along shear fractures in quartz and feldspar, magnetite appears to be more effectively deformed by cataclasis, whereas pre-impact ilmenite deforms by crystal-plastic deformation (i.e., twinning, dislocation glide), consistent with the relatively higher fracture toughness and melting point of magnetite.

The implications of the magnetic properties are:

1. Impact related fracturing of coarse-grained magnetite likely increased the remanence carrying capacity of the existing MD magnetite as found in laboratory experiments (Carporzen and Gilder 2010). This, together with the newly formed fine-grained magnetite exsolutions within ilmenite, increases the remanent magnetization of the host rock and contributes to the strong, negative magnetic km-scale anomaly northwest of the impact structure's center.
2. Quartz Dauphiné twins restricted to PFs imply temperatures around 650–725 °C (given the assumed paleodepth of 11–23 km) during impact cratering and are therefore higher than the Curie temperature of magnetite (580 °C). Therefore, the paleomagnetic remanence is best explained by impact-related uplifting of the initially hot material and cooling in the magnetic field direction present during the Vredefort impact.

3. No lightning-related microfabric or magnetic phase could be identified within the top 100 cm of the drill core, although magnetic properties suggest a strong influence. Those grains likely reside in the SD grain size range (< 100 nm) below the resolution of the SEM.

Acknowledgements The thoughtful and constructive reviews of Wolf Uwe Reimold and Christian Koeberl as well as the editorial handling of Timothy Grove are greatly appreciated and substantially improved the original manuscript. We acknowledge financial support from the Deutsche Forschungsgemeinschaft TR534/9-1 and GI712/20-1. We owe much gratitude to Rodger Hart and Laurent Carporzen, whose enthusiasm and tenacity facilitated the deep drilling project at Vredefort.

Funding Open Access funding enabled and organized by Projekt DEAL.

References

Antoine LAG, Nicolaysen LO, Niccol SL (1990) Processed and enhanced gravity and magnetic images over the Vredefort structure and their interpretation. Tectonophysics 171:63–74. https://doi.org/10.1016/0040-1951(90)90090-U

Appel PWU, Abrahamsen N, Rasmussen TM (2006) Unusual features caused by lightning impact in West Greenland. Geol Mag 143:737–741. https://doi.org/10.1017/S0016756806002391

Armstrong RA, Compston W, Retief EA, Williams IS, Welke HJ (1991) Zircon ion microprobe studies bearing on the age and evolution of the Witwatersrand triad. Precambrian Res 53:243–266. https://doi.org/10.1016/0301-9268(91)90074-K

Bauer M, Davydovskaya P, Janko M, Kaliwoda M, Petersen N, Gilder SA, Stark RW (2011) Raman spectroscopy of laser-induced oxidation of titanomagnetites. J Raman Spectrosc 42:1413–1418. https://doi.org/10.1002/jrs.2849

Broz ME, Cook RF, Whitney DL (2006) Microhardness, toughness, and modulus of Mohs scale minerals. Am Mineral 91:135–142. https://doi.org/10.2138/am.2006.1844

Buddington AF, Lindsley DH (1964) Iron-titanium oxide minerals and synthetic equivalents. J Petrol 5:310–357. https://doi.org/10.1093/petrology/5.2.310

Carporzen L (2003) Magnétisme à très haute pression: Étude du cratère d'impact de Vredefort, Afrique du Sud, Masters Thesis, Institute de Physique du Globe de Paris

Carporzen L (2006) Magnétisme des cratères d'impact de météorite à Vredefort (Afrique du Sud) et Rochechouart (France), PhD Dissertation, Institute de Physique du Globe de Paris

Carporzen L, Gilder SA, Hart RJ (2005) Palaeomagnetism of the Vredefort meteorite crater and implications for craters on Mars. Nature 435:198–201. https://doi.org/10.1038/nature03560

Carporzen L, Gilder SA (2010) Strain memory of the Verwey transition. J Geophys Res 115:B05103. https://doi.org/10.1029/2009JB006813

Carporzen L, Gilder SA, Hart RJ (2006) Origin and implications of two Verwey transitions in the basement rocks of the Vredefort meteorite crater, South Africa. Earth Planet Sci Lett 251:305–317. https://doi.org/10.1016/j.epsl.2006.09.013

Carporzen L, Weiss BP, Gilder SA, Pommier A, Hart RJ (2012) Lightning remagnetization of the Vredefort impact crater: no evidence for impact-generated magnetic fields. J Geophys Res 117:1–17. https://doi.org/10.1029/2011JE003919

Cloete M, Hart RJ, Schmid HK, Drury M, Demanet CM, Sankar KV (1999) Characterization of magnetite particles in shocked quartz by means of electron- and magnetic force microscopy: Vredefort, South Africa. Contrib Mineral Petrol 137:232–245. https://doi.org/10.1007/s004100050548

Coe RS, Paterson MS (1969) The α-β inversion in quartz: a coherent phase transition under nonhydrostatic stress. J Geophys Res 74:4921–4948. https://doi.org/10.1029/jb074i020p04921

Compston W, Kröner A (1988) Multiple zircon growth within early archaean tonalitic gneiss from the ancient gneiss complex, Swaziland. Earth Planet Sci Lett 87:13–28. https://doi.org/10.1016/0012-821X(88)90061-1

Corner B, Durrheim RJ, Nicolaysen LO (1990) Relationships between the Vredefort structure and the Witwatersrand basin within the tectonic framework of the Kaapvaal craton as interpreted from regional gravity and aeromagnetic data. Tectonophysics 171:49–61. https://doi.org/10.1016/0040-1951(90)90089-Q

de Wit MJ, de Ronde CEJ, Tredoux M, Roering C, Hart RJ, Armstrong RA, Green RWE, Peberdy E, Hart RA (1992) Formation of an Archean continent. Nature 357:553–562. https://doi.org/10.1038/357553a0

Deer WA, Howie RA, Zussman J (2013) An introduction to the rock-forming minerals, 3rd edn. Berforts Information Press, Stevenage

Dressler BO, Reimold WU (2004) Order or chaos? Origin and mode of emplacement of breccias in floors of large impact structures. Earth Sci Rev 67:1–54. https://doi.org/10.1016/j.earscirev.2004.01.007

Ebert M, Poelchau MH, Kenkmann T, Schuster B (2020) Tracing shock-wave propagation in the Chicxulub crater: implications for the formation of peak rings. Geology 48:814–818. https://doi.org/10.1130/G47129.1

Eriksson G, Pelton AD (1993) Critical evaluation and optimization of the thermodynamic properties and phase diagrams of the CaO–Al_2O_3, Al_2O_3–SiO_2, and CaO–Al_2O_3–SiO_2 systems. Metall Trans B 24:807–816. https://doi.org/10.1007/BF02663141

Ferrière L, Morrow JR, Amgaa T, Koeberl C (2009) Systematic study of universal-stage measurements of planar deformation features in shocked quartz: implications for statistical significance and representation of results. Meteor Planet Sci 44:925–940. https://doi.org/10.1111/j.1945-5100.2009.tb00778.x

French BM, Koeberl C (2010) The convincing identification of terrestrial meteorite impact structures: what works, what doesn't, and why. Earth Sci Rev 98:123–170. https://doi.org/10.1016/j.earscirev.2009.10.009

Frick C (1973) Kimberlitic Ilmenites. South African. J Geol 76:85–94

Fricke A, Medenbach O, Schreyer W (1990) Fluid inclusions, planar elements and pseudotachylites in the basement rocks of the

Vredefort structure, South Africa. Tectonophysics 171:169–183. https://doi.org/10.1016/0040-1951(90)90097-R
Galwey AK, Brown ME (1999) Thermal decomposition of ionic solids. Elsevier Sci. https://doi.org/10.1016/S0167-6881(99)X8001-3
Gibson RL (2019) The mesoarchaean basement complex of the vredefort dome—a mid-crustal section through the central kaapvaal craton exposed by impact. In: Kröner A, Hofmann A (eds) The archaean geology of the Kaapvaal Craton, Southern Africa. Springer Nature, Switzerland, pp 109–132. https://doi.org/10.1007/978-3-319-78652-0_5
Gibson RL, Armstrong RA, Reimold WU (1997) The age and thermal evolution of the Vredefort impact structure: a single-grain U-Pb zircon study. Geochim Cosmochim Acta 61:1531–1540. https://doi.org/10.1016/S0016-7037(97)00013-6
Gibson RL, Reimold WU, Stevens G (1998) Thermal-metamorphic signature of an impact event in the Vredefort dome, South Africa. Geology 26:787–790. https://doi.org/10.1130/0091-7613(1998)026%3c0787:TMSOAI%3e2.3.CO;2
Gibson RL, Reimold WU (2005) Shock pressure distribution in the Vredefort impact structure, South Africa. Spec Pap Geol Soc Am 384:329–349. https://doi.org/10.1130/0-8137-2384-1.329
Gibson RL, Wallmach T (1995) Low pressure-high temperature metamorphism in the Vredefort Dome, South Africa: anticlockwise pressure-temperature path followed by rapid decompression. Geol J 30:319–331. https://doi.org/10.1002/gj.3350300311
Gijben M (2012) The lightning climatology of South Africa. S Afr J Sci 108:1–10. https://doi.org/10.4102/sajs.v108i3/4.740
Gilder SA, Pohl J, Eitel M (2018) Magnetic signatures of terrestrial meteorite impact craters: a summary. In: Lühr H, Wicht J, Gilder SA, Holschneider M (eds) Magnetic fields in the solar system-planets, moons and solar wind interactions. Springer, Cham, pp 357–382. https://doi.org/10.1007/978-3-319-64292-5_13
Grieve RAF, Coderre JM, Robertson PB, Alexopoulos J (1990) Microscopic planar deformation features in quartz of the Vredefort structure: anomalous but still suggestive of an impact origin. Tectonophysics 171:185–200. https://doi.org/10.1016/0040-1951(90)90098-S
Haggerty SE (1991) Oxide textures—a mini-atlas. Rev Mineral 25:129–219. https://doi.org/10.1515/9781501508684-008
Hargraves RB (1970) Paleomagnetic evidence relevant to the origin of the vredefort ring. J Geol 78:253–263. https://doi.org/10.1086/627516
Harrison RJ, Becker U, Redfern SAT (2000) Thermodynamics of the R3 to R3c phase transition in the ilmenite-hematite solid solution. Am Mineral 85:1694–1705. https://doi.org/10.2138/am-2000-11-1213
Hart RJ, Andreoli MAG, Smith CB, Otter ML, Durrheim R (1990) Ultramafic rocks in the centre of the Vredefort structure (South Africa): possible exposure of the upper mantle? Chem Geol 83:233–248. https://doi.org/10.1016/0009-2541(90)90282-C
Hart RJ, Andreoli MAG, Reimold WU, Tredoux M (1991) Aspects of the dynamic and thermal metamorphic history of the Vredefort cryptoexplosion structure: implications for its origin. Tectonophysics 192:313–331. https://doi.org/10.1016/0040-1951(91)90106-3
Hart RJ, Hargraves RB, Andreoli MAG, Tredoux M, Doucoure CM (1995) Magnetic anomaly near the center of the Vredefort structure: implications for impact-related magnetic signatures. Geology 23:277–280. https://doi.org/10.1130/0091-7613(1995)023%3c0277:MANTCO%3e2.3.CO;2
Hart RJ, Moser DE, Andreoli M (1999) Archean age for the granulite facies metamorphism near the center of the Vredefort structure, South Africa. Geology 27:1091–1094. https://doi.org/10.1130/0091-7613(1999)027%3c1091:AAFTGF%3e2.3.CO;2
Hart RJ, Connell SH, Cloete M, Maré L, Drury M, Tredoux M (2000) "Super magnetic" rocks generated by shock metamorphism from the centre of the Vredefort impact structure, South Africa. S Afr J Geol 103:151–155. https://doi.org/10.2113/103.2.151
Hart RJ, McDonald I, Tredoux M, de Wit MJ, Carlson RW, Andreoli M, Moser DE, Ashwal LD (2004) New PGE and Re/Os-isotope data from lower crustal sections of the Vredefort Dome and a reinterpretation of its "crust on edge" profile. S Afr J Geol 107:173–184. https://doi.org/10.2113/107.1-2.173
Heaney PJ, Veblen DR (1991) Observation and kinetic analysis of a memory effect at the α-β quartz transition. Am Mineral 76:1459–1466
Henkel H, Reimold WU (1998) Integrated geophysical modelling of a giant, complex impact structure: anatomy of the Vredefort structure, South Africa. Tectonophysics 287:1–20. https://doi.org/10.1016/S0040-1951(98)80058-9
Henkel H, Reimold WU (2002) Magnetic model of the central uplift of the Vredefort impact structure, South Africa. J Appl Geophys 51:43–62. https://doi.org/10.1016/S0926-9851(02)00214-8
Huffman AR, Brown JM, Carter NL, Reimold WU (1993) The microstructural response of quartz and feldspar under shock loading at variable temperatures. J Geophys Res. https://doi.org/10.1029/93jb01425
Huffman AR, Reimold WU (1996) Experimental constraints on shock-induced microstructures in naturally deformed silicates. Tectonophysics 256:165–217. https://doi.org/10.1016/0040-1951(95)00162-x
Kaliwoda M, Giordano D, Krüger ME, Uysal I, Akmaz MR, Hoffmann V, Hochleitner R, Schmahl WW (2021) Raman spectroscopy as a tool for the quantitative estimate of chromium aluminium oxide content in chromite. Spectroscopy 36:17–23
Kamo SL, Reimold WU, Krogh TE, Colliston WP (1996) A 2.023 Ga age for the Vredefort impact event and a first report of shock metamorphosed zircons in pseudotachylitic breccias and Granophyre. Earth Planet Sci Lett 144:369–387. https://doi.org/10.1016/s0012-821x(96)00180-x
Killick AM, Reimold WU (1990) Review of the pseudotachylites in and around the Vredefort "Dome'', South Africa". S Afr J Geol 93:350–365
Kletetschka G, Acuna MH, Kohout T, Wasilewski PJ, Connerny JEP (2004) An empirical scaling law for acquisition of thermoremanent magnetization. Earth Planet Sci Lett 226:521–528. https://doi.org/10.1016/j.epsl.2004.08.001
Koenigsberger JG (1938) Natural residual magnetism of eruptive rocks-Part I. Terr Magn Atmos Electr 43:119–130
Lana C, Gibson RL, Kisters AFM, Reimold WU (2003) Archean crustal structure of the Kaapvaal craton, South Africa—evidence from the Vredefort dome. Earth Planet Sci Lett 206:133–144. https://doi.org/10.1016/S0012-821X(02)01086-5
Lana C, Reimold WU, Gibson RL, Koeberl C, Siegesmund S (2004) Nature of the archean midcrust in the core of the Vredefort Dome, central Kaapvaal Craton, South Africa. Geochim Cosmochim Acta 68:623–642. https://doi.org/10.1016/S0016-7037(00)00447-2
Langenhorst F, Deutsch A (1994) Shock experiments on pre-heated α-and β-quartz: I. Optical and density data. Earth Planet Sci Lett 125:407–420. https://doi.org/10.1016/0012-821X(94)90229-1
Leroux H, Reimold WU, Doukhan JC (1994) A TEM investigation of shock metamorphism in quartz from the Vredefort dome, South Africa. Tectonophysics 230:223–239. https://doi.org/10.1016/0040-1951(94)90137-6
Lilly PA (1981) Shock metamorphism in the Vredefort Collar: evidence for internal shock sources. J Geophys Res Solid Earth 86:10689–10700. https://doi.org/10.1029/JB086iB11p10689
Lindsley DH (1991) Experimental studies of oxide minerals. In: Lindsley DH (ed) Oxide minerals: petrologic and magnetic significance. De Gruyter, Berlin, Boston

Markgraaff J (1986) Elastic behavior of quartz during stress induced Dauphiné twinning. Phys Chem Miner 13:10–112. https://doi.org/10.1007/BF00311900

Martini JEJ (1978) Coesite and stishovite in the Vredefort Dome, South Africa. Nature 272:715–717

Martini JEJ (1991) The nature, distribution and genesis of the coesite and stishovite associated with the pseudotachylite of the Vredefort Dome, South Africa. Earth Planet Sci Lett 103:285–300. https://doi.org/10.1016/0012-821X(91)90167-G

Martini JEJ (1992) The metamorphic history of the Vredefort dome at approximately 2 Ga as revealed by coesite-stishovite-bearing pseudotachylites. J Metamorph Geol 10:517–527. https://doi.org/10.1111/j.1525-1314.1992.tb00102.x

McCarthy T, Stanistreet I, Robb L (1990) Geological studies related to the origin of the Witwatersrand Basin and its mineralization-an introduction and a strategy for research and exploration. S Afr J Geol 93:1–4

Melosh HJ (1989) Impact cratering: a geologic process. Oxford University Press, New York

Mernagh TP (1991) Use of the laser Raman microprobe for discrimination amongst feldspar minerals. J Raman Spectrosc 22:453–457. https://doi.org/10.1002/jrs.1250220806

Migault A (1998) Concepts of shock waves. In: Benest D, Froeschle C (eds) Impacts on earth. Springer, Berlin, pp 79–112. https://doi.org/10.1007/978-3-540-69703-9_5

Minkin JA, Chao ECT (1971) Single crystal X-ray investigation of deformation in terrestrial and lunar ilmenite. In: Proceedings of the second lunar science conference. MIT Press,USA, pp 237–246

Mohr-Westheide T, Reimold WU (2010) Microchemical investigation of small-scale pseudotachylitic breccias from the Archean gneiss of the Vredefort Dome, South Africa. In: Gibson RL, Reimold WU (eds) Large meteorite impacts and planetary evolution IV. Geological Society of America Special Paper 465, USA, pp 619–643. https://doi.org/10.1130/2010.2465(30)

Morey GW, Bowen NL (1922) The melting of Potash Feldspar. Am J Sci 4:1–21

Muundjua M, Hart RJ, Gilder SA, Carporzen L, Galdeano A (2007) Magnetic imaging of the Vredefort impact crater, South Africa. Earth Planet Sci Lett 261:456–468. https://doi.org/10.1016/j.epsl.2007.07.044

Nakamura N, Hirose T, Borradaile GJ (2002) Laboratory verification of submicron magnetite production in pseudotachylytes: relevance for paleointensity studies. Earth Planet Sci Lett 201:13–18. https://doi.org/10.1016/S0012-821X(02)00704-5

Nakamura N, Okuno K, Uehara M et al (2010) Coarse-grained magnetites in biotite as a possible stable remanence-carrying phase in Vredefort granites. In: Gibson RL, Reimold WU (eds) Large meteorite impacts and planetary evolution IV. Geological Society of America Special Paper 465, USA, pp 165–172. https://doi.org/10.1130/2010.2465(11)

Nel LT (1927) Geological map of the country around Vredefort, scale 1:63360, Union of South Africa, Department of Mines and Industries. Geological Survey, Pretoria

Nesterenko VF (2001) Dynamics of heterogeneous materials. Springer, New York

Perchuk LL, Tokarev DA, Van Reenen DD, Varlamov DA, Gerya TV, Sazonova LV, Fel'dman VI, Smit CA, Brink MC, Bischoff AA (2002) Dynamic and thermal history of the Vredefort explosion structure in the Kaapvaal craton, South Africa. Petrology 10:395–432

Phillips M, Bussell MA, Mcdonald I, Hart RJ, Andreoli M (1999) A remote sensing and geological investigation of the Vredefort impact structure (South Africa) using landsat thematic mapper imagery. Abstr Meteor Planet Sci 34:A92–A93

Pilkington M, Grieve RAF (1992) The geophysical signature of terrestrial impact craters. Rev Geophys 30:161–181. https://doi.org/10.1029/92RG00192

Pilkington M, Hildebrand AR (2000) Three-dimensional magnetic imaging of the Chicxulub Crater. J Geophys Res Solid Earth 105:23479–23491. https://doi.org/10.1029/2000jb900222

Plado J, Pesonen LJ, Puura V (1999) Effect of erosion on gravity and magnetic signatures of complex impact structures: geophysical modeling and applications. In: Dressler BO, Sharpton VL (eds) Special Paper of the Geological Society of America. Geological Society of America, Boulder, pp 229–239. https://doi.org/10.1130/0-8137-2339-6.229

Poelchau MH, Kenkmann T (2011) Feather features: a low-shock-pressure indicator in quartz. J Geophys Res 116:1–13. https://doi.org/10.1029/2010JB007803

Pohl J, Poschlod K, Reimold WU, Meyer C, Jacob J (2010) Ries crater, Germany: the Enkingen magnetic anomaly and associated drill core SUBO 18. In: Gibson RL, Reimold WU (eds) Large meteorite impacts and planetary evolution IV. Geological Society of America Special Paper 465, USA, pp 141–163. https://doi.org/10.1130/2010.2465(10)

Rakov VA, Uman MA (2003) Lightning: physics and effects. Cambridge University Press, Cambridge. https://doi.org/10.1063/1.1878338

Rankin GA (1915) The ternary system $CaO–Al_2O_3–SiO_2$, with optical study by F. E. Wright. Am J Sci 39:1–79. https://doi.org/10.2475/ajs.s4-39.229.1

Reimold WU (1990) The controversial microdeformations in quartz from the Vredefort structure, South Africa—a discussion. S Afr J Geol 93:645–663

Reimold WU, Gibson RL (2005) "Pseudotachylites" in large impact structures. In: Koeberl C, Henkel H (eds) Impact tectonics. Springer, Berlin, pp 1–53. https://doi.org/10.1007/3-540-27548-7_1

Reimold WU, Gibson RL (2006) The melt rocks of the Vredefort impact structure—Vredefort Granophyre and pseudotachylitic breccias: implications for impact cratering and the evolution of the Witwatersrand Basin. Chem Erde 66:1–35. https://doi.org/10.1016/j.chemer.2005.07.003

Reimold WU, Hoffmann M, Hauser N, Schmitt RT, Zaag PT, Mohr-Westheide T (2016) A geochemical contribution to the discussion about the genesis of impact-related pseudotachylitic breccias: studies of PTB in the Otavi and Kudu Quarries of the Vredefort Dome support the "In Situ Formation" hypothesis. S Afr J Geol 119:453–472. https://doi.org/10.2113/gssajg.119.3.453

Reynolds IM (1984) Tectonically deformed Ilmenite in titaniferous iron ores of the Mambula Complex, Zululand, South Africa. Can Mineral 22:411–416

Reznik B, Kontny A, Fritz J (2017) Effect of moderate shock waves on magnetic susceptibility and microstructure of a magnetite-bearing ore. Meteor Planet Sci 52:1495–1504. https://doi.org/10.1111/maps.12787

Reznik B, Kontny A, Gerhards U (2016) Shock-induced deformation phenomena in magnetite and their consequences on magnetic properties. Geochem Geophys Geosyst 17:2374–2393. https://doi.org/10.1002/2013GC005223.Received

Sakai H, Sunada S, Sakurano H (1998) Study of lightning current by remanent magnetization. Electr Eng Jpn (english Transl Denki Gakkai Ronbunshi) 123:41–47. https://doi.org/10.1002/(SICI)1520-6416(199806)123:4%3c41::AID-EEJ6%3e3.0.CO;2-O

Salminen J, Pesonen LJ, Lahti K, Kannus K (2013) Lightning-induced remanent magnetization-the Vredefort impact structure, South Africa. Geophys J Int 195:117–129. https://doi.org/10.1093/gji/ggt230

Salminen J, Pesonen LJ, Reimold WU, Donadini F, Gibson RL (2009) Paleomagnetic and rock magnetic study of the Vredefort impact structure and the Johannesburg Dome, Kaapvaal Craton, South Africa-Implications for the apparent polar wander path of the Kaapvaal Craton during the Mesoproterozoic. Precambrian Res 168:167–184. https://doi.org/10.1016/j.precamres.2008.09.005

Schreyer W (1983) Metamorphism and fluid inclusions in the basement of the Vredefort dome, South Africa: guidelines to the origin of the structure. J Petrol 24:26–47. https://doi.org/10.1093/petrology/24.1.26

Schreyer W, Medenbach O (1981) CO_2-rich fluid inclusions along planar elements of quartz in basement rocks of the Vredefort Dome, South Africa. Contrib Mineral Petrol 77:93–100. https://doi.org/10.1007/BF00636513

Sclar CB, Bauer JF, Pickart SJ, Alperin HA (1973) Shock effects in experimentally shocked terrestrial ilmenite, lunar ilmenite of rock fragments in 1–10 mm fines (10085,19), and lunar rock 60015,127. In: Proceedings of the fourth lunar science conference. Pergamon Press, Houston, pp 841–859

Scott RG, Pilkington M, Tanczyk EI (1997) Magnetic investigations of the West Hawk, Deep Bay and Clearwater impact structures, Canada. Meteor Planet Sci 32:293–308. https://doi.org/10.1111/j.1945-5100.1997.tb01267.x

Sharp TG, DeCarli PS (2006) Shock effects in meteorites. In: Lauretta DS, McSween HY (eds) Meteorites and the early solar system II. University of Arizona Press, USA, pp 653–677. https://doi.org/10.2307/j.ctv1v7zdmm

Shimada M (1969) Melting of albite at high pressures in the presence of water. Earth Planet Sci Lett 6:447–450. https://doi.org/10.1016/0012-821X(69)90114-9

Shimizu H, Koyama T, Koyama S, Utada H (2007) A geomagnetic total intensity anomaly originated from lightning-induced isothermal remanent magnetization: case of the Yatsugatake Magnetic Observatory, central Japan. Earth Planets Sp 59:141–149. https://doi.org/10.1186/BF03352687

Spray JG (1992) A physical basis for the frictional melting of some rock-forming minerals. Tectonophysics 204:205–221. https://doi.org/10.1016/0040-1951(92)90308-S

Spray JG (1995) Pseudotachylyte controversy: fact or friction? Geology 23:1119–1122. https://doi.org/10.1130/0091-7613(1995)023%3c1119:PCFOF%3e2.3.CO;2

Spray JG (2010) Frictional melting processes in planetary materials: from hypervelocity impact to earthquakes. Annu Rev Earth Planet Sci 38:221–254. https://doi.org/10.1146/annurev.earth.031208.100045

Spray JG, Biren MB (2021) Distinguishing friction-from shock-generated melt products in hypervelocity impact structures. In: Reimold WU, Koeberl C (eds) Large meteorite impacts and planetary evolution VI. Geological Society of America Special Paper 550, USA, pp 147–170. https://doi.org/10.1130/SPE550

Stepto D (1990) The geology and gravity field in the central core of the Vredefort structure. Tectonophysics 171:75–103. https://doi.org/10.1016/0040-1951(90)90091-L

Stöffler D, Grieve RAF (2007) Impactites. In: Fettes D, Desmons J (eds) Metamorphic rocks: a classification and glossary of terms, recommendations of the international union of geological sciences. Cambridge University Press, Cambridge. https://doi.org/10.3749/canmin.45.6.1545

Stöffler D, Hamann C, Metzler K (2018) Shock metamorphism of planetary silicate rocks and sediments: proposal for an updated classification system. Meteor Planet Sci 53:5–49. https://doi.org/10.1111/maps.12912

Stöffler D, Langenhorst F (1994) Shock metamorphism of quartz in nature and experiment: I. Basic observation and theory. Meteoritics 29:155–181. https://doi.org/10.1111/j.1945-5100.1994.tb00670.x

Tada T, Kurosawa K, Ono H, Hamann C, Okamoto T, Niihara T, Matsui T (2022) Shock recovery of granite with a decaying shock wave: feather features formation in quartz. In: Abstract of 52nd Lun and Planet Sci Conf, pp 1733

Tan W, He H, Wang CY, Dong H, Liang X, Zhu J (2016) Magnetite exsolution in ilmenite from the Fe–Ti oxide gabbro in the Xinjie intrusion (SW China) and sources of unusually strong remnant magnetization. Am Mineral 101:2759–2767. https://doi.org/10.2138/am-2016-5688

Therriault AM, Grieve RAF, Reimold WU (1997) Original size of the Vredefort structure: implications for the geological evolution of the Witwatersrand Basin. Meteor Planet Sci 32:71–77. https://doi.org/10.1111/j.1945-5100.1997.tb01242.x

Trepmann CA (2008) Shock effects in quartz: compression versus shear deformation—an example from the Rochechouart impact structure, France. Earth Planet Sci Lett 267:322–332. https://doi.org/10.1016/j.epsl.2007.11.035

Trepmann CA, Spray JG (2005) Planar microstructures and Dauphiné twins in shocked quartz from the Charlevoix impact structure. In: Kenkmann T, Hörz F, Deutsch A (eds) Large meteorite impacts III. Geological Society of America Special Paper, Canada, pp 315–328. https://doi.org/10.1130/0-8137-2384-1.315

Trepmann CA, Stöckhert B, Dorner D, Moghadam RH, Küster M, Röller K (2007) Simulating coseismic deformation of quartz in the middle crust and fabric evolution during postseismic stress relaxation—an experimental study. Tectonophysics 442:83–104. https://doi.org/10.1016/j.tecto.2007.05.005

Tröger WE (1982) Optische Bestimmung der gesteinsbildende Minerale. In: Bambauer H, Taborszky F, Trochim HD (eds) E. Schweizerbart'sche Verlagsbuchhandlung, Stuttgart

Tromans D, Meech JA (2002) Fracture toughness and surface energies of minerals: theoretical estimates for oxides, sulphides, silicates and halides. Miner Eng 15:1027–1041. https://doi.org/10.1016/j.mineng.2003.09.006

Tullis J (1970) Quartz: preferred orientation in rocks produced by dauphiné twinning. Science 168:1342–1344. https://doi.org/10.1126/science.168.3937.1342

Ugalde HA, Artemieva N, Milkereit B (2005) Magnetization on impact structures - Constraints from numerical modeling and petrophysics. In: Kenkmann T, Hörz F, Deutsch A (eds) Large Meteorite Impacts III. Geological Society of America, Boulder, pp 25–42

Verrier V, Rochette P (2002) Estimating peak currents at ground lightning impacts using remanent magnetization. Geophys Res Lett 29:2–5. https://doi.org/10.1029/2002GL015207

Wenk HR, Chen K, Smith R (2011) Morphology and microstructure of magnetite and ilmenite inclusions in plagioclase from Adirondack anorthositic gneiss. Am Mineral 96:1316–1324. https://doi.org/10.2138/am.2011.3760

Whitney DL, Broz ME, Cook RF (2007) Hardness, toughness, and modulus of some common metamorphic minerals. Am Mineral 92:281–288. https://doi.org/10.2138/am.2007.2212

Zeh A, Gerdes A, Millonig L (2011) Hafnium isotope record of the Ancient Gneiss Complex, Swaziland, southern Africa: evidence for Archaean crust-mantle formation and crust reworking between 3.66 and 2.73 Ga. J Geol Soc Lond 168:953–963. https://doi.org/10.1144/0016-76492010-117

Note: This version is not the official pre-print of the journal American Mineralogist (available here: 10.2138/am-2023-8985). For a better reading-experience, this version has been created for this thesis.

Ilmenite phase transformations in suevite from the Ries impact structure (Germany) record evolution in pressure, temperature, and oxygen fugacity conditions

Fabian Dellefant[1*] · Claudia A. Trepmann[1] · Wolfang W. Schmahl[1,2] · Stuart A. Gilder[1] · Iuliia V. Sleptsova[1] · Melanie Kaliwoda[1,2]

[1]Department of Earth and Environmental Sciences, Ludwig-Maximilians-University, Theresienstr. 41, 80333 Munich

[2]Mineralogical State Collection Munich (MSM), SNSB (natural science collections of Bavaria), Theresienstr. 41, 80333 Munich

*Corresponding author: fabian.dellefant@lmu.de

Abstract Aggregates of ilmenite with varying amounts of rutile, ferropseudobrookite, and pseudorutile in suevites from the Ries impact structure have been analyzed by light microscopy, analytical scanning electron microscopy, electron microscope analysis, and Raman spectroscopy to constrain their formation conditions. The 10s-100s µm aggregates comprise isometric ilmenite grains up to 15 µm in diameter that form a foam structure (i.e., smoothly curved grain boundaries and 120° angles at triple junctions). Grains with foam structure show no internal misorientations, indicating a post-impact formation. In contrast, ilmenite grains with internal misorientation occurring in the core of the aggregates are interpreted as shocked remnant ilmenite originating from the target gneisses. They can contain twin lamellae that share a common $\{11\bar{2}0\}$ plane with the host and the *c-axis* is oriented at an angle of 109° to that of the host. Similarly, the new grains with foam structure display up to three orientation domains, sharing one common $\{11\bar{2}0\}$ plane for each pair of domains and *c*-axes at angles of 109° and 99°, respectively. This systematic orientation relationship likely reflects a cubic supersymmetry resulting from the transformation of the initial ilmenite upon shock (>16 GPa) to a transient perovskite-type high-pressure phase (liuite), subsequent retrograde transformation to the polymorph wangdaodeite, and then back-transformation to ilmenite. Whereas the new grains with foam structure formed from complete transformation, the twin domains in the shocked ilmenite are interpreted to represent only partial transformation. Ferropseudobrookite occurs mostly near the rim of the aggregates. An intergrowth of ferropseudobrookite, ilmenite, and rutile as well as magnetite or rarely armalcolite occurs at contact with the (devitrified) matrix. The presence of ferropseudobrookite indicates high temperature (>1140°C) and reducing conditions. The surrounding matrix provided Mg^{2+} to form the ferropseudobrookite-armalcolite solid solution. Rutile can occur within the aggregates and/or along the ilmenite boundaries; it is interpreted to have formed together with iron during the decomposition of ilmenite at lower temperatures (850°-1050°C). We suggest magnetite in the rims formed by electrochemical gradients driven by the presence of a reducing agent, where Fe^{2+} within ilmenite diffused towards the rim. Subsequent cooling under oxidizing conditions led to the formation of magnetite from the iron-enriched rim as well as pseudorutile around ilmenite grains.

Our study demonstrates that the specific crystallographic relationships of ilmenite grains with foam structure indicate a back-transformation from high (shock) pressures >16 GPa; moreover, the presence of associated Fe-Ti oxides helps indicate local temperature and oxygen fugacity conditions.

Keywords

ilmenite shock effects; transformation twinning; liuite; wangdaodeite; ferropseudobrookite; armalcolite

Introduction

Ilmenite ($Fe^{2+}TiO_3$) is a common Fe-Ti-bearing opaque mineral in magmatic and metamorphic rocks. Its deformation and transformation to ferrimagnetic phases during impact cratering can change the magnetic properties of impactites (e.g., El Goresy 1964; El Goresy et al. 2010; Dellefant et al. 2022), which in turn can result in large-scale magnetic anomalies in impact structures (Pilkington and Grieve 1992; Scott et al. 1997; Plado et al. 1999; Pilkington and Hildebrand 2000; Ugalde et al. 2005; Pohl et al. 2010). Heating of ilmenite under oxidizing conditions leads to the formation of hematite (Fe_2O_3), rutile (TiO_2), and nFe_2O_3 x $nTiO_2$ from 500°-800°C, whereas a complete transformation of ilmenite to pseudobrookite (Fe_2TiO_5) occurs at temperatures above 800°C (Fu et al. 2010). Pseudorutile ($Fe^{3+}{}_2Ti_3O_9$) forms as a transitional phase from ilmenite alteration towards rutile (Teufer and Temple 1966), commonly observed under high oxygen fugacity and below 700°C (Gupta et al. 1991) in combination with iron removal by a leaching agent, such as water, along grain boundaries (Mücke and Bhadra Chaudhuri 1991) and/or structural discontinuities within the grain (Temple 1966; Grey and Reid 1975).

Under reducing conditions, ilmenite dissociates to elemental iron and rutile at temperatures ranging from 850° to 1050°C (Taylor et al. 1972) and forms ferropseudobrookite ($Fe^{2+}Ti_2O_5$) at >1140°C (Lindsley 1965; Keil et al. 1970; Tuthill and Sato 1970; Sargeant et al. 2020), which is mostly found in extraterrestrial material (Keil et al. 1970; Fujimaki et al. 1981). Armalcolite [$(Fe^{2+},Mg)Ti_2O_5$] can be formed from ferropseudobrookite when part of Fe^{2+} is substituted by Mg^{2+} (Anderson et al. 1970). High-temperature experiments with reducing agents can produce a rim of pure iron around ilmenite grains (Gupta et al. 1990; Zhao and Shadman 1990) with various amounts of rutile, ilmenite, and elemental iron (Gupta et al. 1990; Kucukkaragoz and Eric 2006; Sargeant et al. 2020). Ilmenite is reduced with carbon in an argon atmosphere at 1000°C, resulting in Ti-oxides and finely distributed iron within the core and a rim of metallic iron (Gupta et al. 1990), as well as in veinlets of Ti-oxides within the grain as similarly reported by H_2-reduced ilmenites (Sargeant et al. 2020). Experiments of synthetic ilmenite under reducing conditions with CO between 900 and 1100°C resulted in a core of ilmenite encompassed by an inner rim of rutile and an outer rim of pure iron (Zhao and Shadman 1990). The formation of the iron-enriched rim is attributed to the migration of iron to the grain boundaries (Zhao and Shadman 1990; Kucukkaragoz and Eric 2006), whereas finely distributed iron within the grain is interpreted by a movement of a reducing agent into and out of the grain (Li et al. 2012; Dang et al. 2015; Sargeant et al. 2020).

Liu (1975) described a high-pressure phase transition of ilmenite to an orthorhombic perovskite structure at 14 GPa at 1400-1800°C based on X-ray diffraction data. Furthermore, Leinenweber et al. (1991) documented an unquenchable, high-pressure polymorph of ilmenite with a perovskite structure forming at 16 GPa and ≈27°C using a diamond-anvil cell and in-situ powder diffraction. Upon decompression, the high-pressure phase transformed into a meta-stable $FeTiO_3$ phase with a lithium niobate structure (Mehta et al. 1994). Further studies documented these high-pressure phase transitions as a function of temperature [7-10 GPa at 1327-1527°C (Mehta et al. 1994); 10-20 GPa at ≈400°C (Ming et al. 2006); 20-30GPa at ≈1337°C (Nishio-Hamane et al. 2012)]. The orthorhombic perovskite-type $FeTiO_3$ phase named liuite was reported by Ma and Tschauner (2018) from the Shergotty martian meteorite. Xie et al. (2020) described a natural occurrence of the lithium niobate-type $FeTiO_3$ named wangdaodeite from the Suizhou L6 chondrite. Wangdaodeite was reported for the first time in terrestrial rocks from Zipplingen in the Ries impact structure by Tschauner et al. (2020).

Further shock experiments with pressures ranging from 23 to 53 GPa reported quenchable orthorhombic Fe_2TiO_4 (Hashishin et al. 2014), Fe_2TiO_4 (Ca_2TiO_4-Type) + TiO_2 and wüstite (FeO) + TiO_2 (Nishio-Hamane et al. 2012), wüstite and orthorhombic $FeTi_3O_7$ (Nishio-Hamane et al. 2010), as well as $Fe_{1-\delta}Ti_\delta O$ and $Fe_{1+\delta}Ti_{2-\delta}O_\delta$ (Wu et al. 2009). Based on hybrid-density functional modelling, Wilson et al. (2005) predicted a phase transition of $FeTiO_3$ above 65 GPa to TiO_2 (cotunnite) + FeO (wüstite).

Studies of ilmenite shock effects in ilmenite from natural impactites, however, are relatively scarce (Minkin and Chao 1971; Sclar et al. 1973; Syono et al. 1981; Tschauner et al. 2020; Dellefant et al. 2022). This study aims to shed light on the potential of ilmenite as a recorder of temperature, pressure, and oxygen fugacity conditions in impactites based on microfabric and phase relation analyses. To this aim, we investigated 35 ilmenite aggregates within suevites from the Ries impact structure (Zipplingen and Aumühle) with optical light microscopy (transmitted and reflected), Raman spectroscopy, and scanning electron microscopy (SEM) in combination with electron backscatter diffraction (EBSD), as well as electron microprobe (EMP) measurements.

Geological overview

The ≈26 km diameter Ries impact structure formed about 14.8 Ma ago (Rocholl et al. 2017, 2018; Schmieder et al. 2018a, 2018b; Schwarz et al. 2020; Di Vincenzo 2022). The Ries impactor hit a 600-700 m thick, sedimentary layer of limestones, shales, and sandstones that overlay Variscan basement (Bolten and Müller 1969; Pohl et al. 1977) mainly composed of various paragneisses, amphibolites, and metagranites (Schmidt-Kaler 1969; Pohl et al. 1977; Hüttner and Schmidt-Kaler 1999; Stöffler et al. 2013). The Ries structure can be divided into the inner crater, the inner wall [being presumably the rim of the primary inner crater, (Wünnemann et al. 2005)], the megablock zone, and the outer crater rim (Stöffler et al. 2013). Suevite constitutes the most important ejecta blanket that contains polymict impact breccia bearing both lithic clasts and cogenetic melt particles (Stöffler and Grieve 2007; Stöffler et al. 2013). On a microscopic scale, (devitrified) glass represents a heterogeneous distribution of incompletely mixed melts of different compositions interspersed with vesicles indicating gas phases (von Engelhardt et al. 1995). Based on the occurrence of high-temperature phases such as baddeleyite + SiO_2 formed from zircon, fused SiO_2 formed from quartz, or pseudobrookite and rutile formed from ilmenite (El Goresy and Chao 1976), von Engelhardt et al. (1995) suggested the initial melt temperature exceeded 2000°C. Glass fragments in suevites were reported to contain ilmenite with accompanying rutile, magnetite, and pseudobrookite (El Goresy 1964), as well as armalcolite and polycrystalline ilmenite (El Goresy and Chao 1976).

Here, we studied ilmenite aggregates in suevite from a small outcrop between the outer and inner ring in the northwestern part of the Ries impact structure, close to the village of Zipplingen (sample CT827a, Lat 48.92615°, Long 10.40889°) and in a shocked gneiss clast within suevite sampled close to the contact of the underlying bunte breccia in the Aumühle quarry at the northeastern rim of the structure (sample R20-16A, Lat 48.97151°, Long 10.62908°).

Methods

Uncovered and polished thin sections (25 µm) were prepared from the samples and investigated by polarization microscopy (Leica DM2700 P) using both reflected and transmitted light. Photomicrographs were taken with a Leica MC170 HD camera and processed with the Leica Application Suite X 3.08.19082 software.

In-situ micro-Raman spectroscopy was carried out at the Mineralogical State Collection Munich (SNSB) to identify the iron-bearing phases with a HORIBA JOBIN YVON XploRa ONE system. The Raman spectrometer is equipped with a Peltier-cooled CCD detector and edge filters. An 1800g/mm grating was used in combination with a 532 nm 2ω-Nd:YAG laser on iron-bearing phases in an attenuated mode (10% laser power) corresponding to max. 0.9 mW on the sample surface to avoid oxidation (Bauer et al. 2011; Kaliwoda et al. 2021), which could transform magnetite to hematite thereby leading to a false phase determination. Hole and slit diameters were 300 µm and 100 µm, respectively, using an integration time of 2 x 16 s. On the sample surface, a 100x long working distance objective resulted in a 0.9 µm laser spot size. Wavelength calibration was conducted with a pure Si-wafer chip on the predominant 520±1 cm^{-1} peak. The precision in the Raman peak position is estimated at ±1.5 cm^{-1}.

The samples were studied with a Hitachi SU5000 SEM, equipped with a NordlysNano high-sensitivity EBSD detector (Oxford Instruments), energy-dispersive X-ray spectroscopy (EDS) detector (Oxford Instruments), field emission gun, as well as backscattered electron (BSE) and secondary electron (SE) detectors at the Department for Earth and Environmental Sciences, LMU Munich. Thin sections were chemo-mechanically polished with a colloidal silicon suspension (Syton) for EBSD to reduce the surface damage produced from preparation. SEM observations used accelerating voltages of 20 kV and a working distance ranging from 10 to 25 mm. The sample holder was tilted at 70° with respect to the electron beam. EBSD patterns were acquired and automatically indexed with the AZtec analysis software 4.2 (Oxford Instruments). Step sizes for automatic mapping were between 0.5 µm and 2 µm, depending on the resolution and the desired EBSD-pattern quality. EBSD data were processed by the Channel software 5.12.74.0 (Oxford Instruments). The inferred different crystallographic orientations were analyzed by characterizing the smallest angle required to rotate one orientation into another, i.e., by the misorientation angle and the misorientation axis [e.g., Wheeler et al. (2001)]. Grains are detected by a misorientation angle threshold of 10°. Stereograms in the proceeding figures are equal-angle projections of the lower hemisphere with viewing directions identical to the EBSD map.

The chemical compositions of ilmenite, ferropseudobrookite, armalcolite, rutile, and pseudorutile were measured using a Cameca SX-100 electron microprobe (EMP) at the Department for Earth and Environmental Sciences, LMU Munich. As measurement conditions, 15 kV accelerating voltage, 40 nA sample current, and a focused beam were applied. Calibration was performed using silicate and oxide standards: periclase (Mg), albite (Na), bustamite (Mn), Fe_2O_3 (Fe), wollastonite (Ca, Si), rutile (Ti), and orthoclase (K, Al).

Results

Sample description

The investigated suevite sample from Zipplingen (CT827a) consists of ≈85% (devitrified) glass, in which roundish to elongate aggregates of Fe-Ti-oxides with a long axis of 10s to 100s of µm are homogeneously distributed (Fig. 1a, b). The aggregates consist mostly of ilmenite with various amounts of rutile, ferropseudobrookite, and sphene. Magnetite occurs as µm-sized grains dispersed in the matrix and often occurs as a rim around the Fe-Ti-oxide aggregates (Fig. 1a). Calcite grains (≈15%) can have (devitrified) glass as inclusions (Fig. 1b, yellow arrows) and calcite can be included in (devitrified) glass (Fig. 1b, orange arrows). Irregular phase boundaries of calcite are concave with

respect to the glass matrix, where the sharp point of the cusps of the silicate glass-calcite phase boundary points towards the silicate glass (Fig. 1b).

Sample R20-16A from the Aumühle quarry can macroscopically be recognized as a gneiss clast within suevite by its lighter color and foliation. In polarized light, it is characterized by a cryptocrystalline matrix with <10% vesicles (Fig. 1c, d). Elongate ilmenite aggregates with a long axis of several 10s to 100s of µm, as well as secondary hematite, occur homogeneously distributed in the matrix (Fig. 1c). Minerals in the gneiss clast were almost completely amorphized due to the meteorite impact, as evidenced by the cryptocrystalline matrix (Fig. 1d), indicating shock pressures of 35-45 GPa, representing shock stage F-S5 (Stöffler et al. 2018) or II (IUGS system; Stöffler and Grieve 2007).

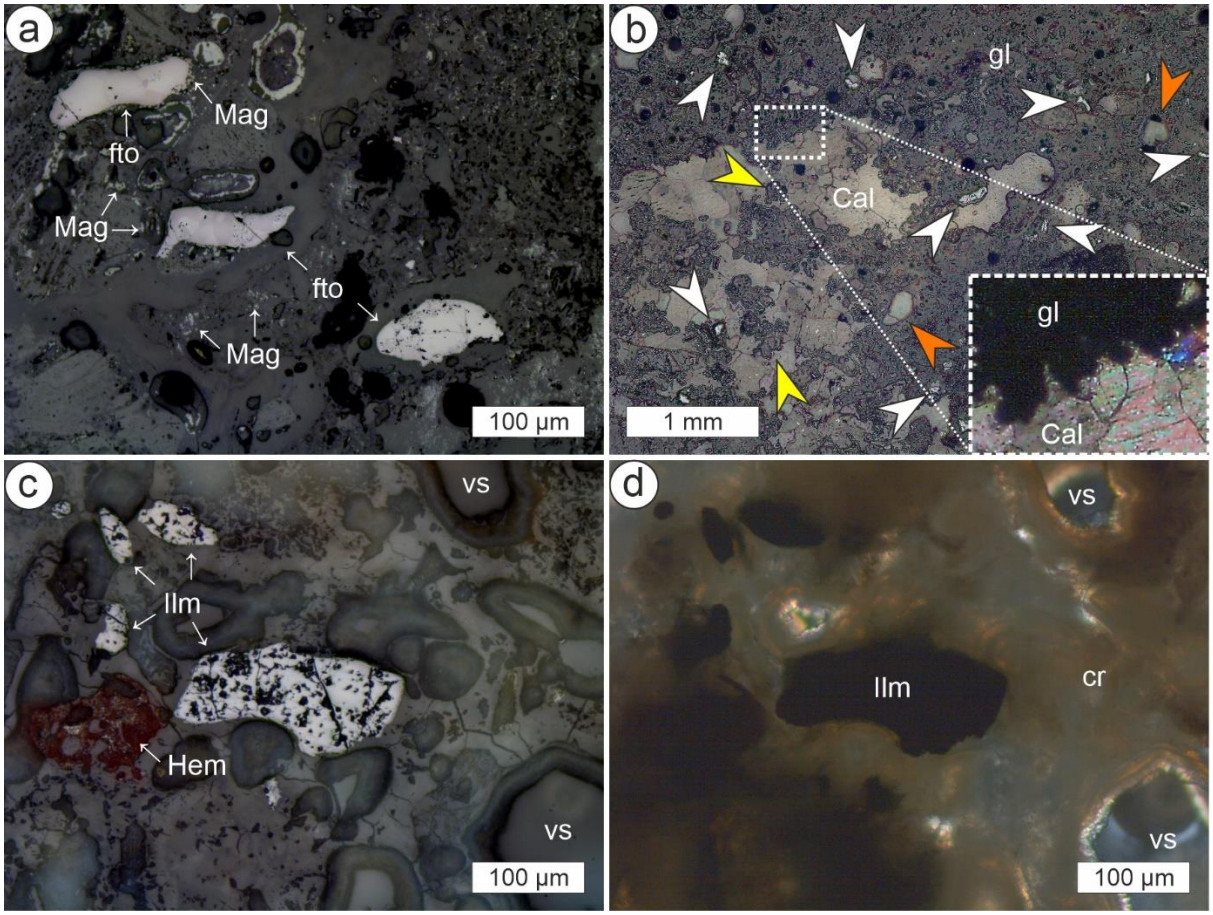

Fig. 1 Polarized light micrographs of ilmenite- and other Fe-Ti-oxide aggregates within samples from the Ries impact structure. **a, b)** Glass fragment (Flädle; sample CT827a) from Zipplingen. **a)** Fe-Ti-oxide (fto) aggregates are associated with magnetite (Mag); reflected light. **b)** Homogeneously distributed Fe-Ti-oxide aggregates (white arrows) and calcite (Cal) within the matrix in reflected polarized light. Note the (devitrified) glass globules within calcite (Cal, yellow arrows) and calcite globules within the matrix (gl, orange arrows). The inset displays the irregular glass-calcite boundary in transmitted light with crossed polarizers. Note that calcite is concave with respect to the glass matrix. **c, d)** Strongly shocked gneiss clast (sample R20-16A) in suevite from the Aumühle quarry that contains ilmenite (Ilm) aggregates, secondary hematite (Hem), and vesicles (vs) within a cryptocrystalline matrix (cr); (c) single plane-polarized reflected light, (d) transmitted light and crossed polarizers.

Phase determination of Fe-Ti-oxides

The Fe-Ti bearing phases in the aggregates were determined by optical reflected light microscopy and confirmed by Raman spectroscopy, chemical EDS and EMP analyses, as well as EBSD patterns. Ilmenite has the main Raman peaks at 227, 333, 371, and 449 cm^{-1} with the prominent peak at 683 cm^{-1} (Fig. 2a) (Wang et al., 2004). The rutile spectra have main Raman peaks at 240, 446, and 611 cm^{-1} (Fig. 2b) (Mazza et al., 2007). Ferropseudobrookite has prominent Raman peaks at 134, 204, 317, and 643 cm^{-1} and a relatively wide peak at 773 cm^{-1} (Fig. 2c), in accordance with spectra of isostructural karooite ($MgTi_2O_5$) (Liermann et al. 2006; He et al. 2017) in combination with a Fe/Ti ratio of ≈1:2 based on EDS and EMP analysis. Peak broadening is associated with a disordered crystal structure (Cynn et al. 1992; Liermann et al. 2006). Magnetite shows typical Raman peaks at 294 and 530 cm^{-1} with the main peak at 661 cm^{-1} (Fig. 2d) (Wang et al., 2004). Within the matrix, magnetite spectra display peaks at 538 and 666 cm^{-1} (Fig. 2e) and thus differ slightly from magnetite at the Fe-Ti-oxide aggregate rim (compare Fig. 2d). We observed additional peaks from the crystallized matrix at 324, 368, and 392 cm^{-1} and a strong peak at 1002 cm^{-1} (Fig. 2e). Sphene displays the main Raman peaks at 166, 254, 335, 468, 548, and 608 cm^{-1} (Fig. 2f) in agreement with Pantić et al. (2014). Within the Aumühle suevite sample (R20-16A), ilmenite has major Raman peaks at 224, 329, 372, and 681 cm^{-1} (Fig. 2g) (Wang et al., 2004). The Raman peaks of pseudorutile are very broad and overlapping, with main peaks at about 153, 264, 312, 419, 557, 599, 693, and 823 cm^{-1} (Fig. 2h) as reported by Imperial et al. (2022).

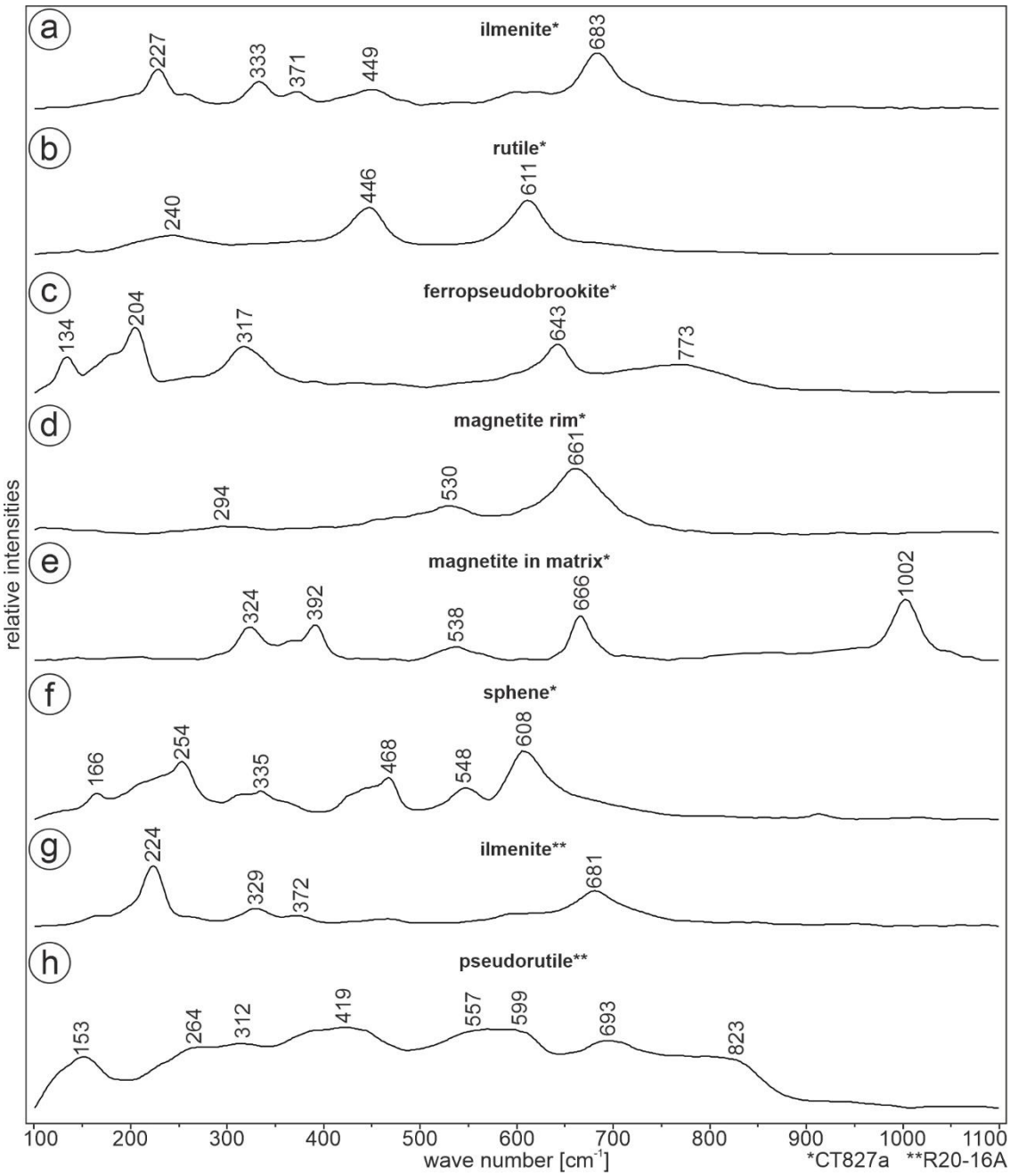

Fig. 2 Raman spectra of **(a)** ilmenite, **(b)** rutile, **(c)** ferropseudobrookite, **(d)** magnetite rim surrounding ilmenite, **(e)** magnetite within the (devitrified) glass matrix, and **(f)** sphene within sample CT827a; as well as **(g)** ilmenite and **(h)** pseudorutile within sample R20-16A.

Microfabrics of ilmenite and associated Fe-Ti-phases in suevite from Zipplingen

Ilmenite within the Zipplingen suevite (CT827a) has a composition ranging from $Fe_{0.88}Mn_{0.08}Mg_{0.06}Ti_{0.98}O_3$ to $Fe_{0.88}Mn_{0.12}Mg_{0.02}Ti_{0.98}O_3$ (Fig. 3a-g; Tab. 1) with small amounts of Al_2O_3. Chemical profiles from the core of the ilmenite aggregate towards the rim conducted with the EMP show an increase in the Fe/Ti ratio (0.83 – 1.03), which correlates with an increase in the Al_2O_3 content (0.07-0.33 wt.%) and a decrease of the analytical total (98.56-96.92 wt.%) (Fig. 3g, h; Tab. S1). The deviation from a total of 100 wt.% of ilmenite can be explained by the presence of a Fe_2O_3 component, which decreases the total wt.% when expressed as FeO. Rutile occurs with variable amounts of FeO

(Tab. S1: #1-#4), up to 20 µm in diameter in the cores of the aggregates (Fig. 3a, g) or distributed as µm-sized grains along ilmenite boundaries (Fig. 3c, d). (Sub-)euhedral magnetite grains, <5 µm in diameter, can occur at the rim or within the matrix at a close distance to the ilmenite aggregate (Figs. 3a, c, e, f, 4a).

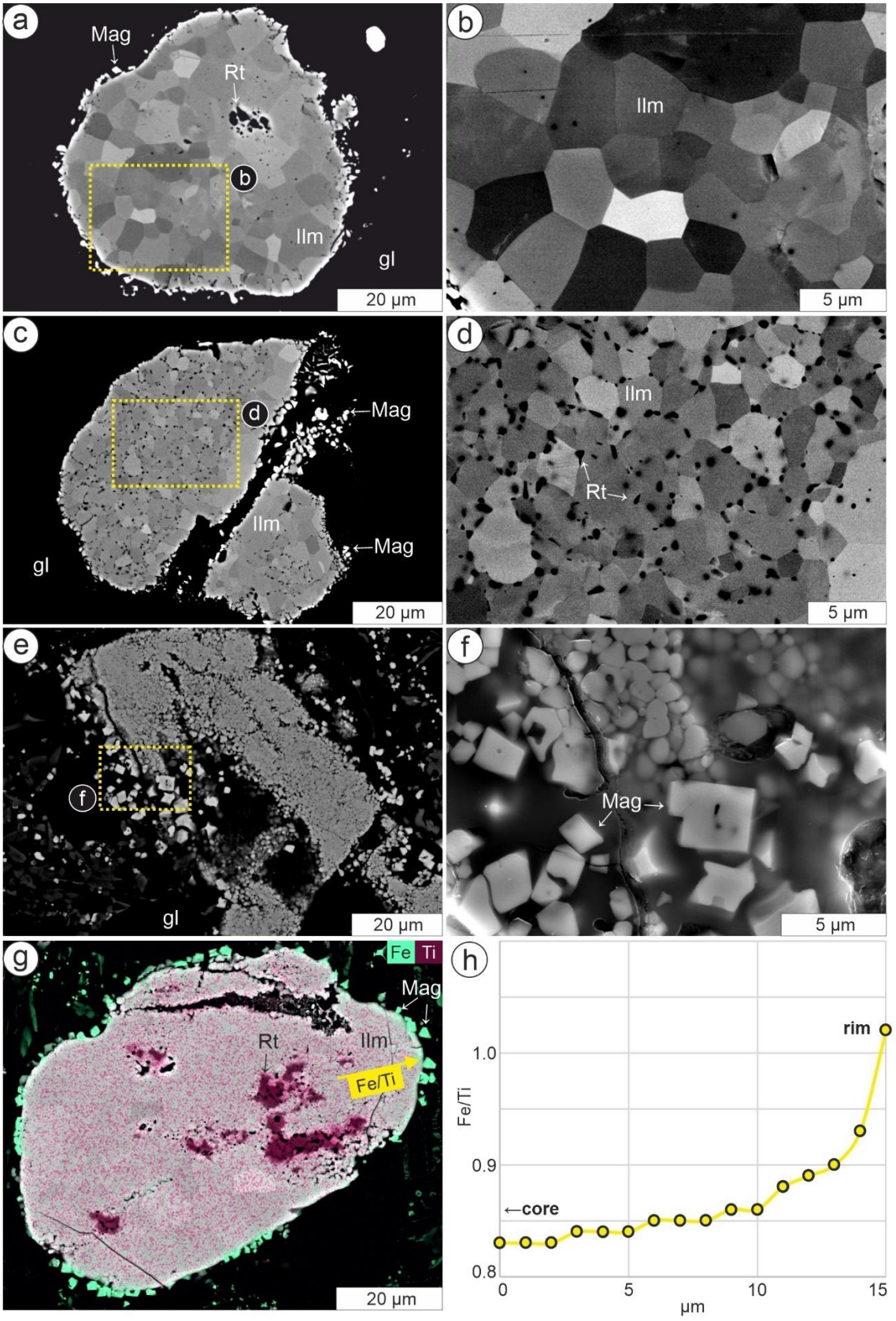

Fig. 3 SEM analyses of Fe-Ti-oxide aggregates embedded in a (devitrified) glass matrix (gl) sample CT827a, Zipplingen; (a-e, g) are BSE images and (f) is a SE image. **a, b)** Foam-structured ilmenite (Ilm) aggregate containing rutile (Rt; black) with a magnetite (Mag; white) rim. The yellow rectangle displays the area depicted in (b). **c, d)** Foam-structured ilmenite (Ilm) aggregate with isolated small rutile (Rt; black) grains along ilmenite boundaries. Note that the image contrast was optimized to show the orientation contrast of ilmenite grains (grey shades), rutile appears black. Magnetite (Mag; white) occurs at the rim. The yellow rectangle displays the area depicted in (d). **e, f)** (Sub-)euhedral magnetite (Mag) occurring at the rim of Fe-Ti-oxide aggregates. The yellow rectangle displays the area depicted in (f). **g)** Fe (green) and Ti (purple) map of the aggregate consisting of ilmenite (Ilm) with rutile (Rt) in the core and a rim of magnetite (Mag). The yellow arrow indicating the Fe/Ti gradient displayed in (h). **h)** Increasing Fe/Ti gradient from the core towards the rim of the aggregate based on EMP data (Tab. S1).

Tab. 1 EMP data (wt.%) of ilmenite (Ilm), ferropseudobrookite (Fpb), and armalcolite (Arm) from sample CT827a (Figs. 4, 8) as well as ilmenite and pseudorutile (Prt) from sample R20-16A (Fig. 9c, d). Note that the detection limit in ppm is given in brackets for a concentration below 0.004 wt.% and/or a not detectable (n.d.) component (*=data as Fe_2O_3). The deviation of the total wt.% can be explained for ilmenite due to the presence of a Fe_2O_3 component, which binds more oxygen and thus would increase the calculated total. Porosity of ferropseudobrookite(-armalcolite solid solution) (Fig. 7c-f) leads to a decrease in the total wt.%, whereas in pseudorutile, the presence of water and/or hydroxyl groups decreases the total wt.%.

Phase	Fig.	FeO / Fe_2O_3*	TiO_2	MnO	MgO	SiO_2	Al_2O_3	Na_2O	CaO	K_2O	Total
Ilm	4 (core)	41.35	51.86	3.80	1.55	0.08	n.d. (253)	0.03	0.05	n.d. (239)	98.72
Ilm	4 (core)	41.52	51.91	3.91	1.55	0.10	n.d. (253)	0.01	0.05	0.02	99.07
Ilm	4 (core)	41.41	51.91	3.90	1.54	0.07	n.d. (253)	n.d. (370)	0.06	n.d. (239)	98.88
Ilm	4 (rim)	40.86	51.89	3.65	2.08	0.09	0.02	0.02	0.06	(249)	98.67
Ilm	4 (rim)	41.88	51.27	3.90	1.47	0.06	0.09	0.02	0.09	0.01	98.80
Ilm	4 (rim)	41.44	51.61	4.01	1.60	0.10	0.11	0.02	0.07	(240)	98.96
Ilm	8	41.83	50.79	5.68	0.41	0.06	n.d. (239)	0.03	0.04	0.01	98.87
Ilm	8	41.42	51.28	5.49	0.43	0.10	(239)	0.02	0.05	0.01	98.85
Ilm	8	42.14	50.68	5.74	0.40	0.07	n.d. (239)	0.03	0.04	(242)	99.11
Fpb	8	33.89	59.69	1.86	0.37	0.75	0.10	0.02	0.56	0.02	97.31
Fpb	8	34.47	59.39	2.20	0.21	0.55	0.11	0.01	0.10	0.02	97.07
Fpb	8	34.31	60.33	1.72	0.40	0.45	0.14	n.d. (379)	0.12	0.01	97.50
Arm	8	30.54	57.72	0.93	2.61	3.17	0.82	0.10	0.29	0.16	96.45
Arm	8	29.83	59.98	1.20	2.05	1.35	0.32	0.04	0.20	0.04	95.09
Arm	8	31.08	60.30	1.32	1.64	2.51	0.30	0.09	0.33	0.06	97.76
Ilm	9c, d	50.74	44.46	1.70	0.52	0.07	n.d. (242)	0.02	0.03	(249)	97.56
Ilm	9c, d	46.74	48.66	1.94	0.66	0.04	0.01	0.03	0.06	0.03	98.16
Ilm	9c, d	48.56	46.64	1.70	0.69	0.08	n.d. (242)	0.04	0.03	n.d. (241)	97.78
Prt	9c, d	41.93*	52.84	1.06	0.11	0.29	n.d. (242)	0.01	0.04	0.01	96.33
Prt	9c, d	41.96*	52.53	0.81	0.07	0.33	n.d. (242)	0.02	0.04	(233)	95.79
Prt	9c, d	41.42*	52.80	0.80	0.08	0.37	n.d. (242)	0.01	0.06	n.d. (233)	95.56

We distinguish two different types of ilmenite grains in the aggregates based on their internal misorientations, grain shape, and composition (Figs. 3-6): (i) Small, isometric grains of up to 15 µm in diameter show smoothly curved grain boundaries and 120° angles at triple junctions, forming a so-

called foam structure (Fig. 3a, b, d). They have generally low internal misorientations with angles <3° (Figs. 4b, c, e, 6b). (ii) In contrast, in the core of the aggregates coarse ilmenite grains can occur that have a short wavelength lamellar internal misorientation with misorientation angles of >10° (Figs. 4 c, d, 5a). These deformed grains can contain a few µm wide twin lamellae that are characterized by a misorientation angle of ≈75° around a misorientation axis parallel to [$\bar{2}$110], which corresponds to *c-axes* at an angle of ≈109° and a common {11$\bar{2}$0} plane (Fig. 5a, c, e). This crystallographic relationship does not correspond to the known (0001), {10$\bar{1}$1}, and {10$\bar{1}$2} twin systems of ilmenite (Minkin and Chao 1971; Sclar et al. 1973; Syono et al. 1981; Dellefant et al. 2022). In some aggregates, only isolated ilmenite grains with internal misorientations are preserved (Fig. 6b, white arrows). The deformed ilmenites have similar crystallographic orientations within single aggregates (Fig. 6e, f).

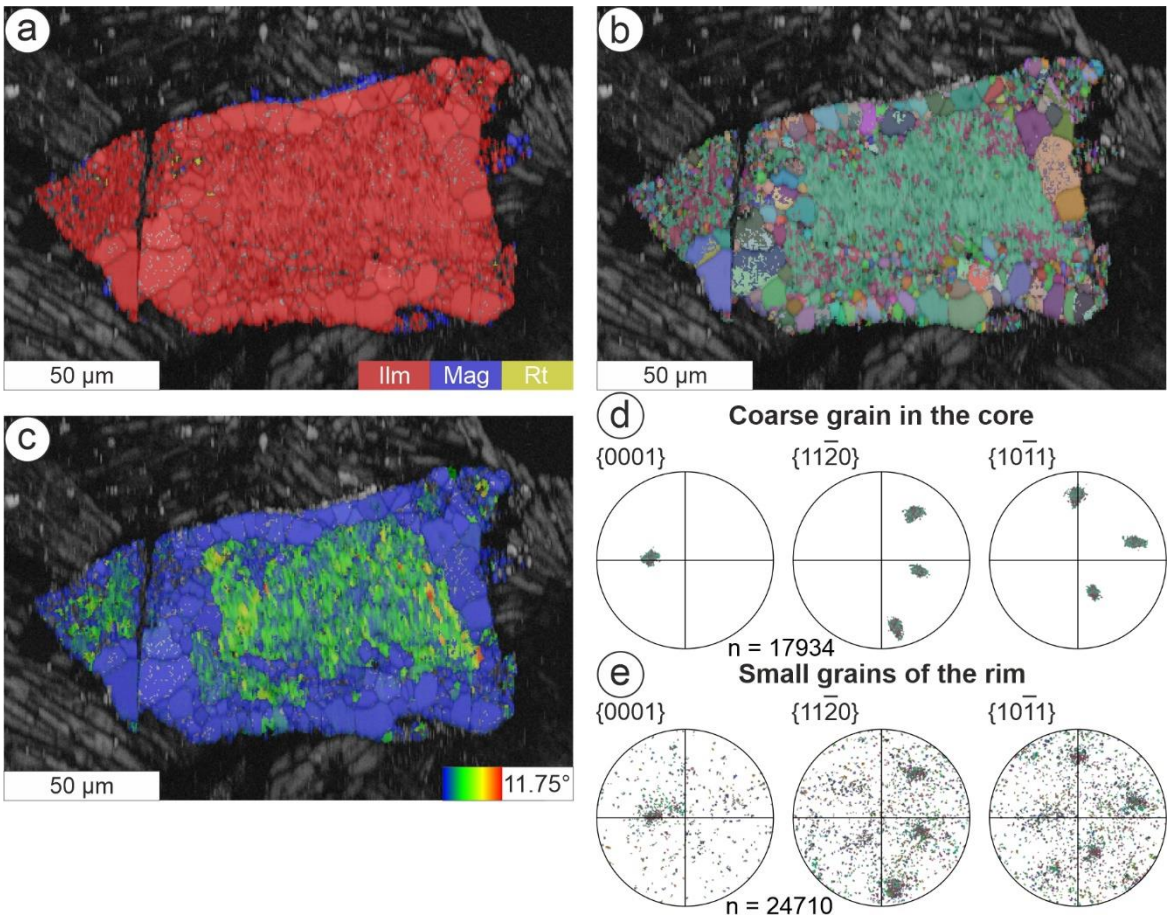

Fig. 4 EBSD data of ilmenite aggregate, sample CT827a, Zipplingen. **a)** Phase map of ilmenite (red), magnetite (blue), and rutile (yellow). **b)** Orientation map (all Euler coloring) of (a). **c)** Grain Reference Orientation Distribution map (GROD) displaying the angular deviation from the average grain orientation. Note the short wavelength misorientation pattern in the core. **d, e)** Pole figures of the {0001}, {11$\bar{2}$0}, and {10$\bar{1}$1} planes of the (d) coarse grain in the core and (e) polycrystalline ilmenite rim.

The ilmenite grains with foam structure and low internal misorientation (Fig. 4a-c, 5a, 6) can show crystallographic orientations scattering largely around that of the deformed ilmenite with internal misorientations (Fig. 4d, e, 5a, c, e, 6). The orientations depict maxima that correspond to the twin relationship, i.e., they share a common {11$\bar{2}$0} plane and *c*-axes that are at an angle of ≈109° (Figs. 5, 6f). Up to three distinct orientation domains were observed with 109° or 99° angles, respectively, between the *c*-axes (Fig. 5b, d, f, 6f).

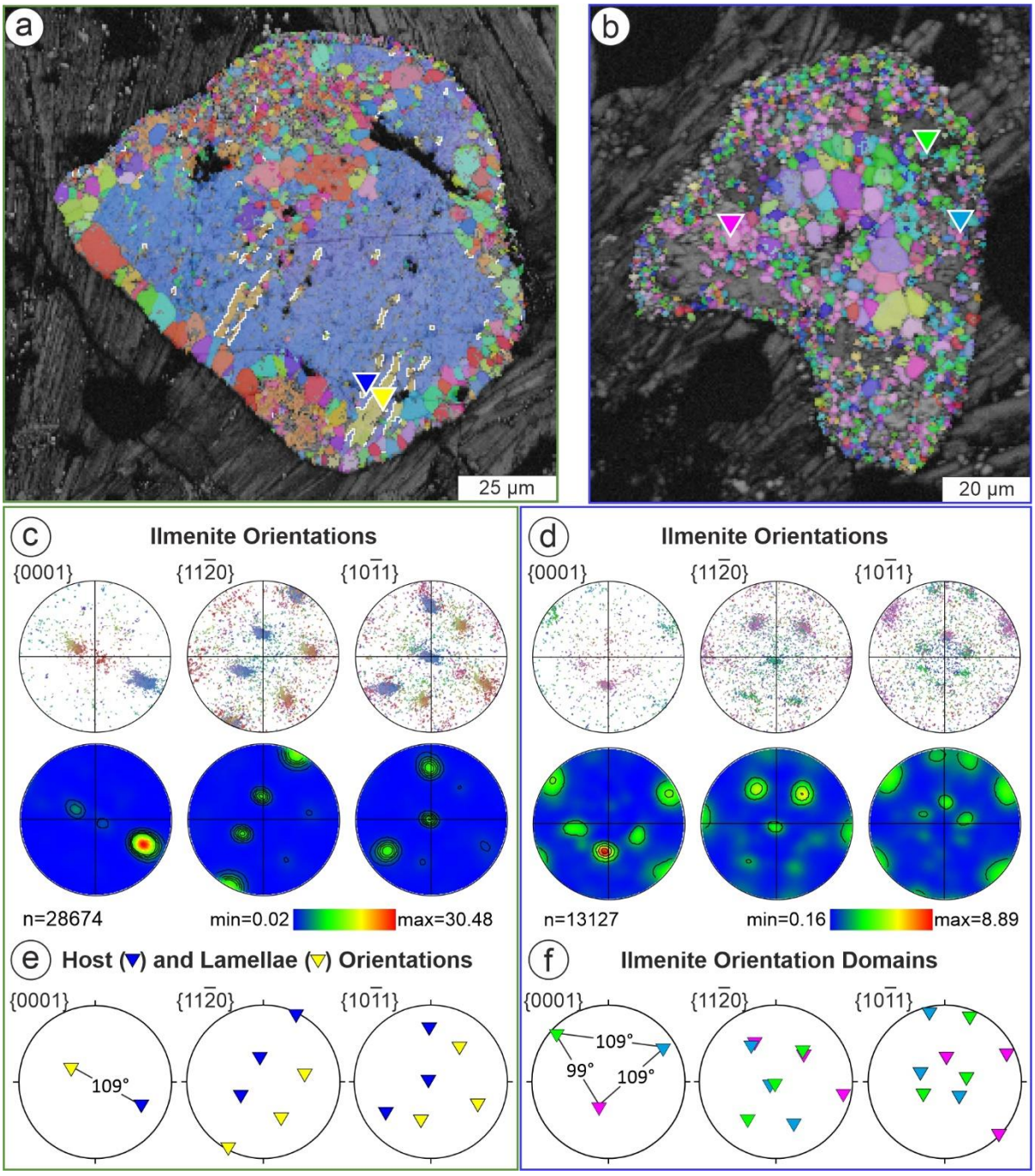

Fig. 5 Crystallographic orientations within ilmenite aggregates, sample CT827a, Zipplingen. **a)** Orientation map (inverse pole figure of z-direction) of rim and core, which displays twin lamellae (orange; twin boundaries in white). The blue and yellow triangles depict the positions of representative core and lamellae orientations depicted in (e). **b)** Orientation map (inverse pole figure of z-direction) with green, blue, and pink triangles, which depict the positions of representative crystallographic orientations displayed in (f). **c, d)** Pole figures and density plots of the {0001}, {11$\bar{2}$0}, and {10$\bar{1}$1}, corresponding to the orientation map in (a) and (b), respectively. **e)** Representative orientations of the host (blue triangle) and lamellae (yellow triangle) depicted in (a) of the {0001}, {11$\bar{2}$0}, and {10$\bar{1}$1} planes. **f)** Representative orientations (green, blue, and pink triangles) of the three different crystallographic domains depicted in (b) of the {0001}, {11$\bar{2}$0}, and {10$\bar{1}$1} planes.

The grains with foam structure can show varying grain sizes (Figs. 5b, 6a, b). Larger grains (>10 µm) are commonly concave and have a high number of neighbors (>6, Fig. 6a, white arrows), and smaller new grains are mostly convex and have fewer neighbors (<6), which suggests some grain boundary migration driven by the reduction in interfacial free energy, i.e., grain growth (e.g., Nicolas and Poirier,

1976; Evans et al., 2001). Strain-free grains with foam structure can contain minor amounts of alumina (0.02-0.11 wt.%), whereas the deformed grains are alumina-free (Tab. 1).

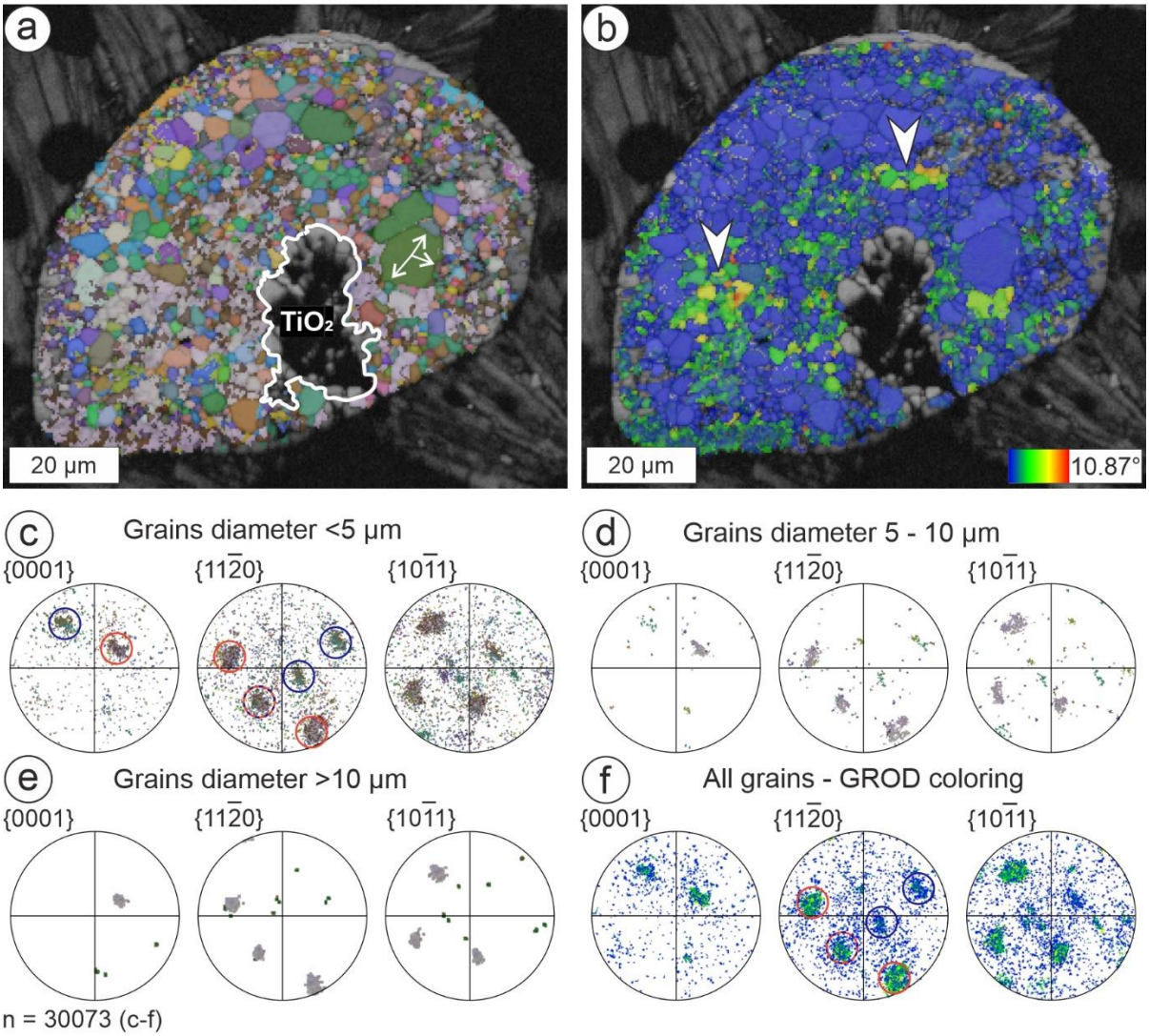

Fig. 6 EBSD data of ilmenite aggregate within sample CT827a, Zipplingen. **a)** All Euler orientation map. Note the larger grains with concave grain boundaries indicated by the three arrows as well as the region strongly enriched in TiO_2 displayed by the white line. **b)** GROD map displaying the angular deviation from the average grain orientation. Note the grains with internal misorientation and irregular grain boundaries indicated by the white arrows. **(c-e)** Ilmenite pole figures of the {0001}, {11$\bar{2}$0}, and {10$\bar{1}$1} planes of **c)** grains <5 µm, **d)** grains 5 – 10 µm, **e)** grains >10 µm. **f)** Orientation of all grains with GROD coloring as displayed in (b). Blue circles indicate that the enclosed orientation data is mostly derived from grains with low internal misorientation, whereas red circles indicate that the enclosed orientation data is mostly derived from grains with relatively high internal misorientation.

Ferropseudobrookite occurs at the boundary of the aggregate with the matrix, or along cracks (Fig. 7b-f), and is locally associated with sphene ($CaTi[O|SiO_4]$) (Figs. 7b, c, 8b), with grains diameters of up to 10s of µm in diameter (Figs. 7b-f, 8a, b, d). Ferropseudobrookite displays a symplectitic intergrowth with ilmenite and rutile towards the core of the aggregate (Fig. 7c-e) with random orientations (Fig. 8d, f), whereas ilmenite displays one maximum but also dispersed crystallographic orientations (Fig. 8c, e) and can occur locally as a fine-grained rim around the aggregate (Fig. 8b, c). In contrast to ilmenite, ferropseudobrookite has minor Mn concentrations (Fig. 8b, g). Locally, at the Fe-Ti-oxide boundary towards the matrix, Mg-enrichment indicates compositions within the

ferropseudobrookite-armalcolite solid solution ($Fe_{1.02}$ $Mn_{0.04}Mg_{0.13}Ti_{1.79}Si_{0.09}Al_{0.02}Ca_{0.01}Na_{0.01}O_5$; Fig. 8h; Tab. 1). The occurrence of ferropseudobrookite and/or rutile in the aggregates correlates with the presence of µm-sized (sub-)euhedral magnetite at the rim or a close distance within the matrix (Fig. 7f).

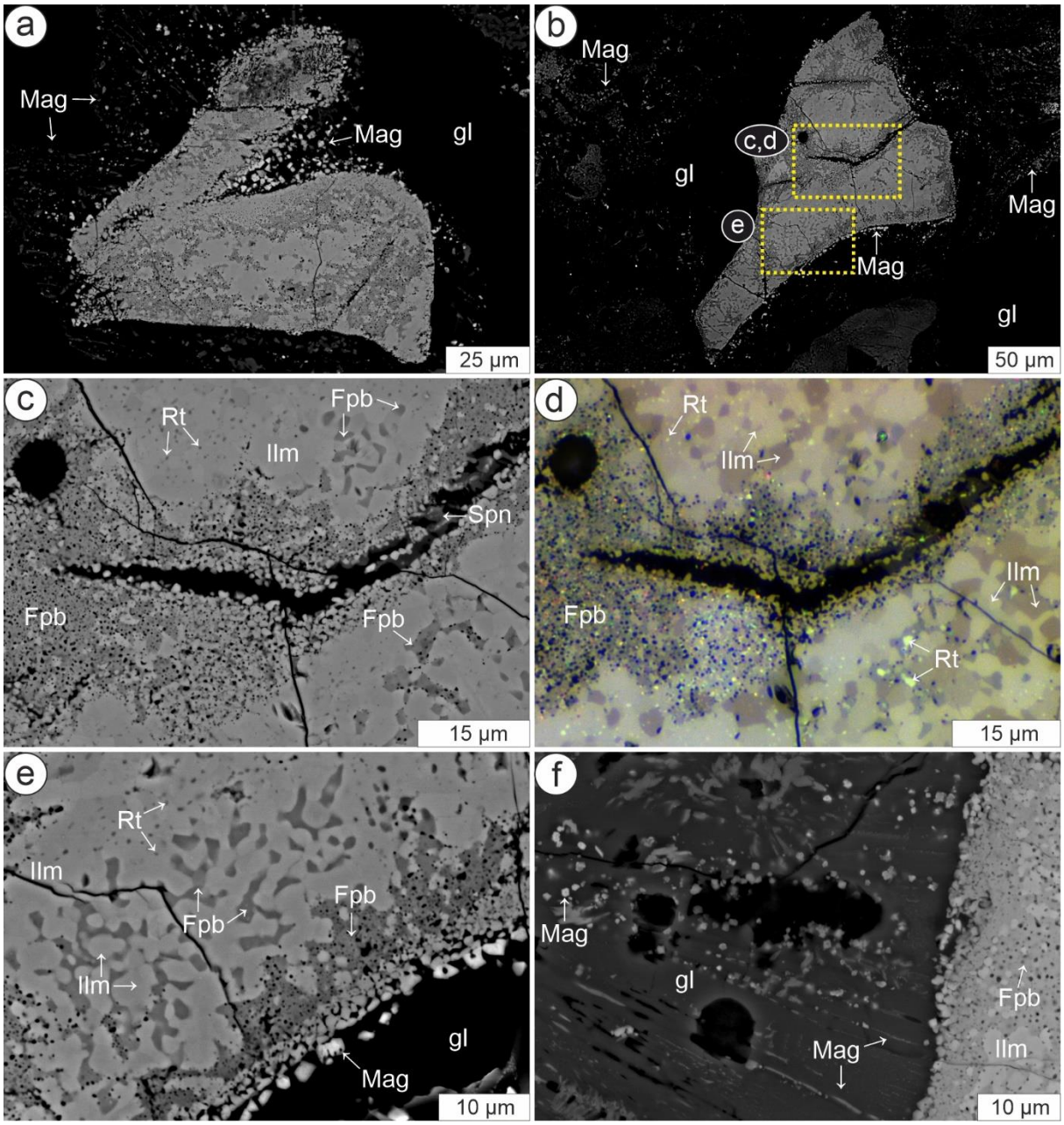

Fig. 7 Ferropseudobrookite in Fe-Ti oxide aggregates, sample CT827a, Zipplingen. **a, b)** Fe-Ti-oxide aggregate with magnetite (Mag) at the rim and within the (devitrified) matrix (gl); BSE images. Yellow rectangles in (b) indicate the close-ups in (c), (d), and (e). **c, d)** Ferropseudobrookite (Fpb) along a fracture within the ilmenite aggregate, where sphene (Spn) is locally present. Note symplectic intergrowth of ferropseudobrookite and ilmenite (Ilm) as well as rutile grains [Rt; dark grey in (c) and white in (d)] along ilmenite grain boundaries at the top of the images; BSE and reflected single plane-polarized light, respectively. **e)** Close-up of rutile (Rt) along ilmenite (Ilm) boundaries, as well as a symplectic intergrowth of ilmenite and ferropseudobrookite (Fpb) at the contact to the (devitrified) matrix (gl), where (sub-)euhedral magnetite grains (Mag) also occur; BSE image. **f)** Traces of (sub-)euhedral magnetite grains (Mag) within the (devitrified) matrix (gl) in close distance to an intergrowth of ilmenite (Ilm) and porous ferropseudobrookite (Fpb).

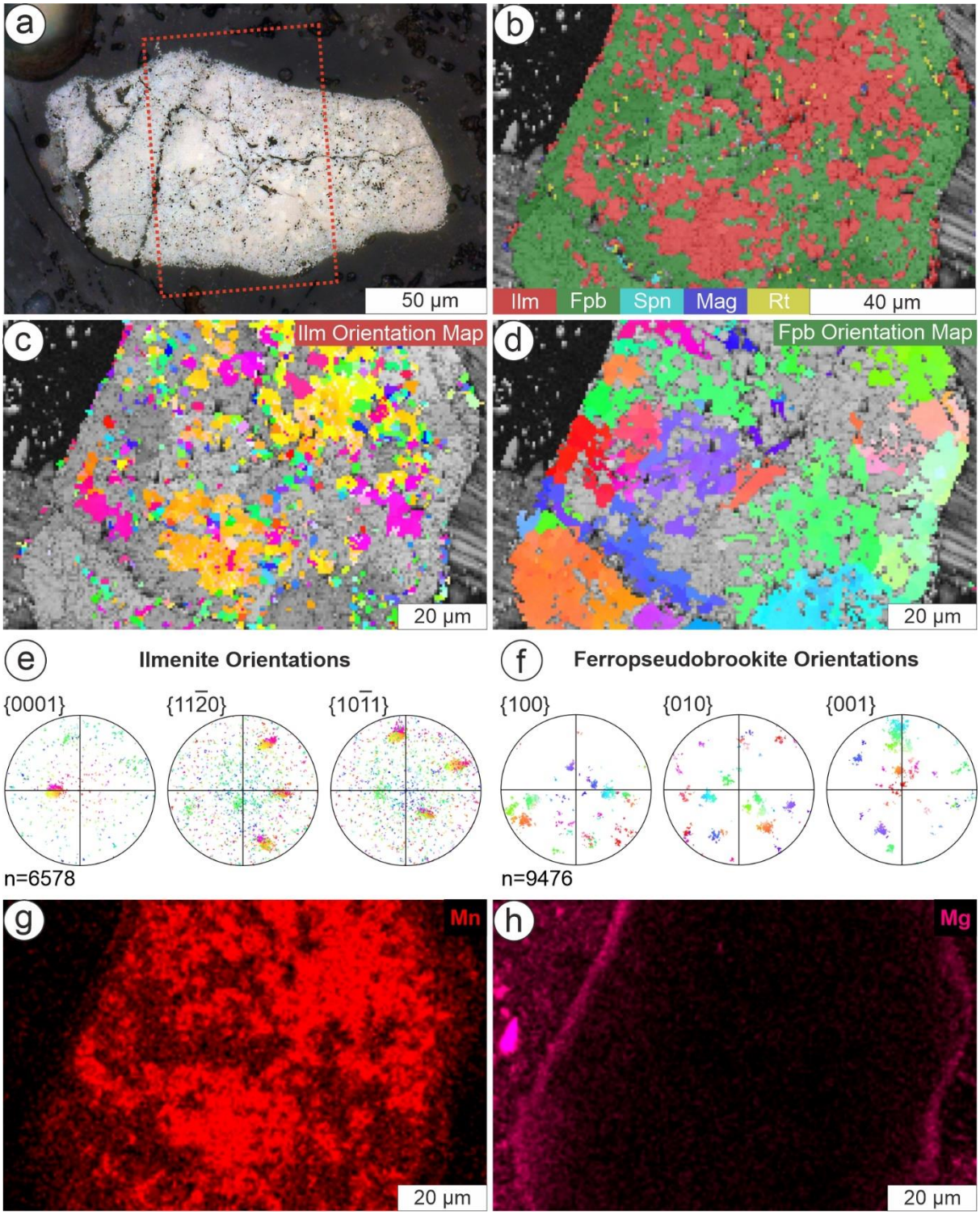

Fig. 8 EBSD and EDS data of ilmenite and ferropseudobrookite aggregates, sample CT827, Zipplingen. **a)** Reflected light micrograph of a Fe-Ti-oxide aggregate. The red rectangle depicts the area displayed in (b-d, g, h). **b)** Phase distribution map of ilmenite (Ilm; red), ferropseudobrookite (Fpb; green), sphene (Spn; light blue), magnetite (Mag; dark blue), and rutile (Rt; yellow). **c)** Ilmenite orientation map (inverse pole figure of z-direction). **d)** Ferropseudobrookite orientation map (inverse pole figure of z-direction). **e)** Pole figures of the {0001}, {11$\bar{2}$0}, and {10$\bar{1}$1} planes of ilmenite displayed in (c). **f)** Pole figures of the {100}, {010}, and {001} planes of ferropseudobrookite displayed in (d). **g)** Manganese (Mn) and **h)** magnesium (Mg) distribution within the Fe-Ti-oxide aggregate.

Microfabrics of ilmenite and associated Fe-Ti-phases in suevite from Aumühle

Within sample R20-16A from the Aumühle quarry, ilmenite aggregates have an average composition of $Fe_{0.92}Mg_{0.04}Mn_{0.04}TiO_3$, with a very similar polycrystalline microfabric as Zipplingen sample CT827a, possessing a foam structure of single grains up to 15 µm in diameter (Figs. 3a, b, 9a) with intergranular cracks (Fig. 9b). No ferropseudobrookite was detected, instead, pseudorutile can be present as µm-sized rim surrounding single ilmenite grains, as larger crystals with some ilmenite remnants in the core (Fig. 9c, d), or completely replacing ilmenite with elongated pores exhibiting a preferred orientation (Fig. 9e). A few aggregates have a ≤5 µm wide rim of 0.5 µm x 2µm-sized intergrown ilmenite needles (Fig. 9f).

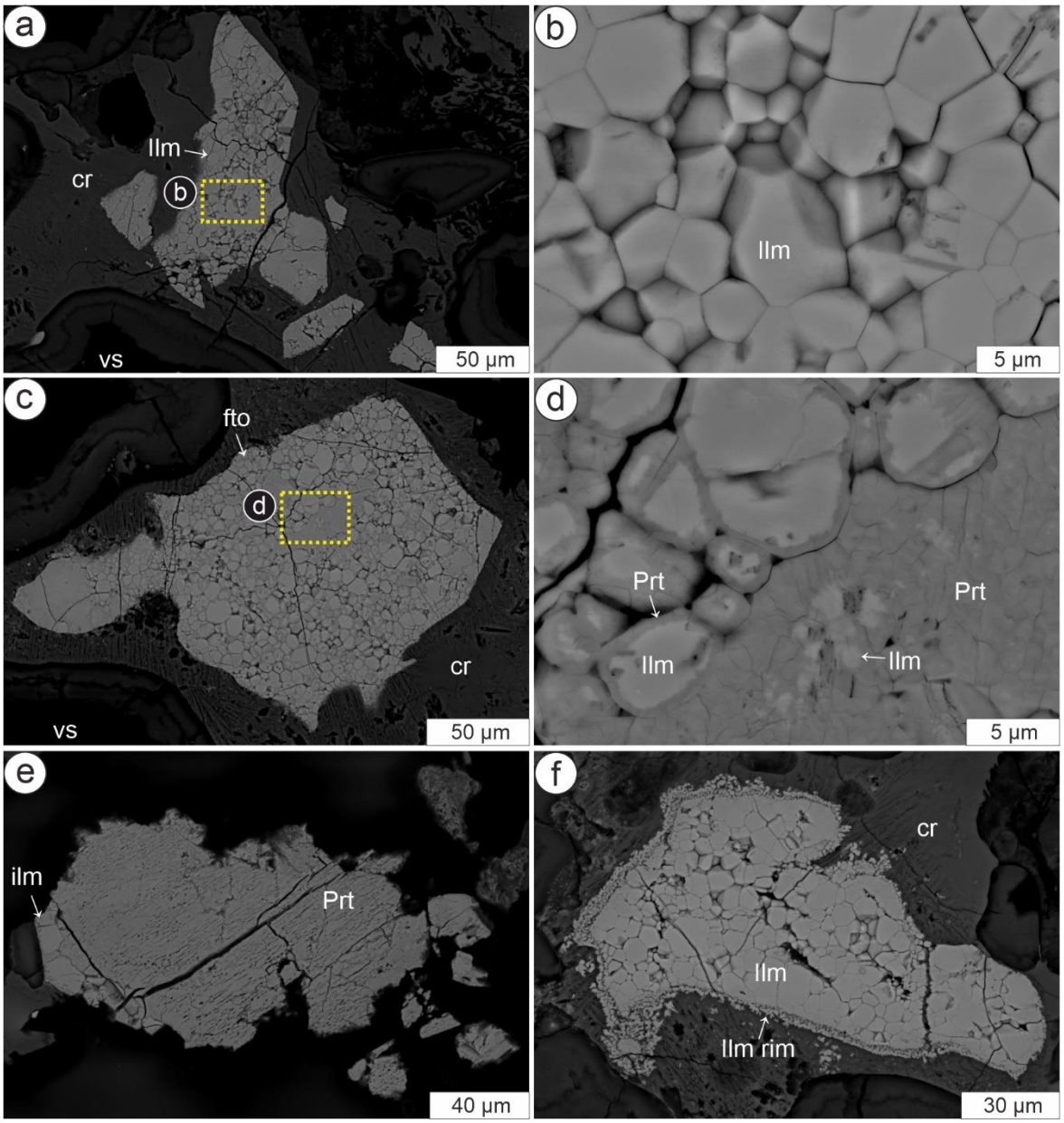

Fig. 9 BSE images of Fe-Ti-oxide microfabrics within suevite sample R20-16A from Aumühle. **a)** Coarse ilmenite grain (Ilm) within a cryptocrystalline matrix (cr) containing vesicles (vs). The yellow rectangle depicts the area in (b). **b)** Ilmenite (Ilm) with foam structure. **c)** Fe-Ti-oxide (fto) reaction fabric within a vesicle-bearing (vs) cryptocrystalline matrix (cr). The yellow rectangle depicts the area in (d). **d)** Ilmenite with a rim of pseudorutile (Prt). Remnants of ilmenite in the bottom right are mostly covered by pseudorutile. **e)** Former ilmenite grain transformed almost completely to pseudorutile (Prt) with preferentially oriented pores/cracks and remnants of foam-structured ilmenite (Ilm). **f)** Foam-structured ilmenite (Ilm) with a finer-scaled ilmenite rim (Ilm rim) embedded in a cryptocrystalline matrix (cr).

Distribution of aggregates within the samples

Of 35 ilmenite orientation investigations within aggregates from Zipplingen and Aumühle, three display three distinct maxima with a common {11$\bar{2}$0} plane, eight display two orientation maxima with a common {11$\bar{2}$0} plane, and ten display one weak to moderate maxima, whereas 14 display only dispersed orientations. Three aggregates show coarse irregular ilmenite with short wavelength lamellar misorientations, in two of these aggregates the deformed ilmenites have twin lamellae.

In total, 23 aggregates of Fe- and/or Ti-bearing phases within the Zipplingen suevite (CT827a) were investigated with SEM/EBSD, where ilmenite is always present (Tab. 2). Aggregates range from 10 µm x 10 µm to 160 µm x 80 µm in size and often show a distinct rim (n=15) comprised of different Fe-Ti-oxides. We observed no size or distribution dependence of aggregates with (10 µm x 10 µm – 160 µm x 80 µm) or without rims (40 µm x 20 µm – 160 µm x 50 µm), as well as no preferred occurrence of distinct phases as a function of size. The aggregates are distributed homogeneously throughout the thin section.

Tab. 2 Investigated rim and core of aggregates of Fe- and/or Ti-bearing phases (Ilm = ilmenite; Mag = magnetite; Rt = rutile; Spn = sphene; Fpb = ferropseudobrookite; Arm = armalcolite) within sample CT827a. The lowercase numbers indicate their occurrence in %.

Size [µm]	Rim phase(s)	Core phase(s)
160 x 80	Ilm_{50}, Arm_{50}	Fpb_{60}, Ilm_{35}, $Spn_{<5}$, $Rt_{<5}$
120 x 100	Mag	Ilm_{85}, Fpb_{10}, $Spn_{<5}$, $Rt_{<5}$
160 x 70	Mag	Ilm_{85}, $Spn_{<15}$, $Rt_{<1}$
170 x 50	Ilm_{80}, Mag_{20}	Ilm_{95}, Rt_{5}
160 x 50	-	Ilm
120 x 80	Fpb	Ilm_{85}, $Rt_{<10}$, $Spn_{<5}$
100 x 90	Ilm	Ilm_{95}, Rt_{5}
120 x 60	$Mag_{>95}$, $Ilm_{<5}$	$Ilm_{>95}$, $Rt_{<5}$
100 x 60	Mag	$Ilm_{>95}$, $Rt_{<5}$
80 x 70	Mag	Ilm_{85}, Fpb_{10}, $Mag_{<5}$, $Rt_{<5}$
80 x 60	-	$Ilm_{>95}$, $Rt_{<5}$
70 x 60	-	$Ilm_{>95}$, $Rt_{<5}$

Size [µm]	Rim phase(s)	Core phase(s)
100 x 40	Ilm_{50}, Rt_{50}	Ilm
70 x 50	Mag	$Ilm_{>95}$, $Rt_{<5}$
100 x 30	-	$Ilm_{>95}$, $Rt_{<5}$
60 x 50	-	$Ilm_{>95}$, $Rt_{<5}$
140 x 20	-	$Ilm_{>95}$, $Rt_{<5}$
100 x 25	Mag	Ilm_{95}, Rt_{5}
70 x 30	Mag	Ilm_{95}, Rt_{5}
40 x 30	Mag	Ilm_{85}, Rt_{15}
40 x 30	-	Spn_{50}, Mag_{20}, Ilm_{15}, Rt_{15}
40 x 20	-	Ilm
10 x 10	Mag	$Ilm_{>95}$, $Rt_{<5}$

From Aumühle (R20-16A), 12 aggregates of Fe- and/or Ti-bearing phases were investigated with SEM/EBSD where ilmenite was consistently present (Tab. 3). Aggregates range from 10 µm x 5 µm to 180 µm x 120 µm in size and can display rims (n=4) composed of ilmenite. The aggregates are distributed homogeneously throughout the thin section.

Tab. 3 Investigated rim and core of aggregates of Fe- and/or Ti-bearing phases (Ilm = ilmenite; Prt = pseudorutile; Rt = rutile) within sample R20-16A. The lowercase numbers indicate their occurrence in % (* = sub-aggregates of fractured ilmenite).

Size [µm]	Rim phase(s)	Core phase(s)
180 x 120	Ilm	Ilm_{95}, Prt_{5}
220 x 70	Ilm	Ilm
70 x 30	-	Ilm
50 x 20	Ilm	$Ilm_{>95}$, $Prt_{<5}$
40 x 25	Ilm	Ilm
40 x 20	-	$Ilm_{>95}$, $Rt_{<5}$

Size [µm]	Rim phase(s)	Core phase(s)
20 x 10	-	Ilm_{95}, Prt_{5}
15 x 10	-	$Ilm_{>95}$, $Prt_{<5}$
*140 x 50	-	Ilm
*40 x 15	-	Ilm
*30 x 20	-	Ilm
*10 x 5	-	Ilm

Discussion

Ilmenite grains from Variscan gneisses shocked to low pressure-temperature conditions from the Ries impact structure show neither a comparable foam structure (Figs. 3a, b, 4, 5, 6) nor short wavelength lamellar misorientation patterns, nor twinning (Figs. 4, 5a), as described in this study. The coarse ilmenite with short wavelength lamellar internal misorientation (Figs. 4, 5a) is interpreted to be preserved shocked ilmenites originating from the target gneisses. The strain-free grains with foam structure (Figs. 3a, b, 4, 5) document an equilibrium fabric and some grain growth, which is indicative of isostatic conditions during their formation (e.g., Nicolas and Poirier, 1976; Evans et al. 2001). Therefore, they are interpreted to have formed after the shock event. Possible processes for the formation of the new grains, which will be discussed in the following, might be (i) strain-induced grain boundary migration, i.e., recrystallization of the originally shocked ilmenite, (ii) crystallization from a Fe-Ti-oxide glass or melt formed upon shock loading and unloading or (iii) phase transformations from transient high-pressure phases formed during shock compression.

Similar ilmenite aggregates as those studied here have been found in kimberlite pipes (Pasteris 1980; Haggerty 1991; Kostrovitsky et al. 2020), which were interpreted as having formed from cumulates in the deep mantle that were deformed and recrystallized during ascent to the crust (Frick 1973; Mitchell 1973). Recrystallization, i.e., grain boundary migration driven by the reduction in strain energy, to replace the shocked original ilmenite grain would result in sutured grain boundaries (Drury and Urai 1990), which is rarely observed for some remnant shocked grains (Fig. 6a, b). In contrast, the foam structure indicates that the reduction in interfacial free energy was the driving force for the grain boundary microstructure formation (e.g., Nicolas and Poirier, 1976; Evans et al. 2001). Furthermore, recrystallization cannot explain the specific crystallographic relationships with up to three distinct orientation maxima with a common $\{11\bar{2}0\}$ plane, comparable to the twin relationship of the shocked remnant grains (Fig. 5b, d, f, 6). Nor can recrystallization explain the occurrences of the different Fe-Ti-phases. The same holds for crystallization of ilmenite grains from a glass or melt. Foam-structured ilmenite aggregates also occur in the suevite sample from Aumühle, which does not display high-temperature phases, such as ferropseudobrookite or pseudobrookite, indicating that temperatures were insufficient for melting.

We suggest that (1) the ilmenite aggregates with foam structure and (2) specific crystallographic relationship similar to the twin relationship in remnant shocked grains, both reflect phase transformations from transient high-pressure phases that were generated upon shock compression

and decompression, as discussed below. We then discuss the formation conditions of the other Fe-Ti phases in the aggregates.

Ilmenite transformation twins and associated orientation relationship between new grains

The observed twin lamellae in shocked ilmenite with a misorientation angle of ≈75° around a misorientation axis parallel to $[\overline{2}110]$, and a common $\{11\overline{2}0\}$ plane (Fig. 5a, c, e) has not been reported for ilmenite so far. Shocked ilmenites in nature and laboratory experiments generate (0001), $\{10\overline{1}1\}$, and $\{10\overline{1}2\}$ twins (Minkin and Chao 1971; Sclar et al. 1973; Syono et al. 1981; Dellefant et al. 2022). No similar mechanical twins are observed in our study.

The two observed twin domains (host and lamellae) in Figure 5a, c, e are characterized by an angle of ≈109° between the *c*-axes, i.e., the threefold axes (Fig. 5e); this angle is very close to the value of the tetrahedral angle between threefold axes in the cubic system (109.47°). The threefold axes of the two twin domains in Figure 5e span a plane which is perpendicular to the apparent interface plane of the host and the twin (Fig. 5a, c, e). The crystallographic preferred orientations of the aggregates with foam structure (Fig. 5f) are characterized by three orientation domains, where the *c*-axes enclose similar angles of 109° and 99°, respectively. Furthermore, each of the three distinct orientation domains shows one common $\{11\overline{2}0\}$ plane with the other two domains, reflecting the same twin operation as in Figure 5a ,c, e that maps any two of the domains onto each other. These characteristics suggest a twinning process related to a cubic supersymmetry: While two of the three orientation domains have a common $\{11\overline{2}0\}$ plane, the deviation from a cubic matrix does not allow a third domain to have a common pole with the other two simultaneously (e.g., Bueble et al. 1998; Hahn and Klapper 2006; Janovec and Přívratská 2006), explaining the 99° angle between the *c*-axes of two of the observed orientation domains. The space group of ilmenite is $R\overline{3}$ (No. 148) (Barth and Posnjak 1934) corresponding to point group $\overline{3}$. A twin operation must not be element of the space- or point group of the twinned phase and the twin operation is, accordingly, not an element of $\overline{3}$. The observed twin operation can be expressed as (a) a 180° rotation around the bisecting angle axis of the c-axes of the twin pair (Fig. 5e) combined with (b) a 180° rotation around the c-axis of one of the twins. Further, combining the $\overline{3}$ point group symmetries of the ilmenite twin domains in their observed mutual orientation with the (a) 180° rotation, leads to a compound supersymmetry equal to the cubic crystallographic point group $m\overline{3}m$ (Fig. 10). The order of point group $m\overline{3}m$ is 48, whereas the order of point group $\overline{3}$ is 6. Therefore, eight (48/6 = 8) equivalent twin domains are theoretically possible. The rhombohedral $\overline{3}$ axis can be chosen along any of the four <111> directions of the cubic compound supersymmetry. Moreover, for each choice of $<111>_{cub}$ direction, there are two choices for the orientation of the $\vec{a}$, $\vec{b}$-axes, since $m\overline{3}m$ also has a threefold rotation axis parallel to the $\overline{3}$ roto-inversion. In the case of the pole figure shown in Figure 5e, the projection is approximately along a fourfold axis of the supersymmetry group $m\overline{3}m$ with only two of the 8 theoretically equivalent twin states realized in the investigated ilmenite grain. In Figure 5f, however, the projection is approximately along a threefold axis of the $m\overline{3}m$ compound supersymmetry and three orientation domains out of the 8 possible orientation domains are present. The Bain lattice-correspondence matrix between the rhombohedral and the cubic lattice, expressed for one out of the 8 possibilities is:

$$(\vec{a} \quad \vec{b} \quad \vec{c})_{cub} = (\vec{a} \quad \vec{b} \quad \vec{c})_{hex} \begin{pmatrix} -1/3 & -1/3 & -2/3 \\ +1/3 & -2/3 & -1/3 \\ +1/6 & +1/6 & -1/6 \end{pmatrix} \text{(Eq. 1)}$$

$$(\vec{a} \quad \vec{b} \quad \vec{c})_{hex} = (\vec{a} \quad \vec{b} \quad \vec{c})_{cub} \begin{pmatrix} 1 & 0 & 2 \\ 0 & -1 & 2 \\ 1 & -1 & -2 \end{pmatrix} \text{(Eq. 2)}$$

(the columns of the matrix give the new lattice basis vectors in terms of the old)

Twins where the twin element is a symmetry element of a supergroup $\mathbb{G}$ of the space- or point group $\mathbb{H}$ of the twinned phase are frequent in cases where a phase transition occurs from a high-symmetry phase of symmetry $\mathbb{G}$ (usually at high temperature) to a low-symmetry phase with subgroup symmetry $\mathbb{H}$ of $\mathbb{G}$. They are called transformation twins (Janovec and Přívratská 2006).

A high-pressure polymorph of ilmenite, liuite, with an orthorhombic (space group Pnma, No.62) perovskite structure (Ma and Tschauner 2018) is reported to form at pressures >16 GPa (Liu 1975; Leinenweber et al. 1991). The Pnma perovskite structure results from a simple displacive distortion of the ideal cubic $Pm\bar{3}m$ perovskite structure (Fig. 10) as similarly discussed by Wang et al. (1991). Upon decompression, liuite transforms first to wangdaodeite (Xie et al. 2020), which is a meta-stable $FeTiO_3$ with a lithium niobate structure, space group R3c (No.161) (Abrahams et al. 1966; Weis and Gaylord 1985; Mehta et al. 1994; Ma and Tschauner 2018) and a related generation of transformation twins due to the many symmetry-equivalent ways of forming wangdaodeite from liuite. Moreover, Wangdaodeite finally transforms to ilmenite (space group $R\bar{3}$) with resulting transformation twins reported in ilmenite (Leinenweber et al. 1994; Mehta et al. 1994). Typically, transformation twins result from phase transitions of the displacive or order-disorder type (e.g., Bueble et al. 1998; Hahn and Klapper 2006; Janovec and Přívratská 2006). However, the ilmenite, $LiNbO_3$, and perovskite structure types are topologically different but nevertheless have related unit cell geometries (Fig. 10). Therefore, the observed twins are interpreted as transformation twins generated by phase transitions with some reconstructive character, albeit with a topotactic relationship between the lattices involved. The experimentally observed prograde and retrograde phase transition sequence (Wang et al. 1991; Leinenweber et al. 1994; Mehta et al. 1994) is sketched in Figure 10a. Leinenweber et al. (1994) argued that as a result of the retrograde perovskite-type to $LiNbO_3$-type phase transition, the mirror planes $(100)_{orth}$, $(010)_{orth}$, and $(001)_{orth}$ in the Pnma perovskite point group disappear, with the latter causing the formation of twinning as similarly discussed by Wang et al. (1991). We follow essentially a similar line of argument and extend it by the new information of the 109° angle between the *c*-axes of the twin domains: additionally, it must be considered that the symmetry of the orthorhombic perovskite liuite Pnma (point group mmm) is also a subgroup of the cubic perovskite symmetry $Pm\bar{3}m$ (point group $m\bar{3}m$). Thus, the $m\bar{3}m$ symmetry is a common supergroup of the lattices of all involved phases (Fig. 10b) and becomes the inherent compound symmetry of the twinning process, without an actual cubic perovskite phase necessarily needing to occur during the impact or the retrograde process. Therefore, the transformation from ilmenite to liuite upon shock compression and transformation to wangdaodeite and finally ilmenite upon unloading (Fig. 10) explains the observed twinning in shocked ilmenite and orientation relationship of new grains in our EBSD maps.

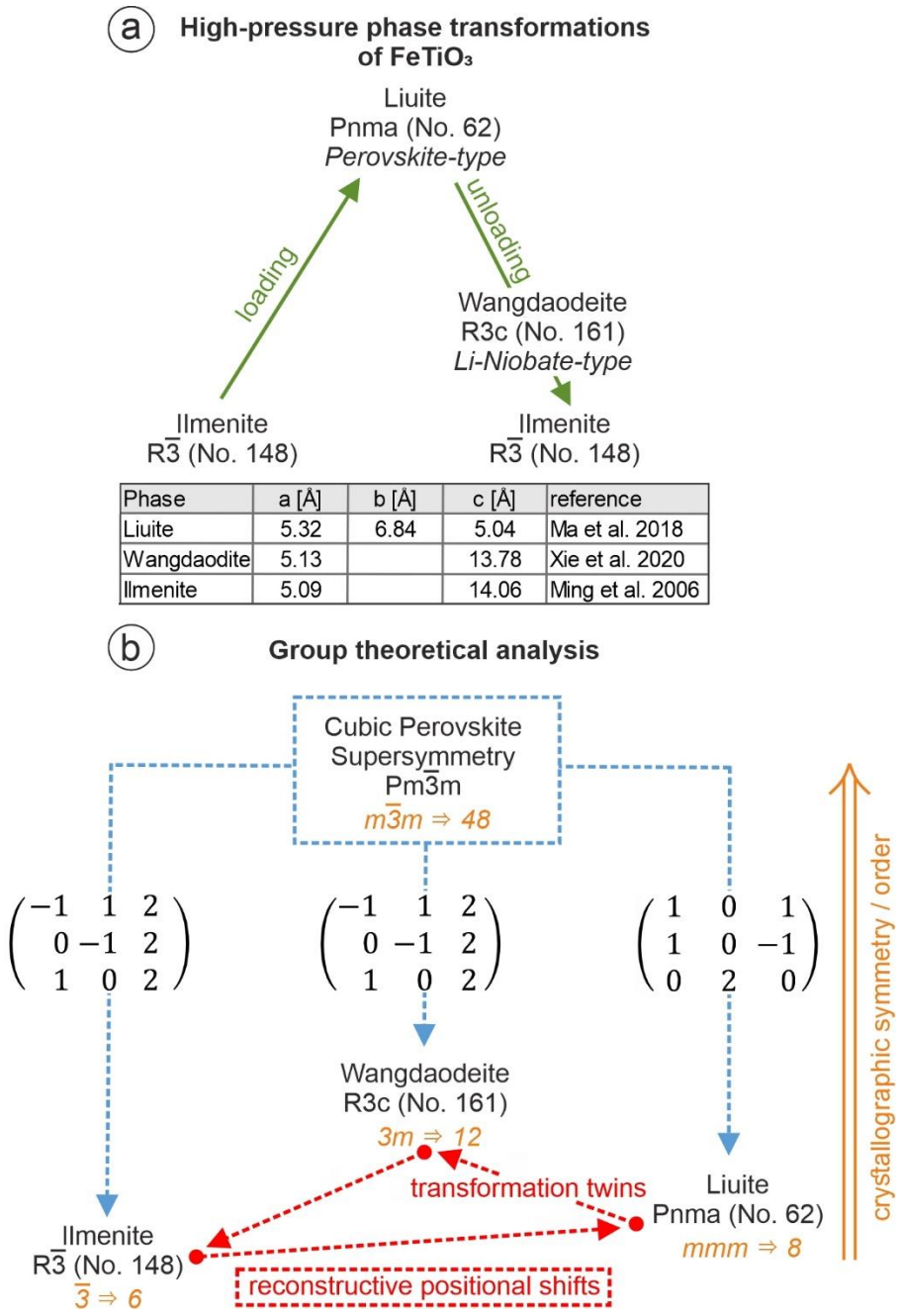

Phase	a [Å]	b [Å]	c [Å]	reference
Liuite	5.32	6.84	5.04	Ma et al. 2018
Wangdaodite	5.13		13.78	Xie et al. 2020
Ilmenite	5.09		14.06	Ming et al. 2006

Fig. 10 High-pressure phase transformations of $FeTiO_3$. **a)** Phase transformations during loading and unloading of $FeTiO_3$ with their respective symmetries, space group numbers (No.), as well as crystallographic lattice parameters a, b, and c. **b)** Group theoretical analysis of the symmetry conversion (blue dashed lines) of ilmenite, wangdaodeite, and liuite with the respective Bain-correspondence matrix. Note that all symmetries derive from the cubic perovskite supersymmetry. Point groups and their respective order are in orange. The red dashed line indicates reconstructive positional shifts of the phase transitions. The generation of transformation twins occurs from the transformation of liuite to wangdaodeite.

Wangdaodeite has recently been detected in gneiss inclusions within suevites from Zipplingen, the same locality as our samples, where the documented BSE images of Tschauner et al. (2020, Fig. 1b) show similar microstructures, as those analyzed here (Figs. 3, 7, 8a). However, with Raman spectroscopy, we did not detect wangdaodeite as there was no indication of the characteristic peak of 739±1 cm^{-1} compared to the Raman spectrum of ilmenite (Xie et al. 2020). The metastability of naturally occurring wangdaodeite in the Ries structure was suggested by Tschauner et al. (2020) due to doping of a few mol.% of $MnTiO_3$, which increases the kinetic barrier for a back-transformation to ilmenite. In contrast to the ilmenite-wangdaodeite-bearing gneiss inclusions investigated by the latter

authors, our sample is comprised of ilmenites within a (devitrified) glass matrix indicating higher temperatures, which could favor the back-transformation to ilmenite despite a few mol.% of $MnTiO_3$ being present (Fig. 8h; Tab. 1).

Similar microstructures as observed in our study have been documented within shocked zircons, where the high-pressure phase reidite occurs as lamellae or, with increasing shock pressures, replaces the entire grain. For the latter, back-transformation to µm-sized granular zircon leads to a systematic orthogonal disorientation relationship of ≈90° around <110> directions between adjacent granules, topotactically controlled by the crystallographic structure of the reidite, leading to a similar orientation relationship of the metastable reidite lamellae and the host zircon (Erickson et al. 2017; Timms et al. 2017; Cavosie et al. 2018). Similarly, the foam structure of ilmenite with distinct orientation maxima of the crystallographic orientations of ilmenite grains can be used as a geobarometer to indicate pressure conditions >16 GPa realized for example in impactites and kimberlites.

Ferropseudobrookite and armalcolite formation conditions

Ferropseudobrookite ($Fe^{2+}Ti_2O_5$) requires >1140°C and a low oxygen fugacity to form (Lindsley 1965; Keil et al. 1970; Tuthill and Sato 1970; Sargeant et al. 2020). In contrast, ferrous-ferric pseudobrookite solid solution forms >800°C under oxidizing conditions (Fu et al. 2010). Therefore, in the Zipplingen sample (CT827; Figs. 7c-f, 8b, d), we interpret that the ferropseudobrookite at the boundary of the Fe-Ti-oxide near the matrix, representing quenched melt, formed from ilmenite as a result of shock-heating after shock-unloading at >1140°C and low oxygen fugacity according to:

$$2FeTiO_3 \rightarrow FeTi_2O_5 + FeO \text{ (Eq. 3)}$$

Maximum temperatures could have exceeded the FeO-TiO_2 melting point of ≈1400°C (Eriksson and Pelton 1993) locally at the aggregate boundary towards the silicate melt. However, the foam structure of ilmenite grains with specific crystallographic relationship documents that solid-state phase transformations dominated.

Armalcolite [$(Fe^{2+},Mg)Ti_2O_5$] is stable above 1010±20°C at ambient pressure (Lindsley et al. 1974) with a pseudobrookite structure (Bowles 1988). Armalcolite was first documented in lunar samples from the Apollo 11 (Anderson et al. 1970) and Apollo 17 missions (Haggerty 1973; El Goresy et al. 1974) and later on Earth in kimberlites (e.g., Haggerty 1975) and lower crustal / mantle xenoliths (e.g., Grégoire et al. 2000; Hayob and Essene 1995; Spiridonov et al. 2019). El Goresy and Chao (1976) first described the occurrence of armalcolite and associated ilmenite in the Ries impact structure within glasses in suevite from diverse localities based on FeO/MgO of 21.1 to 4.5. Microscopic observation and microprobe data of a rutile core and an armalcolite rim suggest a reaction of pre-existing rutile and silicate melt (El Goresy and Chao 1976). In our study, chemical interaction of the silicate melt, represented by the (devitrified) matrix with the Fe-Ti-oxide aggregates, presumably led to the formation of a rim of Mg-bearing ferropseudobrookite-armalcolite solid solution formed from ilmenite (Fig. 8a, b, d, f, h), as also suggested by El Goresy and Chao (1976):

$$2(Fe,Mg)TiO_3 \rightarrow (Fe,Mg)Ti_2O_5 + FeO \text{ (Eq. 4)}$$

An interaction of ferropseudobrookite with the surrounding silicate melt, where the latter provides MgO in exchange for FeO could also produce armalcolite:

$$FeTi_2O_5 + MgO \rightarrow (Fe,Mg)Ti_2O_5 + FeO \text{ (Eq. 5)}$$

In each case, FeO would be enriched within the silicate melt close to the Fe-Ti-oxide aggregates. Temperature stability experiments found that armalcolite decomposes unless rapidly quenched

(Lindsley et al. 1974). Adjacent to the Fe-Ti-oxide aggregate and within fractures, sphene can be present (Figs. 2f, 7c, 8b), which was also likely generated from a chemical reaction with the silicate melt. In contrast to our observations, lunar armalcolites exhibit an inverse core-rim relationship of ilmenite and armalcolite with the latter forming the core (El Goresy et al. 1974; Smyth 1974; Kesson and Lindsley 1975), which therefore indicates different possible modes of formation.

Formation of rutile within aggregates and magnetite outside aggregates

From the 23 Fe-Ti-oxide aggregates analyzed from Zipplingen, 10 display magnetite rims on the boundary towards the (devitrified) matrix and rutile within the aggregate core (Fig. 3, 7a-e, Tab.1). The phase assemblage resembles a Fe concentration gradient, where the rim is enriched in Fe, residing within µm-sized sub(-euhedral) magnetite (Fe_3O_4; Fig. 3a, g). Further inwards, the Fe content decreases to ilmenite ($FeTiO_3$) and finally, Fe is absent, where rutile (TiO_2) exists (Figs. 3a, g, 7a-e). Moreover, the occurrence of ferropseudobrookite and/or rutile within the Fe-Ti-oxide aggregates (Figs. 7c-f, 8b, d) correlates with the presence of µm-sized (sub-)euhedral magnetite at the rim or in proximity to the (devitrified) glass. Only two ilmenite aggregates were observed without magnetite rims — they contain neither rutile nor ferropseudobrookite (Tab. 2).

We suggest that the association of µm-sized rutile along ilmenite grain boundaries included in the aggregates (Figs. 3c, d, 7c-e) was generated due to the thermal decomposition of ilmenite to rutile and Fe^0 after generation of the ilmenite aggregates, i.e., after shock unloading and under a low oxygen fugacity at temperatures ranging from 850° to 1050°C (Taylor et al. 1972) along sites of increased diffusivity like grain boundaries:

$$FeTiO_3 \rightarrow TiO_2 + Fe + ½O_2 \text{ (Eq. 6)}$$

However, a sub-solidus re-equilibration, where ferropseudobrookite first formed at grain boundaries at the expense of ilmenite, with a subsequent back-transformation during cooling below 1140°C (Lindsley 1965) could, furthermore, lead to the formation of ilmenite and rutile (Haggerty and Lindsley 1969; Haggerty 1983; Anovitz et al. 1985):

$$FeTi_2O_5 \rightarrow FeTiO_3 + TiO_2 \text{ (Eq. 7)}$$

Experiments under temperatures from 900° to 1350°C with ilmenite and reducing agents of C (Gupta et al. 1990), CO (Zhao and Shadman 1990), or H_2 (Sargeant et al. 2020) generally form elemental iron at the rim, which is interpreted as a migration of iron towards the grain boundaries (Zhao and Shadman 1990; Kucukkaragoz and Eric 2006). Furthermore, ilmenite, rutile, and iron within the product aggregates can form through diffusion of a reducing agent into ilmenite along vacancies and/or pathways through interstitial structures, such as grain boundaries (Merk and Pickles 1988; Dang et al. 2015; Sargeant et al. 2020).

The presence of a reducing agent could donate electrons to ilmenite at the rim, where Fe^{2+} is reduced to Fe^0. More available electrons would then generate a gradient attracting Fe^{2+} to diffuse from within the aggregate, which agrees with fast Fe^{2+} diffusion in ilmenite modelled by Kuganathan et al. (2019). As a result, Fe^{2+} diffuses towards the rim and vacancies towards the core, thereby leaving TiO_2 inside the ilmenite aggregates, as observed in our study (Figs. 3a, g, 6a). Consistently, we observe an increasing Fe/Ti ratio for ilmenite from the core of the aggregates towards the rim (Fig. 3g, h; Tab. S1). Therefore, we interpret the process of iron enrichment at the rims of the aggregates in terms of an electrochemical solid-state model, where ilmenite aggregates serve as the anode and a reducing agent as the cathode, which generates an electrochemical potential as a driving force for Fe^{2+} diffusion inside the ion-conducting ilmenite (Kuganathan et al. 2019).

The high-temperature (>1140°C) phase transformation of ilmenite to ferropseudobrookite (Eq. 3) only occurs at a low oxygen fugacity and results in the formation of FeO (Lindsley 1965), which was not observed throughout the sample. We suggest that the absence of FeO together with the pores within ferropseudobrookite (Fig. 7c-e) as well as magnetite along the rim (Fig. 7b, e) are also the result of Fe^{2+} migration towards the Fe-Ti-oxide aggregate – melt/matrix boundary. In general, the oxygen fugacity and thus the Fe^{3+}/Fe^{2+} ratio increases with decreasing temperature in silicate melts (Sack et al. 1981; Kilinc et al. 1983). Therefore, oxidation of elemental iron along the Fe-Ti-oxide boundaries could form magnetite at intermediate oxygen fugacity conditions, as experimentally produced from 400° to 700°C (Mitchell et al. 1982; Kuroda and Mitchell 1983). The experiments of Kuroda and Mitchell (1983) produced dispersed oriented magnetite as the first iron oxide phase to form, as observed in our study:

$$3Fe + 2O_2 \rightarrow Fe_3O_4 \text{ (Eq. 8)}$$

The formation of armalcolite leads to a local enrichment of FeO in the silicate melt (Eqs. 4, 5), which likely contributed to the (sub-)euhedral magnetite due to oxidation, as observed within the matrix (Figs. 1a, 2e, 3e, 7a, f):

$$3FeO + ½O_2 \rightarrow Fe_3O_4 \text{ (Eq. 9)}$$

Magnetite formation by oxidation of ilmenite can be excluded because the reaction would stoichiometrically lead to the additional formation and local enrichment of TiO_2, which is not observed at the Fe-Ti-oxide boundaries:

$$3FeTiO_3 + ½O_2 \rightarrow Fe_3O_4 + 3TiO_2 \text{ (Eq. 10)}$$

Furthermore, oxidation of ilmenite above 800°C would only form pseudobrookite (Fe_2TiO_5) and hematite (Fe_2O_3) (Fu et al., 2010). Neither of the ferric phases were observed in the sample material from Zipplingen.

Fluorite-structured TiO_2 and rock salt-structured FeO were experimentally generated from ilmenite at shock pressures >60 GPa (Liu 1975; King and Ahrens 1976). In our study, TiO_2 is observed structurally only as rutile (Fig. 2b) and generally occurs within the cores of the Fe-Ti-oxide aggregates (Fig. 3a, g) or along grain boundaries of single ilmenite grains (Figs. 3c, d, 7c, d, e), and not together with a Fe-rich phase, as could be expected for the breakdown of ilmenite to FeO and TiO_2. We cannot exclude that other breakdown reactions of ilmenite took place in addition to the described breakdown reactions in the presence of a reducing agent but we do not observe evidence from the microfabric.

The investigated sample from Zipplingen consists of ≈15% of calcite, which either occurs as globules within the (devitrified) silicate matrix or as coarse xenomorphic calcite grains incorporating globules of (devitrified) silicate glass (Fig. 1b). The calcite phase boundary is irregular and concave with respect to the silicate matrix. Philpotts and Ague (2009) used such observations to interpret a silicate and an adjacent carbonatic melt based on the viscosities and, therefore, the surface energies of the respective systems. Graup (1999) discussed a liquid immiscibility of silicate and carbonatic melt in suevites from Zipplingen, which is in agreement with Osinski et al. (2008), who considered melting as the common behavior of calcite in impact cratering. On the other hand, Hörz et al. (2015, 2020) proposed devolatilization of calcite as the dominant process based on SEM, electron microprobe analysis, thermal analyses, and shock experiments. Temperatures of a melt vapor mixture formed from basement gneisses, where the ilmenites from our study were likely derived, were modelled to be in excess of 2000°C (von Engelhardt and Graup 1984). Carbonaceous sedimentary target rocks were first hit by the impactor and thus experienced even higher temperature conditions (Bolten and Müller 1969). Thermal decomposition of calcite produces CO_2 at temperatures above ≈650°C (Galwey and Brown 1999) and CO when temperatures exceed 1500°C (Itoh et al. 1993). Furthermore, the initial impact melt was presumably at pressure conditions above the stability conditions for CO_2. Above 30

GPa, oxygen and diamond can form, which during subsequent unloading may react to CO (Nellis et al. 1991; Tschauner et al. 2001). Overall, we suggest CO as a potential reducing agent, which was mixed into the silicate melt due to suevite formation.

Ilmenites in lunar basaltic breccia have ≈3 µm spaced, parallel veins of rutile in combination with droplets of metallic iron inside glass with a well-developed flow texture containing trains of minute iron spherules (Sclar et al. 1973). Ilmenite aggregates were not reported to be enriched in Fe at the ilmenite-glass phase boundary. The presence of a reducing agent as a result of the Ries impact could, therefore, explain the iron-enriched rim of the Fe-Ti-oxide aggregates in comparison to lunar samples, where elemental iron is occurring within the grain (Sclar et al. 1973).

Pseudorutile formation

In the Aumühle gneiss (R20-16A), pseudorutile ($Fe_2Ti_3O_9$) forms a rim around individual ilmenite grains within the aggregates (Fig. 9c, d) or as a nearly complete replacement of coarse ilmenite (Fig. 9e). Broad peaks in the Raman spectra indicate a fairly amorphous structure (Fig. 2h) (Imperial et al. 2022). Ilmenite alteration to pseudorutile occurs when water acts as a transport medium for iron leaching (Mücke and Bhadra Chaudhuri 1991) at a high oxygen fugacity below 700°C (Gupta et al. 1991), which proceeds along grain boundaries and structural discontinuities within the grain (Teufer and Temple 1966; Temple 1966; Grey and Reid 1975). Ilmenite aggregates in sample R20-16A have intergranular microcracks (Fig. 9b), which could have allowed fluids to circulate along the grain boundaries, thereby favoring pseudorutile formation surrounding single ilmenite grains during a late stage of hydrothermal activity. A paleomagnetic study by Sleptsova et al. (2022) shows that the suevites from Aumühle, including from sample R20-16A, were partially overprinted by hydrothermal activity, compatible with our observations. Arp et al. (2013) suggested hydrothermal activity lasted ≈250 ka after the Ries impact.

Conclusions and summary

The homogeneously distributed ilmenite aggregates within the investigated samples contain a suite of Fe-Ti-oxide phases created by pressure-, temperature-, and oxygen-fugacity-changes during impact cratering. Figure 11 summarizes our proposed scenario of how the modification of ilmenite via solid-state transformation through time can explain the phase assemblages in the Ries impact structure.

(I) Upon shock loading, target ilmenites were (partly) transformed into the high-pressure phase liuite (>16 GPa), then transformed upon unloading to wangdaodeite and subsequently ilmenite forming a foam structure (Fig. 11-I). In ≈5% of the observed cases, shocked ilmenite is preserved in the core of the aggregates, which can contain transformation twins that share a common $\{11\bar{2}0\}$ plane with the host and the *c-axis* is oriented at an angle of 109° to that of the host (Figs. 4, 5a, 6b). The transformation from the high-pressure phase liuite is reflected by the crystallographic relationship of the new grains that exhibit up to three orientation domains that share a common $\{11\bar{2}0\}$ plane and whose *c*-axes enclose angles of 109° and 99°, respectively, similar to the twin lamellae within the only partly transformed remnant shocked ilmenite (Fig. 5), which are suggested to represent transformational twins (Fig. 10).

(II+III+IV) Heat production during shock unloading leads to a decrease in oxygen fugacity, however, high-temperature gradients produce different phases and microfabrics. The formation of ferropseudobrookite from ilmenite, occurring mostly at aggregate boundaries and along fractures (Fig. 11-II), indicates temperatures >1140°C with a low oxygen fugacity. Rutile grains along boundaries of ilmenite in the aggregates (Fig. 11-III) indicate thermal decomposition of ilmenite between 850° and 1050°C favored along sites of increased diffusivity. The presence of a reducing agent (likely CO) generated an electron enrichment, which resulted in an electrochemical potential driving Fe^{2+} to migrate from within the ilmenite aggregate cores towards the rim, forming TiO_2 inside the ilmenite aggregates (Fig. 11-IV). Depending on whether the influence of heating or reduction locally prevailed, either µm-sized rutile on grain boundaries (Fig. 11-III) or larger TiO_2 residues were formed (Fig. 11-IV), respectively. The chemical interaction of the silicate melt with ferropseudobrookite formed rare armalcolite-ferropseudobrookite solid solution (Fig. 8a, b, h).

(V) Oxygen fugacity increased as temperature decreased after the impact, which oxidized the iron-enriched rim of the ilmenite aggregates, thereby resulting in the formation of µm-sized (sub-)euhedral magnetite (Fig. 11-V).

(VI) In the aftermath of the impact at temperatures <700°C in combination with high oxygen fugacity, pseudorutile locally formed along intergranular cracks within the ilmenite aggregate in the presence of a fluid (Fig. 11-VI).

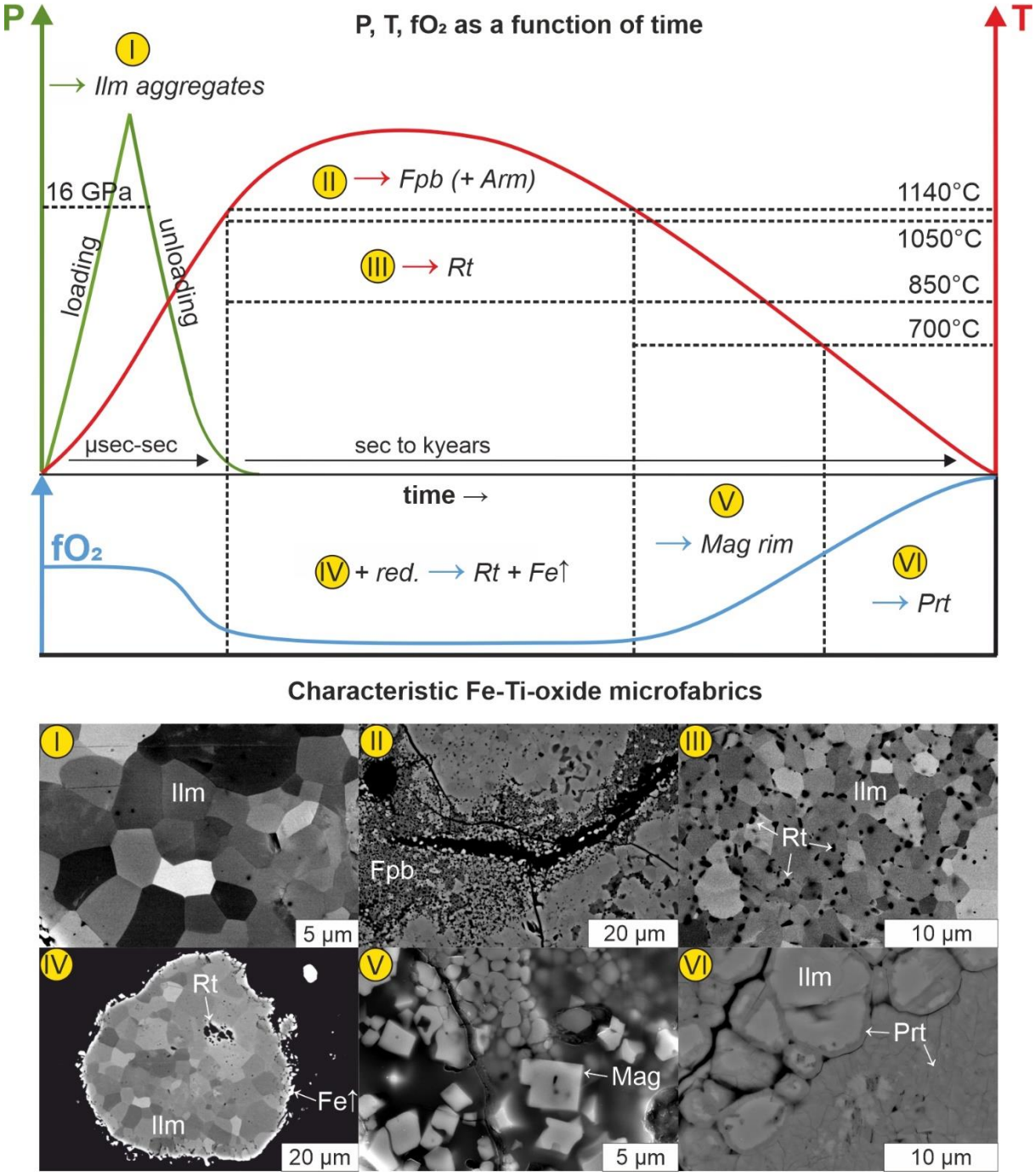

Fig. 11 Summary and interpretations of this study. Pressure (P; green), temperature (T; red), and relative oxygen fugacity (fO_2; blue) conditions as a function of time based on the observed characteristic Fe-Ti-oxide microfabrics. **I)** Foam-structured ilmenite (Ilm). **II)** Ferropseudobrookite (Fpb; dark grey) along a fracture within a Fe-Ti-oxide aggregate. Note that rarely observed armalcolite (Arm) likely formed from Fpb. **III)** Rutile (Rt) along grain boundaries of ilmenite (Ilm). **IV)** Ilmenite (Ilm) aggregate containing rutile (Rt) and with a rim enriched in Fe (Fe↑). **V)** (Sub-)euhedral magnetite (Mag). **VI)** Pseudorutile (Prt) as rim around grains of ilmenite aggregates (Ilm). (bI) – (bV) sample CT827a and (bVI) sample R20-16A. Note that reactions as a function of temperature (red arrows) are always coupled to oxygen fugacity reaction (blue arrows) conditions and vice versa, in contrast to the high-pressure reaction (green arrows). The dashed lines represent pressure, temperature, and oxygen fugacity regimes in which the corresponding reactions take place, except for reaction IV, which presumably takes place up to the ferropseudobrookite stability field (1140°C). BSE images (bI)-(bIV), (bVI) and SE image (bV). Pressure conditions after Leinenweber et al. (1991); temperature and oxygen fugacity conditions after Lindsley (1965), Keil et al. (1970), Tuthill and Sato (1970), Taylor et al. (1972), Mitchell et al. (1982), Kuroda and Mitchell (1983), Gupta et al. (1991), and Sargeant et al. (2020).

Outlook and implications

The interpretations of our study rely on experiments conducted in thermodynamic equilibrium. The shock conditions during meteorite impacts, however, are far from thermodynamic equilibrium conditions (Melosh 1989; Stöffler et al. 2018). Future shock experiments with subsequent high-temperature quenching under controlled oxygen fugacity should yield insight into more realistic temperature, pressure, and oxygen fugacity conditions of shocked ilmenites in the natural environment.

Ilmenite-bearing material, such as the regolith of the moon, may constitute an in-situ oxygen source (Badescu 2012 and references therein) and produces water when heated to temperatures between 850° and 1050°C and reduced with H_2 (Li et al. 2012; Dang et al. 2015; Sargeant et al. 2020). Our study demonstrates that ilmenite microfabrics can be largely modified due to meteorite impacts, resulting in aggregates that consist of various Fe- and/or Ti-bearing phases, which change the physical, chemical, and/or magnetic properties of the host rocks. Our findings might also be relevant for the consideration of breakdown reactions of Fe/Ti-phases in the scope of in-situ resource utilization (ISRU) on planetary objects, whose surfaces are blanketed by meteorite impact structures.

Acknowledgements

We greatly appreciate the constructive and thoughtful comments of Aaron Cavosie and an anonymous reviewer as well as the editorial handling of Susannah Dorfman. We thank Dirk Müller for the help with the electron microprobe analyses, Jean Pohl for his helpful comments on the manuscript, and Rhander Taufner for help with the MTEX scripts. We acknowledge financial support from the Deutsche Forschungsgemeinschaft TR534/9-1 and GI712/20-1.

References

Abrahams, S.C., Reddy, J.M., and Bernstein, J.L. (1966) Ferroelectric lithium niobate. 3. Single crystal X-ray diffraction study at 24°C. Journal of Physics and Chemistry of Solids, 27, 997–1012.

Anderson, A.T., Boyd, F.R., Bunch, T.E., Cameron, E.N., El Goresy, A., and Finger, L.W. (1970) Armalcolite: A new mineral from the Apollo 11 samples. In Geochimica et Cosmochimica Acta Supplement Vol. 1, p. 55.

Anovitz, L.M., Treiman, A.H., Essene, E.J., Hemingway, B.S., Westrum, E.F., Wall, V.J., Burriel, R., and Bohlen, S.R. (1985) The heat-capacity of ilmenite and phase equilibria in the system Fe-T-O. Geochimica et Cosmochimica Acta, 49, 2027–2040.

Arp, G., Kolepka, C., Simon, K., Karius, V., Nolte, N., and Hansen, B.T. (2013) New evidence for persistent impact-generated hydrothermal activity in the Miocene Ries impact structure, Germany. Meteoritics and Planetary Science, 48, 2491–2516.

Badescu, V., Ed. (2012) Moon. Springer Berlin Heidelberg, Berlin, Heidelberg.

Barth, T.F.W., and Posnjak, E. (1934) The Crystal Structure of Ilmenite. Zeitschrift für Kristallographie - Crystalline Materials, 88, 265–270.

Bauer, M., Davydovskaya, P., Janko, M., Kaliwoda, M., Petersen, N., Gilder, S.A., and Stark, R.W. (2011) Raman spectroscopy of laser-induced oxidation of titanomagnetites. Journal of Raman Spectroscopy, 42, 1413–1418.

Bolten, R., and Müller, D. (1969) Das Tertiär im Nördlinger Ries und in seiner Umgebung. Geologica Bavarica, 61, 87–130.

Bowles, J.F.W. (1988) Definition and range of composition of naturally occurring minerals with the pseudobrookite structure. American Mineralogist, 73, 1377–1383.

Bueble, S., Knorr, K., Brecht, E., and Schmahl, W.W. (1998) Influence of the ferroelastic twin domain structure on the {100} surface morphology of $LaAlO_3$ HTSC substrates. Surface Science, 400, 345–355.

Cavosie, A.J., Timms, N.E., Ferrière, L., and Rochette, P. (2018) FRIGN zircon-The only terrestrial mineral diagnostic of high-pressure and high-temperature shock deformation. Geology, 46, 891–894.

Cynn, H., Sharma, S.K., Cooney, T.F., and Nicol, M. (1992) High-temperature Raman investigation of order-disorder behavior in the $MgAl_2O_4$ spinel. Physical Review B, 45, 500–502.

Dang, J., Zhang, G.H., and Chou, K.C. (2015) Kinetics and mechanism of hydrogen reduction of ilmenite powders. Journal of Alloys and Compounds, 619, 443–451.

Dellefant, F., Trepmann, C.A., Gilder, S.A., Sleptsova, I. V, Kaliwoda, M., and Weiss, B.P. (2022) Ilmenite and magnetite microfabrics in shocked gneisses from the Vredefort impact structure, South Africa. Contributions to Mineralogy and Petrology, 5.

Di Vincenzo, G. (2022) High precision multi-collector $^{40}Ar/^{39}Ar$ dating of moldavites (Central European tektites) reconciles geochrological and paleomagnetic data. Chemical Geology, 608, 121026.

Drury, M.R., and Urai, J.L. (1990) Deformation-related recrystallization processes. Tectonophysics, 172, 235–253.

El Goresy, A. (1964) Die Erzmineralien in den Ries- und Bosumtwi-Krater-Gläsern und ihre genetische deutung. Geochimica et Cosmochimica Acta, 28.

El Goresy, A., and Chao, E.C.T. (1976) Identification and significance of armalcolite in the Ries glass. Earth and Planetary Science Letters, 30, 200–208.

El Goresy, A., Ramdohr, P., Medenbach, O., and Bernhardt, H.-J. (1974) Taurus-Littrow TiO_2-basalts: Opaque mineralogy and geochemistry. In Geochimica et Cosmochimica Acta Supplement Vol. 1, pp. 627–652.

El Goresy, A., Dubrovinsky, L., Gillet, P., Graup, G., and Chen, M. (2010) Akaogiite: An ultra-dense polymorph of TiO_2 with the baddeleyite-type structure, in shocked garnet gneiss from the Ries Crater, Germany. American Mineralogist, 95, 892–895.

Erickson, T.M., Pearce, M.A., Reddy, S.M., Timms, N.E., Cavosie, A.J., Bourdet, J., Rickard, W.D.A., and Nemchin, A.A. (2017) Microstructural constraints on the mechanisms of the transformation to reidite in naturally shocked zircon. Contributions to Mineralogy and Petrology, 172.

Eriksson, G., and Pelton, A.D. (1993) Critical evaluation and optimization of the thermodynamic properties and phase diagrams of the CaO-Al_2O_3, Al_2O_3-SiO_2, and CaO-Al_2O_3-SiO_2 systems. Metallurgical Transactions B, 24, 807–816.

Evans, B., Renner, J., and Hirth, G. (2001) A few remarks on the kinetics of static grain growth in rocks. International Journal of Earth Sciences, 90, 88–103.

Frick, C. (1973) Kimberlitic Ilmenites. South African Journal of Geology, 76, 85–94.

Fu, X., Wang, Y., and Wei, F. (2010) Phase transitions and reaction mechanism of ilmenite oxidation. Metallurgical and Materials Transactions A: Physical Metallurgy and Materials Science, 41, 1338–1348.

Fujimaki, H., Matsu-Ura, M., Sunagawa, I., and Aoki, K. (1981) Chemical compositions of chondrules and matrices in the ALH-77015 chondrite (L3). Memoirs of National Institute of Polar Research. Special issue, 20, 161–174.

Galwey, A.K., and Brown, M.E. (1999) Thermal Decomposition of Ionic Solids, 596 p. Vol. 86. Elsevier.

Graup, G. (1999) Carbonate-silicate liquid immiscibility upon impact melting: Ries Crater, Germany. Meteoritics and Planetary Science, 34, 425–438.

Grégoire, M., Lorand, J.P., O'Reilly, S.Y., and Cottin, J.Y. (2000) Armalcolite-bearing, Ti-rich metasomatic assemblages in harzburgitic xenoliths from the Kerguelen Islands: Implications for the oceanic mantle budget of high-field strength elements. Geochimica et Cosmochimica Acta, 64, 673–694.

Grey, I.E., and Reid, A.F. (1975) The Structure of Pseudorutile and Its Role in The Natural Alteration of Ilmenite. The American Mineralogist, 60, 898–906.

Gupta, S.K., Rajakumar, V., and Grieveson, P. (1990) The role of preheating in the kinetics of reduction of ilmenite with carbon. Canadian Metallurgical Quarterly, 29, 43–49.

Gupta, S.K., Rajakumar, V., and Grieveson, P. (1991) Phase transformations during heating of Ilmenite concentrates. Metallurgical Transactions B, 22, 711–716.

Haggerty, S.E. (1973) Armalcolite and genetically associated opaque minerals in the lunar samples. In Proceedings of the Fourth Lunar Science Conference Vol. 1, pp. 777–797.

Haggerty, S.E. (1975) The chemistry and genesis of opaque minerals in kimberlites. Physics and Chemistry of the Earth, 9, 295–307.

Haggerty, S.E. (1983) The mineral chemistry of new titanates from the jagersfontein kimberlite, South Africa: Implications for metasomatism in the upper mantle. Geochimica et Cosmochimica Acta, 47, 1833–1854.

——— (1991) Oxide Textures - A Mini-Atlas. Reviews in Mineralogyv, 25, 129–219.

Haggerty, S.E., and Lindsley, D.H. (1969) Stabihty of the pseudobrookite (Fe_2TiO_5)-ferropseudobrookite ($FeTi_2O_5$) series. In Carniege Institution of Washington Yearbook 68 pp. 247–249.

Hahn, T., and Klapper, H. (2006) Twinning of crystals. In International Tables for Crystallography Vol. D, pp. 393–448. International Union of Crystallography, Chester, England.

Hashishin, T., Tan, Z., Yamamoto, K., Qiu, N., Kim, J., Numako, C., Naka, T., Valmalette, J.C., and Ohara, S. (2014) Quenching ilmenite with a high-temperature and high-pressure phase using super-high-energy ball milling. Scientific Reports, 4, 1–6.

Hayob, J.L., and Essene, E.J. (1995) Armalcolite in crustal paragneiss xenoliths, central Mexico. American Mineralogist, 80, 810–822.

He, M., Winkler, B., Bauer, J.D., Bayarjargal, L., Ruiz-Fuertes, J., Alencar, I., Morgenroth, W., Refson, K., and Milman, V. (2017) Lattice dynamics and Mg/Ti order in orthorhombic pseudobrookite-type $MgTi_2O_5$. Journal of Alloys and Compounds, 699, 16–24.

Hörz, F., Archer, P.D., Niles, P.B., Zolensky, M.E., and Evans, M. (2015) Devolatilization or melting of carbonates at Meteor Crater, AZ? Meteoritics and Planetary Science, 50, 1050–1070.

Hörz, F., Cintala, M.J., Thomas-Keprta, K.L., Ross, D.K., and Clemett, S.J. (2020) Unconfined shock experiments: A pilot study into the shock-induced melting and devolatilization of calcite. Meteoritics and Planetary Science, 55, 102–129.

Hüttner, R., and Schmidt-Kaler, H. (1999) Die Geologische Karte des Rieses 1: 50 000 (2., überarbeitete Auflage). Geologica Bavarica, 104, 7–76.

Imperial, A., Pe-Piper, G., Piper, D.J.W., and Grey, I.E. (2022) Identifying Pseudorutile and Kleberite Using Raman Spectroscopy. Minerals, 12, 1210.

Itoh, N., Sanchez, M.A., Xu, W.C., Haraya, K., and Hongo, M. (1993) Application of a membrane reactor system to thermal decomposition of CO_2. Journal of Membrane Science, 77, 245–253.

Janovec, V., and Přívratská, J. (2006) Domain structures. In International Tables for Crystallography Vol. D, pp. 449–505. International Union of Crystallography, Chester, England.

Kaliwoda, M., Giordano, D., Krüger, M.E., Uysal, I., Akmaz, M.R., Hoffmann, V., Hochleitner, R., and Schmahl, W.W. (2021) Raman spectroscopy as a tool for the quantitative estimate of chromium aluminium oxide content in chromite. Spectroscopy, 36, 17–23.

Keil, K., Prinz, M., and Bunch, T.E. (1970) Mineral Chemistry of Lunar Samples. Science, 167, 597–599.

Kesson, S.E., and Lindsley, D.H. (1975) The effects of Al^{3+}, Cr^{3+}, and Ti^{3+} on the stability of armalcolite. Proceedings of the 6th Lunar Science Conference, 911–920.

Kilinc, A., Carmichael, I.S.E., Rivers, M.L., and Sack, R.O. (1983) The ferric-ferrous ratio of natural silicate liquids equilibrated in air. Contributions to Mineralogy and Petrology, 83, 136–140.

King, D.A., and Ahrens, T.J. (1976) Shock compression of ilmenite. Journal of Geophysical Research, 81, 931–935.

Kostrovitsky, S.I., Yakovlev, D.A., Soltys, A., Ivanov, A.S., Matsyuk, S.S., and Robles-Cruz, S.E. (2020) A genetic relationship between magnesian ilmenite and kimberlites of the Yakutian diamond fields. Ore Geology Reviews, 120, 103419.

Kucukkaragoz, C.S., and Eric, R.H. (2006) Solid state reduction of a natural ilmenite. Minerals Engineering, 19, 334–337.

Kuganathan, N., Srikaran, R., Fossati, P.C.M., and Chroneos, A. (2019) Theoretical Modeling of Defects, Dopants, and Diffusion in the Mineral Ilmenite. Minerals, 9, 610.

Kuroda, K., and Mitchell, T.E. (1983) TEM studies of oxidation and passivation of iron. In R.M. Fisher, R. Gronsly, and K.H. Wetmacott, Eds., Seventh International Conference on High Voltage Electron Microscopy pp. 261–267. University of California, Berkeley.

Leinenweber, K., Utsumi, W., Tsuchida, Y., Yagi, T., and Kurita, K. (1991) Unquenchable high-pressure perovskite polymorphs of $MnSnO_3$ and $FeTiO_3$. Physics and Chemistry of Minerals, 18, 244–250.

Leinenweber, K., Yanbin Wang, Yagi, T., and Yusa, H. (1994) An unquenchable perovskite phase of $MgGeO_3$ and comparison with $MgSiO_3$ perovskite. American Mineralogist, 79, 197–199.

Li, Y., Li, X., Wang, S., Tang, H., Gan, H., Li, S., and Ouyang, Z. (2012) In-situ water production by reducing ilmenite. In V. Badescu, Ed., Moon pp. 189–200. Springer, New York.

Liermann, H.P., Downs, R.T., and Yang, H. (2006) Site disorder revealed through Raman spectra from oriented single crystals: A case study on karooite ($MgTi_2O_5$). American Mineralogist, 91, 790–793.

Lindsley, D.H. (1965) Iron-Titanium Oxides. In Carniege Institute Washington Yearbook 64 pp. 144–148.

Lindsley, D.H., Kesson, S.E., Hartzman, M.J., and Cushman, M.K. (1974) The stability of armacolite: Experimantal studies in the system MgO-Fe-Ti-O. In Proceedings of the Fifth Lunar Conference pp. 521–534. Pergamon Press.

Liu, L.G. (1975) High-pressure phase transformations and compressions of ilmenite and rutile, I. Experimental results. Physics of the Earth and Planetary Interiors, 10, 167–176.

Ma, C., and Tschauner, O. (2018) Liuite, IMA 2017-042a. CNMNC Newsletter No. 46. Mineralogical Magazine, 82, 1369–1379.

Mazza, T., Barborini, E., Piseri, P., Milani, P., Cattaneo, D., Li Bassi, A., Bottani, C.E., and Ducati, C. (2007) Raman spectroscopy characterization of TiO_2 rutile nanocrystals. Physical Review B - Condensed Matter and Materials Physics, 75, 1–5.

Mehta, A., Leinenweber, K., Navrotsky, A., and Akaogi, M. (1994) Calorimetric study of high pressure polymorphism in $FeTiO_3$: Stability of the perovskite phase. Physics and Chemistry of Minerals, 21, 207–212.

Melosh, H.J. (1989) Impact cratering: a geologic process, 245 p. Oxford University Press, New York.

Merk, R., and Pickles, C.A. (1988) Reduction of ilmenite by carbon monoxide. Canadian Metallurgical Quarterly, 27, 1–7.

Ming, L.C., Kim, Y.H., Uchida, T., Wang, Y., and Rivers, M. (2006) In situ X-ray diffraction study of phase transitions of $FeTiO_3$ at high pressures and temperatures using a large-volume press and synchrotron radiation. American Mineralogist, 91, 120–126.

Minkin, J.A., and Chao, E.C.T. (1971) Single crystal X-ray investigation of deformation in terrestrial and lunar ilmenite. In Proceedings of the Second Lunar Science Conference pp. 237–246. M.I.T. Press.

Mitchell, R.H. (1973) Magnesian Ilmenite and Its Role in Kimberlite Petrogenesis. The Journal of Geology, 81, 301–311.

Mitchell, T.E., Voss, D.A., and Butler, E.P. (1982) The observation of stress effects during the high temperature oxidation of iron. Journal of Materials Science, 17, 1825–1833.

Mücke, A., and Bhadra Chaudhuri, J.N. (1991) The continuous alteration of ilmenite through pseudorutile to leucoxene. Ore Geology Reviews, 6, 25–44.

Nellis, W.J., Mitchell, A.C., Ree, F.H., Ross, M., Holmes, N.C., Trainor, R.J., and Erskine, D.J. (1991) Equation of state of shock-compressed liquids: Carbon dioxide and air. The Journal of Chemical Physics, 95, 5268–5272.

Nicolas, A., and Poirier, J.P., 1976. Crystalline Plasticity and Solid State Flow in Metamorphic Rocks. John Wiley & Sons, New York.

Nishio-Hamane, D., Yagi, T., Ohshiro, M., Niwa, K., Okada, T., and Seto, Y. (2010) Decomposition of perovskite $FeTiO_3$ into wüstite $Fe_{1-x}Ti_{0.5x}O$ and orthorhombic $FeTi_3O_7$ at high pressure. Physical Review B, 82, 092103.

Nishio-Hamane, D., Zhang, M., Yagi, T., and Ma, Y. (2012) High-pressure and high-temperature phase transitions in $FeTiO_3$ and a new dense $FeTi_3O_7$ structure. American Mineralogist, 97, 568–572.

Osinski, G.R., Spray, J.G., and Grieve, R.A.F. (2008) Impact melting in sedimentary target rocks: An assessment. Special Paper of the Geological Society of America, 437, 1–18.

Pantić, J., Urbanovich, V., Poharc-Logar, V., Jokić, B., Stojmenović, M., Kremenović, A., and Matović, B. (2014) Synthesis and characterization of high-pressure and high-temperature sphene ($CaTiSiO_5$). Physics and Chemistry of Minerals, 41, 775–782.

Pasteris, J.D. (1980) The significance of groundmass ilmenite and megacryst ilmenite in kimberlites. Contributions to

Mineralogy and Petrology, 75, 315–325.

Philpotts, A., and Ague, J. (2009) Principles of Igneous and Metamorphic Petrology, 2nd ed., 667 p. Cambridge University Press, New York.

Pilkington, M., and Grieve, R.A.F. (1992) The geophysical signature of terrestrial impact craters. Reviews of Geophysics, 30, 161–181.

Pilkington, M., and Hildebrand, A.R. (2000) Three-dimensional magnetic imaging of the Chicxulub Crater. Journal of Geophysical Research: Solid Earth, 105, 23479–23491.

Plado, J., Pesonen, L.J., and Puura, V. (1999) Effect of erosion on gravity and magnetic signatures of complex impact structures: Geophysical modeling and applications. In B.O. Dressler and V.L. Sharpton, Eds., Special Paper of the Geological Society of America Vol. 339, pp. 229–239. Geological Society of America, Boulder, Colorado.

Pohl, J., Stöffler, D., Gall, H., and Ernston, K. (1977) The Ries impact crater. In D.J. Roddy, R.O. Pepin, and R.B. Merrill, Eds., Impact and Explosion Cratering pp. 343–404. Pergamon Press, New York.

Pohl, J., Poschlod, K., Reimold, W.U., Meyer, C., and Jacob, J. (2010) Ries crater, Germany: The Enkingen magnetic anomaly and associated drill core SUBO 18. In R.L. Gibson and W.U. Reimold, Eds., Large Meteorite Impacts and Planetary Evolution IV Vol. 465, pp. 141–163. Geological Society of America.

Rocholl, A., Schaltegger, U., Gilg, H.A., Wijbrans, J., and Böhme, M. (2017) The age of volcanic tuffs from the Upper Freshwater Molasse (North Alpine Foreland Basin) and their possible use for tephrostratigraphic correlations across Europe for the Middle Miocene. International Journal of Earth Sciences, 107, 387–407.

Rocholl, A., Böhme, M., Gilg, H.A., Pohl, J., Schaltegger, U., and Wijbrans, J. (2018) Comment on "A high-precision $^{40}Ar/^{39}Ar$ age for the Nördlinger Ries impact crater, Germany, and implications for the accurate dating of terrestrial impact events" by Schmieder et al. (Geochimica et Cosmochimica Acta 220 (2018) 146–157). Geochimica et Cosmochimica Acta, 238, 599–601.

Sack, R.O., Carmichael, I.S.E., Rivers, M., and Ghiorso, M.S. (1981) Ferric-ferrous equilibria in natural silicate liquids at 1 bar. Contributions to Mineralogy and Petrology, 75, 369–376.

Sargeant, H.M., Abernethy, F.A.J., Barber, S.J., Wright, I.P., Anand, M., Sheridan, S., and Morse, A. (2020) Hydrogen reduction of ilmenite: Towards an in situ resource utilization demonstration on the surface of the Moon. Planetary and Space Science, 180, 104751.

Schmidt-Kaler, H. (1969) Versuch einer Profildarstellung für das Rieszentrum vor der Kraterbildung. Geologica Bavarica, 61, 38–40.

Schmieder, M., Kennedy, T., Jourdan, F., Buchner, E., and Reimold, W.U. (2018a) A high-precision $^{40}Ar/^{39}Ar$ age for the Nördlinger Ries impact crater, Germany, and implications for the accurate dating of terrestrial impact events. Geochimica et Cosmochimica Acta, 220, 146–157.

——— (2018b) Response to comment on "A high-precision $^{40}Ar/^{39}Ar$ age for the Nördlinger Ries impact crater, Germany, and implications for the accurate dating of terrestrial impact events" by Schmieder et al. (Geochimica et Cosmochimica Acta 220 (2018) 146–157). Geochimica et Cosmochimica Acta, 238, 602–605.

Schwarz, W.H., Hanel, M., and Trieloff, M. (2020) U-Pb dating of zircons from an impact melt of the Nördlinger Ries crater. Meteoritics and Planetary Science, 55, 312–325.

Sclar, C.B., Bauer, J.F., Pickart, S.J., and Alperin, H.A. (1973) Shock effects in experimentally shocked terrestrial ilmenite, lunar ilmenite of rock fragments in 1-10 mm fines (10085,19), and lunar rock 60015,127. In Proceedings of the Fourth Lunar Science Conference Vol. 1, pp. 841–859. Pergamon Press, Texas.

Scott, R.G., Pilkington, M., and Tanczyk, E.I. (1997) Magnetic investigations of the West Hawk, Deep Bay and Clearwater impact structures, Canada. Meteoritics and Planetary Science, 32, 293–308.

Sleptsova, I. V., Gilder, S.A., Dellefant, F., Trepmann, C.A., and Pohl, J. (2022) Remanent magnetization in Bunte Breccia from the Ries impact structure, Germany. In S. Frančišković-Bilinski, H. Böhnel, R. Egli, A. Hirt, E. Petrovský, S. Spassov, and T. Werner, Eds., 17th Castle Meeting p. 126.

Smyth, J.R. (1974) The crystal chemistry of armalcolites from Apollo 17. Earth and Planetary Science Letters, 24, 262–270.

Spiridonov, E.M., Semikolennykh, E.S., Lysenko, V.I., Filimonov, S. V., Korotayeva, N.N., and Krivitskaya, N.N. (2019) Armalcolite-Bearing Island Arc Plagiolherzolites and Olivine Gabbro–Norite–Dolerites of the Balaklava Area (Crimea). Moscow University Geology Bulletin, 74, 380–392.

Stöffler, D., and Grieve, R.A.F. (2007) Impactites. In D. Fettes and J. Desmons, Eds., Metamorphic Rocks: A Classification and Glossary of Terms, Recommendations of the International Union of Geological Sciences pp. 82–92, 111–125 and 126–242. Cambridge University Press, Cambridge.

Stöffler, D., Artemieva, N.A., Wünnemann, K., Reimold, W.U., Jacob, J., Hansen, B.K., and Summerson, I.A.T. (2013) Ries crater and suevite revisited-Observations and modeling Part I: Observations. Meteoritics & Planetary Science, 48, 515–589.

Stöffler, D., Hamann, C., and Metzler, K. (2018) Shock metamorphism of planetary silicate rocks and sediments: Proposal for an updated classification system. Meteoritics & Planetary Science, 53, 5–49.

Syono, Y., Takei, H., Goto, T., and Ito, A. (1981) Single crystal X-ray and Mössbauer study of shocked ilmenite to 80 GPa. Physics and Chemistry of Minerals, 7, 82–87.

Taylor, L.A., Williams, R.J., and McCallister, R.H. (1972) Stability relations of ilmenite and ulvöspinel in the Fe-Ti-O system and application of these data to lunar mineral assemblages. Earth and Planetary Science Letters, 16, 282–288.

Temple, A.K. (1966) Alteration of ilmenite. Economic Geology, 61, 695–714.

Teufer, G., and Temple, A.K. (1966) Pseudorutile—a New Mineral Intermediate between Ilmenite and Rutile in the N Alteration of Ilmenite. Nature, 211, 179–181.

Timms, N.E., Erickson, T.M., Pearce, M.A., Cavosie, A.J., Schmieder, M., Tohver, E., Reddy, S.M., Zanetti, M.R., Nemchin, A.A., and Wittmann, A. (2017) A pressure-temperature phase diagram for zircon at extreme conditions. Earth-Science Reviews, 165, 185–202.

Tschauner, O., Mao, H.K., and Hemley, R.J. (2001) New transformations of CO_2 at high pressures and temperatures. Physical Review Letters, 87, 75701-1-75701–4.

Tschauner, O., Ma, C., Newville, M.G., and Lanzirotti, A. (2020) Structure analysis of natural wangdaodeite—$LiNbO_3$-type $FeTiO_3$. Minerals, 10, 1–12.

Tuthill, R.L., and Sato, M. (1970) Phase relations of a simulated lunar basalt as a function of oxygen fugacity, and their bearing on the petrogenesis of the Apollo 11 basalts. Geochimica et Cosmochimica Acta, 34, 1293–1302.

Ugalde, H.A., Artemieva, N.A., and Milkereit, B. (2005) Magnetization on impact structures - Constraints from numerical modeling and petrophysics. In T. Kenkmann, F. Hörz, and A. Deutsch, Eds., Large meteorite impacts III: Geological Society of America Special Paper 384 Vol. Special Pa, pp. 25–42. Geological Society of America, Boulder.

von Engelhardt, W., and Graup, G. (1984) Suevite of the Ries crater, Germany: Source rocks and implications for cratering mechanics. Geologische Rundschau, 73, 447–481.

von Engelhardt, W., Arndt, J., Fecker, B., and Pankau, H.G. (1995) Suevite breccia from the Ries crater, Germany: Origin, cooling history and devitrification of impact glasses. Meteoritics, 30, 279–293.

Wang, A., Kuebler, K.E., Jolliff, B.L., and Haskin, L.A. (2004) Raman spectroscopy of Fe-Ti-Cr-oxides, case study: Martian meteorite EETA79001. American Mineralogist, 89, 665–680.

Wang, Y., Liu, X., Yao, G.D., Liebermann, R.C., and Dudley, M. (1991) High temperature transmission electron microscopy and X-ray diffraction studies of twinning and the phase transition at 145°C in LaGaO3. Materials Science and Engineering A, 132, 13–21.

Weis, R.S., and Gaylord, T.K. (1985) Lithium niobate: Summary of physical properties and crystal structure. Applied Physics A Solids and Surfaces, 37, 191–203.

Wheeler, J., Prior, D.J., Jiang, Z., Spiess, R., and Trimby, P.W. (2001) The petrological significance of misorientations between grains. Contributions to Mineralogy and Petrology, 141, 109–124.

Wilson, N.C., Muscat, J., Mkhonto, D., Ngoepe, P.E., and Harrison, N.M. (2005) Structure and properties of ilmenite from first principles. Physical Review B - Condensed Matter and Materials Physics, 71, 1–9.

Wu X, Steinle-Neumann G, Narygina O, et al (2009) High-pressure behavior of perovskite: $FeTiO_3$ dissociation into $(Fe_{1-\delta},Ti_\delta)O$ and $Fe_{1+\delta}Ti_{2-\delta}O_5$. Phys Rev Lett 103:1–4. https://doi.org/10.1103/PhysRevLett.103.065503

Wünnemann, K., Morgan, J. V., and Jödicke, H. (2005) Is ries crater typical for its size? An analysis based upon old and new geophysical data and numerical modeling. In T. Kenkmann, F. Hörz, and A. Deutsch, Eds., Large meteorite impacts III: Geological Society of America Special Paper 384 Vol. 384, pp. 67–83. Geological Society of America, Boulder.

Xie, X., Gu, X., Yang, H., Chen, M., and Li, K. (2020) Wangdaodeite, the $LiNbO_3$-structured high-pressure polymorph of ilmenite, a new mineral from the Suizhou L6 chondrite. Meteoritics and Planetary Science, 55, 184–192.

Zhao, Y., and Shadman, F. (1990) Kinetics and mechanism of ilmenite reduction with carbon monoxide. AIChE Journal, 36, 1433–1438.

Supplementary data

Tab. S1 EMP data [wt.%] of profile (step size ≈1 µm) from core (#1) to rim (#29) depicted in Figure 3g, h with the at.%-ratio of iron and titanium (Fe/Ti). Note that Fe/Ti increases towards the aggregate's rim and #1-#4 correspond to rutile with varying amounts of FeO. The detection limit in ppm is given in brackets for either a concentration below 0.004 wt.% or a not detectable (n.d.) component. The deviation of the total wt.% can be explained due to the presence of Fe_2O_3, which binds more oxygen and thus would increase the calculated total.

#	FeO	TiO_2	MnO	MgO	SiO_2	Al_2O_3	Na_2O	CaO	K_2O	Total	Fe/Ti
1	32.16	61.35	2.17	2.72	0.24	(249)	0.01	0.06	0.01	98.72	0.58
2	7.13	86.93	0.64	0.59	0.26	(251)	0.02	0.08	0.01	95.67	0.09
3	2.57	95.05	0.20	0.17	0.34	n.d. (251)	0.01	0.07	0.02	98.44	0.03
4	12.35	86.26	0.62	1.00	1.30	0.03	0.01	0.08	0.02	101.71	0.16
5	35.43	59.39	2.14	2.93	0.93	0.09	0.02	0.12	0.01	101.09	0.66
6	36.66	57.19	2.39	3.20	0.47	0.02	0.01	0.08	n.d. (249)	100.05	0.71
7	35.76	55.36	2.43	3.27	0.80	0.05	0.02	0.09	0.02	97.81	0.72
8	29.87	67.05	1.74	2.32	0.63	0.04	n.d. (260)	0.09	(247)	101.75	0.50
9	32.45	58.88	2.31	2.87	0.94	0.06	0.05	0.11	0.02	97.73	0.61
10	18.29	74.21	1.40	1.81	0.76	0.09	0.05	0.13	0.02	96.76	0.27
11	23.87	69.43	1.62	2.07	0.46	0.07	0.02	0.09	(248)	97.65	0.38
12	37.60	55.63	2.16	2.82	0.69	0.10	0.01	0.14	0.02	99.19	0.75
13	39.98	52.47	2.43	3.41	0.27	0.09	n.d. (380)	0.10	0.02	98.78	0.85
14	39.53	52.66	2.49	3.47	0.23	0.07	n.d. (380)	0.09	0.02	98.56	0.83
15	39.52	52.82	2.52	3.47	0.22	0.11	n.d. (380)	0.11	0.01	98.80	0.83
16	39.42	52.68	2.58	3.53	0.27	0.10	0.03	0.09	0.01	98.70	0.83
17	39.56	52.42	2.49	3.53	0.26	0.10	0.01	0.11	n.d. (244)	98.48	0.84
18	39.57	52.39	2.45	3.45	0.27	0.11	0.01	0.10	0.01	98.38	0.84
19	39.59	52.40	2.43	3.51	0.31	0.13	0.03	0.08	0.01	98.54	0.84
20	39.84	52.11	2.40	3.37	0.31	0.14	0.03	0.10	0.01	98.34	0.85
21	39.94	51.97	2.45	3.35	0.25	0.14	0.01	0.10	(238)	98.22	0.85
22	39.95	51.98	2.40	3.46	0.29	0.14	0.02	0.13	0.01	98.43	0.85
23	40.21	51.90	2.36	3.36	0.33	0.18	0.02	0.10	0.02	98.51	0.86
24	39.96	51.44	2.29	3.27	0.72	0.23	0.02	0.16	0.02	98.14	0.86
25	40.39	50.87	2.33	3.38	0.40	0.24	n.d. (367)	0.16	0.02	97.81	0.88
26	40.64	50.83	2.27	3.36	0.27	0.24	0.01	0.15	0.02	97.81	0.89
27	40.85	50.50	2.18	3.31	0.36	0.25	0.01	0.18	0.03	97.68	0.90
28	41.24	49.38	2.03	3.22	0.46	0.33	n.d. (373)	0.20	0.04	96.92	0.93
29	41.44	45.28	1.99	3.01	7.75	1.75	0.22	0.29	0.28	102.03	1.02

Note: The content of this chapter was submitted to the International Journal of Earth Sciences. For a better reading-experience, this version has been created for this thesis.

Polymict crystalline breccia in the Ries impact structure - Emplacement of moderately shocked basement clasts during crater excavation and subsequent mixing with weakly shocked sedimentary clasts

Fabian Dellefant[1*], Lina Seybold[2,1], Claudia A. Trepmann[1], Stuart A. Gilder[1], Iuliia V. Sleptsova[1], Stefan Hölzl[2,1], Melanie Kaliwoda[3,1]

[1]Department of Earth and Environmental Sciences, Ludwig-Maximilians-Universität München, Theresienstr. 41, 80333 Munich

[2]RiesKraterMuseum Nördlingen (RKM), Bavarian Natural History Collections; Eugene-Shoemaker-Pl. 1, 86720 Nördlingen

[3]Mineralogical State Collection Munich (MSM), Bavarian Natural History Collections; Theresienstr. 41, 80333 Munich

corresponding author: Fabian Dellefant (fabian.dellefant@lmu.de)

Abstract The Aumühle quarry in the Ries impact structure contains shocked clasts from the Variscan basement mixed with apparently unshocked clasts from the Mesozoic sedimentary cover. Clasts sizes range up to a few decimeters and are embedded in a fine-grained lithic matrix; no glass fragments (Flädle) are observed. We analyzed the clasts by optical microscopy, scanning electron microscopy (SEM/EDS/EBSD) and Raman spectroscopy to unravel their emplacement relation to the overlying suevite and the underlying Bunte Breccia. Basement clasts show shock effects indicating a few 10s of GPa; whereas, the sedimentary clasts show no distinct shock effects, with shock pressures <1 GPa. Amphibolite clasts contain maskelynite with a few lamellar remnants of preserved former feldspar, indicating shock pressures of 28-34 GPa. Amphiboles show cleavage cracks and $(\bar{1}01)$ mechanical twins indicating differential stresses >400 MPa. Felsic gneiss components have optically isotropic SiO_2 indicating shock pressures of ≈35 GPa. Gneiss-breccia components consist of quartz with a high density of fine rhombohedral planar deformation features indicating shock pressures of ≈20 GPa. These strongly shocked basement clasts probably derived from the lower levels of the transient cavity, where they were ballistically ejected during the excavation stage. In accordance with paleo- and rock magnetic data, subsequent turbulent deposition at the top of the Bunte Breccia resulted in an additional mixing with sedimentary clasts forming the basement-rich horizon, independently and before the emplacement of the suevite. This occurrence of basement clasts between suevite and the underlying Bunte Breccia is consisitent with the commonly reported inverse stratigraphy.

Keywords emplacement; inverse stratigraphy; crater excavation stage; shocked basement clasts; shock effects

Introduction

The Nördlinger Ries is one of the best-preserved impact structures in the world, where the impact rocks of the two dominating ejecta blankets, the suevites and the underlying *Bunte Trümmermassen* (german for multi-coloured detritus), are studied intensely since the 1960s. Especially, the discontinuous ejecta layer, the melt-fragment ("Flädle")-bearing suevites has been the subject of many geochemical and structural investigations [see the most recent review on the Ries impact structure by Stöffler et al. (2013) and references therein]. The continuous ejecta layer of the *Bunte Trümmermassen* at the bottom comprises (i) melt-free lithic breccias with components <25 m, the so-called *Bunte Breccia*, and (ii) lithic components of >25 m in size, so-called "megablocks", which both typically show relative low shock conditions (e.g., Hüttner and Schmidt-Kaler 1999; Sturm et al. 2015). Furthermore, lithic polymict crystalline breccias are commonly distinguished because they are dominated by Variscan basement clasts shocked to <10-50 GPa, in contrast to the Bunte Breccia, which is dominated by weakly shocked sedimentary components (Abadian 1972; von Engelhardt and Graup 1984; von Engelhardt 1990; Hüttner and Schmidt-Kaler 1999; Stöffler et al. 2013). The formation conditions and emplacement mechanisms of these polymict crystalline breccias as well as the relation to the other impact breccias in the Nördlinger Ries are still largely unknown (Pohl et al. 1977; von Engelhardt 1990; Stöffler et al. 2013). One reason is that few known occurrences of polymict crystalline breccia in the Nördlinger Ries are documented, and their relation to the Bunte Trümmermassen and suevite is hardly exposed. The particular interest of such lithic polymict crystalline breccias with moderately shocked clasts (>10 GPa) is their spatial relation to components characterized by weak shock conditions (<7 GPa), i.e., the mixing of components from obviously different source positions within the impact structure. Thus, they might carry information on the relative trajectories from excavation to deposition.

In this study, we present a new occurrence of polymict impact breccias with moderately shocked (>10 GPa) Variscan basement clasts and weakly shocked (<7 GPa) sedimentary cover clasts that occur at the contact between Bunte Breccia and suevite in the Aumühle quarry in the Nördlinger Ries (Fig. 1). We characterize the field occurrence and shock effects in the clasts and discuss our findings in combination with the complementary magnetic characterization by Sleptsova et al., (*submitted*), to evaluate the formation conditions and emplacement mechanism of the polymict crystalline breccia considering observations and interpretations of similar breccias of other impact structures.

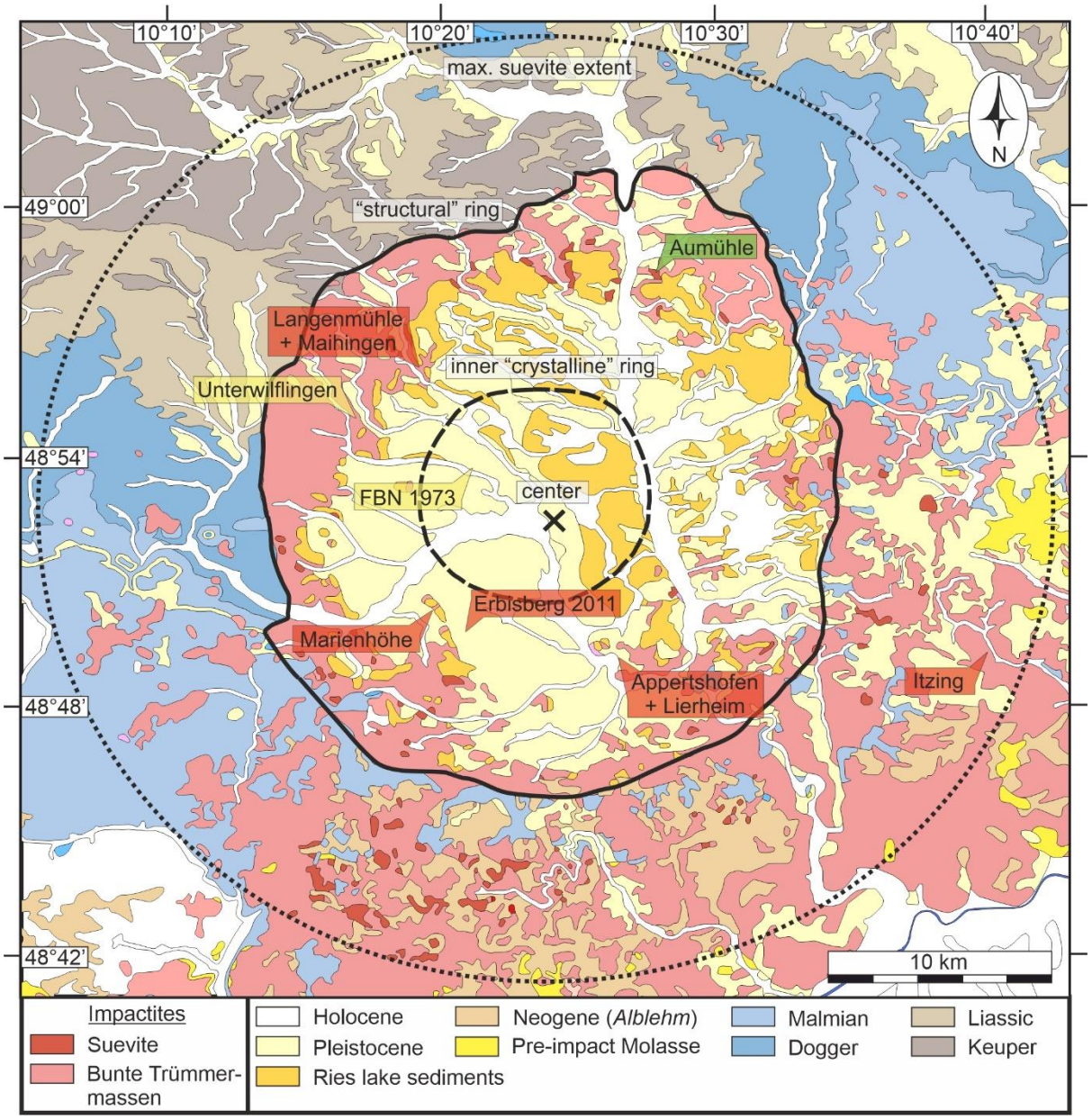

Fig. 1 Simplified geological map of the Ries impact structure with occurrences of polymict crystalline breccia [green for this study; red for documented shock pressures of up to ≈35 GPa (Abadian 1972; Graup 1978; Arp et al. 2019); yellow without estimations on shock pressures (Abadian 1972; Stöffler 1977; Chao et al. 1987; Seybold et al. 2022). Map edited after: The General Geological Map of the Federal Republic of Germany 1:250,000 (GÜK250), © Bundesanstalt für Geowissenschaften und Rohstoffe (BGR).

The Ries impact structure and its impact breccias

The 26 km diameter Ries impact structure was formed by a meteorite impact at ≈14.8 Ma (Di Vincenzo 2022; Lange and Suhr 2022 and references therein). The affected target rocks comprise the approximately 700 m thick Mesozoic sedimentary sequence of the Swabian-Franconian Alb and the underlying Variscan basement, mainly composed of amphibolites, metagranites, and paragneisses (e.g., Graup 1978; von Engelhardt and Graup 1984; Hüttner and Schmidt-Kaler 1999). Stöffler et al. (2013) distinguish five major structural units: I) the central basin r<6 km, II) the uplifted inner crystalline ring r≈6 km, III) the megablock zone r≈6-13 km, IV) the structural rim r≈13-14 km, and VI) the outer continuous ejecta blanket r≈13-45 km. In general, the ejecta masses are distinguished into

the ballistically ejected lithic *Bunte Trümmermasse* and the overlying glass fragment-bearing suevite (e.g., Sturm et al. 2015; Stöffler et al. 2013 and references therein).

Suevite is an allochthonous polymict impact breccia with a fine-grained matrix, which contains mineral and lithic clasts of the target and cogenetic (devitrified) glass fragments (Flädle), both mainly originating from shocked Variscan basement (Pohl et al. 1977; Stöffler and Grieve 2007; Stöffler et al. 2013, 2018). The shock effects indicate a broad range of shock conditions [e.g., felsic components from low shock conditions up to F-S6 (von Engelhardt et al. 1995; Stöffler and Grieve 2007; Stöffler et al. 2018; Stähle et al. 2022)]. Suevites occur inside the inner ring on top of the crystalline basement (crater suevite), outside the inner ring on top of the Bunte Trümmermasse (outer suevite), and as dikes within the parautochthonous crater basement as well as within ejected crystalline megablocks, i.e., dike suevites (Stöffler 1977).

The continuous ejecta blanket of the Bunte Trümmermassen consists of allochthonous rotated rocks that originate from the sedimentary cover and the Variscan basement, which were fragmented and displaced during the formation of the crater (Pohl et al. 1977; Hüttner and Schmidt-Kaler 1999; Stöffler et al. 2013; Sturm et al. 2015). The Bunte Trümmermassen form the volumetrically dominant impact breccia deposit in the Ries (Hörz et al. 1983; Sturm et al. 2015). Megablocks of >25 m in size are comprised dominantly of the Mesozoic sedimentary cover rocks and Variscan basement megablocks are less common (<10% of the area covered by all megablocks, Sturm et al. 2015). These basement megablocks commonly display few shock effects, such as kink bands in biotite, implying shock conditions below 10 GPa (von Engelhardt and Graup 1984). The mm- to m-sized clasts in the Bunte Breccia are dominantly derived from the sedimentary cover rocks that experienced relatively low shock conditions (P<10 GPa; T<100°C) (Hörz et al. 1983; von Engelhardt 1990; Stöffler and Grieve 2007). About 3-10% of the lithic clasts come from the Variscan basement, which has been described as lithic polymict impact breccia that contains basement clasts that experienced various shock conditions (<10-50 GPa; e.g., Stöffler 1971a; Abadian 1972; Pohl et al. 1977; Graup 1978; Stöffler and Ostertag 1983; von Engelhardt 1990). Locally, the components of the Bunte Trümmermassen occur in the Ries impact structure with an inverse stratigraphy, i.e., Ries lower units can be overlain by upper units (e.g., Pohl, 1977; Sturm et al., 2015).

Abadian (1972) and Stöffler (1971a) distinguished monomict and polymict crystalline breccia based on whether they contain one or more types of rocks from the Variscan basement, independent of the shock conditions (<10-50 GPa). Von Engelhardt (1990) defined polymict crystalline breccia as having experienced shock pressures of at least 10 GPa and containing various rock types from the Variscan basement. Graup (1978) defined monomict crystalline breccia as having basement components with similar shock conditions, whereas polymict crystalline breccia has basement components with variable shock conditions. The breccia described in this study consists of heterogeneously shocked clasts from the Variscan basement and Mesozoic sedimentary rocks, consistent with all the above definitions.

Abadian (1972) distinguished three types of polymict crystalline breccias: I) isolated complexes without relationship to the surrounding (Marienhöhe/Leopold-Meyers-Keller); II) occurrences with components likely derived from the adjacent basement megablock (Appetshofen+Lierheim, Itzing); and III) breccia dikes with material different to the basement megablocks in which they occur (Maihingen-Klostermühle) (Abadian et al. 1973; Arp et al. 2019). Furthermore, cataclastic veins consisting of mixed basement and sedimentary clasts are reported to occur within the basement at depths of up to 1187 m, as shown by the FBN1973 research drill core north of Nördlingen (Stöffler et al. 1977). These veins are interpreted as highly energetic and early emplacement during the excavation stage of the cratering process (Stöffler 1977). However, no shock pressure estimations were reported for the veins (Graup 1977; Hüttner 1977; Stöffler 1977; Stöffler et al. 1977). Furthermore, no shock pressure estimations were published for the polymict crystalline breccia of Unterwilflingen to our knowledge (Chao et al. 1987; Seybold et al. 2022). Within the inner ring, polymict crystalline breccia was documented in depth ranging from 55.5 m to 62.43 m in the Erbisberg

drilling 2011 located above upper Triassic sandstone blocks from the Bunte Breccia and below intact gneiss blocks and monomict crystalline breccias (Arp et al. 2019).

Samples and methods

We studied a horizon rich in basement and sedimentary clasts occurring between the overlying suevite and the underlying Bunte Breccia at the northeastern corner of the Aumühle suevite quarry (N 48°58'16.00416" E 10°37'47.59735, Fig. 1-3), which is located in the megablock zone, between the inner crystalline ring and the structural rim, in the north-northeastern part of the Ries impact structure. Fieldwork was conducted between 2020 and 2023 with the main sampling on 15th September 2020. Due to the ongoing excavation work in the quarry, the investigated part of the outcrop is now partly removed or covered (Fig. 2), as also described by Kroepelin et al. (2022). Samples described here (Fig. 2) were taken from one amphibolite clast (R20-4,5; Fig. 2c), one gneiss clast (R20-14; Fig. 2e), one metagranite cataclasite clast (R20-2; Fig. 2b), and one sandstone clast (R20-8; Fig. 2d).

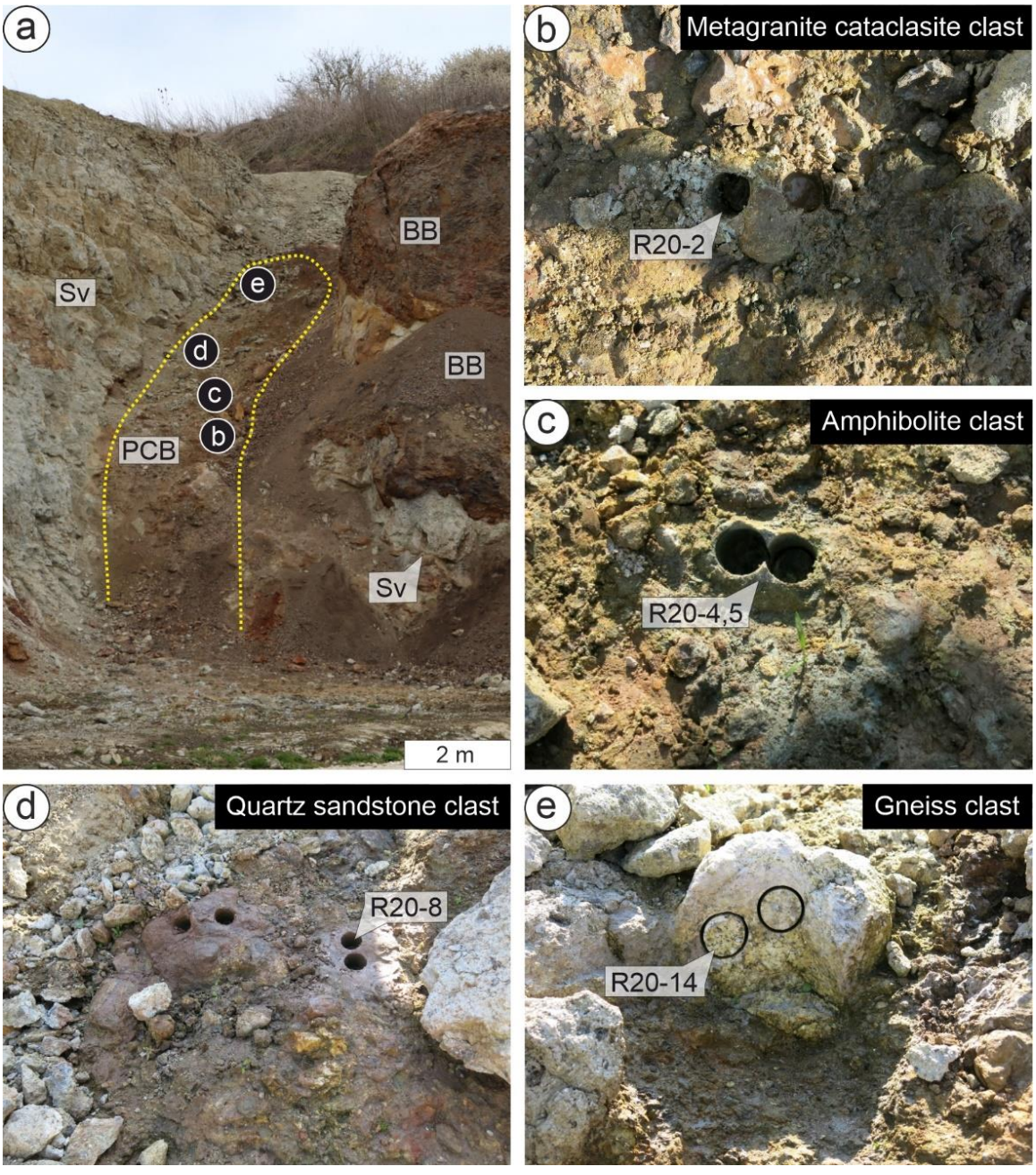

Fig. 2a) Locations of samples R20-2, R20-4,5, R20-8, and R20-14 in the Aumühle quarry within polymict crystalline breccia (PCB) indicated by the references to (b), (c), (d), and (e), respectively. Note the contact to suevite (Sv) and Bunte Breccia (BB) displayed by the yellow dashed line and the suevite locally as lense within the Bunte Breccia. The drill core diameter is 2.5 cm of **b)** metagranite cataclasite clast sample R20-2, **c)** amphibolite clast sample R20-4,5, **d)** quartz sandstone clast sample R20-8, and **e)** gneiss clast sample R20-14.

Polished and uncovered thin sections (25 µm) were prepared from the samples and investigated by polarization microscopy (Leica DM2700 P). Photomicrographs were taken with a Leica MC170 HD camera and processed with the Leica Application Suite X 3.08.19082 software.

Raman spectroscopy was conducted for phase determination with a HORIBA JOBIN YVON XploRa ONE micro-Raman system at the Munich Mineralogical State Collection Munich (SNSB). The system is equipped with a Peltier-cooled CCD detector and edge filters. An 1800 g/mm grating and a 532 nm (green) 2ω-Nd:YAG laser were used. Slit and hole diameters were 100 µm and 300 µm, respectively, combined with an integration time of 5x5 s. For maskelynite, plagioclase, and amphibole, 50% laser power was applied, whereas diaplectic SiO_2 glass was measured with 25% laser power corresponding to max. 5.4 mW or max. 2.5 mW on the sample surface, respectively. A 100x long working distance objective resulted in a 0.9 µm laser spot size on the sample surface. Wavelength calibration was performed with a pure Si-wafer chip on the predominant 520±1.5 cm^{-1} peak. The precision in the Raman peak position is estimated at ±1.5 cm^{-1}.

Samples were studied with a Hitachi SU5000 scanning electron microscope (SEM) equipped with a backscattered electron (BSE) detector, energy-dispersive X-ray spectroscopy (EDS) detector (Oxford Instruments), NordlysNano high-sensitivity electron backscatter diffraction (EBSD) detector (Oxford Instruments), and field emission gun. SEM observations used accelerating voltages of 10-20 kV and a working distance of 10-25 mm. Chemical compositions were acquired with AZtec analysis software 4.2 (Oxford Instruments). Thin sections were chemo-mechanically polished with a colloidal alumina suspension (Syton) for EBSD analysis to reduce the surface damage from preparation. Step sizes for automatic mapping have been chosen between 0.5 µm and 1 µm depending on the EBSD-pattern quality and resolution. A sample holder tilted at 70° with respect to the electron beam was used. EBSD data were processed by the Channel software 5.12.74.0 (Oxford Instruments). All stereograms are equal-angle projections of the lower hemisphere.

Results

Field occurrence of polymict crystalline breccia

The Aumühle quarry is a well-exposed outcrop in the Ries impact structure, where the irregular contact between the lithic components of the Bunte Trümmermassen and the generally overlying melt-fragment-bearing suevite are clearly visible (Fig. 2a; e.g., von Engelhardt 1997; Hüttner and Schmidt-Kaler 1999; Osinski et al. 2004; Stöffler et al. 2013). The suevite can form injection veins into the components of the Bunte Breccia, forming vein-like structures or lenses (Fig. 2a). Ongoing quarry activity continuously albeit transiently exposes melt-fragment-free breccia with a high amount of basement clasts mixed with clasts from the sedimentary cover rocks (Figs. 2, 3).

At the northeastern corner of the Aumühle quarry, the clasts in the Bunte Breccia range from a few cm up to 15 m in diameter (Fig. 2a, 3a-c). Upper Jurassic black shales are overlain by upper Triassic sandstones (Fig. 3a), consistent with an inverse stratigraphy (e.g., Pohl, 1977; Sturm et al., 2015). The overlying matrix-rich and matrix-supported suevite with mm to dm-sized (devitrified) glass fragments (Flädle) and fine-grained to few cm-sized lithic components are typically relative fresh and grey (Fig. 2a, 3a, b, e, f). It can, however, locally be altered at the contact to the Bunte Breccia (Fig. 3b) and polymict crystalline breccia (Fig. 3d), where it is red colored due to a high amount of fine-dispersed hematite (Sleptsova et al., *submitted*).

The contact between the polymict crystalline breccia to (altered) suevite and the components of the Bunte Breccia is always sharp, without a gradual transition of clast sizes and lithologies (Fig. 3b-f). Components of the polymict crystalline breccia have sizes of a few cm- to dm and are characterized as basement rocks (≈50%), such as gneisses and amphibolites, as well as sedimentary rocks (≈50%), such as quartz sandstones and clay stones, embedded in a fine-grained matrix of pulverized component material (Figs. 2b-e, 3e-h). This basement-clast-rich horizon is distinguished from the Bunte Breccia and suevite and referred to as polymict crystalline breccia because no glass fragments have been identified and because the basement clasts are moderately shocked in contrast to the apparently unshocked sedimentary clasts, which will be shown in the following.

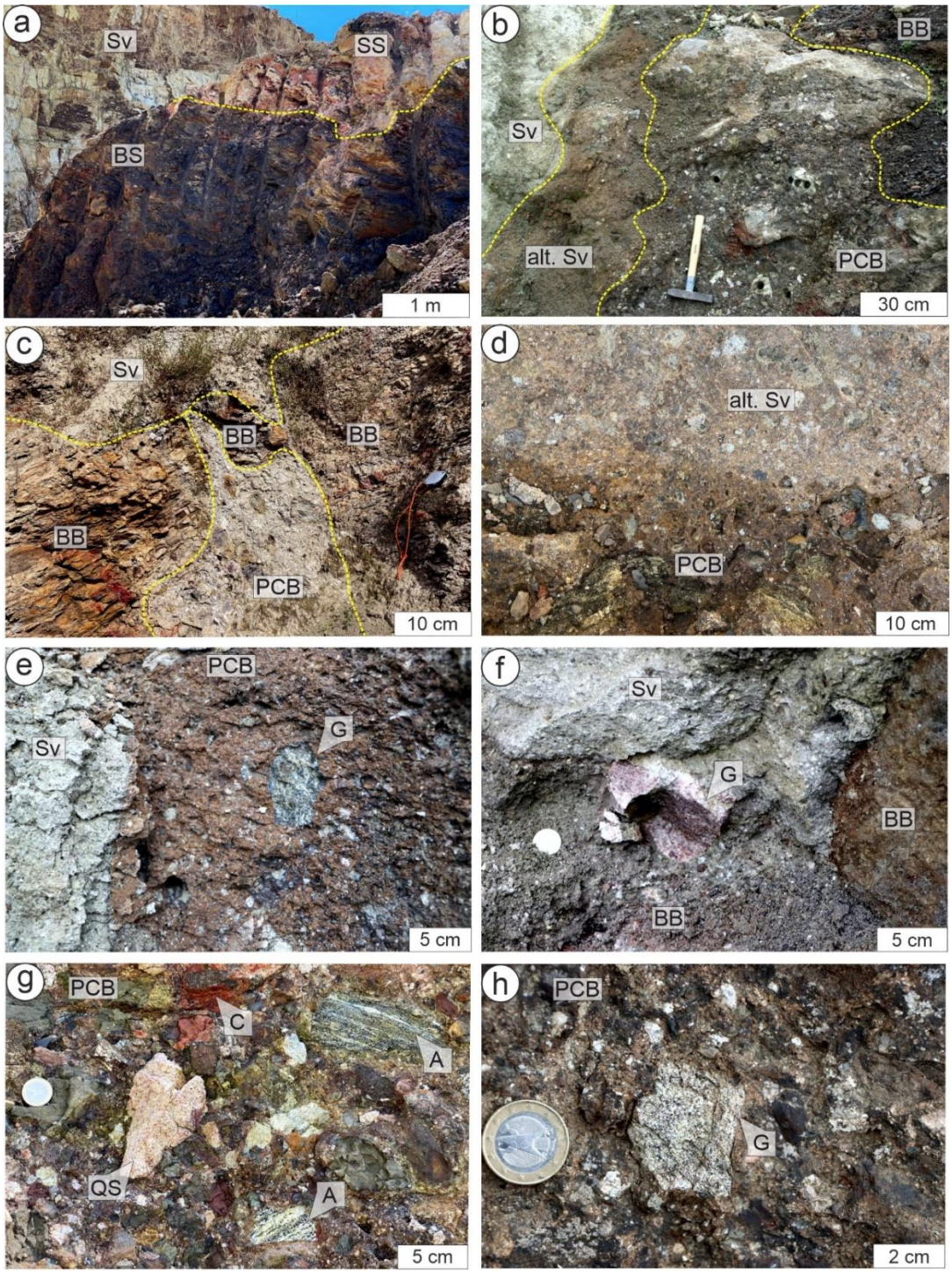

Fig. 3 Polymict impact breccia overlying suevite and Bunte Trümmermassen at the bottom in the Aumühle quarry. **a)** Components of the Bunte Trümmermassen with inverse stratigraphy: lower Jurassic black shales (BS) are overlain by upper Triassic sandstones (SS). Note the suevite (Sv) in the background. **b)** Sharp contacts of suevite (Sv), altered suevite (alt. Sv), polymict crystalline breccia (PCB), and Bunte Breccia (BB). **c)** Polymict crystalline breccia (PCB) as vein-like structure in component of Bunte Breccia (BB, iron sandstone middle Jurassic) covered by suevite (Sv). **d)** Sharp contact of altered suevite (alt. Sv) and polymict crystalline breccia (PCB). **e)** Sharp contact of grey suevite (Sv) and polymict crystalline breccia (PCB), which contains a granitoid clast (G). **f)** Granitoid clast (G) at the interface between Bunte Breccia (BB) and suevite (Sv). **g, h)** Polymict crystalline breccia (PCB) comprised of angular basement clasts [A = amphibolite in (g), G = gneiss in (h)] and sedimentary clasts [C = clay stone; QS = quartz sandstone in (g)].

Shock effects in the basement clasts

The following sections describe the shock effects within clasts of the polymict impact breccia (Fig. 2a), a gneiss clast (Fig. 2b), an amphibolite clast (Fig. 2c), a quartz sandstone clast (Fig. 2d), and a metagranite cataclasite clast (Fig. 2e).

Maskelynite and mechanical $(\bar{1}01)$ twins in amphibole from amphibolite clast

The amphibolite clast (sample R20-4,5; Fig. 2a, c) within the polymict crystalline breccia has a weak foliation consisting of 300 µm to mm-sized constituents (Fig. 4a), which are characterized as amphibole and an optically isotropic transparent phase (Fig. 4b, c) with feldspar composition as indicated by EDS measurements (Fig. 4d). The anorthite-albite ratios range from 0.41 to 0.45, corresponding to an andesine composition. Structurally, this phase can be interpreted as maskelynite (diaplectic feldspar), which has typical broad Raman peaks (Fig. 4g) of approximately 457, 510, and 586 cm^{-1} (Fritz et al. 2005). Locally, lamellae with birefringence, interpreted as remnants of the former feldspar, occur in the maskelynite (Fig. 4b, c), depicting main Raman peaks at 482 and 509 cm^{-1} (Fig. 4b, c, e), indicative of feldspar (Mernagh 1991).

EDS measurements of amphibole measurements indicate actinolite and magnesio-hornblende compositions based on an Mg/(Mg+Fe) ratio of 0.55-0.70 and 6.5-7.6 Si per formula unit according to the nomenclature of Leake et al. (1997). Distinct planar features commonly occur parallel to $(\bar{1}01)$, whereas fractures are oriented parallel (100) and {110} (Fig. 4f, g). Structural analysis via Raman spectroscopy reveals broadening in the respective peaks (Fig. 4e) resulting from a disturbed crystallographic structure.

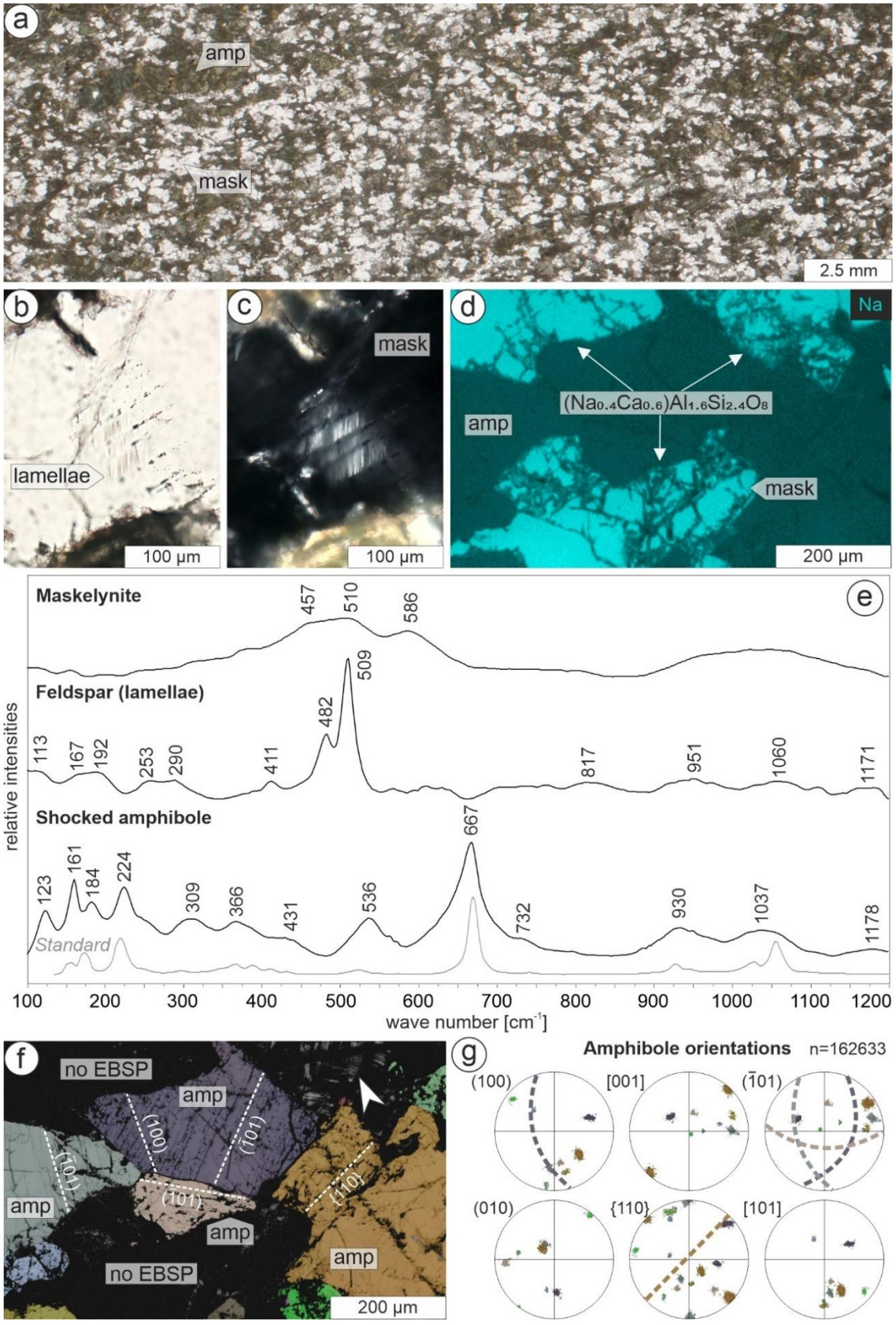

Fig. 4 Amphibolite clast, sample R20-4,5. **a)** Weak foliation of maskelynite (mask; white), i.e., former feldspar and amphibole (amp; green); thin section scan. **b, c)** Polarized light micrographs of maskelynite (mask) with lamellae of residual feldspar; (c) taken with crossed polarizers. **d)** Na distribution map with maskelynite (mask) appearing with turquois colour and amphibole (amp) containing no Na appears black). **e)** Raman spectra of maskelynite, feldspar (lamellae), shocked amphibole, and an

amphibole standard [grey; RRUFF standard (R050025)]. **f)** All Euler orientation map depicting different amphibole (amp) grains with planar fractures (white dashed lines). Note that grains with feldspar composition show mostly no electron backscattered diffraction patterns (no EBSP), but can locally contain remnants of feldspar (white arrow). **g)** Stereographic projections (lower hemisphere) of fractured amphiboles depicted in (f) of (100), ($\bar{1}01$), (010), and {110} planes as well as [001] direction with colored great circles corresponding to fracture orientations of the colored grains in (f).

The planar features along ($\bar{1}01$) are identified as twin lamellae with widths up to ≈10 µm (Fig. 5a-d). The fine-lamellar twins can be bent, indicating that they are mechanical twins resulting from crystal-plastic deformation associated with dislocation glide (Fig. 5c, d). The ($\bar{1}01$) twin plane, a misorientation axis parallel [101], and a misorientation angle of ≈180° (Fig. 5c, d, e) characterizes them as ($\bar{1}01$)[101] twins, known from high-stress crystal plasticity associated with pseudotachylyte formation (Brückner and Trepmann 2021). Twin densities typically range from 10 µm to 80 µm. Cleavage fractures parallel {110} typically are deflected by the {$\bar{1}01$} twin boundaries and do not crosscut them (Fig. 5f).

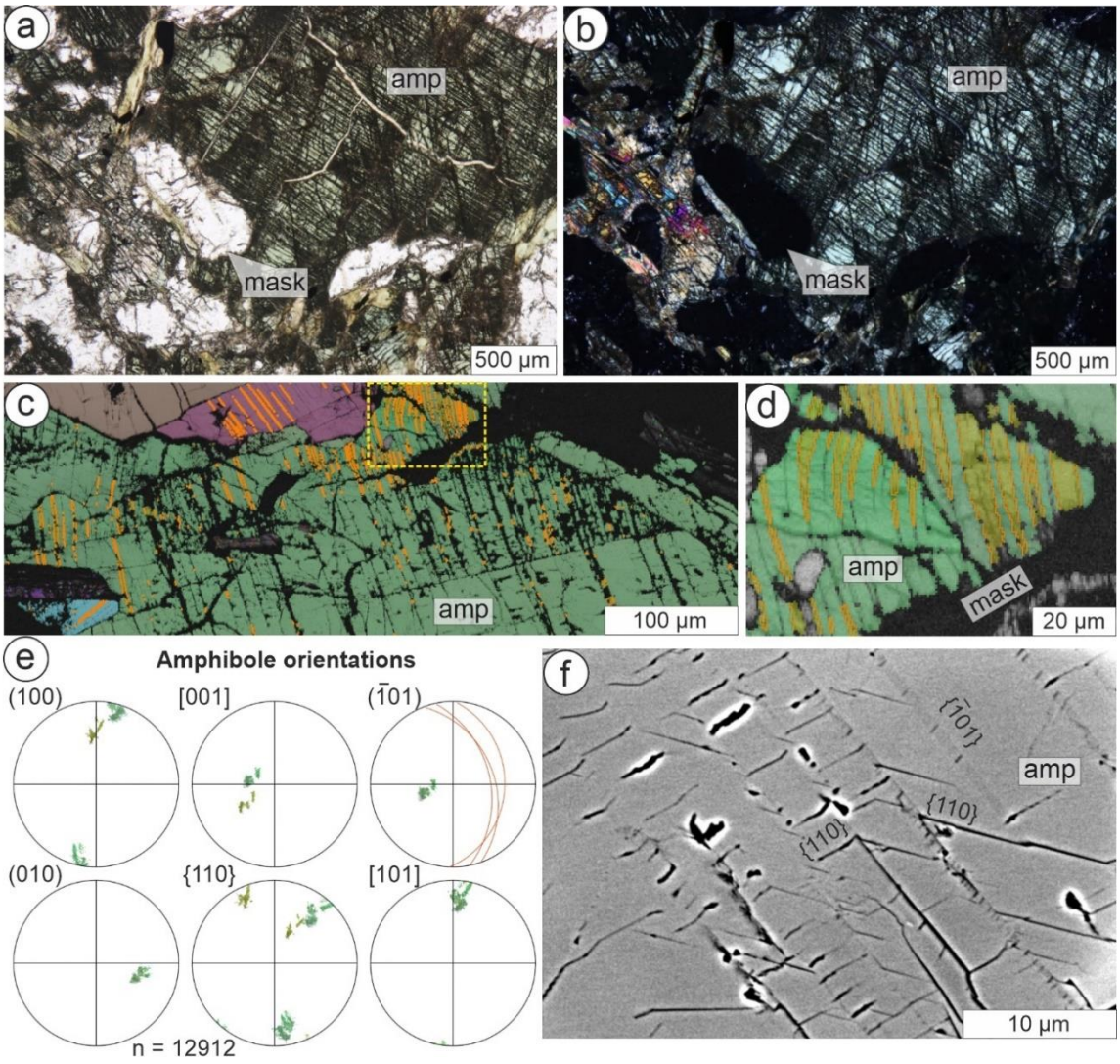

Fig. 5 Twinned amphibole within amphibolite clast in polymict crystalline breccia, sample R20-4,5. **a, b)** Polarized light micrographs of amphibole (amp) with planar features and maskelynite (mask), (b) is taken with crossed polarizers. **c, d)** All Euler orientation map of amphibole (amp) with twin boundaries (orange). The area marked yellow is enlarged in (d). **e)** Stereographic projections (lower hemisphere) of twinned amphibole depicted in (d) with great circle of ($\bar{1}01$)[101] twin boundaries (orange) as well as (101), (010), {110} planes, and the [001] direction. **f)** BSE image of amphibole with {$\bar{1}01$} twins and {110} fractures.

Diaplectic SiO_2 glass in gneiss clast

The gneiss clast (sample R20-14; Fig. 2a, e) within the polymict crystalline breccia has a foliation consisting of altered feldspar with bands of optically isotropic SiO_2, interpreted as former quartz with an mm-sized width in association with biotite (Fig. 6a-c). The optically isotropic diaplectic SiO_2 glass is characterized by main broad Raman peaks (Fig. 6d) approximately at 456, 490, 603, and 813 cm^{-1} (Kowitz et al. 2013b).

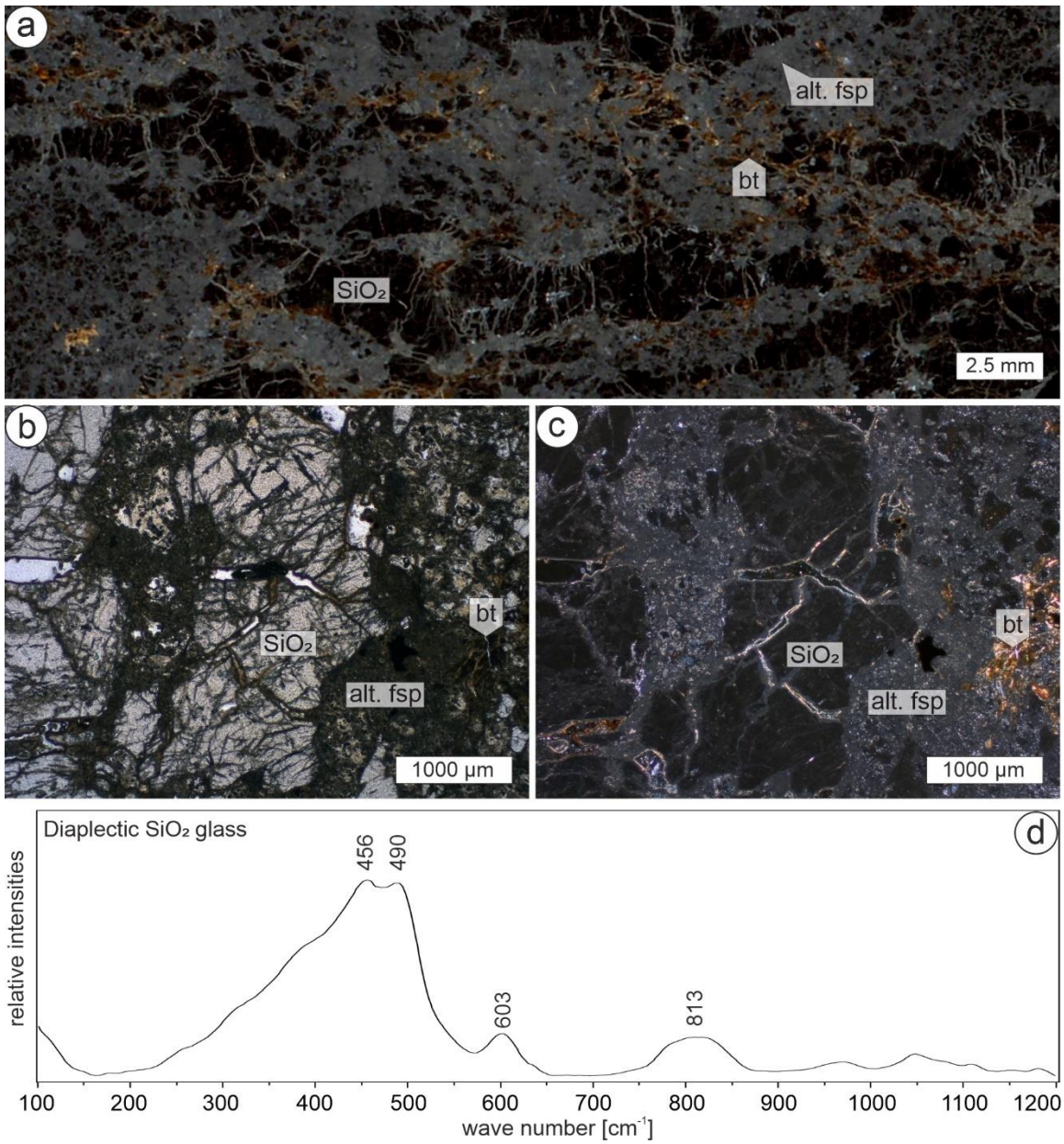

Fig. 6 Gneiss clast, sample R20-14. **a-c)** Diaplectic SiO_2 glass (SiO_2) and altered feldspar (alt. fsp) within foliation fabric of the gneiss host in polarized light (a, c) are taken with crossed polarizers. **d)** Raman spectrum of diaplectic SiO_2 glass.

Metagranite cataclasite clast

The metagranite cataclasite clast (sample R20-2; Fig. 2a, b) occurs as component within the polymict crystalline breccia, which consists of a pronounced fine-grained, phyllosilicate-rich, and red lithic matrix as well as angular foliated metagranite components with diameters ranging from 100 µm up to cm containing shocked feldspar and quartz (Fig. 7a, b). Quartz shows mottled undulatory extinction and a high density of planar deformation features (Fig. 7c, d). Although the shocked quartz still is birefringent (Fig. 7c), it shows a very poor band contrast of the EBSD pattern (EBSP) in the SEM, so indexing was only rarely possible (Fig. 7e). In these cases, an orientation of the most dominant planar deformation features (PDFs) parallel to $\{10\bar{1}3\}$, $\{01\bar{1}3\}$ and $\{01\bar{1}2\}$ is indicated (Fig. 7d, e).

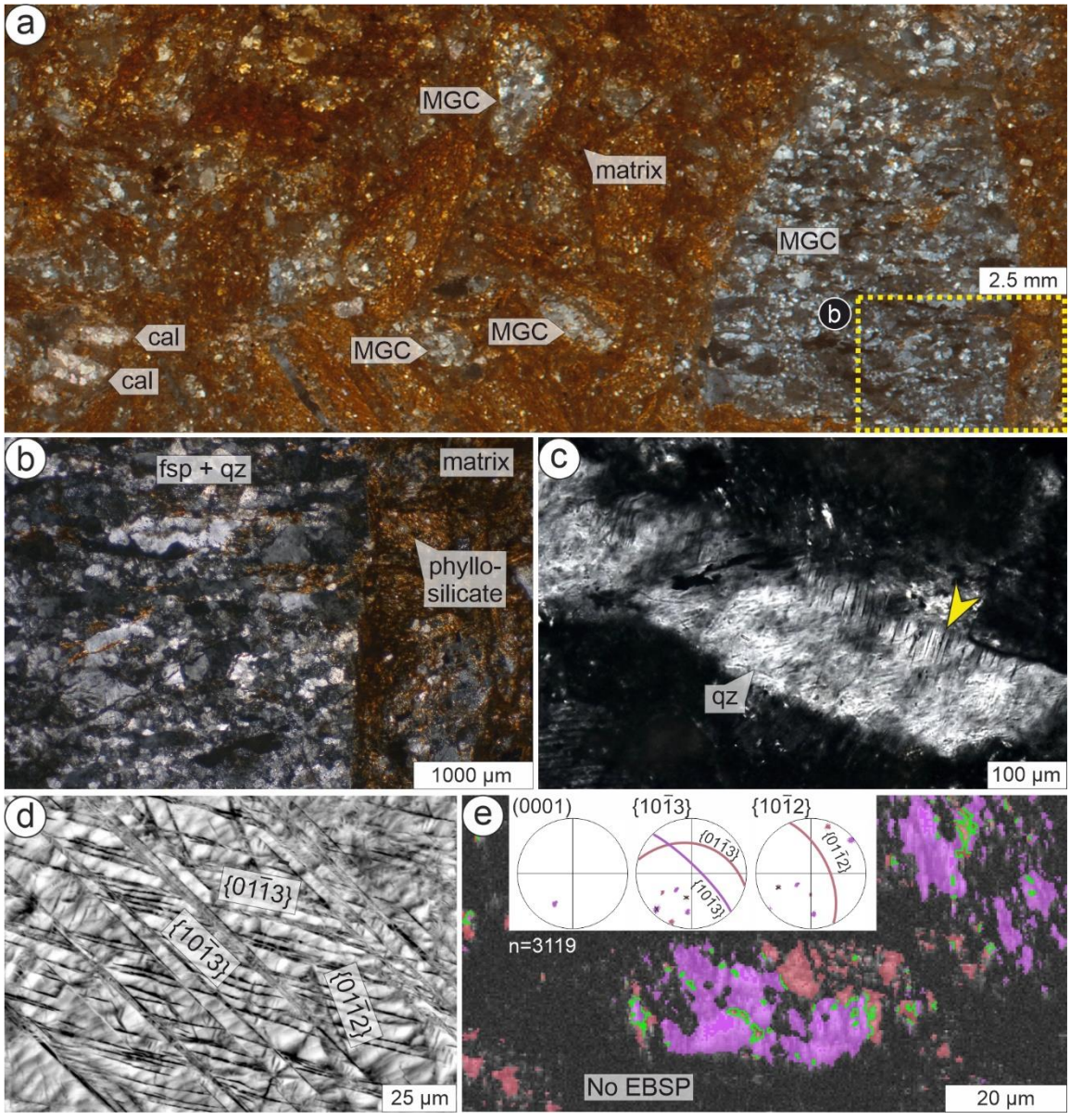

Fig. 7 Metagranite cataclasite clast, sample R20-2. **a)** Overview of metagranite cataclasite (MGC) with fragmented calcite (cal) clasts in a fine-grained red matrix; thin section scan taken with crossed polarizers. The yellow rectangle depicts the area magnified in (b). **b)** Metagranite clast composed of foliated feldspar and quartz (fsp+qz) with adjacent phyllosilicate-rich matrix; polarized light micrograph taken with crossed polarizers. **c)** Quartz (qz) within metagranite cataclasite clast has PDFs (yellow arrow); polarized light micrograph taken with crossed polarizers. **d)** BSE image and **e)** EBSD map with pole figures of quartz with PDFs parallel to $\{10\bar{1}3\}$ and $\{01\bar{1}2\}$. Note that the black areas in (e) indicate no EBSP.

Calcite aggregates occur embedded within the cataclasite, with the long axis of the aggregates ranging up to 1 mm (Fig. 8a). The calcite aggregates are fractured with fragment sizes from 10s of µm to 100s of µm (Fig. 8a-d). Calcite locally exhibits unusual interference colors (white arrow in Fig. 8b) that are indicated by EBSD analysis to represent deformed grains with internal misorientation with angles deviating from the grain average orientation of up to 20° and mechanical twins (Fig. 8b, d). Two twin systems have been recognized, *e*-twins (yellow twin boundaries in Fig. 8d) and *r*-twins (red twin boundaries in Fig. 8d, e), similar to those reported recently from metagranite cataclasites from Maihingen in the Ries (Seybold et al. 2023). Also, undeformed grains with low internal misorientation (Fig. 8c, d) occur adjacent to the deformed grains with mechanical twins and internal misorientation. When comparing the crystallographic orientation of the deformed and undeformed grains (Fig. 8c, d, e), a remarkable orientation relationship with a common $\{11\bar{2}0\}$ plane can be observed (yellow circles in Fig. 8e). The twinned grains with high misorientation angles are characterized in BSE images by a high amount of sub-µm-scale pores (Fig. 8f).

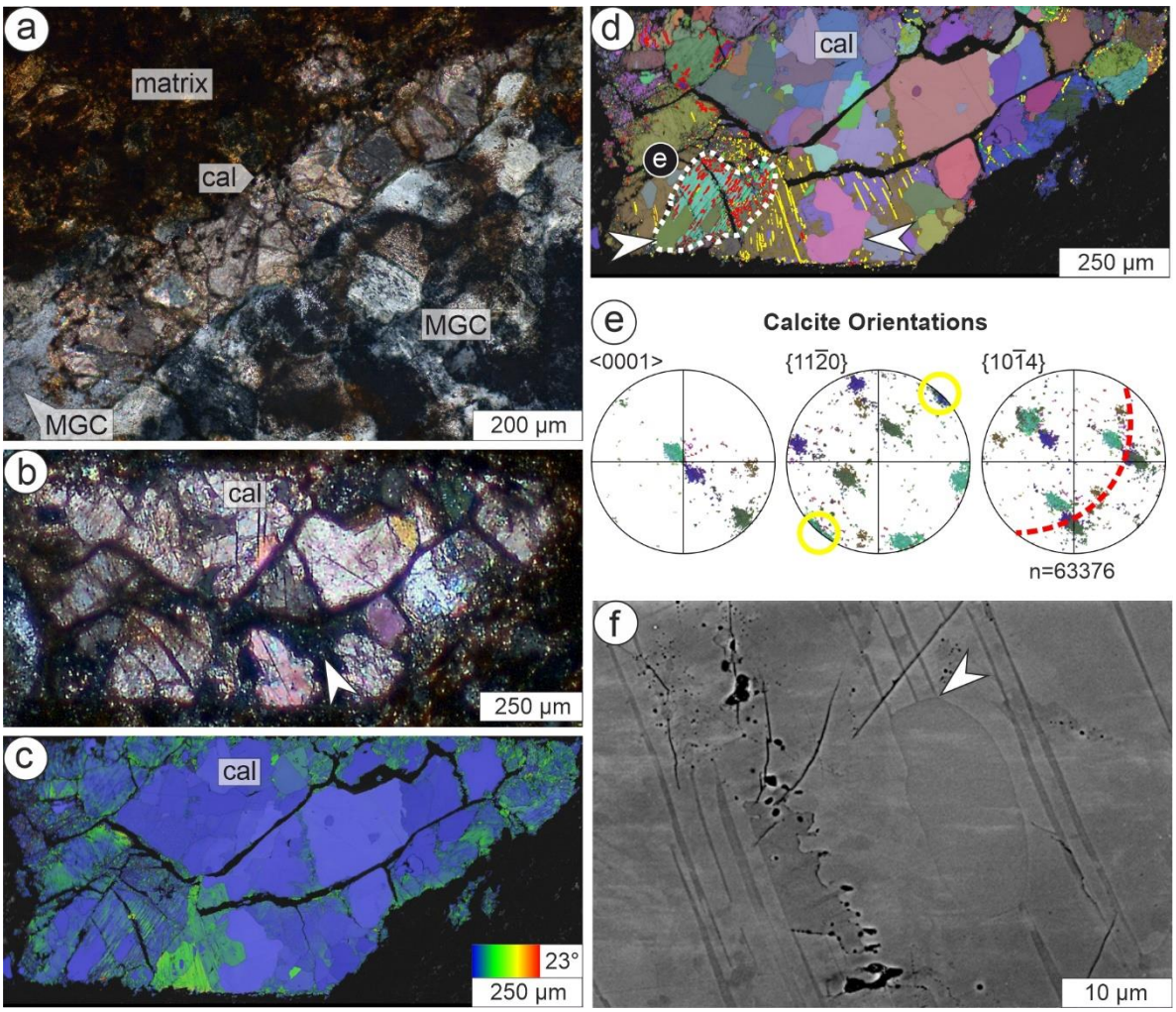

Fig. 8 Shock effects of fractured calcite (cal) aggregate within metagranite cataclasite clast (MGC), sample R20-2. **a, b)** Polarized light micrographs taken with crossed polarizers of calcite aggregates. Note that EBSD data of (b) is presented in (c) – (e). **c)** Grain Reference Orientation Distribution map (GROD) displaying the angular deviation from the average grain orientation. **d)** EBSD All Euler orientation map depicting r-twin boundaries in red and e-twin boundaries in yellow. The dashed line indicates the area, which orientation data is displayed in (e). Note the grains, which crosscut the twins, marked by the white arrows. **e)** Pole figures of the <0001> axis as well as the $\{11\bar{2}0\}$, and $\{10\bar{1}4\}$ planes of the area marked in (c). Note the

overlapping {11$\bar{2}$0} planes of all three orientation maxima indicated by the yellow circles. The red dashed great circle displays the r-twin boundary orientation. **f)** BSE image of twinned grain, which is partly replaced by a new grain (white arrow). Note the pores (black) within the twinned calcite.

Sedimentary clast

Sedimentary clast (sample R20-8; Fig. 2a, d) occurs within the polymict crystalline breccia. The grain-supported and phyllosilicate-cemented, well-sorted iron-rich quartz sandstone (sample R20-8) within the polymict crystalline breccia is composed of grains with sizes ranging from 5 to 40 µm and ≈5% limonite with rarely occurring hematite grains (Fig. 9). No apparent shock effects can be observed, consistent with the study of (Sleptsova et al., *submitted*), which only reports unshocked sedimentary components.

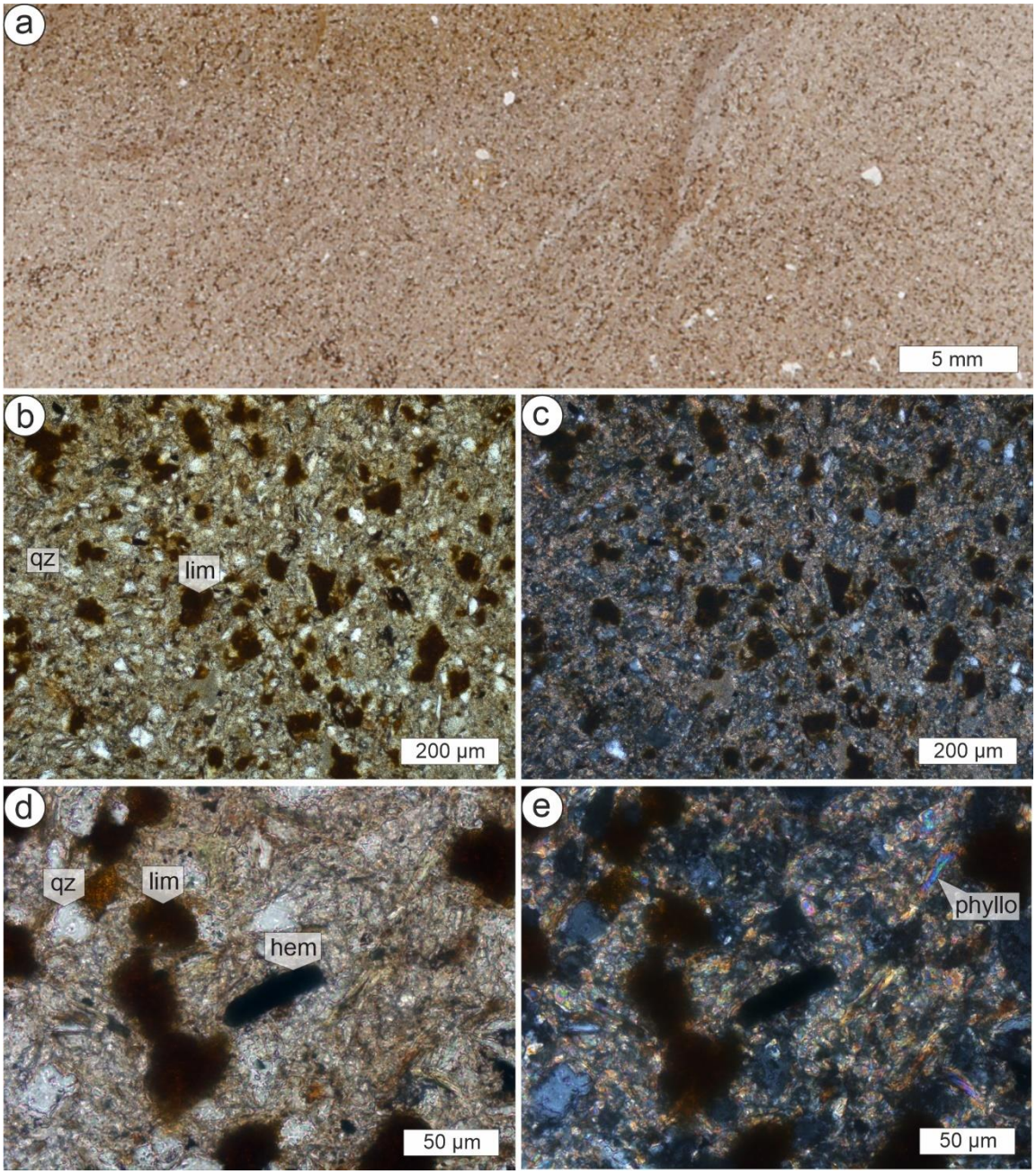

Fig. 9 Polarized light micrographs of quartz sandstone component within polymict crystalline breccia (sample R20-8). Quartz (qz) and limonite (lim) grains occur together with local hematite (hem) grains within a matrix of phyllosilicates (phyllo). No apparent shock effects can be observed; (c, d) are taken with crossed polarizers.

Discussion

Shock and deformation conditions of clasts within polymict crystalline breccia

The observed amphibolite, gneiss, and metagranite cataclasite components in the polymict crystalline breccia compare well with the Variscan gneisses documented from the Nördlingen 1973 drilling project (Graup 1977) as well as the basement components investigated by Graup (1978). The shock effects and shock pressure interpretations are summarized in Table 1.

Diaplectic SiO_2 glass in gneiss clast sample R20-14 (Fig. 6) indicates shock pressures of 35-50 GPa (Stöffler 1971b, 1972; Stöffler and Hornemann 1972; Kowitz et al. 2013a), which can, therefore, be classified as shock stage F-S5 (Stöffler et al. 2018) or shock stage II according to the IUGS system (Stöffler and Grieve 2007). Biotite without adjacent thermal decomposition products, such as fine-grained hematite or magnetite, indicates temperatures below 600°C (Wones and Eugster 1965). For the amphibolite clast (sample R20-4,5), diaplectic glass with an andesine composition (Fig. 4b-e), shock pressures range from 20 to 34 GPa (Schaal and Hörz 1977; Ostertag 1983; Stöffler et al. 2018), equivalent to shock stages M-S3 to M-S4 (Stöffler et al. 2018) or shock stages IIa to IIb according to the IUGS system (Stöffler and Grieve 2007).

The $(\bar{1}01)[101]$ mechanical twins in amphibole (Fig. 4f, g) further indicate crystal plastic deformation at high differential stresses. The $(\bar{1}01)[101]$ twinning is documented in pseudotachylyte (e.g., Brückner and Trepmann 2021), other meteorite craters (Chao 1967), as well as in nuclear explosion sites (Borg 2013). According to the experimentally calibrated critical resolved shear stress of 200-400 MPa (Rooney et al. 1970), differential stresses of ≥400 MPa are required for $(\bar{1}01)[101]$ twinning of amphibole (Fig. 5). Stähle et al. (2022) documented shock veins within shocked amphibolite clasts (shock stages M-S3 to M-S4) in suevite from the Ries impact structure, which is not apparent in the amphibolite clast of our study. Metagranite cataclasite clast sample R20-2 consists of metagranite and calcite clasts. Calcite was likely pre-existing in hydrothermal veins in the crystalline basement prior to impact (Seybold et al., 2023). The occurrence of the metagranite cataclasite components within the breccia (Fig. 7) indicates two stages of fracturing, where initially, the cataclasite formed, which was subsequently incorporated as clast into the breccia. Quartz within the gneiss clast exhibits a high density of fine rhombohedral PDFs (Fig. 7c-e). Shock pressures thus range from 10 to 20 GPa (Hörz 1968; Müller and Hornemann 1969; Stöffler and Langenhorst 1994), representing shock stages F-S2 to F-S3 (Stöffler et al. 2018) or shock stage Ia according to the IUGS system (Stöffler and Grieve 2007). Sandstone clast R20-8 displays no apparent shock effects (Fig. 9), lacking planar fractures or other planar features, high-pressure polymorphs, and/or glass (Kieffer et al. 1976; Kowitz et al. 2016) and is classified by shock stages SR-S1 (Stöffler et al. 2018) or 0 according to the IUGS system (Stöffler and Grieve 2007).

The different shock conditions of the basement clasts of different rock types with shock pressures ranging from 10 to 50 GPa and differential stresses of ≥400 MPa, are in accordance with the observation from other polymict crystalline breccias (e.g., Abadian 1972; Graup, 1978; von Engelhardt 1990). The unshocked sedimentary clast (e.g., R20-8) is derived farther away from the center of the crater. Suevites also contain components shocked under variable conditions, yet they contain glass fragments (e.g., Stöffler et al. 2013), which are not observed in the here-described polymict crystalline breccia samples.

Tab. 1 Summary of shock stage classifications after Stöffler et al. (2018) of the different lithologies investigated in the polymict crystalline breccia of this study with the respective shock pressure interpretations. The magnetic carrier and the paleomagnetic directions are from Sleptsova et al. (*submitted*), with the corresponding sample names in brackets. (Qz = quartz; Amp = amphibole; Fsp = feldspar; Mag = magnetite; Hem = hematite)

Sample	Lithology	Shock effects	Shock pressures	Shock Stage	Apparent magnetic carrier	Paleomagnetic directions
R20-14 (CS01_1)	Gneiss	diaplectic SiO_2	34-50 GPa	F-S5	mostly Mag	Ries
R20-8 (CB03_1)	Sandstone	none	<1 GPa	SR-S1	Hem	Ries
R20-4,5 (CB05_1) (CB05_2)	Amphibolite	Amp twins; diaplectic Fsp with lamellae	20-34 GPa	M-S3 to M-S4	mostly Mag	random
R20-2 (CB06_1)	Gneiss breccia	fracturing; PDFs in Qz	1-20 GPa	F-S2 to F-S3	Hem	random

Comparison of polymict crystalline breccia from the Aumühle quarry with similar outcrops in the Nördlinger Ries

The type locality of the documented polymict crystalline breccia from the Nördlinger Ries is Meyers Keller, where it occurs as an irregular body on top of the Bunte Breccia (e.g., Abadian 1972; Abadian et al. 1973; Graup 1978). This is a similar structural position as in the Aumühle quarry with the difference that in Aumühle quarry the polymict crystalline breccia is overlain by suevite (Fig. 3a, b, f) and in Meyers Keller, Ries lake sediments overlie the breccia. Similarly, in the Erbisberg drillcore documented by Arp et al. (2019), polymict crystalline breccia was detected on top of Bunte Breccia, which contains, like in Meyers Keller and the here-described Aumühle outcrop, highly shocked material (up to 35 GPa, Arp et al. 2019) and no melt products. Yet, in the Erbisberg drillcore, polymict crystalline breccia is overlain by intact gneiss blocks and monomict crystalline breccias of the *Bunte Trümmermassen* (Arp et al. 2019). The apparent systematic structural position on top of the Bunte Breccia at Meyers Keller (Abadian 1972), Aumühle (this study), and Erbisberg drillcore (Arp et al. 2019) indicates that deposition of the polymict crystalline breccia took place after the deposition of the Bunte Breccia.

The emplacement of the *Bunte Trümmermassen* is interpreted as a ballistic sedimentation during secondary cratering, which results in a ground-level debris flow (Oberbeck 1975; Hörz et al. 1983) or/and an emplacement by a rolling-gliding base surge (Chao et al. 1987). The first model is an analogue to ejecta formations on the Moon under dry conditions without an atmosphere (Oberbeck 1975). A continuous Bunte Breccia deposit with a reduced thickness at ~1.00-1.45 Rc (crater radii) compared to a thicker accumulation at ~1.45-2.12 Rc resembling a moat and rampart morphology was revealed by Sturm et al. (2013) through an analysis of the Ries Bunte Breccia thickness. The model of a rolling-gliding base surge (Chao et al. 1987) is based on observations, such as striations on rock surfaces (e.g., Chao 1976; Chao et al. 1987), plastic deformation of carbonatic rock and clay ironstone at isostatic pressures of ≈3 GPa, plastic flow and tight folding of clay-bearing units of distant stratigraphies (Chao et al. 1987), as well as the occurrence of large ejecta in pre-Ries valleys and lowlands (Bader and Schmidt-Kaler 1977). Ductile deformation during emplacement is reported by Pietrek and Kenkmann (2016) based on observations of folding, twisting, and smearing of Tertiary clays, which also occur wrapped around component clasts. Furthermore, the latter authors explain granular flow and the generation of deformation patterns as a result of vaporization of pore water in sand- and siltstones.

Polymict crystalline breccia at Aumühle quarry and relation to suevites

In contrast to all other known outcrops, the polymict crystalline breccia in the Aumühle quarry is overlain directly by suevite (Figs. 2a, 3b-f). The sharp boundary to the suevite (Fig. 3b-f), the absence of glass fragments and the occurrence of larger basement and sedimentary components within the polymict crystalline breccia (Fig. 3f, g) compared to the suevite clearly separates the polymict crystalline breccia from the latter. Furthermore, the basement clasts' magnetic properties differ from those of the suevites (Sleptsova et al., *submitted*). Paleomagnetic studies reveal a reversed polarity in impact-related melts of the Nördlinger Ries, corresponding to reversed polarity chron C5Bn1r (e.g., Pohl et al. 1977; Koch et al. 2012; Rocholl et al. 2018). Generally, suevite has magnetite as magnetic carrier and possesses tightly grouped paleomagnetic directions corresponding to the Ries direction (chron C5Bn1r) as a result of the deposition temperature above the Curie temperature of magnetite (580°C). Basement clasts of the same polymict crystalline breccia in our study were found by (Sleptsova et al., *submitted*) to possess a stable remanent magnetization with randomly oriented paleomagnetic directions for clasts with hematite as magnetic carrier, whereas clasts dominated by magnetite have the Ries direction. Based on the application of a partial thermal remanent magnetization in the laboratory, Sleptsova et al. (*submitted*) determined that the magnetization of the hematite-bearing clasts was blocked before rotation and that the temperature of the post-Ries hydrothermal system was below 300°C. Table 1 summarizes the magnetic properties of the samples investigated in this study.

The emplacement of suevite is discussed as a collapse of an ejecta plume (von Engelhardt 1997), deposition of an impact melt flow (Osinski 2004), via lateral flow (Bringemeier 1994; Meyer et al. 2011), density flow (Newsom et al. 1990), or through a collapse of a post-impact phreatomagmatic plume system, which evolved from a fuel-coolant interaction of an aquifer or water with an impact melt sheet (Artemieva et al. 2013; Stöffler et al. 2013). Siegert et al. (2017) propose an emplacement by a radial, granular fluid-based particulate density current similar to ignimbrite formation of volcanic systems. In neither of these emplacement scenarios, an accumulation of a melt-free polymict crystalline breccia is expected at the base of the suevites. If the basement-rich horizon would have resulted from mixing and reworking of the Bunte Breccia and suevite during turbulent emplacement, the presence of glass fragments and smaller basement clasts (as typical for the overlying suevite) would be expected.

Overall, the stratigraphic position of the polymict crystalline breccia on top of the Bunte Breccia and underlying the suevite as well as the sharp contacts between both (Figs. 2a, 3b-e), together with large basement clasts, without glass fragments and in accordance with the paleomagnetic data, indicates that the suevite was deposited independently and after the emplacement of the polymict crystalline breccia.

Relation to dikes of polymict crystalline breccias within the Ries and other impact structures

Dike occurrences of lithic breccias are reported from the Ries (FBN1973 research drillcore, Stöffler 1977) and various other impact structures: the Rochechouart impact structure (e.g., Lambert, 1981; Bischoff and Oskierski, 1987), the Slate island impact structure (e.g., Dressler and Sharpton, 1997), the Lockne impact structure (e.g., Sturkell and Ormö, 1997), and the Chesapeake Bay impact structure (e.g., Wright Horton et al. (2009). These observations indicate that polymict lithic breccias often occur as dikes within the crystalline basement and basement megablocks in contrast to the isolated complexes of irregular bodies, as observed in Aumühle quarry in this study (Figs. 2, 3). The dike breccias are generally characterized as matrix- or clast-supported injections veins of a few cm to several m in width and >1 km in length [i.e., polymict clastic-matrix breccias in Dressler and Reimold 2004; polymictic clastic matrix breccias in Dressler and Sharpton (1997)]. Similar to the polymict crystalline breccia in Aumühle quarry, they are constituted of mostly shocked fragments from all

stratigraphic levels of the pre-impact target (e.g., Abadian 1972; Abadian et al. 1973; Stöffler 1977; Lambert 1981; Bischoff and Oskierski 1987).

Emplacement of polymict crystalline breccia

The emplacement of vein-like polymict crystalline breccias is interpreted as a highly energetic process, which takes place during the growth of the crater when shocked and fragmented material moves against and along the transient crater wall and intrudes it with a high particle motion (e.g., Stöffler 1977; Lambert 1981). The injected material is transported from 10s of m to a few km (e.g., Stöffler 1977; Dressler and Sharpton 1997). The necessary energies as a function of pressure for the emplacement were only sufficient during the shock compression and the excavation stage of crater formation (Bischoff and Oskierski 1987). The mathematical *Maxwell Z-model* (Maxwell 1977; Croft 1980) predicts that material from within the impact center moves horizontally or vertically along the forming crater wall, whereas the same material is also partially ballistically ejected (Bischoff and Oskierski 1987). The amount of the ballistically ejected material depends on the geometry of the excavation cavity, which is distinct from the transient cavity and the apparent impact structure geometry (Croft 1980). The amount of ballistically ejected material is hard to estimate given the highly energetic and turbulent excavation stage, however, the emplaced basement clasts have the same composition as the injected material (Fig. 10).

The occurrence of polymict crystalline breccia in Aumühle quarry is observed as irregular bodies on top of the Bunte Breccia (Figs. 2a, 3b) or within the components of the Bunte Breccia (Fig. 3b-e) with a sharp contact to the suevite above (Fig. 33b-e). At several locations, we found singular large clasts from crystalline basement rocks located directly at the base of the suevites and the top of the Bunte Breccia (Fig. 3f). Therefore, we suggest an emplacement of the polymict crystalline breccia from the Aumühle quarry as predicted by the *Maxwell Z-model* (Maxwell 1977; Croft 1980). After the incipient crater formation, where temperatures vaporized the target rock (Fig. 10a), first melting and then fracturing occurs upon unloading from shock compression (Davies 1972). The metagranite cataclasite, sample R20-2, likely formed during this initial stage after passage of the shock wave by *in situ* cataclasis of Variscan metagranite with pre-existing calcite veins (Fig. 10a), whereas brecciation with fragmentation of the basement clasts and transport of the clasts occurred upon subsequent crater excavation (Fig. 10b). The shocked and fragmented clasts from the Variscan basement were either injected into fractures within the transient excavation cavity wall or ballistically ejected by cratering flow fields consistent with an inverse stratigraphy (Maxwell 1977; Croft 1980) (Fig. 10b). The ejecta was subsequently deposited on the Bunte Breccia layer, which formed by a rolling-gliding base surge (Chao et al. 1987) and/or ground level debris flow (Oberbeck 1975; Hörz et al. 1983) (Fig. 10c). Additional ballistically transported sedimentary clasts (Oberbeck 1975; Hörz et al. 1983), which only experienced minor shock, were mixed with the shocked basement clasts and form polymict crystalline breccia. Suevite was subsequently deposited above the polymict crystalline breccia and the Bunte Breccia (Fig. 10d). The irregular distribution of larger bodies of polymict breccia (Figs. 2a, 3b) as well as single larger clasts from the crystalline basement at the interface between Bunte Breccia and suevite (Fig. 3f), are consistent to this emplacement mechanism, given the highly energetic and turbulent deposition of impact ejecta (Dressler and Sharpton 1997; Dressler and Reimold 2004; Kenkmann et al. 2014; Siegert et al., 2017).

The inverse stratigraphy as predicted by the Maxwell Z-model (Maxwell 1977; Croft 1980) is displayed in the Aumühle quarry from top to bottom as i) crystalline basement derived suevite (Figs. 2a, 3a-e), ii) polymict crystalline breccia composed of shocked basement clasts and sedimentary components (Figs. 2a, 3b, d, e), iii) Bunte Breccia composed of upper Triassic sandstone (Fig. 3a), and iv) Bunte Breccia consisting of upper Jurassic black shales (Fig. 3a).

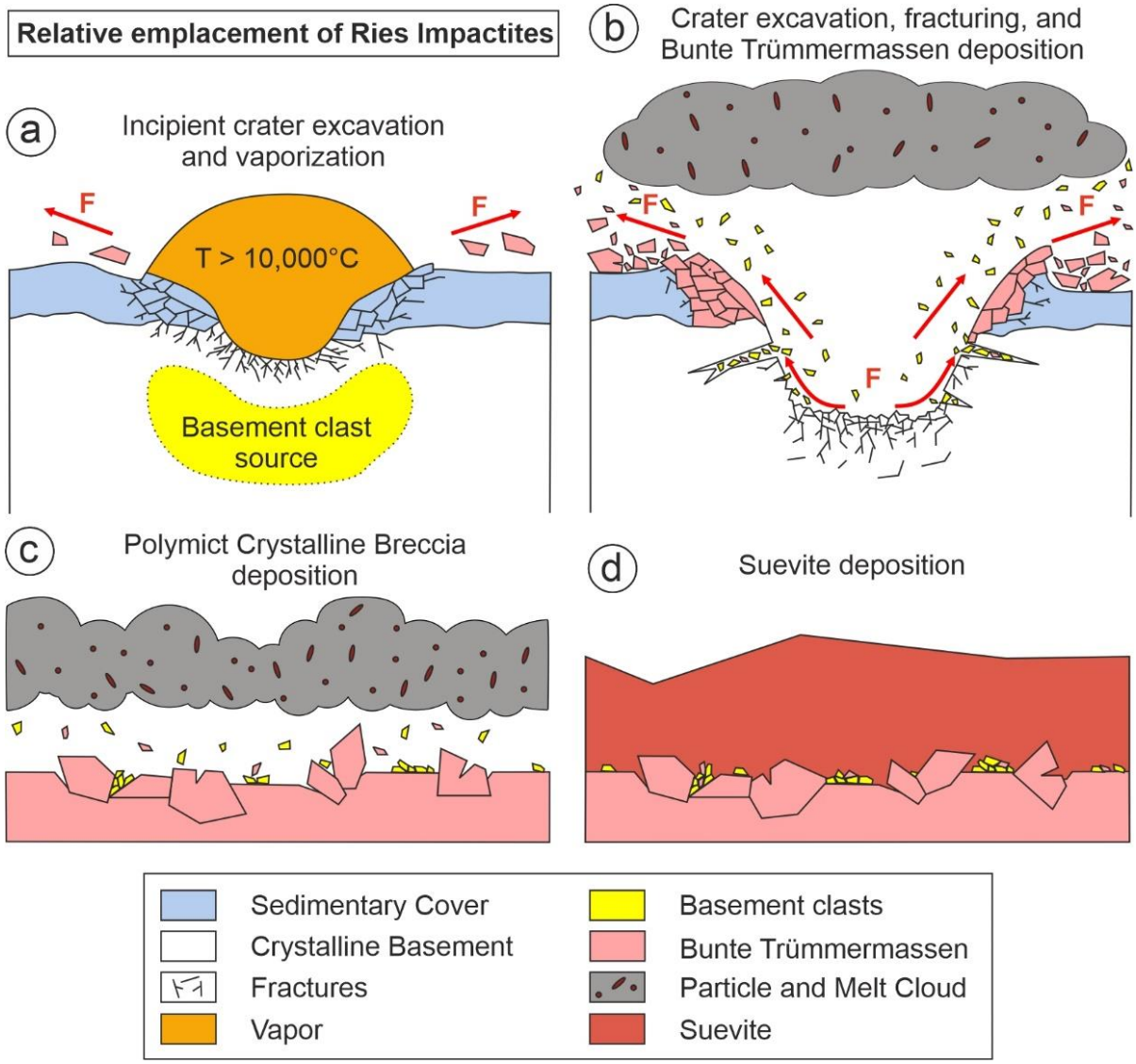

Fig. 10 Relative emplacement of Ries impactites. **a)** Upon incipient crater excavation, Bunte Trümmermassen are ejected from the excavation cavity, where temperatures lead to rock vaporization (Davies 1972). The yellow area indicates the source of the shocked basement clasts. **b)** Ongoing crater excavation results in the formation of a fine-grained particle and melt cloud. Radial forces (F; red) lead to enhanced fracture generation within the crystalline basement and the overlying sedimentary cover sequence. As a result, shocked basement clasts are partially injected into the newly formed fracture system driven by the crater excavation. However, fragmented clasts are also ejected outwards, where Bunte Trümmermassen are already deposited with inverse stratigraphy. **c)** Shocked basement rock fragments and sedimentary clasts settle on top of the Bunte Trümmermassen as irregular bodies and individual clasts before **d)** suevite deposition.

Conclusions

An outcrop of polymict crystalline breccia at the Aumühle quarry, Ries impact structure exhibits a clear depositional relationship with the Bunte Breccia at the base and suevite on top. From the macroscopic observations and microfabric analysis of the clasts, we conclude the following:

1. The missing glass fragments, the random orientation of the paleomagnetic directions in the basement clasts as well as the sharp boundaries between the deposits (Figs. 2, 3) argue against an origin of the polymict crystalline breccia by mixing of Bunte Breccia and suevite upon turbulent deposition of the suevite.
2. The mixture of moderately shocked clasts from the crystalline basement [shock stages up to F-S5 after Stöffler et al. 2018 (35-50 GPa) (Figs. 4-8)] and apparently unshocked sedimentary clasts (Fig. 9) reflects their different source localities within the impact structure (Fig. 10a).
3. The cataclasite clasts (Figs. 7, 8) indicate two stages of fracturing, one stage of *in situ* cataclasis after unloding from shock compression (Fig. 10a) and a later brecciation and transport of the basement clasts (Fig. 10b).
4. The shocked basement clasts were either injected within fractures of the transient crater wall or ballistically ejected on top of the somewhat earlier deposited components of the Bunte Trümmermassen consistent with an inverse stratigraphy (Fig. 10c), where they were mixed with the sedimentary cover clasts to form the polymict crystalline breccia deposit before emplacement of the suevite (Fig. 10d).

Acknowledgements

The fieldwork and assistance with polarized light microscopy and SEM by Ayoub Benhoummad is greatly acknowledged. We thank Jean Pohl for his helpful comments on the manuscript. We acknowledge the financial support of the Deutsche Forschungsgemeinschaft (TR534/9-1 and GI712/20-1).

Declaration of interest

No known competing financial interests or personal relationships influenced the results reported in this study.

References

Abadian M (1972) Petrographie, Stoßwellenmetamorphose und Entstehung polymikter kristalliner Breccien im Nördlinger Ries. Contrib to Mineral Petrol 35:245–262

Abadian M, von Engelhardt W, Schneider W (1973) Spaltenfüllungen in allochthonen Schollen des Nördlinger Ries. In: Geologica Bavarica 67. pp 229–237

Arp G, Reimer A, Simon K, Sturm S, Wilk J, Kruppa C, Hecht L, Hansen BT, Pohl J, Reimold WU, Kenkmann T, Jung D (2019) The Erbisberg drilling 2011: Implications for the structure and postimpact evolution of the inner ring of the Ries impact crater. Meteorit Planet Sci 54:2448–2482. https://doi.org/10.1111/maps.13293

Artemieva NA, Wünnemann K, Krien F, Reimold WU, Stöffler D (2013) Ries crater and suevite revisited-Observations and modeling Part II: Modeling. Meteorit Planet Sci 48:590–627. https://doi.org/10.1111/maps.12085

Bader K, Schmidt-Kaler H (1977) Der Verlauf einer präriesischen Erosionsrinne im östlichen Riesvorland zwischen Treuchtlingen und Donauwörth. In: Schmidt-Kaler H (ed) Geologica Bavarica 75. Bayerisches Geologisches Landesamt, München, pp 401–410

Bischoff L, Oskierski W (1987) Fractures, Pseudotachylite Veins and Breccia Dikes in the Crater Floor of the Rochechouart Impact Structure, SW-France, as Indicators of Crater Forming Processes

Borg IY (2013) Some Shock Effects in Granodiorite to 270 Kilobars at the Piledriver Site. In: Heard HC, Borg IY, Carter NL, Raleigh CB (eds) Flow and Fracture of Rocks. American Geophysical Union Geophysical Monograph Series, Washington DC, pp 293–311

Bringemeier D (1994) Petrofabric examination of the main suevite of the Otting Quarry, Nordlinger Ries, Germany. Meteoritics 29:417–422. https://doi.org/10.1111/j.1945-5100.1994.tb00607.x

Brückner LM, Trepmann CA (2021) Stresses during pseudotachylyte formation - Evidence from deformed amphibole and quartz in fault rocks from the Silvretta basal thrust (Austria). Tectonophysics 817:229046. https://doi.org/10.1016/j.tecto.2021.229046

Chao ECT (1976) Mineral-Produced High-Pressure Striae and Clay Polish: Key Evidence for Nonballistic Transport of Ejecta from Ries Crater. Science (80-) 194:615–618. https://doi.org/10.1126/science.194.4265.615

Chao ECT (1967) Shock effects in certain rock-forming minerals. Science (80-) 156:192–202. https://doi.org/10.1126/science.156.3772.192

Chao ECT, Hüttner R, Schmidt-Kaler H (1987) Aufschlüsse im Ries-Meteoriten-Krater. Bayerisches Geologisches Landesamt, München

Croft SK (1980) Cratering flow fields: implications for the excavation and transient expansion stages of crater formation. Geochim Cosmochim Acta, Suppl 14:2347–2378

Davies GF (1972) Equations of state and phase equilibria of stishovite and a coesitelike phase from shock-wave and other data. J Geophys Res 77:4920–4933. https://doi.org/10.1029/JB077i026p04920

Di Vincenzo G (2022) High precision multi-collector 40Ar/39Ar dating of moldavites (Central European tektites) reconciles geochrological and paleomagnetic data. Chem Geol 608:121026. https://doi.org/10.1016/j.chemgeo.2022.121026

Dressler BO, Reimold WU (2004) Order or chaos? Origin and mode of emplacement of breccias in floors of large impact structures. Earth-Science Rev 67:1–54. https://doi.org/10.1016/j.earscirev.2004.01.007

Dressler BO, Sharpton VL (1997) Breccia formation at a complex impact crater: Slate Islands, Lake Superior, Ontario, Canada. Tectonophysics 275:285–311. https://doi.org/10.1016/S0040-1951(97)00003-6

Fritz J, Greshake A, Stoffler D (2005) Micro-Raman spectroscopy of plagioclase and maskelynite in Martian meteorites: Evidence of progressive shock metamorphism. Antarct Meteor Res 18:96–116

Graup G (1978) Das Kristallin im Nördlinger Ries - Petrographische Zusammensetzung und Auswurdmechanismus der kristallinen Trümmermassen, Struktur des kristallinen Untergrundes und Beziehungen zum Moldanubikum. Ferdinand Enke Verlag, Stuttgart

Graup G (1977) Die Petrographie der kristallinen Gesteine der Forschungsbohrung Nördlingen 1973. In: Schmidt-Kaler H (ed) Geologica Bavarica 75. Bayerisches Geologisches Landesamt, München, pp 219–229

Hörz F (1968) Statistical measurements of deformation structures and refractive indices in experimentally shock loaded quartz. In: French BM, Short NM (eds) Shock metamorphism of natural materials. Mono Book Corps, Baltimore, Maryland, pp 243–254

Hörz F, Ostertag R, Rainey DA (1983) Bunte Breccia of the Ries: Continuous Deposits of Large Impact Craters. Rev Geophys Sp Phys 21:1667–1725

Hüttner R (1969) Bunte Trümmermassen und Suevit. In: Preuss E, Schmidt-Kaler H (eds) Geologica Bavarica 61. Bayerisches Geologisches Landesamt, Munich, pp 142–200

Hüttner R (1977) Makroskopische Beobachtungen zur Deformation des Kristallins in der Forschungsbohrung Nördlingen 1973. In: Schmidt-Kaler H (ed) Geologica Bavarica 75. Bayerisches Geologisches Landesamt, pp 273–283

Hüttner R, Schmidt-Kaler H (1999) Die Geologische Karte des Rieses 1: 50 000 (2., überarbeitete Auflage). Geol Bavarica 104:7–76

Kenkmann T, Poelchau MH, Wulf G (2014) Structural geology of impact craters. J Struct Geol 62:156–182. https://doi.org/10.1016/j.jsg.2014.01.015

Kieffer SW, Phakey PP, Christie JM (1976) Shock processes in porous quartzite: Transmission electron microscope observations and theory. Contrib to Mineral Petrol 59:41–93. https://doi.org/10.1007/BF00375110

Koch SA, Gilder SA, Pohl J, Trepmann C (2012) Geomagnetic field intensity recorded after impact in the Ries meteorite crater, Germany. Geophys J Int 189:383–390. https://doi.org/10.1111/j.1365-246X.2012.05399.x

Kowitz A, Güldemeister N, Reimold WU, Schmitt RT, Wünnemann K (2013a) Diaplectic quartz glass and SiO2 melt experimentally generated at only 5 GPa shock pressure in porous sandstone: Laboratory observations and meso-scale numerical modeling. Earth Planet Sci Lett 384:17–26. https://doi.org/10.1016/j.epsl.2013.09.021

Kowitz A, Güldemeister N, Schmitt RT, Reimold WU, Wünnemann K, Holzwarth A (2016) Revision and recalibration of existing shock classifications for quartzose rocks using low-shock pressure (2.5–20 GPa) recovery experiments and mesoscale numerical modeling. Meteorit Planet Sci 51:1741–1761. https://doi.org/10.1111/maps.12712

Kowitz A, Reimold WU, Schmitt RT (2013b) DIAPLECTIC QUARTZ GLASS AND SiO2 MELT EXPERIMENTALLY GENERATED AT ONLY 5 GPa SHOCK PRESSURE: LABORATORY OBSERVATIONS VERSUS MESOSCALE MODELING. Lunar Planet Sci Conf 44:5–6

Kroepelin K, Wimmer K, Hoffmann VH (2022) Recent Observations in Suevite outcrops (Ries Impact, Germany). Jahresberichte und Mitteilungen des Oberrheinischen Geol Vereins 104:163–184. https://doi.org/10.1127/jmogv/104/0005

Lambert P (1981) Breccia dikes: geological constraints on the formation of complex craters. Multi-ring basins Form Evol 59–78

Lange J-M, Suhr P (2022) The distal Effects of the Ries Impact – a Synopsis. Jahresberichte und Mitteilungen des Oberrheinischen Geol Vereins 104:11–90. https://doi.org/10.1127/jmogv/104/0001

Leake BE, Woolley AR, Arps CES, Birch WD, Gilbert MC, Grice JD, Howthorne FC, Kato A, Kisch HJ, Krivovichev VG, Linthout K, Laird J, Mandarino JA, Maresch WV, Nickel EH, Rock NMS, Schumacher JC, Smith DC, Stephenson NCN, Ungaretti L, Whittaker EJW, Youzhi G (1997) Nomenclature of amphiboles: Report of the subcommittee on amphiboles of the international mineralogical association, commission on new minerals and mineral names. Am Mineral 82:1019–1037. https://doi.org/10.1180/minmag.1997.061.405.13

Maxwell DE (1977) Simple Z model for cratering, ejection, and the overturned flap. In: Roddy DJ, Pepin RO, Merrill RB (eds) Impact and Explosion Cratering. Pergamon Press, New York, pp 1003–1008

Mernagh TP (1991) Use of the laser Raman microprobe for discrimination amongst feldspar minerals. J Raman Spectrosc 22:453–457. https://doi.org/10.1002/jrs.1250220806

Meyer C, Jébrak M, Stöffler D, Riller U (2011) Lateral transport of suevite inferred from 3D shape-fabric analysis: Evidence from the Ries impact crater, Germany. Bull Geol Soc Am 123:2312–2319. https://doi.org/10.1130/B30393.1

Müller WF, Hornemann U (1969) Elektronenmikroskopischer Nachweis amorpher Bereiche in stoßwellenbeanspruchtem Quarz. Naturwissenschaften 56:279–279. https://doi.org/10.1007/BF00633926

Newsom HE, Graup G, Iseri DA, Geissman JW, Keil K (1990) The formation of the Ries Crater, West Germany; Evidence of atmospheric interactions during a larger cratering event. In: Sharpton VL, Ward PD (eds) Global catastrophes in Earth history; an interdisciplinary conference on impacts, volcanism, and mass mortality: Geological Society of America Special Paper 247. pp 195–206

Oberbeck VR (1975) The role of ballistic erosion and sedimentation in lunar stratigraphy. Rev Geophys 13:337–362. https://doi.org/10.1029/RG013i002p00337

Osinski GR (2004) Impact melt rocks from the Ries structure, Germany: An origin as impact melt flows? Earth Planet Sci Lett 226:529–543. https://doi.org/10.1016/j.epsl.2004.08.012

Osinski GR, Grieve RAF, Spray JG (2004) The nature of the groundmass of surficial suevite from the Ries impact structure, Germany, and constraints on its origin. Meteorit Planet Sci 39:1655–1683. https://doi.org/10.1111/j.1945-5100.2004.tb00065.x

Ostertag R (1983) Shock experiments on feldspar crystals. In: Proceedings of the 14th Lunar and Planetary Science Conference. pp B364–B376

Pietrek A, Kenkmann T (2016) Ries Bunte Breccia revisited: Indications for the presence of water in Itzing and Otting drill cores and implications for the emplacement process. Meteorit Planet Sci 51:1203–1222. https://doi.org/10.1111/maps.12656

Pohl J, Stöffler D, Gall H, Ernston K (1977) The Ries impact crater. In: Roddy DJ, Pepin RO, Merrill RB (eds) Impact and Explosion Cratering. Pergamon Press, New York, pp 343–404

Rocholl A, Böhme M, Gilg HA, Pohl J, Schaltegger U, Wijbrans J (2018) Comment on “A high-precision 40Ar/39Ar age for the Nördlinger Ries impact crater, Germany, and implications for the accurate dating of terrestrial impact events” by Schmieder et al. (Geochimica et Cosmochimica Acta 220 (2018) 146–157). Geochim Cosmochim Acta 238:599–601. https://doi.org/10.1016/j.gca.2018.05.018

Rooney TP, Riecker RE, Ross M (1970) Deformation twins in Hornblende. Science (80-) 169:173–175. https://doi.org/10.1126/science.169.3941.173

Schaal RB, Hörz F (1977) Shock Metamorphism of Lunar and Terrestrial Basalts. Proc Lunar Sci Conf 2:1697–1729

Seybold L, Hölzl S, Trepmann C, Ernst V, Bahmer L (2022) Megablocks from the crystalline basement – the Lehberg outcrop, Unterwilflingen, Nördlinger Ries. Jahresberichte und Mitteilungen des Oberrheinischen Geol Vereins 104:147–161. https://doi.org/10.1127/jmogv/104/0004

Seybold L, Trepmann CA, Hölzl S, Pollok K, Langenhorst F, Dellefant F, Kaliwoda M (2023) Twinned calcite as an indicator of high differential stresses and low shock pressure conditions during impact cratering. Meteorit Planet Sci 19:. https://doi.org/10.1111/maps.14056

Siegert S, Branney MJ, Hecht L (2017) Density current origin of a melt-bearing impact ejecta blanket (Ries suevite, Germany). Geology 45:855–858. https://doi.org/10.1130/G39198.1

Sleptsova IV, Gilder SA, Dellefant F, Trepmann CA, Ahanin N, Pohl J (*submitted*) Thermal and structural history of impact ejecta deposits, Ries impact structure, Germany. J Geophys Res Solid Earth

Stähle V, Chanmuang N. C, Schwarz WH, Trieloff M, Varychev A (2022) Newly detected shock-induced high-pressure phases formed in amphibolite clasts of the suevite breccia (Ries impact crater, Germany): Liebermannite, kokchetavite, and other ultrahigh-pressure phases. Contrib to Mineral Petrol 177:80. https://doi.org/10.1007/s00410-022-01936-3

Stöffler D (1977) Research drilling Nördlingen 1973: Polymict breccias, crater basement, and cratering model of the Ries impact structure. In: Schmidt-Kaler H (ed) Geologica Bavarica 75. Bayerisches Geologisches Landesamt, Munich, pp 163–189

Stöffler D (1971a) Progressive metamorphism and classification of shocked and brecciated crystalline rocks at impact craters. J Geophys Res 76:5541–5551. https://doi.org/10.1029/jb076i023p05541

Stöffler D (1971b) Coesite and stishovite in shocked crystalline rocks. J Geophys Res 76:5474–5488. https://doi.org/10.1029/jb076i023p05474

Stöffler D (1972) Deformation and transformation of rock-forming minerals by natural and experimental shock processes. Fortschritte der Mineral. 49:50–113

Stöffler D, Artemieva NA, Wünnemann K, Reimold WU, Jacob J, Hansen BK, Summerson IAT (2013) Ries crater and suevite revisited-Observations and modeling Part I: Observations. Meteorit Planet Sci 48:515–589. https://doi.org/10.1111/maps.12086

Stöffler D, Ewald U, Ostertag R, Reimold WU (1977) Research drilling Nördlingen 1973: Composition and texture of polymict impact breccias. In: Schmidt-Kaler H (ed) Geologica Bavarica 75. Bayerisches Geologisches Landesamt, Munich, pp 163–189

Stöffler D, Grieve RAF (2007) Impactites. In: Fettes D, Desmons J (eds) Metamorphic Rocks: A Classification and Glossary of Terms, Recommendations of the International Union of Geological Sciences. Cambridge University Press, Cambridge, pp 82–92, 111–125 and 126–242

Stöffler D, Hamann C, Metzler K (2018) Shock metamorphism of planetary silicate rocks and sediments: Proposal for an updated classification system. Meteorit Planet Sci 53:5–49. https://doi.org/10.1111/maps.12912

Stöffler D, Hornemann U (1972) Quartz and feldspar glasses produced by natural and experimental shock. Meteoritics 7:371–394

Stöffler D, Langenhorst F (1994) Shock metamorphism of quartz in nature and experiment: I. Basic observation and theory. Meteoritics 29:155–181. https://doi.org/10.1111/j.1945-5100.1994.tb00670.x

Stöffler D, Ostertag R (1983) The Ries Impact Crater. Fortschritte der Mineral 61:71–116

Sturkell EFF, Ormö J (1997) Impact-related clastic injections in the marine Ordovician Lockne impact structure, Central Sweden. Sedimentology 44:793–804. https://doi.org/10.1046/j.1365-3091.1997.d01-54.x

Sturm S, Kenkmann T, Willmes M, Pösges G, Hiesinger H (2015) The distribution of megablocks in the Ries crater, Germany: Remote sensing, field investigation, and statistical analyses. Meteorit Planet Sci 50:141–171. https://doi.org/10.1111/maps.12408

Sturm S, Wulf G, Jung D, Kenkmann T (2013) The ries impact, a double-layer rampart crater on earth. Geology 41:531–534. https://doi.org/10.1130/G33934.1

von Engelhardt W (1990) Distribution, petrography and shock metamorphism of the ejecta of the Ries crater in Germany-a review. Tectonophysics 171:259–273. https://doi.org/10.1016/0040-1951(90)90104-G

von Engelhardt W (1997) Suevite breccia of the Ries impact crater, Germany: Petrography, chemistry and shock metamorphism of crystalline rock clasts. Meteorit Planet Sci 32:545–554. https://doi.org/10.1111/j.1945-5100.1997.tb01299.x

von Engelhardt W, Arndt J, Fecker B, Pankau HG (1995) Suevite breccia from the Ries crater, Germany: Origin, cooling history and devitrification of impact glasses. Meteoritics 30:279–293. https://doi.org/10.1111/j.1945-5100.1995.tb01126.x

von Engelhardt W, Graup G (1984) Suevite of the Ries crater, Germany: Source rocks and implications for cratering mechanics. Geol Rundschau 73:447–481. https://doi.org/10.1007/BF01824968

Wones DR, Eugster HP (1965) Stability of biotite: Experiment, theory, and application. Am Mineral 50:1228–1272

Wright Horton J, Gibson RL, Reimold WU, Wittmann A, Gohn G, Edwards L (2009) Geologic columns for the ICDP-USGS Eyreville B core, Chesapeake Bay impact structure: Impactites and crystalline rocks, 1766 to 1096 m depth. Spec Pap Geol Soc Am 458:21–49. https://doi.org/10.1130/2009.2458(02)

The Meteoritical Society

Meteoritics & Planetary Science 55, Nr 11, 2360–2374 (2020)
doi: 10.1111/maps.13590

Quartz and cristobalite ballen in impact melt rocks from the Ries impact structure, Germany, formed by dehydration of shock-generated amorphous phases

Claudia A. TREPMANN[1*], Fabian DELLEFANT[1], Melanie KALIWODA[2], Kai-Uwe HESS[1], Wolfgang W. SCHMAHL[1,2], and Stefan HÖLZL[3]

[1]Department of Earth and Environmental Sciences, Ludwig-Maximilians-University, 80333 Munich, Germany
[2]Mineralogische Staatssammlung, Staatliche naturwissenschaftliche Sammlungen Bayerns, 80333 Munich, Germany
[3]RiesKraterMuseum, Staatliche naturwissenschaftliche Sammlungen Bayerns, 86720 Nördlingen, Germany
[*]Corresponding author. E-mail: claudia.trepmann@lmu.de

(Received 19 March 2020; revision accepted 06 October 2020)

Abstract–Quartz and cristobalite ballen aggregates surrounded by dendritic cristobalite in gneiss clasts of impact melt rocks from the Ries impact structure are analyzed by Raman spectroscopy, microscopy, and electron backscattered diffraction to elucidate the development of the characteristic polycrystalline ballen that are defined by curved interfaces between each other. We suggest that the investigated ballen aggregates represent former fluid inclusion-rich quartz grains from the granitic gneiss protolith. Upon shock loading, they transformed into an amorphous phase that partly retained information on the precursor structure. Volatiles from inclusions dissolved into the amorphous phase. During decompression and cooling, dehydration takes place and causes fracturing of the amorphous phase and disintegration into small globular ballen, with the fluid being expelled along the fractures. A similar formation of small globules due to dehydration of silica-rich glass is known for perlitic structures of volcanic rocks. Remnants of the precursor structure are present in the amorphous phase and enabled topotactic crystallization of quartz, leading to a crystallographic preferred orientation. Crystallization of more distorted parts of the amorphous phase led to random orientations of the quartz crystals. Ballen comprised of cristobalite formed from a dehydrated amorphous phase with no structural memory of the precursor. Dendritic cristobalite exclusively occurring at the rim of quartz ballen aggregate is interpreted to have crystallized directly from a melt enriched in fluids that were expelled during dehydration of the amorphous phase.

INTRODUCTION

"Ballen" of quartz and cristobalite aggregates have been observed in impactites from a number of terrestrial impact structures, predominantly from impact melt rocks, suevites, and target rock clasts affected by high post-shock temperatures ($T \geq 1200$ °C, e.g., Short 1970; Engelhardt 1972; Carstens 1975; Bischoff and Stöffler 1984; Rehfeldt-Oskierski et al. 1986; French 1998; Osinski 2004; Ferrière et al. 2008, 2009, 2010; Buchner et al. 2010; Chen et al. 2010; Schmieder et al. 2014; Chanou et al. 2015). The ballen are characterized by aggregates of globular quartz and/or cristobalite that can in rare cases contain small inclusions of coesite (Ferrière et al. 2010). Based on polarized light microscopy, Bischoff and Stöffler (1984) distinguished three types of ballen, which they interpreted to crystallize at various shock pressures from an impact-generated diaplectic glass that can preserve the shape of the original quartz grain and retains remnants of the original crystalline structure. Type A (~30–35 GPa) is described as optically homogeneous, type B (~45–55 GPa) shows variable crystallographic orientations, and type C (>50 GPa) is described as newly crystallized from a melt. Ferrière et al. (2008, 2009) distinguished five different types: Type I is defined as α-cristobalite ballen with homogeneous extinction, types II–V as α-quartz ballen with either homogeneous extinction (type

II), heterogeneous extinction (type III), intraballen crystallization (type IV), or chert-like ballen (type V). Ferrière et al. (2009) concluded that the ballen aggregates are the result of back-transformations from shock-induced states and different types of ballen do not indicate specific shock pressures, but that shock pressures in excess of ~35 GPa are required for all of them to form either from diaplectic glass or from a silica melt (lechatelierite). Furthermore, brownish colored, so-called "toasted" ballen have been reported (Whitehead et al. 2002; Ferrière et al. 2010). Various models for the formation of the ballen aggregates have been proposed to date, which mostly include multiple silica phase transformations (Short 1970; Engelhardt 1972; Carstens 1975; French 1998; Ferrière et al. 2009, 2010). Ferrière et al. (2010) suggested from a compilation of quartz and cristobalite ballen aggregates from different impact structures that α-quartz in ballen is the product of back-transformation of β-quartz and/or α-cristobalite with time.

Yet, the detailed formation mechanism of the ballen shape and especially the role of multiple phase transformations from quartz to amorphous phases back to cristobalite and/or quartz, as well as the conditions under which ballen form, remain unclear (Ferrière et al. 2010). The existing ballen classifications are based on the dominant phase comprising the ballen (quartz or cristobalite) and the optical extinction characteristics (Bischoff and Stöffler 1984; Ferrière et al. 2008, 2009). Optical extinction characteristics result from crystallographic misorientations, which can be analyzed and quantified by the electron backscatter diffraction (EBSD) technique. Using EBSD, we will describe this microfabric, including the crystallographic orientations of quartz and cristobalite in ballen aggregates within granitic gneiss clasts from the Polsingen impact melt rocks of the Ries impact structure, Germany, and we discuss the conditions and the formation mechanisms of ballen based on these observations. Although quartz ballen aggregates and dendritic rims of cristobalite around ballen aggregates are well known from the Ries (e.g., Engelhardt 1972; Ferrière et al. 2009, 2010; Osinski 2004), cristobalite ballen aggregates have, to our knowledge, not been described from the Ries impact structure so far.

METHODS

Impact melt rocks were sampled in April 2018 at the old quarry southwest of Polsingen, in the Ries impact structure, Germany (e.g., Stöffler et al. 2013). From five samples, polished thin sections (~30 μm) were prepared that were analyzed by polarized light microscopy. Two samples (CT915, CT917) were chosen for detailed scanning electron microscopy (SEM) and Raman spectroscopy.

EBSD allow us to measure the 3-D crystallographic orientation of crystalline material by SEM (scanning electron microscope) and to quantify misorientations within crystals and between different grains. For EBSD analyses, an additional chemo-mechanical polish with a colloidal silica solution (Syton) was applied. SEM investigations including EBSD and energy dispersive spectroscopy (EDS) were performed on the carbon-coated thin sections using a Hitachi SU5000 microscope, equipped with a field emission gun, NordlysNano high-sensitivity detector (Oxford Instruments), EDS detector (Oxford instruments), and MiniCL detector (Gatan). For EDS and EBSD data acquisition, the AZtec analysis software (Oxford Instruments) was used. The SEM was operated at accelerating voltages of 20 kV and a working distance of 10–25 mm. The step size for automatic EBSD mapping using a sample holder pre-tilted at 70° with respect to the electron beam was in the range of 0.5–2 μm, dependent on the EBSD pattern quality and required resolution. The EBSD data were processed using the Channel software (Oxford Instruments). All pole figures are stereographic projections of the lower hemisphere.

Silica displays abundant polymorphism as a function of temperature and pressure (e.g., Boyer et al. 1985; Stähle et al. 2008). Therefore, in situ Raman spectroscopic investigations were carried out to identify the SiO_2 phases present in a sample by using a HORIBA JOBIN YVON XploRa ONE micro Raman machine at the Mineralogical State Collection Munich (SNSB). This specific Raman spectrometer was equipped with edge filters, a Peltier-cooled CCD detector, and three different lasers working at 532 nm (green), 638 nm (red), and 785 nm (near IR). A green 2ω-Nd:YAG laser (532 nm) was used in an attenuated mode of 50% laser power belonging to 5.5 + 0.1 mW on the sample surface. Focusing was completed through a 100 LWD (long working distance) objective, resulting in a 0.9 μm laser spot size on the sample surface. The wavelength calibration of the green laser was performed by manual calibration with a pure Si wafer chip; the main peak was located in the interval of 520 ± 1 cm^{-1}. The wave number reproducibility was checked several times a day within deviations of less than <0.2 cm^{-1}. Monthly deviation was in the range of 1 cm^{-1} before calibration. Hole and slit were set to 300 and 100 μm. The 1200T/1800 T grating was used to obtain a better spectral resolution. Short counting times (2 × 8 s) were chosen. The precision of determining Raman peak positions by this method is estimated to be ±1 to ±1.5 cm^{-1}. In addition to single point measurements,

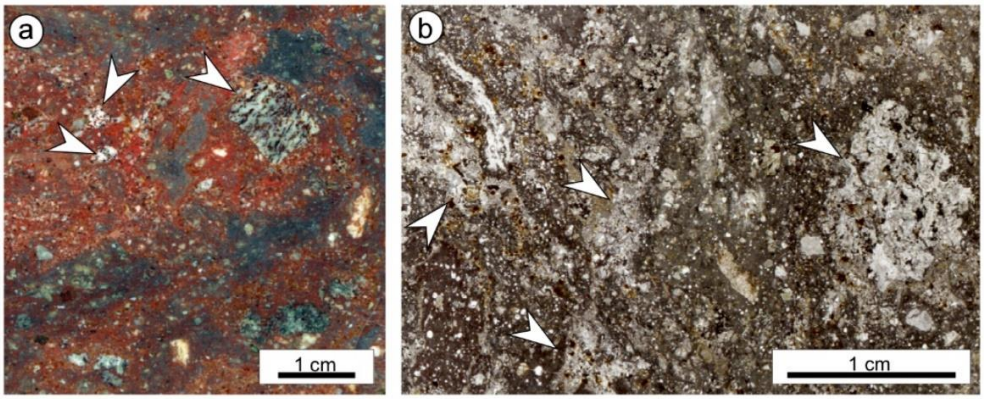

Fig. 1. Impact melt rock from Polsingen. a) Hand specimen and (b) thin section of sample CT917 showing a red matrix and clasts of granitic gneisses (arrows). (Color figure can be viewed at wileyonlinelibrary.com.)

several mapping efforts inside the quartz and cristobalite ballen have been performed to check the phase distributions.

SAMPLES

The studied ballen occur in impact melt rocks from the old quarry southwest of Polsingen within the 15 Ma old, 26 km diameter Ries impact structure, Germany (for a recent review of the Ries, see Stöffler et al. 2013). The outcrop is located about 11 km to the northeast of the assumed center of the crater, and is located in the megablock zone (N48°55′03″/E10°42′21″, Fig. 1), beyond the inner ring, the typical radial range for these rare, melt-rich deposits of the Ries (e.g., Engelhardt 1997; Buchner et al. 2010; Stöffler et al. 2013). These impact melt rocks are characterized by a large amount of biotite-bearing granitic gneiss fragments in a red melt matrix due to finely dispersed hematite (Fig. 1). In the granitic gneiss clasts, ballen aggregates, vesicles, and decomposed biotite are common (Figs. 2a and 2b). The composition of the Polsingen impact melt matrix has been reported to be similar to the impact melt rock drilled at Enkingen, as well as to the melt particles in the frequently occurring "outer suevites," containing about 6–9 wt% $Na_2O + K_2O$ and 60–65 wt% SiO_2 (Osinski 2004; Stöffler et al. 2013). This vesicle-rich impact melt rock from Polsingen with decomposed biotite indicates a shock stage F6 (former shock stage III), for granitic target rocks after Stöffler et al. (2018), representing a shock pressure range of 45–60 GPa and postshock temperatures of 900–1300 °C. The occurrence of these melt rocks at Polsingen most likely represents an erosional remnant of an originally more widespread impact melt sheet (e.g., Engelhardt and Graup 1984; Osinski 2004; Buchner et al. 2010; Stöffler et al. 2013).

RESULTS

The ballen aggregates comprised of individual ballen occur within the granitic gneiss clasts of the impact melt rocks (Fig. 2). They are mostly composed of pure α-quartz (Fig. 3A) and more rarely partly composed of α-cristobalite (Figs. 2f, 2g, and 3B). The spectra of α-quartz show the typical Raman peaks at 127, 205, 262, 354, 394, and 800 cm^{-1} as well as a main peak at 464 cm^{-1} (Fig. 3A). α-cristobalite in the ballen shows the typical triplet at 113, 231, and 418 cm^{-1} and a weaker peak at 785 cm^{-1} (Fig. 3B). A rim of brownish cristobalite is surrounding a ballen aggregate only where it is in contact with a vesicle in the impact melt rock (Figs. 2h and 3C).

The ballen aggregates have typically a diameter of a few hundreds of μm to 1 mm and show a rectangular (Fig. 2b) or an irregular shape (Figs. 2c and 2f–h). Partly, they can preserve the shape of the original quartz grain from the host rock (Fig. 2b) or they can exhibit the shape of a droplet (Fig. 2c). No structures indicating significant viscous flow within the aggregates are evident. The individual ballen are globules of a few tens of μm in diameter (Fig. 2). Quartz within individual ballen is characterized by undulatory extinction (Figs. 2c–f), which is also apparent as orientation contrast in BSE images (Figs. 4a and 4b). Cristobalite ballen show a radiating orientation contrast in BSE images (Fig. 4d). The curved interfaces defining the individual ballen can be open (Figs. 4a and 4b) or partly filled by siliceous material rich in Fe, K, Al, and Mg (Figs. 4c and 4d), as indicated by EDS measurements. Quartz that retains its original shape but with curved fractures forming incipient individual ballen can show several sets of planar features parallel to the basal plane (0001) and {10-13} rhombohedral planes, as indicated by EBSD measurements (Figs. 4e and 4f).

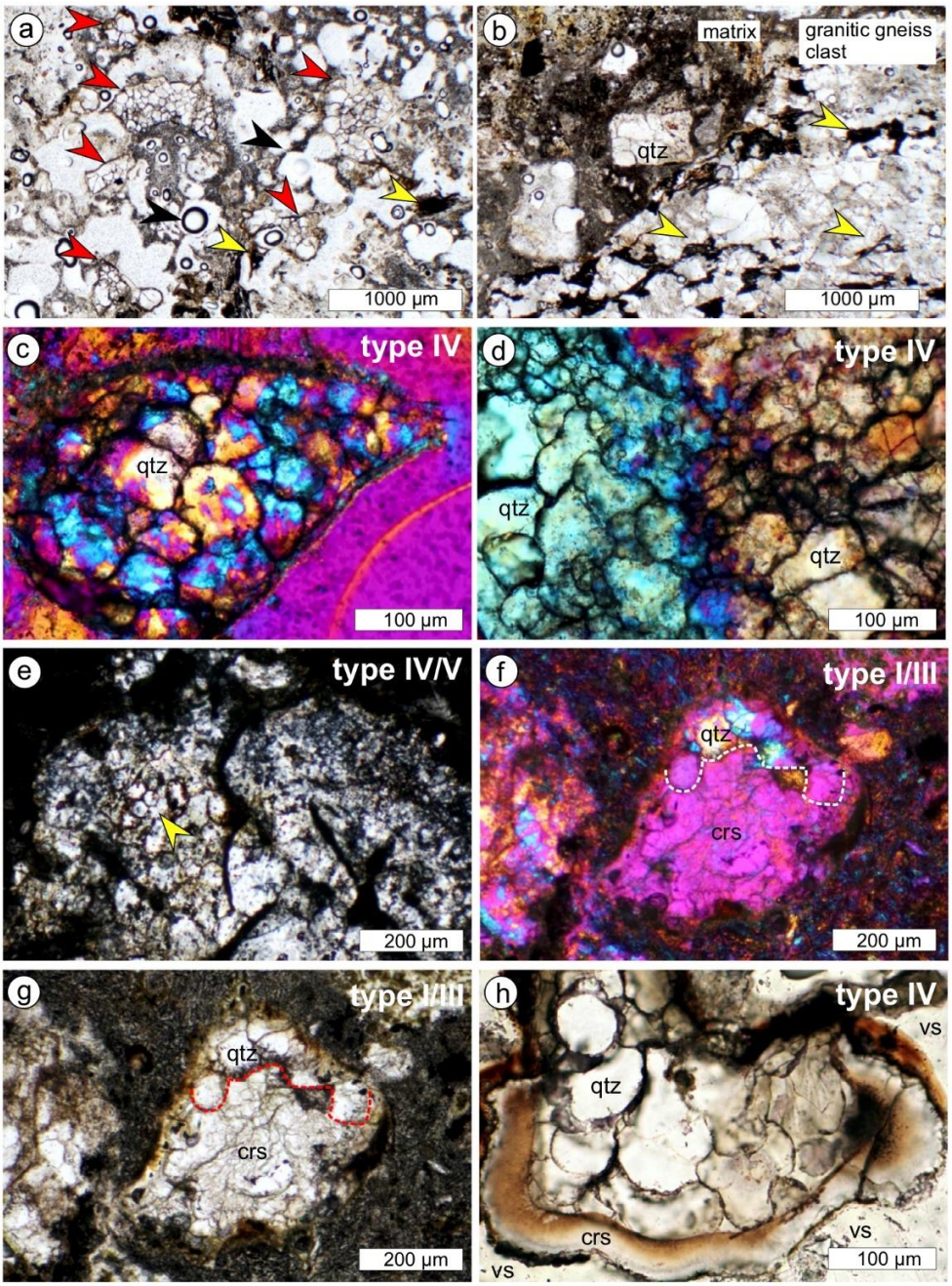

Fig. 2. Polarized light micrographs of ballen silica. a) Irregular aggregates of quartz with ballen (red arrows) in matrix rich in vesicles, sample CT915. Yellow arrows mark decomposed biotite. Black arrows point to vesicles. b) Quartz grain with preserved original shape and incipient ballen (qtz, type IV), sample CT917, compare Figs. 4e, 4f, and 9. Yellow arrows mark decomposed biotite in coarse-grained granitic gneiss clast component. c) Droplet-shaped quartz aggregate with ballen and heterogeneous extinction (type IV), crossed polarizers, and compensator plate inserted, sample CT915. d) Ballen showing two domains with slightly different crystallographic orientations and heterogeneous extinction of single ballen (type IV), crossed polarizers and compensator plate inserted, sample CT915. e) Ballen quartz with "chert-like" extinction (type V, where quartz ballen are hardly visible) but also areas displaying a heterogeneous extinction (type IV, ballen distinct, yellow arrow). f, g) Ballen aggregate of quartz (qtz) with relatively homogeneous extinction of ballen (type III) and cristobalite (crs, type I). Image (f) taken with crossed polarizers and compensator plate inserted, sample CT917, compare Fig. 6. h) Quartz aggregate with ballen surrounded by brownish rim of cristobalite in contact with vesicle (vs, type IV, compare Figs. 6, 8a, 8b, 9c and 9d). (Color figure can be viewed at wileyonlinelibrary.com.)

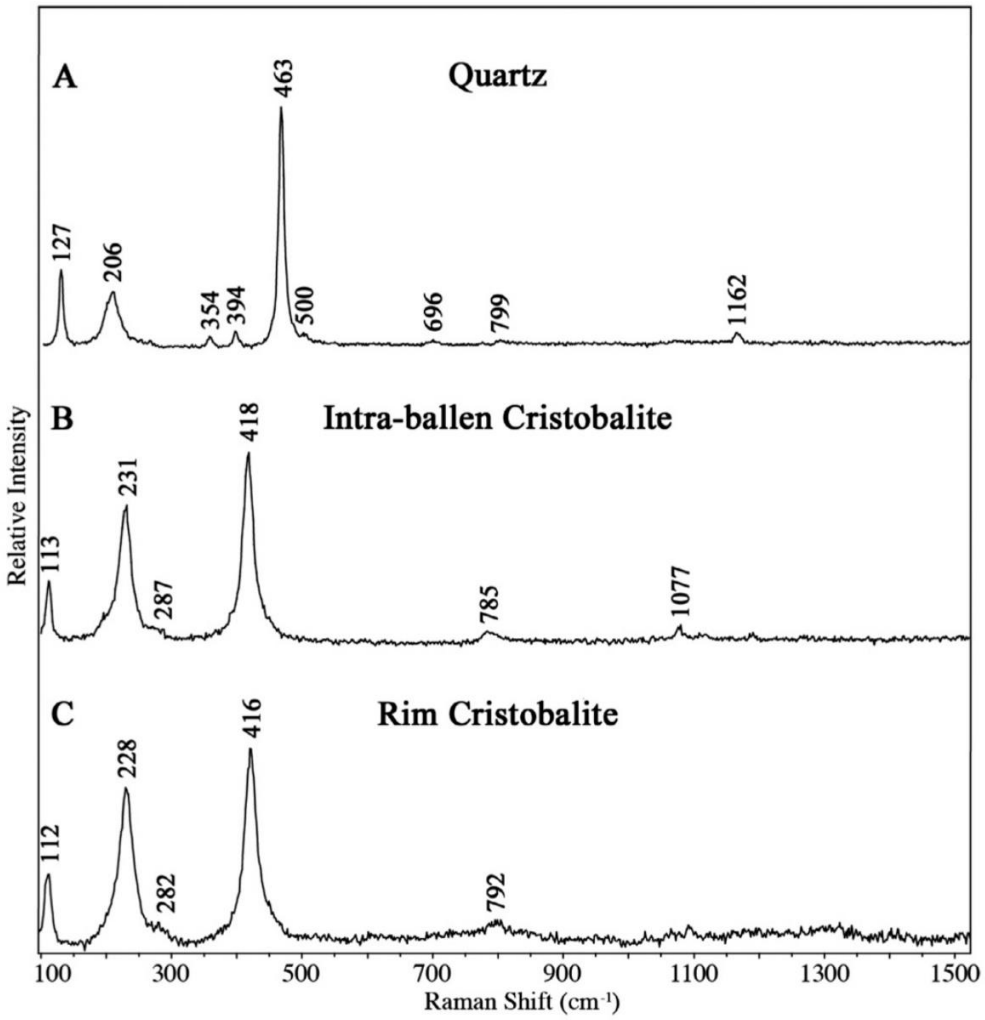

Fig. 3. Raman spectra of (A) α-quartz and (B) α-cristobalite aggregates with ballen (compare Figs. 2d and 2e, respectively). In (C), the Raman spectra of α-cristobalite at the rim surrounding ballen aggregates in contact with vesicles are shown (compare Fig. 2f).

In Table 1, the classification of ballen quartz and cristobalite aggregates after Ferrière et al. (2009), using their extinction characteristics in polarized light, is applied to our observations. The classification is, however, not always explicitly applicable to our samples, as single aggregates commonly show different extinction characteristics in polarized light. Most ballen aggregates (67%) can be classified as type IV, as they show undulatory extinction of individual ballen (Figs. 2c–f and 4a,b). However, 20% of the quartz ballen aggregates show coarser domains of similar extinction, although individual ballen show undulatory extinction (Fig. 2d). About 32% show a "chert-like" extinction characteristic of type V (Fig. 2e), where individual ballen show on small-scale largely different extinction positions. However, ballen aggregates with "chert-like" extinction (type V) can in other parts show rather a heterogeneous type IV extinction (Figs. 2e and 5). Also, ballen aggregates occur that comprise quartz and cristobalite (Figs. 2f and 2g). The cristobalite part of the ballen aggregate would classify as type I with low birefringence; the part comprised by quartz would classify as type III, as it shows relatively homogenous extinction of individual ballen (Fig. 2f). We did not find a systematic difference in the occurrence of the various types within the samples, whether the ballen aggregates are in the center of a granitic gneiss clast, at the rim to the matrix, or within the matrix of the impact melt rock. Yet, in 2-D thin sections, the 3-D distributions of the ballen aggregates within the very heterogeneous impact melt rock are not apparent. To further characterize the ballen aggregates by their crystallographic orientation characteristics, we performed EBSD measurements.

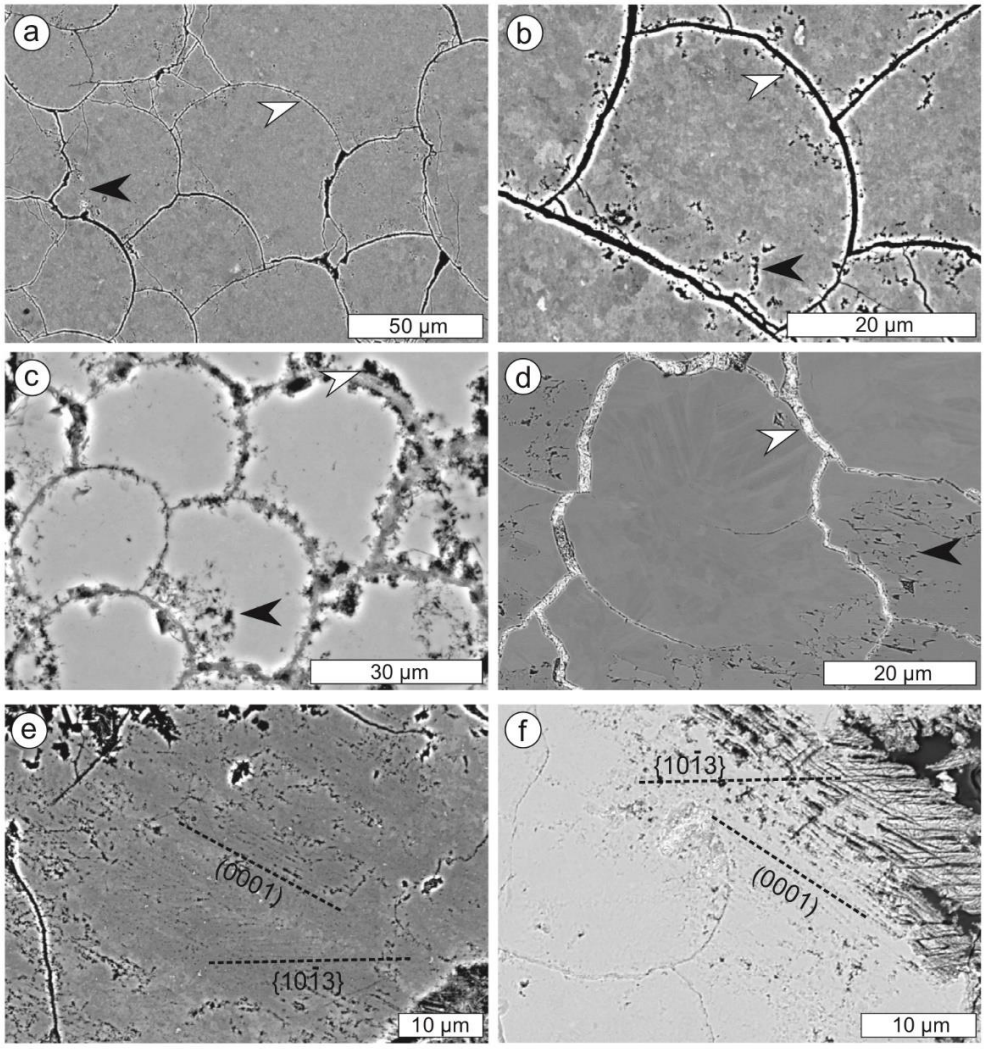

Fig. 4. BSE images of silica aggregates with ballen. a, b) Curved interfaces (white arrows) define the quartz ballen. Note porosity close to the fractures (black arrows) and mottled orientation contrast, sample CT915. c) Siliceous material rich in Fe, K, Al, and Mg decorate fractures (white arrows), sample CT917. d) Cristobalite with radial orientation contrast and siliceous material rich in Si, Fe, K, Al, and Mg along the curved fractures, sample CT917. e, f) Quartz with sets of planes following the basal and the {10-13} rhombohedral planes and ballen aggregate that retains its original shape from the host rock, sample CT917, compare Fig. 2b.

The EBSD measurements reveal that the individual quartz ballen are generally themselves polycrystalline (Figs. 5 and 6a, 6b), consistent with the presence of high-angle grain boundaries (misorientation angle >10°, red lines in Fig. 5c). Low-angle grain boundaries (misorientation angle <10°, yellow lines in Fig. 5c) are relatively rare (Figs. 5c and 6b). The quartz ballen aggregates that classify as types IV and V show a crystallographic preferred orientation (CPO) with one or two dominating orientations, as indicated by EBSD measurements (Figs. 5d, 5f, 5i and 6b, 6c), which is consistent with the optical appearance of similar extinction positions of larger domains (Fig. 2d). These domains are characterized by one marked maximum at low misorientation angles, yet one maximum at about 60° (Fig. 5i), which shows that they contain Dauphiné twin orientations, as also evident from the pole figures (Fig. 5f). Dauphiné twin orientations are characterized by a 60° misorientation angle and a rotation axis parallel to the quartz <c> axis, that is, they do not contribute to a difference in optical extinction. Apart from these dominant orientations characterized by a marked CPO, quartz occurs also in scattered orientations (Figs. 5e and 5g) with an almost random misorientation angle distribution (Fig. 5h).

In a ballen aggregate that comprises cristobalite and quartz (Figs. 2f, 2g and 7), the individual quartz ballen

Table 1. Classification of observed ballen aggregates.

Type according to Ferrière et al. (2009)	Mineral phase	Extinction characteristics in polarized light, crossed polarizers	Textural characteristics		Example shown in Fig.	% in Polsingen samples
			of aggregate	of ballen		
Type I	α-cristobalite	Low birefringence	Almost random	Polycrystalline	2f, 2g, 7	1
Type II	α-quartz	Homogeneous extinction of all ballen in aggregate	–	–	–	–
Type III	α-quartz	Heterogeneous extinction of aggregate but each ballen has relative homogeneous extinction	No CPO	Polycrystalline	2f, 2g, 7	1
Type IV	α-quartz	Heterogeneous extinction of individual ballen	CPO	Polycrystalline	2c, 2e	46
		Homogeneous extinction of domains, individual ballen show heterogeneous extinction			2d, 2f, 6, 9	20
Type V	α-quartz	Chert-like heterogeneous extinction, individual ballen are hardly detectable	CPO	Polycrystalline	2e, 5	32

show a relative homogeneous extinction compared to other observed ballen. EBSD measurements reveal random crystallographic orientations, that is, no CPO (Figs. 7a–c). The cristobalite ballen are polycrystalline with radiating elongate grains (Fig. 4d). The <c> axis orientations are largely scattering but preferentially radiating likewise and the <010> axis is clustered in a point maximum parallel to the normal to the thin section plane (Fig. 7d). The cristobalite found exclusively along the rim of the ballen aggregates (Figs. 2h and 6a, 6b) shows the same texture (compare Figs. 6d and 7d). The shape of the cristobalite grains is dendritic with the long axes of the dendrites radiating outward (Figs. 8a and 8b). The dendritic cristobalite rim shows a high porosity at the direct contact with the ballen aggregate, which is decreasing toward the outer boundary to the matrix (dark area in Figs. 8a and 8b). Barium and sulfur have been detected by EDS to be present at the cristobalite–quartz contact, suggesting the presence of barium sulfate (black arrow, Fig. 8a). More rarely, prismatic cristobalite can occur surrounding the ballen aggregates together with K-feldspar forming the contact with the polyphase matrix of the impact melt rock (Figs. 8c–f and 9c, 9d). Cristobalite in the ballen aggregates as well as cristobalite at the rim and in the matrix is generally enriched in Na_2O (0.4–0.7 wt%) and Al_2O_3 (1.4–1.7 wt%) summing up to about 2 wt%, as indicated from EDS measurements from five different ballen aggregates.

Coarse quartz grains in granitic gneisses of shock stage 0 (Fig. 9a) show typically abundant fluid inclusion trails. In contrast, the quartz ballen aggregates even with only incipient ballen and preserving the original grain shape systematically do not show fluid inclusion trails (Figs. 9b–d).

DISCUSSION

Transition of Quartz to Shock-Induced Amorphous Phase

Bischoff and Stöffler (1984) suggested that different extinction properties of ballen aggregates are characteristic for different shock pressure conditions. Ferrière et al. (2009), however, argued that different types of ballen do not indicate specific shock pressures, as they result from transformations from either shock-induced diaplectic glass or silica melt (lechatelierite). Our observations of different extinction characteristics in polarized light occurring on thin section scale and even within single ballen aggregates confirm that the different types of ballen cannot be taken to indicate specific shock pressures on sample scale. The stress–temperature conditions may vary locally on grain scale or below, given the different response of the polycrystalline and polyphase granitic gneisses to shock loading and unloading. The EBSD measurements show that the ballen types IV and V differentiated by Ferrière et al. (2009, 2010) are characterized by polycrystalline quartz with a varying amount of grains in random orientations relative to dominant orientations resulting in the observed CPO (Figs. 5 and 6). Only in aggregates comprised by both cristobalite and quartz, no CPO is observed (type I/III, Fig. 7). The dominant orientation is interpreted to be inherited from the original quartz grain in the granitic gneiss protolith, opposed to the random orientations, which are interpreted as "new" orientations.

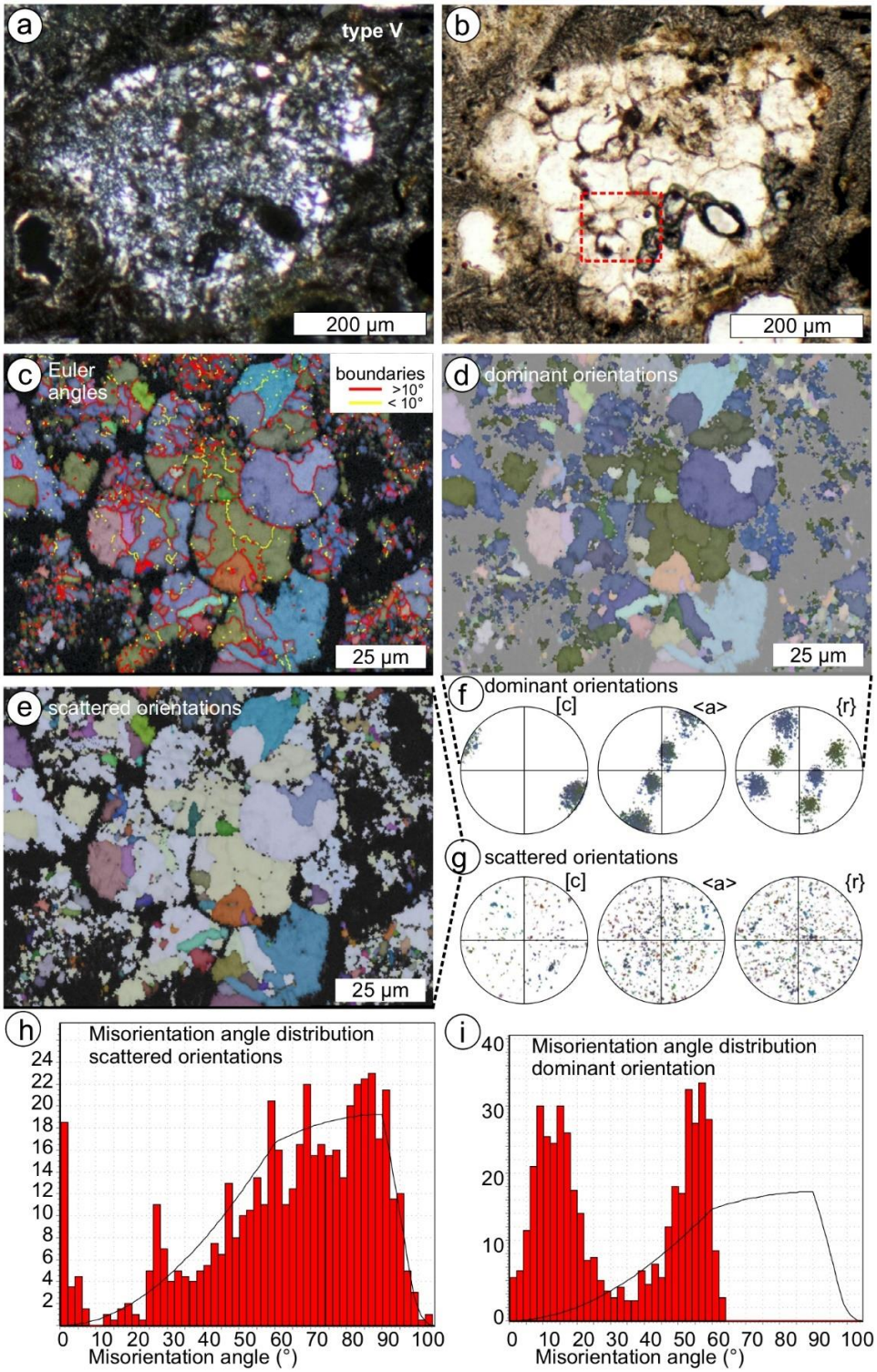

Fig. 5. EBSD data of ballen quartz with "chert-like" extinction (type V), sample CT917. a, b) Polarized light micrographs with and without crossed polarizers, respectively. The red box in (b) indicates the location of the EBSD map. c) Euler angle map overlain by band contrast with boundaries characterized by misorientation angles below (yellow) and above (red) 10°. d, e) Euler angle maps overlain by band contrast, where dominant crystallographic orientation and scattered orientations are highlighted, respectively. f, g) Pole figures of [c], <a>, and {r} axes in stereographic projections of the lower hemisphere, corresponding to the maps in (d) and (e), respectively. h, i) Misorientation angle histograms of scattered, and dominant orientations, corresponding to maps in (d) and (e), respectively.

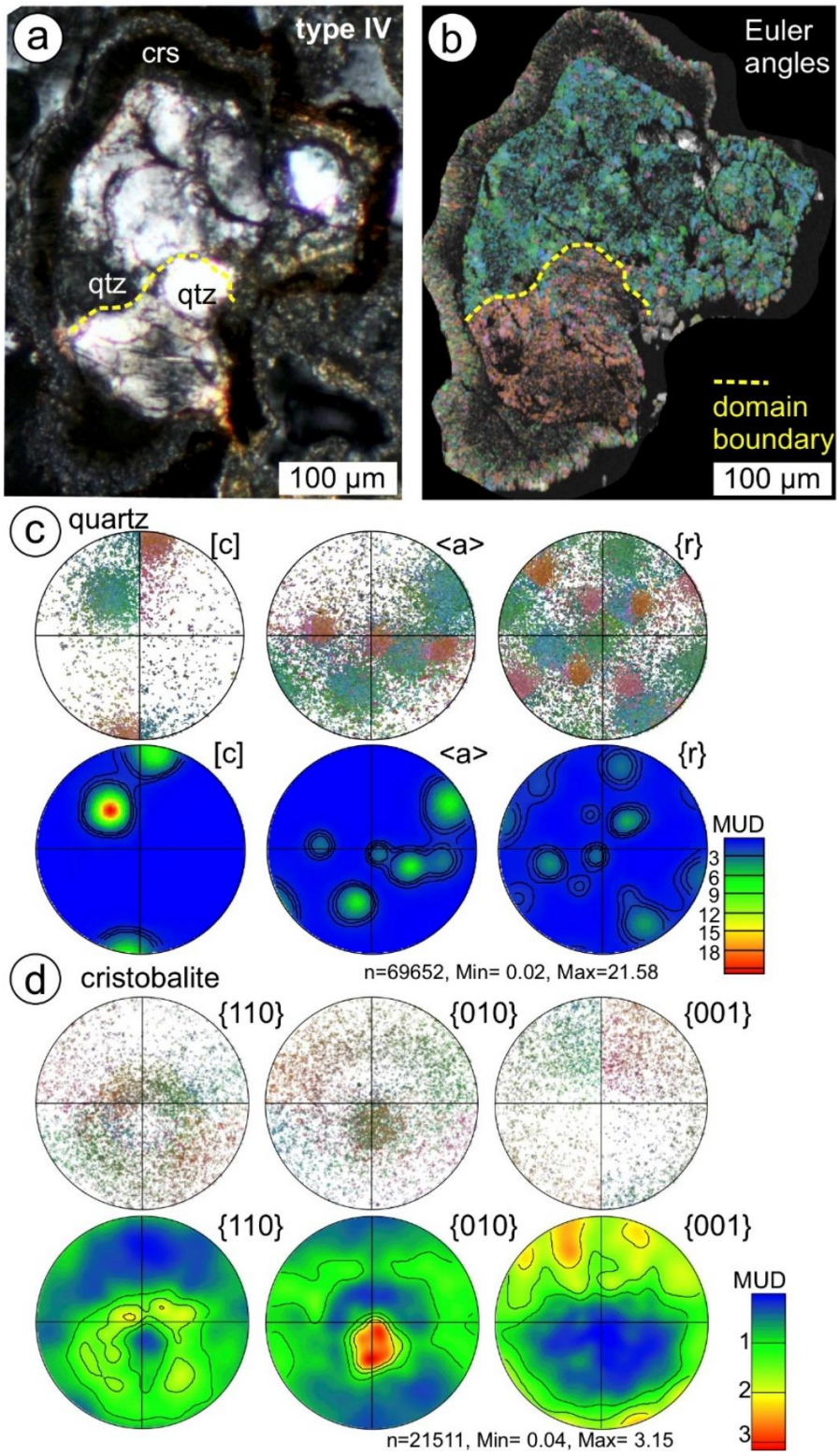

Fig. 6. EBSD data of ballen quartz showing different domains with homogeneous extinction, single ballen show heterogeneous extinction (type IV) and rim of cristobalite, sample CT915 (compare Figs. 2f, h and 7a, b). a, b) Polarized light micrograph (crossed polarizers) and Euler angle map overlain by band contrast, respectively. c) Pole figures of quartz [c], <a>, and {r} axes in stereographic projections of the lower hemisphere, corresponding to the maps in (b). d) Pole figures for cristobalite and density plots in stereographic projections of the lower hemisphere, corresponding to the maps in (b), respectively.

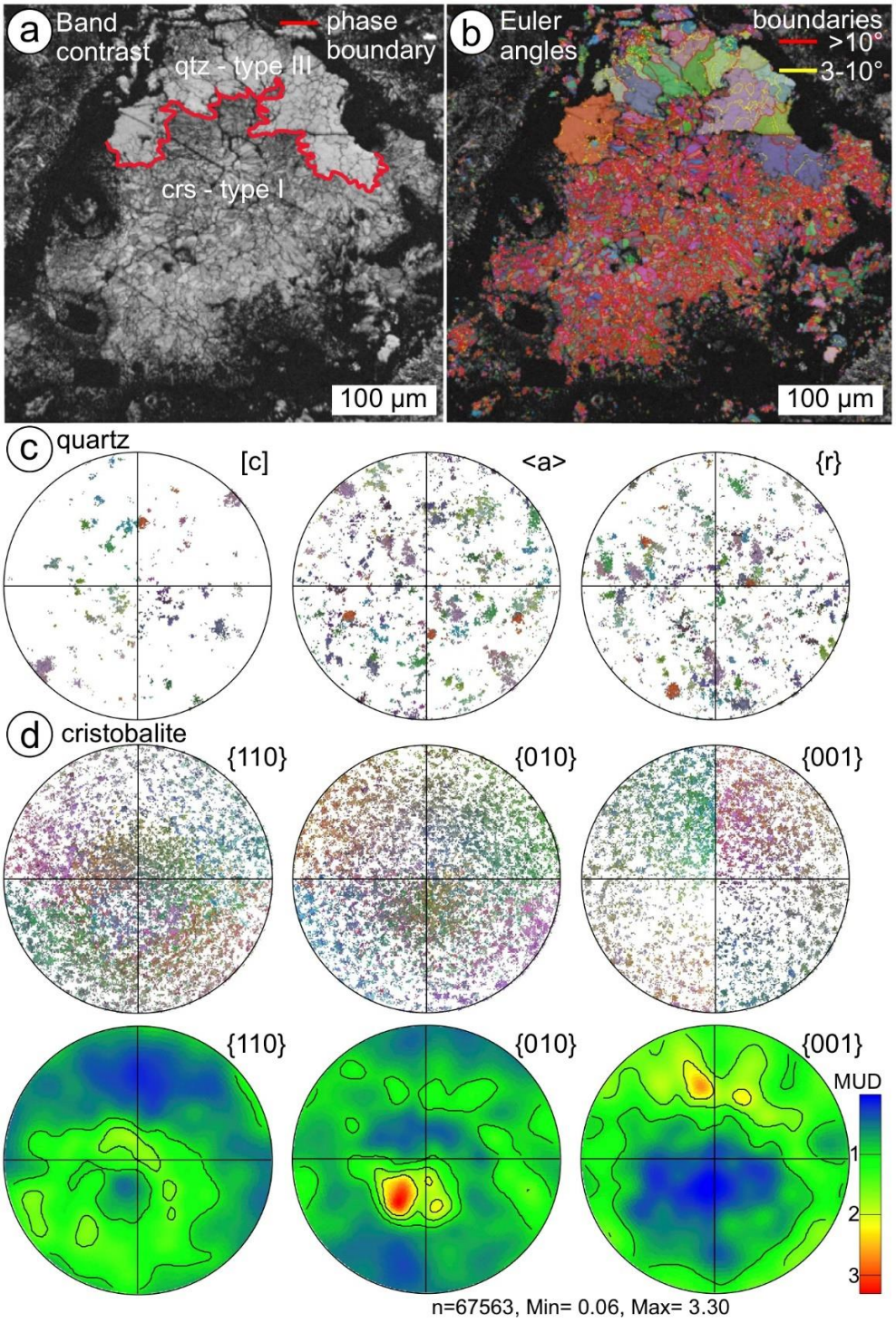

Fig. 7. EBSD data of quartz and cristobalite with ballen, sample CT917 (compare Figs. 2f, 2g). a, b) Band contrast maps with phase boundary between quartz and cristobalite (red line) and map color coded by Euler angles and grain boundaries, respectively. c) Pole figures of quartz [c], <a>, and {r} axes in stereographic projections of the lower hemisphere, corresponding to the maps in (b). d) Pole figures for cristobalite and density plots in stereographic projections of the lower hemisphere, corresponding to the maps in (b), respectively.

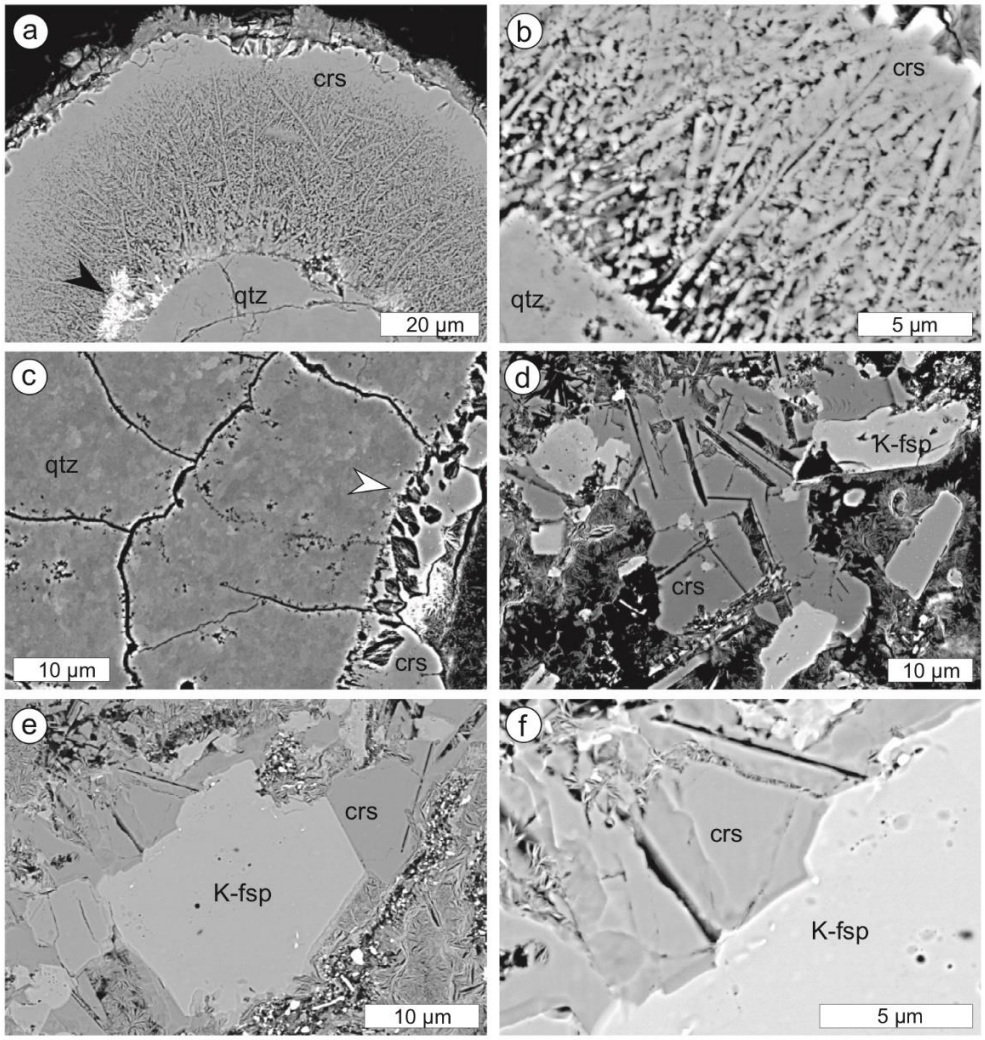

Fig. 8. BSE images of cristobalite microstructures at the rim of ballen aggregates. a, b) Dendritic structure of rim around quartz aggregate with ballen, sample CT915 (compare Fig. 2h and Fig. 6). c) Cristobalite grains at rim of quartz aggregated with ballen, sample CT915. d–f) Cristobalite grains next to K-feldspar at the rim of quartz with incipient ballen, sample CT917 (compare Fig. 2b, Figs. 9b–d). (Color figure can be viewed at wileyonlinelibrary.com.)

We take the observed CPO as a strong indication that the original quartz grains were transformed upon shock loading and rapid unloading into a heterogeneous amorphous phase with varying degree of distortion of the original crystallographic precursor structure. The interpretation, that a transformation from primary quartz from the target rock to a rapidly quenched/decompressed silica melt or diaplectic silica glass is the initial formation mechanism of ballen, is widely accepted (e.g., Carstens 1975; Ferrière et al. 2009, 2010; Buchner et al. 2010). Diaplectic glass is a dense amorphous phase formed during shock compression (e.g., Engelhardt et al. 1967; Hörz and Quaide 1973; Arndt et al. 1982; Kruger and Jeanloz 1990; Langenhorst 1994). Characteristic for diaplectic glass is a preserved short-range order of the precursor structure due to rapid decompression and cooling, such that the glass retains remnants of the original shape and crystal structure. Arndt et al. (1982) suggested that due to the short duration of the shock-induced transient high-temperature excursions, the crystal to melt transition does not come to completion, resulting in a diaplectic glass as disordered transitional state intermediate between the structures of the crystalline and quenched molten phase. As such, any difference between a diaplectic glass without transition to a melt on the one hand and a glass generated from rapidly quenched shock-induced melt on the other hand might not be sharp but rather be of a gradual nature. Diaplectic glass can be expected to be of heterogeneous structure, with variable degrees of the precursor structure

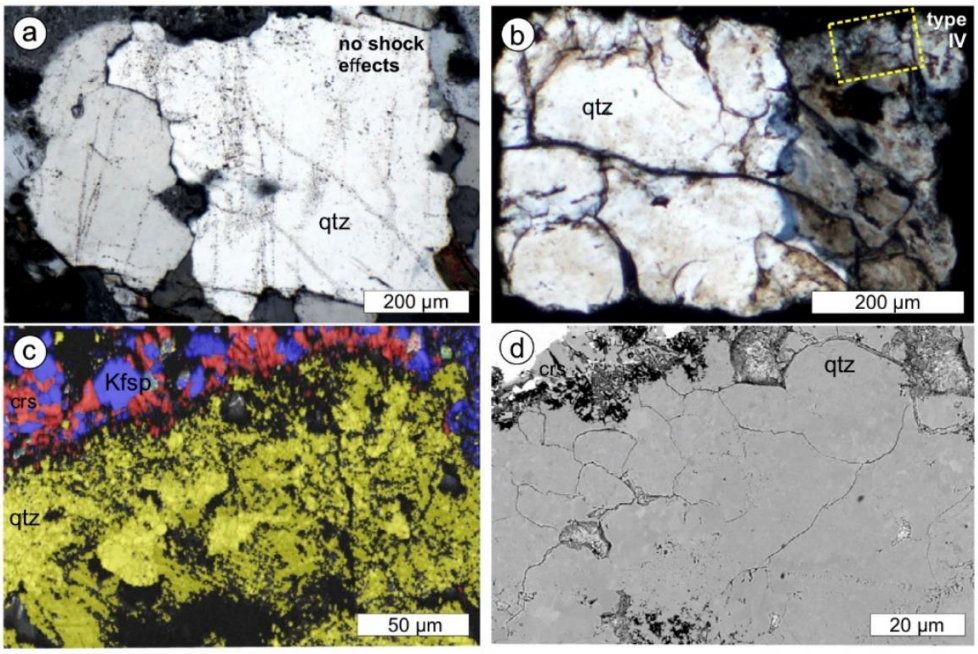

Fig. 9. a) Polarized light micrographs with crossed polarizers showing quartz grain with typical abundant fluid inclusion trails from granitic gneisses, shock stage 0, sample CT830 (Maihingen). b) Polarized light micrographs with crossed polarizers showing polycrystalline quartz aggregate with incipient ballen (type IV), with the shape of the original single crystal preserved sample CT917 (compare Fig. 2b). Yellow rectangle shows location of EBSD map in (c) and BSE image in (d). c) EBSD phase map showing polycrystalline quartz with ballen (yellow), K-feldspar (blue), and cristobalite (red) at the rim. d) BSE image of the same area shown in (c).

being present. Whereas quartz crystallizing from diaplectic silica is found to rather form polycrystalline aggregates (e.g., Rehfeldt-Oskierski et al. 1986; Trepmann 2008), feldspar is typically back-transforming as single crystal with only minor misorientations (e.g., Arndt et al. 1982).

The textural characteristics of the quartz ballen aggregates with CPO together with various amounts of new random orientations (Figs. 5 and 6a–c) are consistent with crystallization of quartz from a diaplectic glass and/or from a rapidly quenched highly viscous, supercooled silica melt, that is, a heterogeneous disordered quenched transition state intermediate between the structure of the crystalline and quenched molten phase. Topotactic crystallization of the diaplectic glass with preserved short range order of the precursor structure leads to the dominating orientation of quartz, whereas crystallization from the more strongly disordered amorphous phase leads to crystallization of quartz with random orientation.

The observed shape of the aggregates is irregular ranging from rectangular (Fig. 2b) to a droplet shape (Fig. 2c), indicating variable degrees of modification from the precursor quartz grain. Independent of their shape, most observed ballen aggregates show a CPO (Table 1). Even in the case of the mixed quartz and cristobalite ballen, the shape of the aggregate is rather rectangular (Figs. 2f and 2g). Given the textural and structural characteristics, we suggest that the ballen aggregates are derived from coarse quartz grains of the granitic gneiss protolith that were transformed to an amorphous silica phase with various amounts of information on the precursor structure upon shock loading and rapid unloading.

Role of Multiple Phase Transformations

To explain the specific microstructure of ballen and the related occurrence of cristobalite, further multiple transformations mostly from cristobalite to quartz have been suggested (e.g., Engelhardt 1972; Carstens 1975; Ferrière et al. 2009, 2010; Buchner et al. 2010). Ferrière et al. (2010) came to the conclusion that α-quartz ballen are the result of back-transformation from either α-cristobalite or β-quartz with time. For our samples, a phase transformation from β-quartz originally crystallized from the shock-induced amorphous phase to α-quartz might be indeed suggested by the occurrence of Dauphiné twin orientations (Fig. 5), as reported, for example, also for shocked quartz from the Charlevoix structure (Trepmann and Spray 2005). Yet, the displacive α-quartz to β-quartz phase transition cannot explain the globular shape of the ballen. Ferrière et al.

(2009) discussed that the volume change from cristobalite to quartz is responsible for the different types of ballen silica (types II, III, IV, V). Yet, as also cristobalite ballen occur, the cristobalite to quartz phase transition cannot be a prerequisite for the globular shape. Furthermore, our observations do not provide any evidence for a cristobalite to quartz transition. In contrast, the commonly observed CPO interpreted as inherited from the precursor quartz suggests direct crystallization of quartz (either α- or β-quartz) from a diaplectic glass. The phase transition from the topology of the cristobalite structure (tetragonal α- or cubic β-cristobalite) to the topology of the quartz structure (hexagonal β- or trigonal α-quartz) would require the complete restructuring of the tetrahedral network, which is incompatible with the observed CPO for symmetry reasons. Likewise, the rarely observed sets of planar features parallel to crystallographic planes in ballen quartz (Figs. 4e and 4f) would be difficult to explain by multiple phase transformations (from quartz to an amorphous phase to cristobalite and back to quartz), as already discussed by other authors (e.g., Buchner et al. 2010; Chanou et al. 2015).

Formation of Ballen Shape—Dehydration of Amorphous Phase

The ballen resembles perlitic structures, that is, globular microstructures, known from cristobalite in silica-rich andesitic to rhyolitic volcanic rocks and hydrated glass (obsidian, e.g., Swanson et al. 1989; Horwell et al. 2013). On the basis of experimental evidence, Marakushev et al. (1988) interpreted perlitic structures to form due to the solidification of hydrous silica-rich melts with hindered dehydration. Due to the separation of the water phase during decompression and cooling, strain concentrations cause peeling and radial cracks in the crystallizing glass (Marakushev et al. 1988). In andesitic–rhyolitic volcanic rocks, cristobalite commonly occurs in pores and fractures as a precipitate from a vapor phase or by devitrification from an amorphous volcanic glass. K-feldspar can be associated within spherulites in devitrified obsidian domes and rhyolitic lavas (e.g., Swanson et al. 1989; Horwell et al. 2013). The cristobalite stability field ranges between 1470 and 1713 °C at <1 GPa, but cristobalite can exist as a metastable phase due to the required activation energy for the reconstructive transformation of cristobalite to low quartz. Cristobalite can grow in dendritic to spherulitic deposits on a cold (200–700 °C) quartz substratum from hydrothermal fluids at high temperature gradients (100–600 °C) as demonstrated in the experiments by Flörke et al. (1990).

We suggest the following: The original quartz crystals from granitic gneisses in the Ries contain abundant fluid inclusions (Fig. 9a). Upon shock loading, the fluid inclusion-rich quartz grains transformed into an amorphous silica phase, in which the volatiles dissolved. During decompression and cooling, the amorphous silica phase dehydrates and a water-rich fluid is generated, which results in strain concentrations causing radial "dehydration cracks," comparable to the perlitic structure in volcanic rocks (Marakushev et al. 1988). Such dehydration is consistent with the common observation of an increased porosity close to the curved interface between the ballen (black arrow in Fig. 4b). The water-rich fluid is expelled along the curved dehydration cracks. Water contents in fluid inclusion-rich quartz in granitoid rocks is typically on the order of 7000–14,000H/10^6 Si (approximately 0.1–0.2 wt% H_2O; Kronenberg and Wolf 1990; Kilian et al. 2016). This water content is close to what is required for the formation of perlitic structures in obsidians (H_2O contents 0.1–4.8 wt%; Marakushev et al. 1988).

Dendritic cristobalite is exclusively observed at the outer rim of the ballen aggregates in contact with vesicles (Figs. 2h, 5a, 5b, 6a). Its occurrence is therefore interpreted to be related to the ballen formation. Cristobalite probably crystallized directly from the volatile-rich melt that was expelled from the amorphous silica phase, possibly involving degassing to form the vesicles, as also suggested for volcanic perlites (e.g., Horwell et al. 2013). If associated with K-feldspar, some prismatic cristobalite can surround the ballen aggregates. These fine-grained polyphase aggregates are likewise interpreted to have crystallized directly from a silica-rich melt (Figs. 8d–f and 9c, 9d).

Cristobalite occurring as radiating elongate crystals within the ballen aggregates together with quartz without CPO (Fig. 7) is suggested to have crystallized from a rapidly quenched highly viscous, supercooled silica amorphous phase with no memory of the precursor phase, as opposed to quartz ballen with CPO. In this sense, the specific microstructures are suggested to reflect a different degree of disordering of the shock-induced amorphous phase from which they formed. (1) Ballen quartz with sets of planar features parallel to crystallographic planes of the precursory quartz grain is indicative of a shocked SiO_2 material, which still retains significant crystalline order; (2) ballen quartz with CPO crystallized from amorphous silica with remnants of crystalline long-range order to dominate nucleation; (3) ballen quartz with random texture crystallized from an amorphous silica, where the long-range order of quartz was totally destroyed; and (4) cristobalite occurs if the quartz-like short-range order is completely lost and/or if contamination of the silica by components like

Na^+ and Al^{3+} has occurred. These different microstructures are interpreted to reflect locally heterogeneous stress–temperature conditions on grain scale or below, due to the different response of the polycrystalline and polyphase granitic gneisses to shock loading and unloading (i.e., differences in crystallographic orientation, structure, phase, shape, fluid content, etc.).

We would like to point out that planar deformation features in quartz are known as shock compression-induced incomplete transformation into diaplectic silica glass localized along crystallographic planes (e.g., Goltrant et al. 1992a, 1992b; Langenhorst 1994). The commonly observed fluid inclusions present along annealed planar deformation features in shocked quartz (e.g., Goltrant et al. 1992a, 1992b; Leroux and Doukhan 1996; Trepmann and Spray 2006; Trepmann 2008) would be consistent with our interpretation of the dissolution of volatiles initially present in fluid inclusions from the precursory quartz grains into diaplectic glass upon shock loading and dissolving of the fluid upon decompression and cooling. Upon shock compression, the water in the crystal segregates locally along specific crystallographically controlled planes and dissolves into the generated diaplectic glass. Upon decompression and cooling, water is expelled again as fluid inclusions that are observable along annealed PDFs.

CONCLUSIONS

Based on our observations on Ries impact melt rocks, we come to the following conclusions:

1. The observed ballen aggregates are derived from coarse original quartz grains from the granitic gneiss protolith. Upon shock loading, quartz is transformed to a diaplectic glass and/or a highly viscous, supercooled silica melt.
2. Topotactic crystallization of the diaplectic glass with preserved short range order of the precursor structure leads to dominant crystallographic orientations, whereas crystallization from the more strongly disordered amorphous phase leads to crystallization of quartz with random orientation.
3. Cristobalite within ballen aggregates crystallized from a shock-induced amorphous phase with no memory of the precursor phase remaining.
4. From the microstructural and textural observations in our samples, there is no indication for a phase transformation from cristobalite to quartz.
5. We suggest that the globular shape of ballen in our samples is due to dehydration and associated cracking during rapid decompression and cooling of the amorphous phase, similar to perlitic structures in volcanic rocks.
6. Cristobalite, quartz with random texture, quartz with CPO, and quartz with remnants of crystallographically controlled planar features present in ballen aggregates are interpreted to represent a decreasing degree of disordering of the amorphous phase originating from shock compression of the precursor quartz grains.
7. In contrast, dendritic cristobalite occurring at the rim of quartz ballen aggregates in contact with vesicles crystallized directly from a melt enriched in fluids that were expelled from the dehydrating glass and/or melt.

Acknowledgments—The thoughtful and constructive reviews of Fred Hörz and Ludovic Ferrière as well as the editorial handling by Christian Koeberl are greatly appreciated. We gratefully acknowledge funding from the *Staatliche naturwissenschaftliche Sammlungen Bayerns* (SNSB-Innovativ). Namvar Jahanmehr and Corrina Franke are acknowledged for thin section preparation and assistance with polarized light microscopy, respectively. Open access funding enabled and organized by Projekt DEAL.

Editorial Handling—Dr. Christian Koeberl

REFERENCES

Arndt J., Hummel W., and Gonzalez-Cabeza I. 1982. Diaplectic labradorite glass from the Manicouagan impact crater—I. Physical properties, crystallization, structural and genetic implications. *Physics and Chemistry of Minerals* 8:230–239.

Bischoff A. and Stöffler D. 1984. Chemical and structural changes induced by thermal annealing of shocked feldspar inclusions in impact melt rocks from Lappajärvi crater, Finland. *Journal of Geophysical Research* 89:B645–B656.

Boyer H., Smith D. C., Chopin C., and Lasnier B. 1985. Raman microprobe (RMP) determinations of natural and synthetic coesite. *Physics and Chemistry of Minerals* 12:45–48.

Buchner E., Schwarz W. H., Schmieder M., and Trieloff M. 2010. Establishing a 14.6 ± 0.2 Ma age for the Nördlinger Ries impact (Germany)—A prime example for concordant isotopic ages from various dating materials. *Meteoritics & Planetary Science* 45:662–674.

Carstens H. 1975. Thermal history of impact melt rocks in the Fennoscandian shield. *Contributions to Mineralogy and Petrology* 50:145–155.

Chanou A., Grieve R. A. F., and Osinski G. R. 2015. Formation of ballen in silica by thermal shock (abstract). In *Bridging the gap III Conference*, University of Freiburg, Conference, organized by Kenkmann T., Poelchau M.H., Deutsch A. University of Freiburg, Freiburg. Germany. pp. 12–13.

Chen M., Xiao W., and Xie X. 2010. Coesite and quartz characteristic of crystallization from shock-produced silica melt in the Xiuyan crater. *Earth and Planetary Science Letters* 297:306–314.

Engelhardt W. von. 1972. Shock produced rock glasses from the Ries crater. *Contributions to Mineralogy and Petrology* 36:265–292.

Engelhardt W. von, and Graup G. 1984. Suevite of the Ries crater, Germany: Source rocks and implications for cratering mechanics. *Geologische Rundschau* 73:447–481.

Engelhardt W. von. 1997. Suevite breccia of the Ries impact crater, Germany: Petrography, chemistry and shock metamorphism of crystalline rock clasts. *Meteoritics & Planetary Science* 32:545–554.

Engelhardt W. von. Arndt J., Stöffler D., Müller W. F., Jeziorkowski H., and Gubser R. A. 1967. Diaplektische Gläser in den Breccien des Ries von Nördlingen als Anzeichen für Stoßwellenmetamorphose. *Contributions to Mineralogy and Petrology* 15:93–102.

Ferrière L., Koeberl C., Reimold W. U., Libowitzky E., and Greshake A. 2008. Ballen quartz and cristobalite in impact breccias: Types, occurrence, and possible origin (abstract #3011). Large Meteorite Impacts and Planetary Evolution IV. Vredefort Dome, South Africa. pp. 3–4.

Ferrière L., Koeberl C., and Reimold W. U. 2009. Characterisation of ballen quartz and cristobalite in impact breccias: New observations and constraints on ballen formation. *European Journal of Mineralogy* 21:203–217.

Ferrière L., Koeberl C., Libowitzky E., Reimold W. U., Greshake A., and Brandstätter F. 2010. Ballen quartz and cristobalite in impactites: New investigations. In *Large meteorite impacts and planetary evolution IV*, edited by Gibson R. L. and Reimold W. U. *Geological Society of America Special Paper* 465:609–618.

Flörke O., Graetsch H., and Jones J. 1990. Hydrothermal deposition of cristobalite. *Neues Jahrbuch für Mineralogie Monatshefte*. 2:81–95.

French B. M. 1998. *Traces of catastrophe: A handbook of shock-metamorphic effects in terrestrial meteorite impact structures*. Houston, Texas: Lunar and Planetary Institute. 120 p.

Goltrant O., Leroux H., Doukhan J. C., and Cordier P. 1992a. Formation mechanisms of planar deformation features in naturally shocked quartz. *Physics of the Earth and Planetary Interiors* 74:219–240.

Goltrant O., Doukhan J.-C, Cordier P., and Courtillot V. 1992b. An investigation by transmission electron microscopy of planar deformation features in naturally shocked quartz. *Terra Nova* 4:405–412.

Horwell C. J., Williamson B. J., Llewellin E. W., Damby D. E., and Le Blond J. S. 2013. The nature and formation of cristobalite at the Soufrière Hills volcano, Montserrat: Implications for the petrology and stability of silicic lava domes. *Bulletin of Volcanology* 75:1–19.

Hörz F. and Quaide W. L. 1973. Debye-Scherrer investigations of experimentally shocked silicates. *The Moon* 6:45–82.

Kilian R., Heilbronner R., Holyoke C.W.I., Kronenberg A. K., and Stunitz H. 2016. Dislocation creep of dry quartz. *Journal of Geophysical Research: Solid Earth* 121:3278–3299.

Kronenberg A. and Wolf G. 1990. Fourier transform infrared spectroscopy determinations of intragranular water content in quartz-bearing rocks: Implications for hydrolytic weakening in the laboratory and within the Earth. *Tectonophysics* 172(3–4):255–271.

Kruger M. B. and Jeanloz R. 1990. Memory glass: An amorphous material formed from $AlPO_4$. *Science* 249:647–649.

Langenhorst F. 1994. Shock experiments on pre-heated α- & β-quartz: II. X-ray and TEM investigations. *Earth and Planetary Science Letters* 128:683–698.

Leroux H. and Doukhan J.-C. 1996. A transmission electron microscope study of shocked quartz from the Manson impact structure. In *The Manson impact structure, Iowa: Anatomy of an impact crater*, edited by Koeberl C. and Anderson R. R. *Geological Society of America Special Paper* 302:267–274.

Marakushev A. A., Persikov E. S., and Bukhtiarov P. G. 1988. Endogenic nature of perlites. In *2nd International Conference on Natural Glasses*, edited by Konta J. Prague, Czech Republic: Charles University. pp. 89–96.

Osinski G. R. 2004. Impact melt rocks from the Ries structure, Germany: An origin as impact melt flows? *Earth and Planetary Science Letters* 226:529–543.

Rehfeldt-Oskierski A., Stöffler D., and Hornemann U. 1986. Deformation, transformation, and thermal annealing of experimentally shocked single crystal quartz (abstract). 17th Lunar and Planetary Science Conference. pp. 697–698.

Schmieder M., Jourdan F., Tohver E., and Cloutis E. A. 2014. $^{40}Ar/^{39}Ar$ age of the Lake Saint Martin impact structure (Canada)—Unchaining the Late Triassic terrestrial impact craters. *Earth and Planetary Science Letters* 406:37–48.

Short N. M. 1970. Progressive shock metamorphism of quartzite ejecta from the Sedan nuclear explosion crater. *The Journal of Geology* 78:705–732.

Stähle V., Altherr R., Koch M., and Nasdala L. 2008. Shock-induced growth and metastability of stishovite and coesite in lithic clasts from suevite of the Ries impact crater (Germany). *Contributions to Mineralogy and Petrology* 155:457–472.

Stöffler D., Artemieva N. A., Wünnemann K., Reimold W. U., Jacob J., Hansen B. K., and Summerson I. A. T. 2013. Ries crater and suevite revisited—Observations and modeling Part I: Observations. *Meteoritics & Planetary Science* 48:515–589.

Stöffler D., Hamann C., and Metzler K. 2018. Shock metamorphism of planetary silicate rocks and sediments proposal for an updated classification system. *Meteoritics & Planetary Science* 53:5–49.

Swanson S. E., Naney M. T., Westrich H. R., and Eichelberger J. C. 1989. Crystallization history of Obsidian Dome, Inyo Domes, California. *Bulletin of Volcanology* 51:161–176.

Trepmann C. A. 2008. Shock effects in quartz: Compression versus shear deformation—An example from the Rochechouart impact structure, France. *Earth and Planetary Science Letters* 267:322–332.

Trepmann C. A. and Spray J. G. 2005. Planar microstructures and Dauphiné twins in shocked quartz from the Charlevoix impact structure, Canada. In *Large meteorite impacts III*, edited by Kenkmann T., Hörz F., and Deutsch A. *Geological Society of America Special Paper*, 384, 315–328.

Trepmann C. A. and Spray J. G. 2006. Shock-induced crystal-plastic deformation and post-shock annealing of quartz: Microstructural evidence from crystalline target rocks of the Charlevoix impact structure, Canada. *European Journal of Mineralogy* 18:161–173.

Whitehead J., Grieve R. A. F., and Spray J. G. 2002. Mineralogy and petrology of melt rocks from the Popigai impact structure, Siberia. *Meteoritics & Planetary Science* 37:623–647.

6 Summary, conclusion, and outlook

6.1 Ilmenite and magnetite, as well as associated Fe/Ti-phases within impactites

6.1.1 Low shock conditions (P<16 GPa)

Within shocked Archean gneisses from the Vredefort impact structure northwest of the impact structure's center (*Chap. 2:* Fig. 1), coarse feldspar (60-75%), quartz (20-40%), phyllosilicates (i.e., biotite and chlorite; ≈5%), and Fe/Ti-bearing phases [i.e., ilmenite, magnetite, pyrite (FeS_2), and chalcopyrite ($CuFeS_2$); 1-5%] occur (*Chap*. *2:* Fig. 2). Quartz contains PFs and FFs, which can be partially recrystallized (*Chap. 2:* Figs. 2c, e, 3). Abundant shear fractures, especially along the central fracture of FFs, indicate shearing (*Chap. 2:* Figs. 2c, e, f, 8g). No (annealed) PDFs could be observed. Based on the quartz shock effects, shock stages F-S2 to F-S3 can be attributed (Stöffler et al. 2018), representing shock stages between 0 and Ia according to the IUGS system (Stöffler and Grieve 2007). In addition to the results on Fe-Ti-oxide microfabrics discussed in Chapter 6.1.2, the Archean gneisses experienced shock conditions of less than 16 GPa as reported from similar positions in the Vredefort impact structure (e.g., Grieve et al. 1990; Reimold and Gibson 2005). These relatively low shock conditions imply shock-related shear deformation, which explains the abundance of shear fractures.

Ilmenite and magnetite occur as coarse grains (*Chap. 2:* Figs. 2b, f, 5a, c). However, coarse ilmenite grains can include tens of µm wide layers of single-grained magnetite, which resembles a sandwich structure (*Chap. 2:* Fig. 5a, c; e.g., Haggerty 1991). Furthermore, spheroidal and fine-lamellar magnetite exsolutions of a few µm are often present (*Chap. 2:* Figs. 5a, b, 7a, b, 10c, d). Ilmenite and magnetite, as well as pyrite and chalcopyrite, can occur along shock-induced PFs as decorations within quartz and fractured feldspar grains (*Chap. 2:* Figs. 2c, d, 5, 6a, 8f, 9b). Those veins emanate from adjacent Fe-bearing phases and are µm to tens of µm wide and become narrower with distance from their source (*Chap. 2:* Fig. 5c). Within the PFs of quartz, magnetite and ilmenite generally display a remarkably homogeneous crystallographic orientation within single fractures. However, no crystallographic control by the quartz host could be observed (*Chap. 2:* Figs. 6, 8, 9). Instead, the crystallographic orientation is likely controlled by the source Fe-oxide grain from which the veins emanate (*Chap. 2:* Fig. 6). Shock-related deformation and non-isostatic stresses presumably led to shear heating of the shear fractured silicates and Fe-phases (*Chap. 2:* Figs. 2c, e, f, 8a). As a result, ilmenite and magnetite mobilization into adjacent quartz and feldspar shear fractures took place (*Chap. 2:* Figs. 2c, d, 5, 6a, 8f, 9b). Shear heating can partially or entirely melt ilmenite and magnetite depending on the eutectic temperature as a function of the composition. Frictional melting is controlled by the fracture toughness and the melting point of the respective phase (Spray 1992, 2010). Therefore, a hierarchy in response to grain size reduction and frictional melting can be interpreted (Spray 2010). Quartz (Broz et al. 2006; Spray 2010; Deer et al. 2013), magnetite (Samsonov 1982; Tromans and Meech 2002), ilmenite (Eriksson and Pelton 1993), feldspar (Rankin 1915; Morey and Bowen 1922; Shimada 1969; Tromans and Meech 2002; Broz et al. 2006; Whitney et al. 2007; Spray 2010), pyrite (Arnold 1971; Tromans and Meech 2002), and chalcopyrite (Živković et al. 1996) display decreasing values of fracture toughness and/or melting/breakdown temperatures (*Chap. 2:* Fig. 12), which leads to an increasing tendency of the respective phase to fracture and melt/breakdown (Spray 2010). Magnetite has a higher fracture toughness and melting point than ilmenite and mainly displays brittle fracturing. In contrast, ilmenite has smoothly curved grain boundaries within shear fractures of silicate phases and occurs more frequently (*Chap. 2:* Figs. 5, 6a, 8a, f). Moreover, fine-grained feldspar additionally occurs within up to 500 µm wide and transgranular shear zones within the Archean

gneisses (*Chap. 2:* Fig. 4), which can be attributed to its relatively low fracture toughness and melting point (*Chap. 2:* Fig. 12). The described microfabrics, thus, seem to correlate with the mechanical properties of the respective phases and might explain the occurrence of ilmenite and magnetite veins within quartz PFs (*Chap. 2:* Fig. 12; Spray 2010).

Lamellar ilmenite twins occur parallel (0001), $\{10\bar{1}1\}$, and $\{\bar{1}012\}$ (*Chap. 2:* Figs. 6, 8). The latter is common in ilmenite, can be generated due to tectonic deformation (Minkin and Chao 1971; Frick 1973; Reynolds 1984), and displays irregular grain boundaries (*Chap. 2:* Fig. 6), indicating modifications by twin boundary migration. They are, therefore, interpreted as pre-shock deformation structures. The fine-lamellar $\{10\bar{1}1\}$ twins, however, show very straight boundaries and offset and thus postdate the $\{\bar{1}012\}$ twins (*Chap. 2:* Fig. 6). Locally, they can be wedge-shaped, indicating mechanical twinning, which is a crystal-plastic and fast deformation mechanism involving dislocation glide at non-isostatic stresses without diffusion and thus not a function of temperature. At a site of high strain, indicated by high internal misorientation angles, a (0001) twin was observed in combination with shear fractures within adjacent quartz and feldspar, which are decorated by ilmenite (*Chap. 2:* Fig. 8). Based on the observations and ilmenite shock experiments, which resulted in the formation of those $\{10\bar{1}1\}$ and (0001 twins (Minkin and Chao 1971; Sclar et al. 1973; Syono et al. 1981), the observed twinning along $\{10\bar{1}1\}$ and (0001) is interpreted as a result of high strain rate deformation at non-isostatic stress conditions related to impact cratering.

Within coarse twinned ilmenite grains, lamellar (≈1 µm x 5 µm) and spheroidal (≈10 µm) exsolutions of magnetite were identified (*Chap. 2:* Fig. 7a, b). Contrary to twinning, diffusion drives exsolution mechanisms. Magnetite exsolutions in ilmenite are reported to form during sub-solidus re-equilibration from slow cooling (Buddington and Lindsley 1964; Tan et al. 2016) and as a result of meteorite shock events (Sclar et al. 1973). Exsolution temperatures must have exceeded the miscibility gap of ilmenite-hematite at 600-700°C. Otherwise, the exsolution of hematite would be expected (Lindsley 1991; Harrison et al. 2000). Spheroidal magnetite occurs mostly along grain boundaries and the $\{10\bar{1}1\}$ twins, which represent sites of increased disorder that facilitate diffusion, indicating heterogeneous nucleation (*Chap. 2:* Figs. 6a, 7a). Whereas the spheroidal magnetite exsolutions display neither shape nor crystallographic preferred orientation (CPO) with respect to the ilmenite host (*Chap. 2:* Fig. 7a, c, e), the lamellar magnetite exsolutions show an epitactic relationship. They occur shape-controlled and parallel $\{10\bar{1}1\}$ planes and their {110} planes are oriented parallel $\{10\bar{1}0\}$ of the ilmenite host (*Chap. 2:* Fig. 7b, d, e). Lamellar magnetite and fine-lamellar $\{10\bar{1}1\}$ twins crosscut and offset the twins parallel $\{\bar{1}012\}$ and, therefore, postdate them (*Chap. 2:* Figs. 6a, 7a). Therefore, the lamellar magnetite exsolutions likely formed during cooling after impact.

6.1.2 Moderate shock conditions (P>16 GPa)

Two suevites from Zipplingen and the Aumühle quarry within the Ries impact structure, which contain ilmenite aggregates with foam structure, were investigated and compared. The sample from Zipplingen consists primarily (≈85%) of devitrified glass with embedded coarse Fe-Ti-oxide aggregates as well as calcite (≈15%) (*Chap. 3:* Fig. 1a, b). Based on the presence of devitrified glass, shock stages F-S6 to F-S7 can be attributed (Stöffler et al. 2018), representing shock stages between III and IV according to the IUGS system (Stöffler and Grieve 2007) corresponding to 45-60 GPa. The sample from the Aumühle quarry is a gneiss clast, which microscopically displays a cryptocrystalline matrix with embedded coarse Fe-Ti-oxides and <10% vesicles (*Chap. 3:* Fig. 1c, d). All silicate phases were amorphized as a result of the meteorite impact. Therefore, shock stage F-S5 (Stöffler et al. 2018) or II

according to the IUGS system (Stöffler and Grieve 2007) can be attributed, representing shock pressures of 35-45 GPa. The lower limit of 16 GPa will be discussed in this chapter.

The 100 µm-sized ilmenite aggregates (*Chap. 3:* Fig. 1a, c) consist of isometric grains up to 15 µm in size with smoothly curved grain boundaries and 120° angles at triple junctions (*Chap. 3:* Figs. 3a-d, 5a, 6a, 9a, b). Locally, a rim of smaller ilmenite grains surrounds a coarse ilmenite core, which displays internal misorientations (*Chap. 3:* Fig. 4c) and lamellae with common $\{11\bar{2}0\}$ planes with respect to the host. Furthermore, the twin *c*-axis is oriented at an angle of 109° to that of the host (*Chap. 3:* Fig. 5a, c, e). The twin domain can be defined by a misorientation angle of ≈75° around a misorientation axis parallel to $[\bar{2}110]$ (*Chap. 3:* Fig. 5a, c, e). The same crystallographic orientation relationship is displayed by ilmenite with foam structure with up to three orientation domains, which display *c*-axes at angles of 109° and 99° and share one common $\{11\bar{2}0\}$ plane for each pair of domains, respectively (*Chap. 3:* Figs. 5b, d, e, 6). High-pressure experiments revealed that ilmenite transforms into the high-pressure polymorph liuite at shock pressures >16 GPa, which has an orthorhombic perovskite structure and belongs to the Pnma space group (Liu 1975; Leinenweber et al. 1994; Ma and Tschauner 2018). Subsequent unloading leads to a retrograde formation of the polymorph wangdaodeite with a lithium niobate structure (Mehta et al. 1994), which belongs to the R3c space group (Abrahams et al. 1966; Weis and Gaylord 1985). The shocked ilmenites investigated from the Ries impact structure likely experienced the same high-pressure excursion (*Chap. 3:* Fig. 10a). Wangdaodite was identified within a shocked gneiss clast from the same outcrop (i.e., Zipplingen, Tschauner et al. 2020). Together with the space group $R\bar{3}$ of ilmenite (Barth and Posnjak 1934), the space groups of the high-pressure polymorphs belong to a supersymmetry equal to the cubic crystallographic point group $Pm\bar{3}m$ (*Chap. 3:* Fig. 10b), which is indicated by the tetrahedral angle of ≈109° between the *c*-axis of the lamellae and the host (*Chap. 3:* Fig. 5). As a result, the retrograde transformation from liuite to wangdaodeite leads to a symmetry loss, which is expressed by transformation twin domains with common $\{11\bar{2}0\}$ planes within ilmenite as similarly suggested by Mehta et al. (1994) and expressed for this type of phase transitions by, e.g., Wang et al. (1991). Wangdaodeite is metastable (Mehta et al. 1994), especially with elevated temperatures as inferred by the adjacent devitrified glass, i.e., former melt (*Chap. 3:* Figs. 1a, b, 3a, c, 7a, b, f), and transforms to ilmenite by some reconstructive character, which eventually documents the phase transformation evolution with the observed transformation twin lamellae (*Chap. 3:* Fig. 5a, c, e). Ilmenite aggregates document the same orientation relationship with a foam structure, where up to three dominant orientation domains share two common $\{11\bar{2}0\}$ planes and display 109° or 99° angles between their respective *c*-axis orientations (*Chap. 3:* Fig. 5d, d, f). Therefore, the foam structure indicates iso-static stress conditions represented by smoothly curved grain boundaries and 120° angles at triple junctions and documents phase transformations as a function of high-pressure excursions.

Exclusively within the sample from Zipplingen, rutile can occur at the core of ilmenite aggregates (tens of µm; C3: Fig. 3a, g) or distributed along triple junctions (sub-µm; C3: Fig. 3c, d), whereas magnetite can occur as euhedral µm-sized grains at the rim (*Chap. 3:* Figs. 3a, c, e, f, g, 7a, b, e) or at a close distance within the matrix (*Chap. 3:* Fig. 7a, e, f). Additionally, ferropseudobrookite(-armalcolite solid-solution) [$(Fe,Mg)Ti_2O_5$) can be present at the rim or within fractures of ilmenite aggregates (*Chap. 3:* Figs. 7b-f, 8a, b, h). Ferropseudobrookite forms from ilmenite at temperatures >1140°C and low oxygen fugacity (Lindsley 1965; Keil et al. 1970; Tuthill and Sato 1970; Sargeant et al. 2020). This phase transition explains the occurrence of ferropseudobrookite at ilmenite aggregate boundaries towards the adjacent melt and within fractures (*Chap. 3:* Figs. 7b-f, 8a, b). The melting point of $FeO\text{-}TiO_2$ at temperatures above ≈1400°C (Eriksson and Pelton 1993) could have been reached. However, the presence of the foam structure, which preserved the crystallographic orientation relationships derived

from high-pressure polymorphs, indicates that solid-state reactions prevailed. Armalcolite requires temperatures of 1010°C to form (Lindsley et al. 1974). Locally, ferropseudobrookite-armalcolite solid-solution likely formed from ilmenite in combination with a chemical exchange with the adjacent melt, which provided Mg (*Chap. 3:* Fig. 8a, b, h), as suggested by El Goresy and Chao (1976). However, a chemical interaction with the melt, which provided Mg to form ferropseudobrookite-armalcolite solid-solution from ferropseudobrookite would also be possible.

The occurrence of rutile and/or ferropseudobrookite correlates with magnetite as a rim around Fe-Ti-oxide aggregates or within the matrix at a close distance. The Fe-Ti-oxide aggregates often resemble a decreasing Fe concentration gradient with µm-sized sub(-euhedral) magnetite (Fe_3O_4) at the rim, ilmenite ($FeTiO_3$) further inwards, to an absence of iron within rutile (TiO_2) (*Chap. 3:* Fig. 3a, g). Chemical profiles conducted with EMP of ilmenite from the rim to the core of the aggregates consistently show a decreasing Fe/Ti value based on at% (1.02 to 0.83; C3: Fig. 3g, h, Tab. S1). Within temperatures of 850-1050°C and a low oxygen fugacity, ilmenite thermally disproportions to TiO_2, Fe, and oxygen (Taylor et al. 1972). This reaction likely starts at sites of increased diffusivity, such as grain boundaries, which can explain the occurrence of µm-sized rutile at triple junctions of the ilmenite foam structure (*Chap. 3:* Fig. 3c, d). High-temperature experiments with ilmenite conducted with a reducing agent, such as CO (Zhao and Shadman 1990) or C (Gupta et al. 1990), generally form a rim of elemental iron, which is interpreted as an iron migration toward grain boundaries (Zhao and Shadman 1990; Kucukkaragoz and Eric 2006). Therefore, a reducing agent could have donated e^- to the rim of the ilmenite aggregates from the Zipplingen sample, with a subsequent reduction of Fe^{2+} to Fe^0. An accumulation of negative charges would have generated a gradient, which attracted Fe^{2+} from within the aggregate via diffusion, consistent with a fast Fe^{2+} diffusion in ilmenite (Kuganathan et al. 2019). Consequently, Fe^{2+} diffused towards the phase boundary and/or within the silicate melt, whereas vacancies moved towards the core, leaving TiO_2 within central parts of the aggregates, as observed in backscattered electron (BSE) images and chemical profiles (*Chap. 3:* Fig. 3a, g, h). This process resembles a solid-state electrochemical reaction, where the reduction agent serves as the cathode and ilmenite as the anode, which generates an electrochemical potential and, thus, a driving force for Fe^{2+} diffusion. The stability of ferropseudobrookite consistently requires a low oxygen fugacity and thus similar conditions (Lindsley 1965). With decreasing temperatures, the Fe^{3+}/Fe^{2+} ratio increases in silicate melts (Sack et al. 1981; Kilinc et al. 1983). Therefore, oxidation of elemental iron could have formed magnetite at the rim (*Chap. 3:* Figs. 3a, c, e, f, 7a, b, e) at intermediate oxygen fugacity conditions between temperatures of 400-700°C as similarly reported by Mitchell et al. (1982) and Kuroda and Mitchell (1983). Around 15% of the sample of Zipplingen consists of calcite, which either occurs as xenomorphic grains incorporating globules of devitrified silicate glass or as globules within the matrix (*Chap. 3:* Fig. 1b). The phase boundary is irregular and convex with respect to the silicate matrix. Based on similar observations, Philpotts and Ague (2009) interpreted a carbonatic and an adjacent silicate melt elicited from the surface energies as a function of the respective viscosities. A liquid immiscibility for melt fragments from Zipplingen, the same outcrop as this study, was discussed by Graup (1999). Osinski et al. (2008) consider melting as the typical phase transition of calcite in impact cratering. Contrarily, devolatilization of calcite was proposed as the dominant process based on shock experiments, thermal analyses, microprobe analysis, and SEM observation by Hörz et al. (2015, 2020). The investigated material of this study likely derives from the basement gneisses, which were modelled to be heated above 2000°C (von Engelhardt and Graup 1984). The sedimentary cover, where the calcite within our sample material likely derives from, was first hit by the meteorite and, therefore, could have experienced even higher temperature excursions (Bolten and Müller 1969). Above 650°C, calcite ($CaCO_3$) decomposes to CO_2 (Galwey and Brown 1999), which in turn disproportions to CO at temperatures above ≈1500°C (Itoh et al. 1993). Therefore, CO might have

been a potential reduction agent, which likely mixed into the silicate melt, contributing to the observed microfabrics from the Fe-Ti-oxides.

Besides ilmenite, different Fe-Ti-oxide phases within the sample from the Aumühle quarry are pseudorutile ($Fe_2Ti_3O_9$; : Fig. 9) as well as hematite (*Chap. 3:* Fig. 1c). Pseudorutile occurs either as a rim around single ilmenite grains or as an almost complete replacement of former ilmenite. Ilmenite transformations to pseudorutile occur under a high oxygen fugacity below temperatures of ≈700°C (Gupta et al. 1991) in combination with a leaching agent, such as water (Temple 1966; Teufer and Temple 1966; Grey and Reid 1975; Mücke and Bhadra Chaudhuri 1991). Ilmenite aggregates have intergranular microcracks as a result of high-pressure excursions and resulting high-pressure phase (back-)transformations, which facilitates fluid circulation and subsequent pseudorutile formation along grain boundaries and fractures during a hydrothermal activity within the Ries impact structure (Arp et al. 2013).

6.2 Implications for properties of Archean basement rocks from the magnetic anomaly northwest of the Vredefort impact structure center

The investigation of the Archean gneiss from the crystalline basement within the magnetic high-amplitude anomaly northwest of the center of the impact structure (e.g., Muundjua et al. 2007; *Chap. 2*: Fig. 1) aimed primarily to disentangle effects that might have been related to lightning strikes from Fe-oxide microstructures, which resulted from the meteorite impact. Carporzen et al. (2012) reported a strong remagnetization from lightning strikes within the uppermost meter of the drill cores (total depth ≈10 m). However, no evidence for lightning-generated microstructures in the uppermost meter of each of the two drill cores (V2 and V3) could be found when comparing to samples from depths >1 m (*Chap. 2:* Fig. 11). Based on low Verwey transition temperatures (90°K to 110°K) and high coercivities (>30 mT), oxidized single domain (SD) magnetite (<100 nm) was suggested to have formed as a result of lightning strikes at the surface (Carporzen et al. 2012). Opaque phases along PFs were suggested as potential magnetic carriers of the surficial magnetic properties (Carporzen et al. 2012), however, those microstructures could be identified in all depths of both drill cores and are, therefore, not a result of lightning strikes. Generally, the grain sizes of the carriers of the lightning-induced magnetic signals might be too small for the analytical techniques (optical microscopy and SEM) used.

Information about the temperature before impact is crucial for interpreting the magnetic remanence and the magnetic carriers of shocked rocks. Dauphiné twin boundaries within quartz grains often correlate with PFs (*Chap. 2:* Figs. 8g, 9a), which implies that they were generated after impact. The fracture surfaces served as sites of preferred twin nucleation, as reported by, e.g., Trepmann and Spray (2005). Dauphiné twinning can occur as a result of a retrograde phase transformation from hexagonal β-quartz to trigonal α-quartz below the transition temperature of ≈573°C at atmospheric pressure conditions (Tullis 1970; Markgraaff 1986; Heaney and Veblen 1991). Under confining pressure, this temperature increases by 25°C per 0.1 GPa (Coe and Paterson 1969). Structural uplift due to impact is estimated at 3-12 km, and erosion at 8-11 km since then (Gibson et al. 1998; Gibson 2019). Taking this paleo-depth-range into account, in addition to a geothermal gradient of 30°C/km (Gibson and Wallmach 1995) and an average density of 2700 kg/m^3, the stabilization temperature for β-quartz can be estimated to be 650-725°C. Therefore, the Archean gneiss was likely at temperatures above the Curie temperature of 580°C of magnetite during impact cratering (Henkel and Reimold 2002; Salminen et al. 2009). This is consistent with temperature estimations of 650-750°C based on reaction fabrics (orthopyroxene-plagioclase coronas and cordierite-orthopyroxene symplectites) in

metapelites, which are interpreted as a result of phase recalibration after impact (Perchuk et al. 2002). Consequently, the magnetic anomaly was generated due to structural uplifting and subsequent cooling through the Curie temperature of magnetite. Given those new observations, referring to the magnetic anomaly as shock remanent magnetization might not be correct.

Grain sizes and shapes of magnetic carriers, such as magnetite, strongly influence their magnetic carrying capacity. Coarse-grained magnetite exists within the multi-domain (MD > 10 µm) state, which remanence carrying capacity is lower compared to pseudo-single-domain (PSD = 700 nm – 10 µm). Single-domain (SD = 50 nm – 700 nm) grains have the highest magnetic carrying capacities. Below, magnetite occurs as super-paramagnetic (SP) grains, which cannot acquire a stable thermal remanent magnetization (Dunlop 2002b, 2002a; Hatfield and Stoner 2013). The generation of exsolved lamellar (≈5 µm x 1 µm) and spheroidal magnetite (≈10 µm) within coarse ilmenite grains (*Chap. 2:* Figs. 5a, b, 7) increases the magnetic carrier density in the Archean gneisses. Furthermore, fracturing of coarse-grained magnetite likely results in a transition from MD to PSD/SD magnetite, thereby increasing the carrying capacity in combination with additional internal strain, which also leads to an increase as reported from laboratory experiments (Carporzen and Gilder 2010).

6.3 Polymict crystalline breccia emplacement

At the Aumühle quarry in the northwestern part of the Ries impact structure (*Chap. 4:* Fig. 1), polymict crystalline breccia with a width of dm to m occurs overlying Bunte Breccia (*Chap. 4:* Figs. 2a, 3b, c) and covered by suevite (*Chap. 4:* Figs. 2a, 3d). The grain-supported lithology comprises ≈50% shocked crystalline clasts (up to 50 GPa; C4: Figs. 4-8; Tab. 1) from the crystalline basement and ≈50% clasts from the sedimentary cover sequence (*Chap. 4:* Fig. 3d, g, h). There, the investigated sandstone clast has no apparent shock effects (*Chap. 4:* Fig. 9). The matrix of the polymict crystalline breccia is composed of fine-grained clast material. A complementary study by Sleptsova et al. (*submitted*), who magnetically characterized impactites, including the samples of this study, found that suevite has tightly grouped paleomagnetic directions, which can be attributed to the Ries impact. Clasts within the polymict crystalline breccia with hematite as magnetic carrier have paleomagnetic directions with random distribution, whereas magnetite-dominated clasts have the Ries direction (*Chap. 4:* Tab. 1).

Generally, polymict crystalline breccia was rarely documented within the Nördlinger Ries. An isolated body of polymict crystalline breccia overlying Bunte Breccia is reported from the outcrop Meyers Keller (Abadian 1972), however, without a suevite cover layer, as similarly reported from the Erbisberg drillcore (Arp et al. 2019). Our observations, combined with the findings from Meyers Keller and the Erbisberg drillcore, therefore, indicate that the emplacement of the polymict crystalline breccia occurred after the emplacement of the underlying Bunte Breccia and before the emplacement of the suevite. The absence of glass fragments within the polymict crystalline breccia in combination with random paleomagnetic directions and a sharp contact with the suevite (*Chap. 4:* Fig. 3b, d, e) rules out that polymict crystalline breccia represents a mixed horizon of components of Bunte Breccia and suevite.

Impact breccias, similarly characterized as the polymict crystalline breccias from the Ries with cm to dm-sized, crystalline-rich, and shocked clasts with a contribution of sedimentary components, are reported from various other impact structures. They occur as dike structures, i.e., lithic impact breccias in the Chesapeake Bay impact structure (e.g., Wright Horton et al. 2009), polymict clastic matrix breccias in the Slate Island impact structure (e.g., Dressler and Sharpton 1997), dike breccias in the Rochechouart impact structure (e.g., Lambert 1981; Bischoff and Oskierski 1987), clastic injections in

the Lockne impact structure (e.g., Sturkell and Ormö 1997), and dike breccias in the Ries impact structure in the crystalline basement (e.g., Stöffler et al. 1977). Dike structures have widths of cm to m and lengths of >1 km [i.e., polymictic clastic matrix breccias in Dressler and Sharpton (1997) as well as polymict clastic-matrix breccias in Dressler and Reimold (2004)]. Their emplacement is interpreted as a highly energetic process during crater excavation, where fragmented and shocked material moves against and along the excavation cavity wall and intrudes local fracture systems with a high particle motion (e.g., Stöffler 1977; Lambert 1981). The Maxwell Z-model (Maxwell 1977; Croft 1980) suggests flow fields, which move material horizontally or vertically along the forming excavation cavity walls, whereas the same material is also ballistically ejected (Bischoff and Stöffler 1984). Given the highly energetic and turbulent process, the amount of the ballistically ejected material is hard to estimate. However, emplaced deposits have similar shock stages and compositions as the injected material within dikes.

Polymict crystalline breccia in the Aumühle quarry is systematically observed as irregular bodies (one larger and several smaller outcrops) overlying Bunte Breccia with a sharp contact towards the suevite (*Chap. 4:* Figs. 2a, 3b, d, e). Singular large clasts from the crystalline basement can occur directly on the interface of suevite with underlying Bunte Breccia (*Chap. 4:* Fig. 3f). Those observations can be interpreted as the result of ballistically ejected material predicted by the Maxwell Z-model (Maxwell 1977; Croft 1980). The irregular distribution of larger polymict crystalline breccia bodies (*Chap. 4:* Figs. 2a, 3b) and the occurrence of single larger clasts from the crystalline basement (*Chap. 4:* Fig. 3f) is likely due to the highly energetic and turbulent character of impact cratering and subsequent impactite emplacement (e.g., Kenkmann et al. 2014). Combined with an irregular and still moving Bunte Breccia surface, the distribution and emplacement of polymict crystalline breccia likely occurs heterogeneously as clusters as similarly observed by, e.g., Dressler and Reimold (2004), or as singular clasts. Occurring sedimentary clasts indicate the turbulent character during emplacement, where unshocked material from the sedimentary cover is intermixed.

6.4 Formation of ballen SiO_2

For the investigation of SiO_2 ballen structures, which are characteristic globular aggregates, two impact melt rock samples were chosen for a detailed study from an old quarry southwest of Polsingen within the Ries impact structure to unravel the formation processes and conditions. The samples contain a large amount of biotite-bearing granitic gneiss fragments within a (devitrified) matrix, which has finely dispersed hematite (*Chap. 5:* Fig. 1). The gneiss clasts contain decomposed biotite, vesicles, and ballen SiO_2 (*Chap. 5:* Fig. 2a, b). Based on the decomposition of biotite and the presence of melt, shock stage F-S6 (Stöffler et al. 2018) or III according to the IUGS system (Stöffler and Grieve 2007) can be attributed, indicating shock pressures of 45-60 GPa and post-shock temperatures of 900-1300°C.

Ballen aggregates typically have a diameter of hundreds of µm to mm and show either an irregular and drop-like (*Chap. 5:* Fig. 2c, f-h) or a rectangular shape (*Chap. 5:* Fig. 2b), which is interpreted as the shape of the initial quartz grain from the host rock (*Chap. 5:* Fig. 9a, b). The individual globule-shaped ballen have a diameter of a few tens of µm (*Chap. 5:* Fig. 2) and are comprised of quartz with undulatory extinction (*Chap. 5:* Fig. 2c-f) or radially oriented cristobalite (*Chap. 5:* Fig. 4a, b). Intergranular curved interfaces of ballen can be filled by siliceous material (*Chap. 5:* Fig. 4c, d) or be open (*Chap. 5:* Fig. 4a, b). Around 67% of the investigated ballen aggregates display undulatory extinction of individual ballen (*Chap. 5:* Figs. 2c-f, 4a, b), whereas ≈20% are comprised of quartz, which

shows coarser domains of similar extinction (*Chap. 5:* Fig. 2d). A "chert-like" texture, where singular ballen display vastly different extinction positions on a small scale (*Chap. 5:* Fig. 2e) or a heterogeneous extinction (*Chap. 5:* Figs. 2e, 5), occurs at ≈32% of the ballen aggregates. Rarely, planar features oriented parallel (0001) and $\{10\bar{1}3\}$ of the host quartz ballen can be observed (*Chap. 5:* Fig. 4e, f). Additionally, ballen aggregates consisting of quartz and cristobalite occur, where the latter displays a low birefringence and quartz displays a relatively homogeneous extinction of individual ballen (*Chap. 5:* Fig. 2f). A rim of dendritic cristobalite occurs locally around ballen aggregates in contact with vesicles (*Chap. 5:* Figs. 2h, 6a), which displays a radiating crystallographic orientation of the {110}, and {001} planes as well as a point maximum parallel to the thin section normal of the {010} plane (*Chap. 5:* Fig. 6a, b, d), which is similar to cristobalite orientations within ballen aggregates (*Chap. 5:* Fig. 7a, d).

The initial formation mechanism of ballen aggregates is widely accepted as a transformation from primary quartz from the target rock to a quenched/decompressed silicate melt or diaplectic glass (e.g., Carstens 1975; Ferrière et al. 2009, 2010; Buchner et al. 2010). Diaplectic glass is formed as a dense amorphous phase during shock compression (e.g., von Engelhardt et al. 1967; Arndt et al. 1982; Kruger and Jeanloz 1990; Langenhorst 1994). However, the short-range order and grain shape of the pre-cursor structure can be preserved, resulting in remnants of the crystallographic structure as a function of disorder (Hörz and Quaide 1973). The ballen aggregates of our study were likely formed from quartz grains within the crystalline basement, similar to the fluid-inclusion-rich granitic gneisses (*Chap. 5:* Fig. 9a, b). The dominating orientations of quartz likely derive from a topotactic crystallization of the diaplectic glass with preserved crystallographic memory. In contrast, a more strongly disordered amorphous phase leads to random orientations. The shapes of the ballen aggregates can be droplet-like to rectangular, which indicates that the pre-cursor quartz grain experienced variable degrees of modifications. However, most observed ballen SiO_2 aggregates display a CPO independent of their shape (*Chap. 5:* Tab. 1). The microstructure of ballen and the related occurrence of cristobalite is explained by multiple transformations, mainly from cristobalite to quartz (Carstens 1975; von Engelhardt 1997; Ferrière et al. 2009, 2010; Buchner et al. 2010). The occurrence of α-quartz ballen is explained by Ferrière et al. (2010) as a transformation from β-quartz or α-cristobalite over time, which does not explain the significant round interfaces of the ballen. Ferrière et al. (2009) proposed the phase transition from cristobalite to quartz and the subsequent volume change as a mechanism for the globular microstructure. However, we observed cristobalite with a ballen structure (*Chap. 5:* Figs. 2f, g, 7a). Therefore, the cristobalite to quartz transformation cannot be a prerequisite for the ballen structure. Within our samples, CPOs within ballen quartz are commonly observed, suggesting a direct crystallization from diaplectic glass with a crystallographic memory of the pre-cursor quartz grain, which is consistent with the observation of remnant planar features (*Chap. 5:* Fig. 4e, f). In contrast, diaplectic SiO_2 glass crystallization to cristobalite would require restructuring the tetrahedral network, which is not indicated by the crystallographic orientations.

Globular microstructures of cristobalite within silica-rich volcanic glass, i.e., obsidian, is known as perlitic structure and can occur in andesitic to rhyolitic rocks and hydrated glasses (e.g., Swanson et al. 1989; Horwell et al. 2013). Marakushev et al. (1988) interpreted perlitic structures to form due to the solidification of water-bearing silica-rich melts with inhibited dehydration based on experimental evidence. During decompression and cooling, strain concentrations cause peeling and resulting radial cracks in the crystallizing glass as a result of the separation of the fluid phase (Marakushev et al. 1988). Based on experiments, Flörke et al. (1990) demonstrated that cristobalite can grow from hydrothermal fluids at high-temperature gradients (100-600°C) in dendritic to spherulitic deposits on a quartz substratum (200-700°C).

Upon shock loading, the original fluid-inclusion-rich quartz crystals from granitic gneisses in the Nördlinger Ries were likely transformed into an amorphous silica phase, where the volatiles could dissolve. Upon decompression and subsequent cooling, the amorphous silica phase dehydrated, which generated a water-rich fluid. The resulting strain concentration caused radial “dehydration cracks “, similar to perlitic structures in volcanic rocks (Marakushev et al. 1988), at which the fluids could expel. Therefore, ballen aggregates cannot be used as a diagnostic criterion for meteorite impacts. Dendritic cristobalite only occurs at the rim of ballen aggregates adjacent to vesicles. Therefore, it is likely related to the ballen formation. The volatile-rich melt was expelled from the amorphous silica phase, possibly degassed forming vesicles, where cristobalite then crystallized, as similarly suggested for volcanic perlites by Horwell et al. (2013). Cristobalite occurring as radiating crystals within the ballen aggregates (*Chap. 5:* Fig. 4d) together with quartz without a CPO likely crystallized from a highly viscous, rapidly quenched, and thus supercooled silica amorphous phase with no orientation memory of the pre-cursor phase. Ballen with a CPO, however, probably crystallized from an amorphous phase with an orientation memory.

6.5 Conclusions

Investigations of shocked ilmenites have proven their great potential for revealing a broad range of shock conditions. For shock pressures <16 GPa, the following shock effects were recorded:

1. Shearing attributed to the impact led to fracturing of ilmenite with subsequent frictional melting and intrusion in adjacent fractures.
2. Mechanical twinning occurred along (0001) and $\{10\bar{1}1\}$.
3. Lamellar and spheroidal magnetite exsolved above T=600-700°C.

At shock pressures >16 GPa, various microfabrics were generated:

4. The high-pressure polymorph liuite formed upon shock loading, transforming upon decompression to wangdaodeite and, finally, ilmenite. As a result, transformation twins developed that share a common $\{11\bar{2}0\}$ plane and *c*-axes of host and twin spanning a 109° angle. Furthermore, a foam structure was generated where the individual grains have a similar crystallographic relationship as the observed transformation twins, which implies that the microfabric is also the result of the retrograde transformation.
5. At low oxygen fugacity conditions, shock heating formed rutile along grain boundaries (T=850-1050°C) and/or ferropseudobrookite (T>1140°C) adjacent to the silicate melt.
6. A reducing agent, such as CO, generated an electrochemical gradient, producing an iron-enriched rim around Fe-Ti-oxide aggregates. Subsequent oxidation formed euhedral magnetite grains.
7. High oxygen fugacity conditions in combination with the presence of water and temperatures below 700°C formed pseudorutile around single ilmenite grains.

Investigations on shocked Archean gneisses from the Vredefort impact structure revealed the occurrence of Dauphiné twins in quartz, which have twin boundaries restricted to PFs, indicating that they formed after shock unloading. Given a paleo depth of 11-23 km, temperatures were higher (650-725°C) than the Curie temperature of magnetite (580°C) before impact. Thus, the paleomagnetic remanence can be explained by impact-related uplifting and subsequent cooling in the magnetic field direction present during the Vredefort impact. Fe-Ti-bearing phases along PFs occur independently of the depths of the drill cores (≈10m). Therefore, a generation as a result of lightning strikes can be ruled out.

Polymict crystalline breccia at the Aumühle quarry in the Ries impact structure reveals sharp contacts to the underlying Bunte Trümmermassen and the overlying suevite, representing the first clear deposition relation in the Nördlinger Ries. A generation by re-working of Bunte Breccia and suevite can be excluded due to the absence of glass fragments in the polymict crystalline breccia in combination with the sharp lithological contacts as well as larger clast sizes and partially random paleomagnetic directions compared to the suevite, which has tightly grouped paleomagnetic intensities attributed to the magnetic field direction present during the Ries impact. The emplacement likely occurred as deposition from ballistic ejecta from within the transient excavation cavity, as inferred from the Maxwell Z-model. Mixing is indicated by the additional occurrence of unshocked clasts from the sedimentary cover sequence.

Ballen aggregates of SiO_2 polymorphs within melt rocks from the Nördlinger Ries originated from fluid inclusion-rich coarse-grained quartz from a granitic gneiss protolith. Upon shock, quartz transformed into a diaplectic glass, where the fluid inclusions could dissolve. Decompression and cooling led to dehydration of the amorphous phase resulting in radial cracks. Topotactic crystallization of diaplectic glass with preserved short-range order resulted in dominant crystallographic domains within quartz, independent of the crack network. Without a structural memory, highly disordered domains within the amorphous phase crystallized as cristobalite or quartz with a random crystallographic orientation as a function of temperature. The formation mechanism is similar to the formation of perlitic structures formed from obsidian in volcanic systems. Therefore, ballen aggregates are not a diagnostic criterion for meteorite impacts.

6.6 Outlook

The emplacement of impactites, such as suevite, Bunte Breccia, and polymict crystalline breccia, is poorly understood and heavily debated. Investigations on Fe-Ti-oxides have shown great potential to narrow down the evolution of pressure, temperature, and oxygen fugacity conditions combined with the magnetic properties essential for distinguishing different emplacement conditions. The studies of Fe-Ti-oxides within the framework of this thesis indicate various modification and formation conditions, which result in distinct phase relationships often attributed to characteristic microfabrics. Interpretations are based on thermodynamic studies, where products were equilibrated to the respective laboratory reaction conditions. However, meteorite impacts are characterized as highly energetic, fast, and thus turbulent events far from thermodynamic equilibrium (e.g., Melosh 1989; Kenkmann et al. 2014; Stöffler et al. 2018). To better understand the observed microfabrics, shock and high-temperature quenching experiments under controlled oxygen fugacity should yield insights into more representative conditions of Fe-Ti-oxides in the natural environment.

Ilmenite occurs within impactites on the lunar surface and is discussed as an in-situ oxygen source (Badescu 2012 and references therein) and produces water when heated and reduced with H_2 (Li et al. 2012; Dang et al. 2015; Sargeant et al. 2020). This thesis indicates that ilmenite can be largely modified due to meteorite impacts. The resulting product phases might strongly affect the physical and chemical bulk properties. Therefore, this thesis's findings might be relevant for optimizing the in-situ resource utilization (ISRU) on planetary objects, such as the Moon and Mars, whose surfaces are blanketed by impact structures. Ilmenite aggregates from kimberlite pipes (e.g., Solov'eva et al. 2019) document a foam structure strikingly similar to the foam structure reported in this thesis. Pressure conditions in the mantle could also stabilize the high-pressure polymorph liuite, which might have transformed to ilmenite during ascent and subsequent unloading, forming a foam structure, as this thesis discusses.

Generally, ilmenite is a common mineral in igneous and metamorphic rocks on the Earth's crust and mantle, as well as on the Moon and Mars. Therefore, the complex phase relations and microfabrics can document diverse formation and modification conditions in various geological settings on planetary surfaces.

References

Abadian, M. (1972) Petrographie, Stoßwellenmetamorphose und Entstehung polymikter kristalliner Breccien im Nördlinger Ries. Contributions to Mineralogy and Petrology, 35, 245–262.

Abadian, M., von Engelhardt, W., and Schneider, W. (1973) Spaltenfüllungen in allochthonen Schollen des Nördlinger Ries. In Geologica Bavarica 67 pp. 229–237.

Abrahams, S.C., Reddy, J.M., and Bernstein, J.L. (1966) Ferroelectric lithium niobate. 3. Single crystal X-ray diffraction study at 24°C. Journal of Physics and Chemistry of Solids, 27, 997–1012.

Armstrong, R.W. (2015) Material grain size and crack size influences on cleavage fracturing. Philosophical Transactions of the Royal Society A: Mathematical, Physical and Engineering Sciences, 373.

Arndt, J., Hummel, W., and Gonzalez-Cabeza, I. (1982) Diaplectic labradorite glass from the Manicouagan impact crater - I. Physical properties, crystallization, structural and genetic implications. Physics and Chemistry of Minerals, 8, 230–239.

Arnold, R.G. (1971) Evidence for liquid immiscibility in the system FeS-S. Economic Geology, 66, 1121–1130.

Arp, G., Kolepka, C., Simon, K., Karius, V., Nolte, N., and Hansen, B.T. (2013) New evidence for persistent impact-generated hydrothermal activity in the Miocene Ries impact structure, Germany. Meteoritics and Planetary Science, 48, 2491–2516.

Arp, G., Reimer, A., Simon, K., Sturm, S., Wilk, J., Kruppa, C., Hecht, L., Hansen, B.T., Pohl, J., Reimold, W.U., and others (2019) The Erbisberg drilling 2011: Implications for the structure and postimpact evolution of the inner ring of the Ries impact crater. Meteoritics and Planetary Science, 54, 2448–2482.

Artemieva, N.A., Wünnemann, K., Krien, F., Reimold, W.U., and Stöffler, D. (2013) Ries crater and suevite revisited-Observations and modeling Part II: Modeling. Meteoritics and Planetary Science, 48, 590–627.

Bader, K., and Schmidt-Kaler, H. (1977) Der Verlauf einer präriesischen Erosionsrinne im östlichen Riesvorland zwischen Treuchtlingen und Donauwörth. In H. Schmidt-Kaler, Ed., Geologica Bavarica 75 pp. 401–410. Bayerisches Geologisches Landesamt, München.

Badescu, V., Ed. (2012) Moon. Springer Berlin Heidelberg, Berlin, Heidelberg.

Barth, T.F.W., and Posnjak, E. (1934) The Crystal Structure of Ilmenite. Zeitschrift für Kristallographie - Crystalline Materials, 88, 265–270.

Basavaiah, N. (2011) GEOMAGNETISM Soild Earth and Upper Atmosphere Prespectives, 486 p. Springer, Capital Publishing Company, New Delhi.

Bischoff, A., and Stöffler, D. (1984) Chemical and structural changes induced by thermal annealing of shocked feldspar inclusions in impact melt rocks from Lappajärvi crater, Finland. Journal of Geophysical Research, 89, B645–B656.

Bischoff, L., and Oskierski, W. (1987) Fractures, Pseudotachylite Veins and Breccia Dikes in the Crater Floor of the Rochechouart Impact Structure, SW-France, as Indicators of Crater Forming Processes, 5–29 p. Research in Terrestrial Impact Structures.

Bolten, R., and Müller, D. (1969) Das Tertiär im Nördlinger Ries und in seiner Umgebung. In H. Schmidt-Kaler, Ed., Geologica Bavarica 61 pp. 87–130. Bayerisches Geologisches Landesamt, Munich.

Bringemeier, D. (1994) Petrofabric examination of the main suevite of the Otting Quarry, Nordlinger Ries, Germany. Meteoritics, 29, 417–422.

Broz, M.E., Cook, R.F., and Whitney, D.L. (2006) Microhardness, toughness, and modulus of Mohs scale minerals. American Mineralogist, 91, 135–142.

Brückner, L.M., Dellefant, F., and Trepmann, C.A. (*submitted*) Quartz cleavage fracturing and subsequent recrystallization along the damage zone – Record of fast stress unloading. Journal of Structural Geology.

Buchner, E., Schwarz, W.H., Schmieder, M., and Trieloff, M. (2010) Establishing a 14.6 ± 0.2 Ma age for the Nördlinger Ries impact (Germany) - A prime example for concordant isotopic ages from various dating materials. Meteoritics & Planetary Science, 45, 662–674.

Buddington, A.F., and Lindsley, D.H. (1964) Iron-titanium oxide minerals and synthetic equivalents. Journal of Petrology, 5, 310–357.

Butler, R.F. (1992) Paleomagnetism: magnetic domains to geologic terranes. Choice Reviews Online, 29, 29-5708-29–5708.

Canup, R.M. (2012) Forming a moon with an Earth-like composition via a giant impact. Science, 338, 1052–1055.

Carporzen, L., and Gilder, S.A. (2010) Strain memory of the Verwey transition. Journal of Geophysical Research: Solid Earth, 115, 1–12.

Carporzen, L., Gilder, S.A., and Hart, R.J. (2005) Palaeomagnetism of the Vredefort meteorite crater and implications for craters on Mars. Nature, 435, 198–201.

——— (2006) Origin and implications of two Verwey transitions in the basement rocks of the Vredefort meteorite crater, South Africa. Earth and Planetary Science Letters, 251, 305–317.

Carporzen, L., Weiss, B.P., Gilder, S.A., Pommier, A., and Hart, R.J. (2012) Lightning remagnetization of the Vredefort impact crater: No evidence for impact-generated magnetic fields. Journal of Geophysical Research, 117, 1–17.

Carstens, H. (1975) Thermal history of impact melt rocks in the Fennoscandian shield. Contributions to Mineralogy and Petrology, 50, 145–155.

Chanou, A., Grieve, R.A.F., and Osinski, G.R. (2015) Formation of ballen in silica by thermal shock. In Bridging the Gap III: Impact Cratering In Nature, Experiments, and Modeling pp. 12–13. Freiburg.

Chao, E.C.T. (1976) Mineral-Produced High-Pressure Striae and Clay Polish: Key Evidence for Nonballistic Transport of Ejecta from Ries Crater. Science, 194, 615–618.

Chao, E.C.T., Hüttner, R., and Schmidt-Kaler, H. (1987) Aufschlüsse im Ries-Meteoriten-Krater, 84 p. Bayerisches Geologisches Landesamt, München.

Chen, M., Xiao, W., and Xie, X. (2010) Coesite and quartz characteristic of crystallization from shock-produced silica melt in the Xiuyan crater. Earth and Planetary Science Letters, 297, 306–314.

Clement, B.M. (2004) Dependence of the duration of geomagnetic polarity reversals on site latitude. Nature, 428, 637–640.

Cloete, M., Hart, R.J., Schmid, H.K., Drury, M., Demanet, C.M., and Sankar, K.V. (1999) Characterization of magnetite particles in shocked quartz by means of electron- and magnetic force microscopy: Vredefort, South Africa. Contributions to Mineralogy and Petrology, 137, 232–245.

Coe, R.S., and Paterson, M.S. (1969) The α-β Inversion in Quartz: A Coherent Phase Transition Under Nonhydrostatic Stress. Journal of Geophysical Research, 74, 4921–4948.

Crangle, J., and Goodman, G.M. (1971) The magnetization of pure iron and nickel. Proceedings of the Royal Society of London. A. Mathematical and Physical Sciences, 321, 477–491.

Croft, S.K. (1980) Cratering flow fields: implications for the excavation and transient expansion stages of crater formation. Geochimica et Cosmochimica Acta, Supplement, 14, 2347–2378.

Dang, J., Zhang, G.H., and Chou, K.C. (2015) Kinetics and mechanism of hydrogen reduction of ilmenite powders. Journal of Alloys and Compounds, 619, 443–451.

Deer, W.A., Howie, R.A., and Zussman, J. (2013) An Introduction to the Rock-Forming Minerals, 3rd ed., 549 p. Berforts Information Press, Stevenage, Hertfordshire.

Dekkers, M.J. (2012) End-member modelling as an aid to diagnose remagnetization: A brief review. Geological Society Special Publication, 371, 253–269.

Dellefant, F., Trepmann, C.A., Gilder, S.A., Sleptsova, I. V, Kaliwoda, M., and Weiss, B.P. (2022) Ilmenite and magnetite microfabrics in shocked gneisses from the Vredefort impact structure, South Africa. Contributions to Mineralogy and Petrology, 5.

Dellefant, F., Trepmann, C.A., Schmahl, W.W., Gilder, S.A., Sleptsova, I. V., and Kaliwoda, M. (2023) Ilmenite phase transformations in suevite from the Ries impact structure (Germany) record evolution in pressure, temperature, and oxygen fugacity conditions. American Mineralogist, in press.

Dellefant, F., Seybold, L., Trepmann, C.A., Gilder, S.A., Sleptsova, I. V., Hölzl, S., and Kaliwoda, M. (*submitted*) Polymict crystalline breccia in the Ries impact structure - Emplacement of moderately shocked basement clasts during crater excavation and subsequent mixing with weakly shocked sedimentary clasts. International Journal of Earth Sciences.

Dence, M.R. (1971) Impact melts. Journal of Geophysical Research, 76, 5552–5565.

Di Toro, G., Nielsen, S., and Pennacchioni, G. (2005) Earthquake rupture dynamics frozen in exhumed ancient faults. Nature, 436, 1009–1012.

Dressler, B.O., and Reimold, W.U. (2004) Order or chaos? Origin and mode of emplacement of breccias in floors of large impact structures. Earth-Science Reviews, 67, 1–54.

Dressler, B.O., and Sharpton, V.L. (1997) Breccia formation at a complex impact crater: Slate Islands, Lake Superior, Ontario, Canada. Tectonophysics, 275, 285–311.

Dunlop, D.J. (2002a) Theory and application of the Day plot (Mrs/Ms versus Hcr/Hc) 1. Theoretical curves and tests using titanomagnetite data. Journal of Geophysical Research, 107, 2056.

——— (2002b) Theory and application of the Day plot (Mrs/Ms versus Hcr/Hc) 2. Application to data for rocks, sediments, and soils. Journal of Geophysical Research, 107, 2057.

Ebert, M., Poelchau, M.H., Kenkmann, T., and Schuster, B. (2020) Tracing shock-wave propagation in the Chicxulub crater: Implications for the formation of peak rings. Geology, 48, 814–818.

El Goresy, A., and Chao, E.C.T. (1976) Identification and significance of armalcolite in the Ries glass. Earth and Planetary Science Letters, 30, 200–208.

El Goresy, A., Gillet, P., Chen, M., Künstler, F., Graup, G., and Stähle, V. (2001) In situ discovery of shock-induced graphite-diamond phase transition in gneisses from the Ries Crater, Germany. American Mineralogist, 86, 611–621.

Eriksson, G., and Pelton, A.D. (1993) Critical evaluation and optimization of the thermodynamic properties and phase diagrams of the CaO-Al_2O_3, Al_2O_3-SiO_2, and CaO-Al_2O_3-SiO_2 systems. Metallurgical Transactions B, 24, 807–816.

Ferrière, L., Koeberl, C., Reimold, W.U., Libowitzky, E., and Greshake, A. (2008) Ballen quartz and cristobalite in impact breccias: types, occurence, and possible origin. In 4th Large Meteorite Impacts and Planetary Evolution pp. 3–4. Parys.

Ferrière, L., Koeberl, C., and Reimold, W.U. (2009) Characterisation of ballen quartz and cristobalite in impact breccias: New observations and constraints on ballen formation. European Journal of Mineralogy, 21, 203–217.

Ferrière, L., Koeberl, C., Libowitzky, E., Reimold, W.U., Greshake, A., and Brandstätter, F. (2010) Ballen quartz and cristobalite in impactites: New investigations. Special Paper of the Geological Society of America, 465, 609–618.

Flörke, O., Graetsch, H., and Jones, J. (1990) Hydrothermal deposition of cristobalite. Neues Jahrbuch für Mineralogie Monatshefte, 81–95.

French, B.M. (1998) Traces of Catastrophe: A handbook of shock-metamorphic effects in terrestrial meteorite impact structures, 120 p. LPI Contribution Vol. 954. Lunar and Planetary Institute, Houston.

French, B.M., and Koeberl, C. (2010) The convincing identification of terrestrial meteorite impact structures: What works, what doesn't, and why. Earth-Science Reviews, 98, 123–170.

Frick, C. (1973) Kimberlitic Ilmenites. South African Journal of Geology, 76, 85–94.

Fu, X., Wang, Y., and Wei, F. (2010) Phase transitions and reaction mechanism of ilmenite oxidation. Metallurgical and Materials Transactions A: Physical Metallurgy and Materials Science, 41, 1338–1348.

Galwey, A.K., and Brown, M.E. (1999) Thermal Decomposition of Ionic Solids, 596 p. Vol. 86. Elsevier.

Gibson, R.L. (2019) The Mesoarchaean Basement Complex of the Vredefort Dome—A Mid-Crustal Section Through the Central Kaapvaal Craton Exposed by Impact. In A. Kröner and A. Hofmann, Eds., The Archaean Geology of the Kaapvaal Craton, Southern Africa pp. 109–132. Springer Nature Switzerland AG 2019.

Gibson, R.L., and Wallmach, T. (1995) Low pressure-high temperature metamorphism in the Vredefort Dome, South Africa: Anticlockwise pressure-temperature path followed by rapid decompression. Geological Journal, 30, 319–331.

Gibson, R.L., Armstrong, R.A., and Reimold, W.U. (1997) The age and thermal evolution of the Vredefort impact structure: A single-grain U-Pb zircon study. Geochimica et Cosmochimica Acta, 61, 1531–1540.

Gibson, R.L., Reimold, W.U., and Stevens, G. (1998) Thermal-metamorphic signature of an impact event in the Vredefort dome, South Africa. Geology, 26, 787–790.

Gilder, S.A., Pohl, J., and Eitel, M. (2018) Magnetic Signatures of Terrestrial Meteorite Impact Craters: A Summary. In H. Lühr, J. Wicht, S.A. Gilder, and M. Holschneider, Eds., Magnetic Fields in the Solar System - Planets, Moons and Solar Wind Interactions pp. 357–382. Springer.

Goltrant, O., Cordier, P., and Doukhan, J.C. (1991) Planar deformation features in shocked quartz; a transmission electron microscopy investigation. Earth and Planetary Science Letters, 106, 103–115.

Goltrant, O., Doukhan, J., Cordier, P., and Courtillot, V. (1992a) An investigation by transmission electron microscopy of planar deformation features in naturally shocked quartz. Terra Nova, 4, 405–412.

Goltrant, O., Leroux, H., Doukhan, J.C., and Cordier, P. (1992b) Formation mechanisms of planar deformation features in naturally shocked quartz. Physics of the Earth and Planetary Interiors, 74, 219–240.

Graup, G. (1978) Das Kristallin im Nördlinger Ries - Petrographische Zusammensetzung und Auswurdmechanismus der kristallinen Trümmermassen, Struktur des kristallinen Untergrundes und Beziehungen zum Moldanubikum, 190 p. Ferdinand Enke Verlag, Stuttgart.

——— (1999) Carbonate-silicate liquid immiscibility upon impact melting: Ries Crater, Germany. Meteoritics and Planetary Science, 34, 425–438.

Grey, I.E., and Reid, A.F. (1975) The Structure of Pseudorutile and Its Role in The Natural Alteration of Ilmenite. The American Mineralogist, 60, 898–906.

Grieve, R.A.F. (1987) Terrestrial Impact Structures. Annual Review of Earth and Planetary Sciences, 15, 245–270.

Grieve, R.A.F. (2013) Economic Deposits at Terrestrial Impact Structures. In G.R. Osinski and E. Pierazzo, Eds., Impact Cratering: Processes and Products Vol. 248, pp. 177–193. Blackwell Publishing Ltd.

Grieve, R.A.F., Coderre, J.M., Robertson, P.B., and Alexopoulos, J. (1990) Microscopic planar deformation features in quartz of the Vredefort structure: Anomalous but still suggestive of an impact origin. Tectonophysics, 171, 185–200.

Grieve, R.A.F., Cintala, M.J., and Therriault, A.M. (2006) Large-scale impacts and the evolution of the Earth's crust: The early years. In W.U. Reimold and R.L. Gibson, Eds., Geological Society of America Special Paper 405: Processes on the Early Earth Vol. 405, pp. 23–31. Boulder, Colorado.

Gupta, S.K., Rajakumar, V., and Grieveson, P. (1990) The role of preheating in the kinetics of reduction of ilmenite with carbon. Canadian Metallurgical Quarterly, 29, 43–49.

Gupta, S.K., Rajakumar, V., and Grieveson, P. (1991) Phase transformations during heating of Ilmenite concentrates. Metallurgical Transactions B, 22, 711–716.

Haggerty, S.E. (1991) Oxide Textures - A Mini-Atlas. Reviews in Mineralogyv, 25, 129–219.

Hahn, T., and Klapper, H. (2006) Twinning of crystals. In International Tables for Crystallography Vol. D, pp. 393–448. International Union of Crystallography, Chester, England.

Hargraves, R.B. (1970) Paleomagnetic Evidence Relevant to the Origin of the Vredefort Ring. The Journal of Geology, 78, 253–263.

Harrison, R.J., Becker, U., and Redfern, S.A.T. (2000) Thermodynamics of the R3 to R3c phase transition in the ilmenite-hematite solid solution. American Mineralogist, 85, 1694–1705.

Hart, R.J., Andreoli, M.A.G., Reimold, W.U., and Tredoux, M. (1991) Aspects of the dynamic and thermal metamorphic history of the Vredefort cryptoexplosion structure: implications for its origin. Tectonophysics, 192, 313–331.

Hart, R.J., Hargraves, R.B., Andreoli, M.A.G., Tredoux, M., and Doucoure, C.M. (1995) Magnetic anomaly near the center of the Vredefort structure: implications for impact-related magnetic signatures. Geology, 23, 277–280.

Hart, R.J., Connell, S.H., Cloete, M., Maré, L., Drury, M., and Tredoux, M. (2000) "Super magnetic" rocks generated by shock metamorphism from the centre of the Vredefort impact structure, South Africa. South African Journal of Geology, 103, 151–155.

Hatfield, R.G., and Stoner, J.S. (2013) Magnetic Proxies and Susceptibility. In S.A. Elias and C.J. Mock, Eds., Encyclopedia of Quaternary Science: Second Edition Vol. 2, pp. 884–898. Elsevier B.V.

Heaney, P.J. (1994) STRUCTURE AND CHEMISTRY OF THE LOW-PRESSURE SILICA POLYMORPHS. In P.J. Heaney, C.T. Prewitt, and G. V. Gibbs, Eds., Silica: Physical Behavior, Geochemistry, and Materials Applications Vol. 29, pp. 1–40. De Gruyter.

Heaney, P.J., and Veblen, D.R. (1991) Observation and kinetic analysis of a memory effect at the α-β quartz transition. American Mineralogist, 76, 1459–1466.

Hemley, R.J., Prewitt, C.T., and Kingma, K.J. (1994) HIGH-PRESSURE BEHAVIOR OF SILICA. In P.J. Heaney, C.T. Prewitt, and G. V. Gibbs, Eds., Silica pp. 41–82. De Gruyter.

Henkel, H., and Reimold, W.U. (1998) Integrated geophysical modelling of a giant, complex impact structure: Anatomy of the Vredefort Structure, South Africa. Tectonophysics, 287, 1–20.

Henkel, H., and Reimold, W.U. (2002) Magnetic model of the central uplift of the Vredefort impact structure, South Africa. Journal of Applied Geophysics, 51, 43–62.

Herwartz, D., Pack, A., Friedrichs, B., and Bischoff, A. (2014) Identification of the giant impactor Theia in lunar rocks. Science, 344, 1146–1150.

Horwell, C.J., Williamson, B.J., Llewellin, E.W., Damby, D.E., and Le Blond, J.S. (2013) The nature and formation of cristobalite at the Soufrière Hills volcano, Montserrat: Implications for the petrology and stability of silicic lava domes. Bulletin of Volcanology, 75, 1–19.

Hörz, F., and Quaide, W.L. (1973) Debye-Scherrer investigations of experimentally shocked silicates. The Moon, 6, 45–82.

Hörz, F., Ostertag, R., and Rainey, D.A. (1983) Bunte Breccia of the Ries: Continuous Deposits of Large Impact Craters. Reviews of Geophysics and Space Physics, 21, 1667–1725.

Hörz, F., Archer, P.D., Niles, P.B., Zolensky, M.E., and Evans, M. (2015) Devolatilization or melting of carbonates at Meteor Crater, AZ? Meteoritics and Planetary Science, 50, 1050–1070.

Hörz, F., Cintala, M.J., Thomas-Keprta, K.L., Ross, D.K., and Clemett, S.J. (2020) Unconfined shock experiments: A pilot study into the shock-induced melting and devolatilization of calcite. Meteoritics and Planetary Science, 55, 102–129.

Huber, M.S., Kovaleva, E., Clark, M.D., Riller, U., and Fourie, F.D. (2022) Evidence from the Vredefort Granophyre Dikes points to crustal relaxation following basin-size impact cratering. Icarus, 374, 114812.

Hüttner, R., and Schmidt-Kaler, H. (1999) Die Geologische Karte des Rieses 1: 50 000 (2., überarbeitete Auflage). Geologica Bavarica, 104, 7–76.

Itoh, N., Sanchez, M.A., Xu, W.C., Haraya, K., and Hongo, M. (1993) Application of a membrane reactor system to thermal decomposition of CO2. Journal of Membrane Science, 77, 245–253.

Jackson, M. (2007) Magnetization, Isothermal Remanent. In D. Gubbins and E. Herrero-Bervera, Eds., Encyclopedia of Geomagnetism and Paleomagnetism pp. 589–594. Springer Netherlands, Dordrecht.

Johnson, T.E., Kirkland, C.L., Lu, Y., Smithies, R.H., Brown, M., and Hartnady, M.I.H. (2022) Giant impacts and the origin and evolution of continents. Nature, 608, 330–335.

Kamo, S.L., Reimold, W.U., Krogh, T.E., and Colliston, W.P. (1996) A 2.023 Ga age for the Vredefort impact event and a first report of shock metamorphosed zircons in pseudotachylitic breccias and Granophyre. Earth and Planetary Science Letters, 144, 369–387.

Katari, K., and Bloxham, J. (2001) Effects of sediment aggregate size on DRM intensity: a new theory. Earth and Planetary Science Letters, 186, 113–122.

Keil, K., Prinz, M., and Bunch, T.E. (1970) Mineral Chemistry of Lunar Samples. Science, 167, 597–599.

Kenkmann, T., Poelchau, M.H., and Wulf, G. (2014) Structural geology of impact craters. Journal of Structural Geology, 62, 156–182.

Kieffer, S.W., Schaal, R.B., Gibbons, R., Hörz, R., Milton, D.J., and Dube, A. (1976) Shocked basalt from Lonar impact crater, India, and experimental analogues. In Lunar and planetary science conference proceedings VII pp. 1391–1412.

Kilinc, A., Carmichael, I.S.E., Rivers, M.L., and Sack, R.O. (1983) The ferric-ferrous ratio of natural silicate liquids equilibrated in air. Contributions to Mineralogy and Petrology, 83, 136–140.

Kontny, A., and Grothaus, L. (2016) Effects of shock pressure and temperature on titanomagnetite from ICDP cores and target rocks of the El'gygytgyn impact structure, Russia. Studia Geophysica et Geodaetica, 61, 162–183.

Kowitz, A., Güldemeister, N., Reimold, W.U., Schmitt, R.T., and Wünnemann, K. (2013) Diaplectic quartz glass and SiO2 melt experimentally generated at only 5 GPa shock pressure in porous sandstone: Laboratory observations and meso-scale numerical modeling. Earth and Planetary Science Letters, 384, 17–26.

Kranz, R.L. (1983) Microcracks in rocks: A review. Tectonophysics, 100, 449–480.

Kruger, M.B., and Jeanloz, R. (1990) Memory glass: An amorphous material formed from AlPO4. Science, 249, 647–649.

Kucukkaragoz, C.S., and Eric, R.H. (2006) Solid state reduction of a natural ilmenite. Minerals Engineering, 19, 334–337.

Kuganathan, N., Srikaran, R., Fossati, P.C.M., and Chroneos, A. (2019) Theoretical Modeling of Defects, Dopants, and Diffusion in the Mineral Ilmenite. Minerals, 9, 610.

Kuroda, K., and Mitchell, T.E. (1983) TEM studies of oxidation and passivation of iron. In R.M. Fisher, R. Gronsly, and K.H. Wetmacott, Eds., Seventh International Conference on High Voltage Electron Microscopy pp. 261–267. University of California, Berkeley.

Lambert, P. (1981) Breccia dikes: geological constraints on the formation of complex craters. Multi-ring basins: Formation and Evolution, 59–78.

Langenhorst, F. (1994) Shock experiments on pre-heated α- & β-quartz: II. X-ray and TEM investigations. Earth and Planetary Science Letters, 128, 683–698.

Langenhorst, F., and Deutsch, A. (1994) Shock experiments on pre-heated α- and β-quartz: I. Optical and density data. Earth and Planetary Science Letters.

Latypov, R., Chistyakova, S., Grieve, R., and Huhma, H. (2019) Evidence for igneous differentiation in Sudbury Igneous Complex and impact-driven evolution of terrestrial planet proto-crusts. Nature Communications, 10, 1–13.

Leinenweber, K., Utsumi, W., Tsuchida, Y., Yagi, T., and Kurita, K. (1991) Unquenchable high-pressure perovskite polymorphs of $MnSnO_3$ and $FeTiO_3$. Physics and Chemistry of Minerals, 18, 244–250.

Leinenweber, K., Yanbin Wang, Yagi, T., and Yusa, H. (1994) An unquenchable perovskite phase of $MgGeO_3$ and comparison with $MgSiO_3$ perovskite. American Mineralogist, 79, 197–199.

Leroux, H., and Doukhan, J.C. (1996) A transmission electron microscope study of shocked quartz from the Manson impact structure. Special Paper of the Geological Society of America, 302, 267–274.

Leroux, H., Reimold, W.U., and Doukhan, J.C. (1994) A TEM investigation of shock metamorphism in quartz from the Vredefort dome, South Africa. Tectonophysics, 230, 223–239.

Li, Y., Li, X., Wang, S., Tang, H., Gan, H., Li, S., and Ouyang, Z. (2012) In-situ water production by reducing ilmenite. In V. Badescu, Ed., Moon pp. 189–200. Springer, New York.

Lindsley, D.H. (1965) Iron-Titanium Oxides. In Carniege Institute Washington Yearbook 64 pp. 144–148.

——— (1991) Experimental studies of oxide minerals. In D.H. Lindsley, Ed., Oxide Minerals: Petrologic and Magnetic Significance pp. 69–106.

Lindsley, D.H., Kesson, S.E., Hartzman, M.J., and Cushman, M.K. (1974) The stability of armacolite: Experimantal studies in the system MgO-Fe-Ti-O. In Proceedings of the Fifth Lunar Conference pp. 521–534. Pergamon Press.

Liu, L.G. (1975) High-pressure phase transformations and compressions of ilmenite and rutile, I. Experimental results. Physics of the Earth and Planetary Interiors, 10, 167–176.

Ma, C., and Tschauner, O. (2018) Liuite, IMA 2017-042a. CNMNC Newsletter No. 46. Mineralogical Magazine, 82, 1369–1379.

Mang, C., and Kontny, A. (2013) Origin of two Verwey transitions in different generations of magnetite from the Chesapeake Bay impact structure, USA. Journal of Geophysical Research: Solid Earth, 118, 5195–5207.

Mang, C., Kontny, A., Fritz, J., and Schneider, R. (2013) Shock experiments up to 30 GPa and their consequences on microstructures and magnetic properties in pyrrhotite. Geochemistry, Geophysics, Geosystems, 14, 64–85.

Marakushev, A.A., Persikov, E.S., and Bukhtiarov, P.G. (1988) Endogenic nature of perlites. In 2nd International Conference on Natural Glasses pp. 89–96. Prague.

Markgraaff, J. (1986) Elastic Behavior of Quartz During Stress Induced Dauphiné Twinning. Physics and Chemistry of Minerals, 13, 102–112.

Maxwell, D.E. (1977) Simple Z model for cratering, ejection, and the overturned flap. In D.J. Roddy, R.O. Pepin, and R.B. Merrill, Eds., Impact and Explosion Cratering pp. 1003–1008. Pergamon Press, New York.

McCarthy, T., Stanistreet, I., and Robb, L. (1990) Geological studies related to the origin of the Witwatersrand Basin and its mineralization - an introduction and a strategy for research and exploration. South African Journal of Geology, 93, 1–4.

Mehta, A., Leinenweber, K., Navrotsky, A., and Akaogi, M. (1994) Calorimetric study of high pressure polymorphism in FeTiO3: Stability of the perovskite phase. Physics and Chemistry of Minerals, 21, 207–212.

Melosh, H.J. (1989) Impact cratering: a geologic process, 245 p. Oxford University Press, New York.

Meyer, C., Jébrak, M., Stöffler, D., and Riller, U. (2011) Lateral transport of suevite inferred from 3D shape-fabric analysis: Evidence from the Ries impact crater, Germany. Bulletin of the Geological Society of America, 123, 2312–2319.

Migault, A. (1998) Concepts of Shock Waves. In D. Benest and C. Froeschle, Eds., Impacts on Earth pp. 79–112. Springer Verlag, Berlin.

Minkin, J.A., and Chao, E.C.T. (1971) Single crystal X-ray investigation of deformation in terrestrial and lunar ilmenite. In Proceedings of the Second Lunar Science Conference pp. 237–246. M.I.T. Press.

Mitchell, T.E., Voss, D.A., and Butler, E.P. (1982) The observation of stress effects during the high temperature oxidation of iron. Journal of Materials Science, 17, 1825–1833.

Morey, G.W., and Bowen, N.L. (1922) The Melting of Potash Feldspar. American Journal of Science, 4, 1–21.

Mücke, A., and Bhadra Chaudhuri, J.N. (1991) The continuous alteration of ilmenite through pseudorutile to leucoxene. Ore Geology Reviews, 6, 25–44.

Mufti, N., Sari, D.R.P., Muyasaroh, A.F., Yudyanto, Sunaryono, and Taufiq, A. (2020) Analyses of magnetic properties and crystal size on Fe_3O_4 nanoparticle from local iron sand using PEG as soft template. Journal of Physics: Conference Series, 1595, 012004.

Muundjua, M., Hart, R.J., Gilder, S.A., Carporzen, L., and Galdeano, A. (2007) Magnetic imaging of the Vredefort impact crater, South Africa. Earth and Planetary Science Letters, 261, 456–468.

Nesterenko, V.F. (2001) Dynamics of Heterogeneous Materials, 510 p. Springer Verlag, New York.

Newsom, H.E., Graup, G., Iseri, D.A., Geissman, J.W., and Keil, K. (1990) The formation of the Ries Crater, West Germany; Evidence of atmospheric interactions during a larger cratering event. In V.L. Sharpton and P.D. Ward, Eds., Global catastrophes in Earth history; an interdisciplinary conference on impacts, volcanism, and mass mortality: Geological Society of America Special Paper 247 Vol. 247, pp. 195–206.

Oberbeck, V.R. (1975) The role of ballistic erosion and sedimentation in lunar stratigraphy. Reviews of Geophysics, 13, 337–362.

Osinski, G.R. (2004) Impact melt rocks from the Ries structure, Germany: An origin as impact melt flows? Earth and Planetary Science Letters, 226, 529–543.

Osinski, G.R., Grieve, R.A.F., and Spray, J.G. (2004) The nature of the groundmass of surficial suevite from the Ries impact structure, Germany, and constraints on its origin. Meteoritics & Planetary Science, 39, 1655–1683.

Osinski, G.R., Spray, J.G., and Grieve, R.A.F. (2008) Impact melting in sedimentary target rocks: An assessment. Special Paper of the Geological Society of America, 437, 1–18.

Osinski, G.R., Grieve, R.A.F., Marion, C., and Chanou, A. (2013) Impact melting. In G.R. Osinski and E. Pierazzo, Eds., Impact Cratering: Processes and Products pp. 125–145. Blackwell Publishing Ltd.

Osinski, G.R., Cockell, C.S., Pontefract, A., and Sapers, H.M. (2020) The Role of Meteorite Impacts in the Origin of Life. Astrobiology, 20, 1121–1149.

Osinski, G.R., Grieve, R.A.F., Ferrière, L., Losiak, A., Pickersgill, A.E., Cavosie, A.J., Hibbard, S.M., Hill, P.J.A., Bermudez, J.J., Marion, C.L., Newman, J.D., and Simpson, S.L. (2022) Impact Earth: A review of the terrestrial impact record. Earth-Science Reviews, 232.

Ostertag, R. (1983) Shock experiments on feldspar crystals. In Proceedings of the 14th Lunar and Planetary Science Conference pp. B364–B376.

Perchuk, L.L., Tokarev, D.A., Van Reenen, D.D., Varlamov, D.A., Gerya, T. V., Sazonova, L. V., Fel'dman, V.I., Smit, C.A., Brink, M.C., and Bisschoff, A.A. (2002) Dynamic and thermal history of the Vredefort explosion structure in the Kaapvaal craton, South Africa. Petrology, 10, 395–432.

Philpotts, A., and Ague, J. (2009) Principles of Igneous and Metamorphic Petrology, 2nd ed., 667 p. Cambridge University Press, New York.

Pietrek, A., and Kenkmann, T. (2016) Ries Bunte Breccia revisited: Indications for the presence of water in Itzing and Otting drill cores and implications for the emplacement process. Meteoritics and Planetary Science, 51, 1203–1222.

Pilkington, M., and Grieve, R.A.F. (1992) The geophysical signature of terrestrial impact craters. Reviews of Geophysics, 30, 161–181.

Pilkington, M., and Hildebrand, A.R. (2000) Three-dimensional magnetic imaging of the Chicxulub Crater. Journal of Geophysical Research: Solid Earth, 105, 23479–23491.

Plado, J., Pesonen, L.J., and Puura, V. (1999) Effect of erosion on gravity and magnetic signatures of complex impact structures: Geophysical modeling and applications. In B.O. Dressler and V.L. Sharpton, Eds., Special Paper of the Geological Society of America Vol. 339, pp. 229–239. Geological Society of America, Boulder, Colorado.

Poelchau, M.H., and Kenkmann, T. (2011) Feather features: A low-shock-pressure indicator in quartz. Journal of Geophysical Research: Solid Earth, 116, 1–13.

Pohl, J., Stöffler, D., Gall, H., and Ernston, K. (1977) The Ries impact crater. In D.J. Roddy, R.O. Pepin, and R.B. Merrill, Eds., Impact and Explosion Cratering pp. 343–404. Pergamon Press, New York.

Pohl, J., Poschlod, K., Reimold, W.U., Meyer, C., and Jacob, J. (2010) Ries crater, Germany: The Enkingen magnetic anomaly and associated drill core SUBO 18. In R.L. Gibson and W.U. Reimold, Eds., Large Meteorite Impacts and Planetary Evolution IV Vol. 465, pp. 141–163. Geological Society of America.

Rahmdor, P. (1969) The ore minerals and their intergrowths, 3rd ed., 1174 p. Vol. 47. Pergamon Press, London.

Rakov, V.A., and Uman, M.A. (2003) Lightning: Physics and Effects, 687 p. Cambridge University Press, Cambridge.

Rankin, G.A. (1915) The ternary system CaO-Al2O3-SiO2 , with optical study by F. E. Wright. American Journal of Science, 39, 1–79.

Rehfeldt-Oskierski, A., Stöffler, D., and Hornemann, U. (1986) Deformation, transformation, and thermal annealing of experimentally shocked single crystal quartz. In 17th Lunar and Planetary Science Conferencerence pp. 697–698.

Reimold, W.U., and Collision, W.P. (1994) Pseudotachylites of the Vredefort Dome and the surrounding Witwatersrand Basin, South Africa. In B.O. Dressler, R.A.F. Grieve, and V.L. Sharpton, Eds., Large Meteorite Impacts and Planetary Evolution pp. 177–196. Geological Society of America, Boulder, Colorado.

Reimold, W.U., and Gibson, R.L. (2005) “Pseudotachylites” in Large Impact Structures. In C. Koeberl and H. Henkel, Eds., Impact Tectonics pp. 1–53. Springer-Verlag, Berlin/Heidelberg.

Reimold, W.U., Koeberl, C., Gibson, R.L., and Dressler, B.O. (2005) Economic Mineral Deposits in Impact Structures: A Review. In C. Koeberl and H. Henkel, Eds., Impact Tectonics pp. 479–552. Springer, Berlin.

Reynolds, I.M. (1984) Tectonically deformed Ilmenite in titaniferous iron ores of the Mambula Complex, Zululand, South Africa. Canadian Mineralogist, 22, 411–416.

Reznik, B., Kontny, A., and Gerhards, U. (2016) Shock-induced deformation phenomena in magnetite and their consequences on magnetic properties. Geochemistry, Geophysics, Geosystems, 17, 2374–2393.

Reznik, B., Kontny, A., and Fritz, J. (2017) Effect of moderate shock waves on magnetic susceptibility and microstructure of a magnetite-bearing ore. Meteoritics and Planetary Science, 52, 1495–1504.

Rocholl, A., Schaltegger, U., Gilg, H.A., Wijbrans, J., and Böhme, M. (2017) The age of volcanic tuffs from the Upper Freshwater Molasse (North Alpine Foreland Basin) and their possible use for tephrostratigraphic correlations across Europe for the Middle Miocene. International Journal of Earth Sciences, 107, 387–407.

Rocholl, A., Böhme, M., Gilg, H.A., Pohl, J., Schaltegger, U., and Wijbrans, J. (2018) Comment on “A high-precision $^{40}Ar/^{39}Ar$ age for the Nördlinger Ries impact crater, Germany, and implications for the accurate dating of terrestrial impact events” by Schmieder et al. (Geochimica et Cosmochimica Acta 220 (2018) 146–157). Geochimica et Cosmochimica Acta, 238, 599–601.

Sack, R.O., Carmichael, I.S.E., Rivers, M., and Ghiorso, M.S. (1981) Ferric-ferrous equilibria in natural silicate liquids at 1 bar. Contributions to Mineralogy and Petrology, 75, 369–376.

Salminen, J., Pesonen, L.J., Reimold, W.U., Donadini, F., and Gibson, R.L. (2009) Paleomagnetic and rock magnetic study of the Vredefort impact structure and the Johannesburg Dome, Kaapvaal Craton, South Africa-Implications for the apparent polar wander path of the Kaapvaal Craton during the Mesoproterozoic. Precambrian Research, 168, 167–184.

Samsonov, G.V., Ed. (1982) The oxide handbook, 463 p. IFI Plenum, New York.

Sargeant, H.M., Abernethy, F.A.J., Barber, S.J., Wright, I.P., Anand, M., Sheridan, S., and Morse, A. (2020) Hydrogen reduction of ilmenite: Towards an in situ resource utilization demonstration on the surface of the Moon. Planetary and Space Science, 180, 104751.

Schaal, R.B., and Hörz, F. (1977) Shock Metamorphism of Lunar and Terrestrial Basalts. Proceedings of the Lunar Science Conference, 2, 1697–1729.

Schettino, A., and Scotese, C.R. (2005) Apparent polar wander paths for the major continents (200 Ma to the present day): a palaeomagnetic reference frame for global plate tectonic reconstructions. Geophysical Journal International, 163, 727–759.

Schmieder, M., Jourdan, F., Tohver, E., and Cloutis, E.A. (2014) $^{40}Ar/^{39}Ar$ age of the Lake Saint Martin impact structure (Canada) - Unchaining the Late Triassic terrestrial impact craters. Earth and Planetary Science Letters, 406, 37–48.

Schmieder, M., Kennedy, T., Jourdan, F., Buchner, E., and Reimold, W.U. (2018a) A high-precision $^{40}Ar/^{39}Ar$ age for the Nördlinger Ries impact crater, Germany, and implications for the accurate dating of terrestrial impact events. Geochimica et Cosmochimica Acta, 220, 146–157.

——— (2018b) Response to comment on "A high-precision $^{40}Ar/^{39}Ar$ age for the Nördlinger Ries impact crater, Germany, and implications for the accurate dating of terrestrial impact events" by Schmieder et al. (Geochimica et Cosmochimica Acta 220 (2018) 146–157). Geochimica et Cosmochimica Acta, 238, 602–605.

Schmitt, R.T. (2000) Shock experiments with the H6 chondrite Kernouve: Pressure calibration of microscopic shock effects. Meteoritics and Planetary Science, 35, 545–560.

Schultz, R.A., Jensen, M.C., and Bradt, R.C. (1994) Single crystal cleavage of brittle materials. International Journal of Fracture, 65, 291–312.

Schwarz, W.H., Hanel, M., and Trieloff, M. (2020) U-Pb dating of zircons from an impact melt of the Nördlinger Ries crater. Meteoritics and Planetary Science, 55, 312–325.

Sclar, C.B., Bauer, J.F., Pickart, S.J., and Alperin, H.A. (1973) Shock effects in experimentally shocked terrestrial ilmenite, lunar ilmenite of rock fragments in 1-10 mm fines (10085,19), and lunar rock 60015,127. In Proceedings of the Fourth Lunar Science Conference Vol. 1, pp. 841–859. Pergamon Press, Texas.

Scott, R.G., Pilkington, M., and Tanczyk, E.I. (1997) Magnetic investigations of the West Hawk, Deep Bay and Clearwater impact structures, Canada. Meteoritics and Planetary Science, 32, 293–308.

Seybold, L., Trepmann, C.A., Hölzl, S., Pollok, K., Langenhorst, F., Dellefant, F., and Kaliwoda, M. (2023) Twinned calcite as an indicator of high differential stresses and low shock pressure conditions during impact cratering. Meteoritics & Planetary Science, 19.

Sharp, T.G., and DeCarli, P.S. (2006) Shock effects in meteorites. In D.S. Lauretta and H.Y. McSween, Eds., Meteorites and the early solar system II pp. 653–677. University of Arizona Press.

Shimada, M. (1969) Melting of albite at high pressures in the presence of water. Earth and Planetary Science Letters, 6, 447–450.

Short, N.M. (1970) Progressive shock metamorphism of quartzite ejecta from the Sedan nuclear explosion crater. The Journal of Geology, 78, 705–732.

Sibum, H., Güther, V., Roidl, O., Habashi, F., and Wolf, H.U. (2012) Titanium, Titanium Alloys, and Titanium Compounds. In Ullmann's Encyclopedia of Industrial Chemistry pp. 51–82. Wiley-VCH Verlag GmbH & Co. KGaA, Weinheim, Germany.

Siegert, S., Branney, M.J., and Hecht, L. (2017) Density current origin of a melt-bearing impact ejecta blanket (Ries suevite, Germany). Geology, 45, 855–858.

Sleptsova, I. V., Gilder, S.A., Dellefant, F., Trepmann, C.A., Ahanin, N., and Pohl, J. (*submitted*) Thermal and structural history of impact ejecta deposits, Ries impact structure, Germany. Journal of Geophysical Research: Solid Earth.

Solov'eva, L. V., Kostrovitsky, S.I., Kalashnikova, T. V., and Ivanov, A. V. (2019) The Nature of Phlogopite–Ilmenite and Ilmenite Parageneses in Deep-Seated Xenoliths from Udachnaya Kimberlite Pipe. Doklady Earth Sciences, 486, 537–540.

Spray, J.G. (1992) A physical basis for the frictional melting of some rock-forming minerals. Tectonophysics, 204, 205–221.

Spray, J.G. (1995) Pseudotachylyte controversy: fact or friction? Geology, 23, 1119–1122.

Spray, J.G. (2010) Frictional Melting Processes in Planetary Materials: From Hypervelocity Impact to Earthquakes. Annual Review of Earth and Planetary Sciences, 38, 221–254.

Stöffler, D. (1971a) Coesite and stishovite in shocked crystalline rocks. Journal of Geophysical Research, 76, 5474–5488.

——— (1971b) Progressive metamorphism and classification of shocked and brecciated crystalline rocks at impact craters. Journal of Geophysical Research, 76, 5541–5551.

——— (1972) Deformation and transformation of rock-forming minerals by natural and experimental shock processes. Fortschritte der Mineralogie.

Stöffler, D. (1977) Research drilling Nördlingen 1973: Polymict breccias, crater basement, and cratering model of the Ries impact structure. In H. Schmidt-Kaler, Ed., Geologica Bavarica 75 pp. 163–189. Bayerisches Geologisches Landesamt, Munich.

Stöffler, D., and Grieve, R.A.F. (2007) Impactites. In D. Fettes and J. Desmons, Eds., Metamorphic Rocks: A Classification and Glossary of Terms, Recommendations of the International Union of Geological Sciences pp. 82–92, 111–125 and 126–242. Cambridge University Press, Cambridge.

Stöffler, D., and Hornemann, U. (1972) Quartz and feldspar glasses produced by natural and experimental shock. Meteoritics, 7, 371–394.

Stöffler, D., and Langenhorst, F. (1994) Shock metamorphism of quartz in nature and experiment: I. Basic observation and theory. Meteoritics, 29, 155–181.

Stöffler, D., Ewald, U., Ostertag, R., and Reimold, W.U. (1977) Research drilling Nördlingen 1973: Composition and texture of polymict impact breccias. In H. Schmidt-Kaler, Ed., Geologica Bavarica 75 pp. 163–189. Bayerisches Geologisches Landesamt, Munich.

Stöffler, D., Ostertag, R., Jammes, C., Pfannschmidt, G., Gupta, P.R.S., Simon, S.B., Papike, J.J., and Beauchamp, R.H. (1986) Shock metamorphism and petrography of the Shergotty achondrite. Geochimica et Cosmochimica Acta, 50, 889–903.

Stöffler, D., Artemieva, N.A., Wünnemann, K., Reimold, W.U., Jacob, J., Hansen, B.K., and Summerson, I.A.T. (2013) Ries crater and suevite revisited-Observations and modeling Part I: Observations. Meteoritics & Planetary Science, 48, 515–589.

Stöffler, D., Hamann, C., and Metzler, K. (2018) Shock metamorphism of planetary silicate rocks and sediments: Proposal for an updated classification system. Meteoritics & Planetary Science, 53, 5–49.

Sturkell, E.F.F., and Ormö, J. (1997) Impact-related clastic injections in the marine Ordovician Lockne impact structure, Central Sweden. Sedimentology, 44, 793–804.

Sturm, S., Wulf, G., Jung, D., and Kenkmann, T. (2013) The ries impact, a double-layer rampart crater on earth. Geology, 41, 531–534.

Sturm, S., Kenkmann, T., Willmes, M., Pösges, G., and Hiesinger, H. (2015) The distribution of megablocks in the Ries crater, Germany: Remote sensing, field investigation, and statistical analyses. Meteoritics & Planetary Science, 50, 141–171.

Swanson, S.E., Naney, M.T., Westrich, H.R., and Eichelberger, J.C. (1989) Crystallization history of Obsidian Dome, Inyo Domes, California. Bulletin of Volcanology, 51, 161–176.

Syono, Y., Takei, H., Goto, T., and Ito, A. (1981) Single crystal X-ray and Mössbauer study of shocked ilmenite to 80 GPa. Physics and Chemistry of Minerals, 7, 82–87.

Tada, T., Kurosawa, K., Ono, H., Hamann, C., Okamoto, T., Niihara, T., and Matsui, T. (2022) Shock recovery of granite with a decaying shock wave: feather features formation in quartz.

Tan, W., He, H., Wang, C.Y., Dong, H., Liang, X., and Zhu, J. (2016) Magnetite exsolution in ilmenite from the Fe-Ti oxide gabbro in the Xinjie intrusion (SW China) and sources of unusually strong remnant magnetization. American Mineralogist, 101, 2759–2767.

Taylor, L.A., Williams, R.J., and McCallister, R.H. (1972) Stability relations of ilmenite and ulvöspinel in the Fe-Ti-O system and application of these data to lunar mineral assemblages. Earth and Planetary Science Letters, 16, 282–288.

Teja, A.S., and Koh, P.Y. (2009) Synthesis, properties, and applications of magnetic iron oxide nanoparticles. Progress in Crystal Growth and Characterization of Materials, 55, 22–45.

Temple, A.K. (1966) Alteration of ilmenite. Economic Geology, 61, 695–714.

Teufer, G., and Temple, A.K. (1966) Pseudorutile—a New Mineral Intermediate between Ilmenite and Rutile in the N Alteration of Ilmenite. Nature, 211, 179–181.

Thompson, A.W., and Knott, J.F. (1993) Micromechanisms of Brittle Fracture. Metallurgical Transactions A, 24, 523–534.

Tonti-Filippini, J., Robert, B., Muller, É., Paul, A.N., Dellefant, F., Wack, M., Meng, J., Zhao, X., Schaltegger, U., and Gilder, S.A. (*in preparation*) Middle Neoproterozoic (Tonian) polar wander of South China: Paleomagnetism and U-Pb geochronology of the Laoshanya Formation. Journal of Geophysical Research: Solid Earth.

Trepmann, C.A. (2008) Shock effects in quartz: Compression versus shear deformation - An example from the Rochechouart impact structure, France. Earth and Planetary Science Letters, 267, 322–332.

Trepmann, C.A. (2009) Shock effects and pre-shock microstructures in hydrothermal quartz veins from the Rochechouart impact structure, France. Journal of Structural Geology, 31, 1183–1196.

Trepmann, C.A., and Spray, J.G. (2005) Planar microstructures and Dauphiné twins in shocked quartz from the Charlevoix impact structure, Canada. In T. Kenkmann, F. Hörz, and A. Deutsch, Eds., Large Meteorite Impacts III Vol. 384, pp. 315–328. Geological Society of America Special Paper.

——— (2006) Shock-induced crystal-plastic deformation and post-shock annealing of quartz: Microstructural evidence from crystalline target rocks of the Charlevoix impact structure, Canada. European Journal of Mineralogy, 18, 161–173.

Trepmann, C.A., Götte, T., and Spray, J.G. (2005) Impact-related Ca-metasomatism in crystalline target-rocks from the Charlevoix structure, Quebec, Canada. Canadian Mineralogist, 43, 553–567.

Trepmann, C.A., Dellefant, F., Kaliwoda, M., Hess, K.U., Schmahl, W.W., and Hölzl, S. (2020) Quartz and cristobalite ballen in impact melt rocks from the Ries impact structure, Germany, formed by dehydration of shock-generated amorphous phases. Meteoritics and Planetary Science, 55, 2360–2374.

Tröger, W.E. (1982) Optische Bestimmung der gesteinsbildende Minerale, 188 p. (H.U. Bambauer, F. Taborszky, & H.D. Trochim, Eds.). E. Schweizerbart'sche Verlagsbuchhandlung, Stuttgart.

Tromans, D., and Meech, J.A. (2002) Fracture toughness and surface energies of minerals: theoretical estimates for oxides, sulphides, silicates and halides. Minerals Engineering, 15, 1027–1041.

Tschauner, O., Ma, C., Newville, M.G., and Lanzirotti, A. (2020) Structure analysis of natural wangdaodeite—$LiNbO_3$-type $FeTiO_3$. Minerals, 10, 1–12.

Tullis, J. (1970) Quartz: Preferred orientation in rocks produced by dauphiné twinning. Science, 168, 1342–1344.

Tuthill, R.L., and Sato, M. (1970) Phase relations of a simulated lunar basalt as a function of oxygen fugacity, and their bearing on the petrogenesis of the Apollo 11 basalts. Geochimica et Cosmochimica Acta, 34, 1293–1302.

Ugalde, H.A., Artemieva, N.A., and Milkereit, B. (2005) Magnetization on impact structures - Constraints from numerical modeling and petrophysics. In T. Kenkmann, F. Hörz, and A. Deutsch, Eds., Large meteorite impacts III: Geological Society of America Special Paper 384 Vol. Special Pa, pp. 25–42. Geological Society of America, Boulder.

von Engelhardt, W. (1972) Shock produced rock glasses from the Ries crater. Contributions to Mineralogy and Petrology, 36, 265–292.

——— (1990) Distribution, petrography and shock metamorphism of the ejecta of the Ries crater in Germany-a review. Tectonophysics, 171, 259–273.

——— (1997) Suevite breccia of the Ries impact crater, Germany: Petrography, chemistry and shock metamorphism of crystalline rock clasts. Meteoritics & Planetary Science, 32, 545–554.

von Engelhardt, W., and Graup, G. (1984) Suevite of the Ries crater, Germany: Source rocks and implications for cratering mechanics. Geologische Rundschau, 73, 447–481.

von Engelhardt, W., Arndt, J., Stöffler, D., Müller, W.F., Jeziorkowski, H., and Gubser, R.A. (1967) Diaplektische Gläser in den Breccien des Ries von Nördlingen als Anzeichen für Stoßwellenmetamorphose. Contributions to Mineralogy and Petrology, 15, 93–102.

von Engelhardt, W., Arndt, J., Fecker, B., and Pankau, H.G. (1995) Suevite breccia from the Ries crater, Germany: Origin, cooling history and devitrification of impact glasses. Meteoritics, 30, 279–293.

Wang, Y., Liu, X., Yao, G.D., Liebermann, R.C., and Dudley, M. (1991) High temperature transmission electron microscopy and X-ray diffraction studies of twinning and the phase transition at 145°C in $LaGaO_3$. Materials Science and Engineering A, 132, 13–21.

Weis, R.S., and Gaylord, T.K. (1985) Lithium niobate: Summary of physical properties and crystal structure. Applied Physics A Solids and Surfaces, 37, 191–203.

Whitney, D.L., Broz, M.E., and Cook, R.F. (2007) Hardness, toughness, and modulus of some common metamorphic minerals. American Mineralogist, 92, 281–288.

Wicht, J., and Sanchez, S. (2019) Advances in geodynamo modelling. Geophysical and Astrophysical Fluid Dynamics, 113, 2–50.

Wones, D.R., and Eugster, H.P. (1965) Stability of biotite: Experiment, theory, and application. The American Mineralogist, 50, 1228–1272.

Wright Horton, J., Gibson, R.L., Reimold, W.U., Wittmann, A., Gohn, G.S., and Edwards, L.E. (2009) Geologic columns for the ICDP-USGS Eyreville B core, Chesapeake Bay impact structure: Impactites and crystalline rocks, 1766 to 1096 m depth. Special Paper of the Geological Society of America, 458, 21–49.

Xie, X., Gu, X., Yang, H., Chen, M., and Li, K. (2020) Wangdaodeite, the $LiNbO_3$-structured high-pressure polymorph of ilmenite, a new mineral from the Suizhou L6 chondrite. Meteoritics and Planetary Science, 55, 184–192.

Yang, C., Zhao, H., Bruzzone, L., Benediktsson, J.A., Liang, Y., Liu, B., Zeng, X., Guan, R., Li, C., and Ouyang, Z. (2020) Lunar impact crater identification and age estimation with Chang'E data by deep and transfer learning. Nature Communications, 11, 1–15.

Zhao, Y., and Shadman, F. (1990) Kinetics and mechanism of ilmenite reduction with carbon monoxide. AIChE Journal, 36, 1433–1438.

Živković, Ž.D., Mitevska, N., and Savović, V. (1996) Kinetics and mechanism of the chalcopyrite - Pyrite concentrate oxidation process. Thermochimica Acta, 282/283, 121–130.

Appendix

Abbreviation glossary

SEM	scanning electron microscope
EBSD	electron backscattered diffraction
BSE	backscattered electron
SE	secondary electron
EDS	energy dispersive X-ray spectroscopy
U-Stage	universal tilting stage microscope
EMP(A)	electron microprobe (analysis)
TEM	transmission electron microscopy
PDF	planar deformation feature
PF	planar fracture
FF	feather feature
CPO	crystallographic preferred orientation
NRM	natural remanent magnetization
TRM	thermal remanent magnetization
IRM	isothermal remanent magnetization
CRM	chemical remanent magnetization
LIRM	lightning-induced remanent magnetization
MD	multi-domain
PSD	pseudo-single-domain
SD	single-domain
SP	super-paramagnetic
IUGS	international union of geological sciences

Chemical formulae of minerals

The following information is based on:

Deer, W.A., Howie, R.A., and Zussman, J. (2013) An Introduction to the Rock-Forming Minerals, 3rd ed., 549 p. Berforts Information Press, Stevenage, Hertfordshire.

Fe-Ti-Oxides	
Ilmenite	$Fe^{2+}TiO_3$
Magnetite	$Fe^{2+}Fe^{3+}{}_2O_4$
Hematite	$Fe^{3+}{}_2O_3$
Ferropseudobrookite	$Fe^{2+}Ti_2O_5$
Armalcolite	$(Fe^{2+},Mg)Ti_2O_5$
Pseudobrookite	$Fe^{3+}{}_2TiO_5$
Pseudorutile	$Fe^{3+}{}_2Ti_3O_9$
Rutile	TiO_2
Anatase	TiO_2
Sulfides	
Pyrite	FeS_2
Chalcopyrite	$CuFeS_2$

Silicates	
(α/β-)Quartz	SiO_2
(α/β-)Cristobalite	SiO_2
(α/β-)Tridymite	SiO_2
(α/β-)Stishovite	SiO_2
Feldspar (group)	solid solution of albite – anorthite – kali-feldspar
Plagioclase (group)	solid solution of albite – anorthite
Albite	$NaAlSi_3O_8$
Anorthite	$CaAl_2Si_2O_8$
Kali-Feldspar	$KAlSi_3O_8$
Amphibole (group)	$(Si,Al)_4O_{11}(OH,F,Cl)_2$ with a large variety of cations
Zircon	$ZrSiO_4$
Chlorite (group)	$(Fe,Mg,Al,Zn)_6(Si,Al)_4O_{10}(OH)_8$
Biotite (group)	$K(Mg,Fe^{2+},Mn)_3[(OH,F)_2\|(Al,Fe^{3+},Ti)Si_3O_{10}]$
Sphene	$CaTi[O\|SiO_4]$
Other	
Apatite	$Ca_5(PO4)_3(OH,F,Cl)$
Calcite	$CaCO_3$

Acknowledgements

I am grateful for the supervision of Claudia Trepmann, who entrusted me with the research position, which led to my PhD Thesis. Without her guidance and support in developing my scientific understanding and workflow, only a fraction of the results would have been possible. Furthermore, I thank my second supervisor Stuart Gilder, who always encouraged me to follow my theories and simultaneously achieved to argue against them. Both supervisors motivated me with their spirit, knowledge, and humor and always took their time for discussions, explanations, chats, and jokes; I know that is uncommon!

I thank my colleagues Lisa Brückner and Iuliia Sleptsova for being companions on the way of our rocky paths (but that's why we chose Geosciences) towards the PhD and the collaborative projects with plenty of coffee and tea. Moreover, I highly appreciate the possibility of working with Lina Seybold and Giulia D'Ercole on projects on and off my thesis, which helped me reset and sharpen my mind for scientific questions. The same is true for the ongoing research with Nastaran Ahanin and Justin Tonti-Filippini. The discussions with Wolfgang Schmahl and Kai-Uwe Hess about research questions and everything under the sun (and Sci-Fi) are greatly acknowledged.

The constant support during my Bachelor's, Master's, and the PhD of the curators of the Museum Mineralogia, namely Melanie Kaliwoda, Rupert Hochleitner, and recently Malte Junge, of course, with the presence of Amanda Günther, always created a familiar and comforting atmosphere. The acquisition of sample materials for investigations of the Ries and the Vredefort impact structure wouldn't have been possible without the help of Stefan Hölzl and Ben Weiss, respectively. The direct and fast action by David Planner (IT) and Rosa Susnjar (administration) was a substantial help when needed. Furthermore, the Deutsche Forschungsgemeinschaft is acknowledged for funding the project (DFG Grant no. TR534/9-1). Julian Waldenmaier, Anna Huber, Hans Heusterberg, and Amanda Günther are thanked for proof-reading.

And last but not least, I want to thank my family and friends, especially my partner Milena Auhagen for her support and endurance and my daughter Tara Dellefant for her vitality, who saw the light of the day during my PhD.